Electronic excitations in complex molecular environments

Document status and date:
Published: 08/12/2023

Document Version:
Publisher's PDF, also known as Version of Record (includes final page, issue and volume numbers)

Please check the document version of this publication:

• A submitted manuscript is the version of the article upon submission and before peer-review. There can be important differences between the submitted version and the official published version of record. People interested in the research are advised to contact the author for the final version of the publication, or visit the DOI to the publisher's website.
• The final author version and the galley proof are versions of the publication after peer review.
• The final published version features the final layout of the paper including the volume, issue and page numbers.

[Link to publication](#)

Electronic excitations in complex molecular environments: a computational investigation via many-body perturbation theory

PROEFSCHRIFT

ter verkrijging van de graad van doctor aan de Technische Universiteit Eindhoven, op gezag van de rector magnificus prof.dr. S.K. Lenaerts, voor een commissie aangewezen door het College voor Promoties, in het openbaar te verdedigen op vrijdag 8 december 2023 om 13:30 uur

door

Gianluca Tirimbò

geboren te Frosinone, Italië

Dit proefschrift is goedgekeurd door de promotoren en de samenstelling van de promotiecommissie is als volgt:

voorzitter:	prof. dr. ir. S. Borst
promotor:	dr. B. Baumeier
co-promotor:	prof. dr. R. Coehoorn
leden:	prof. dr. M. Rohlfing (Universität Münster)
	prof. dr. ir. R.A.J. Janssen
	dr. P. Rinke (Aalto University, Aalto University)
	dr. L. Leppert (Universiteit Twente, TNW)

To the ones who fill my heart with boundless love, unwavering support, and endless inspiration offering invaluable companionship along this arduous path we call life.

Summary

This thesis focuses on the study of electronic excitations in complex disordered materials. The primary objectives include the development of a multi-scale modeling approach that combines classical and quantum mechanics to accurately describe electronic excitations, the exploration of specific materials with intriguing characteristics to validate the computational methods, and the advancement of theoretical and computational tools for studying electronic excitations in materials. The theoretical background is presented, covering quantum mechanics, the many-electron problem, and mean-field theories like Hartree-Fock and Density Functional Theory. Furthermore, this work provides an introduction to Green's Functions and the theoretical discussion on ab-initio methods (GW-BSE) for computing excited state properties. Description of the multiscale approach involving classical-quantum embedding (QM/MM) is described. Implementation within localized basis-expansion methods and their application in computational tools like VOTCA-XTP is also explained extensively in the thesis. Various results are presented, where the computational methods are used to interpret experimental spectroscopy data and study the dynamic interactions between localized and charge-transfer excitations in solar cell materials. The thesis concludes with a summary of the contributions and implications of the research.

In summary, this thesis provides valuable insights into electronic excitations in complex materials and presents innovative computational methods for studying these phenomena. The research and the developed methodologies advance the understanding of material properties alongside their quantitative estimation. It paves the way for new methodologies that might be of help for new applications in opto-electronic devices and energy-efficient materials.

Contents

Preliminaries

In this thesis atomic units are used in all equations unless stated otherwise. Frequently used constants are set equal to one: $m_e = \hbar = e = c = 4\pi\epsilon_0 = 1$. The constants are the mass of an electron m_e, the elementary charge e, which is the charge of a proton or the absolute of the charge of an electron, the reduced Planck constant $\hbar$, that connects the frequency of a photon to its energy, and the inverse Coulomb constant $4\pi\epsilon_0$. To clarify the dimensions of certain quantities the constants can be reintroduced later.

"What do we mean by 'understanding' something? We can imagine that this complicated array of moving things which constitutes 'the world' is something like a great chess game being played by the gods, and we are observers of the game. We do not know what the rules of the game are; all we are allowed to do is to watch the playing. Of course, if we watch long enough, we may eventually catch on to a few of the rules. The rules of the game are what we mean by fundamental physics. Even if we knew every rule, however, we might not be able to understand why a particular move is made in the game, merely because it is too complicated and our minds are limited. If you play chess you must know that it is easy to learn all the rules, and yet it is often very hard to select the best move or to understand why a player moves as he does. So it is in nature, only much more so; but we may be able at least to find all the rules. Actually, we do not have all the rules now. (Every once in a while something like castling is going on that we still do not understand.) Aside from not knowing all of the rules, what we really can explain in terms of those rules is very limited, because almost all situations are so enormously complicated that we cannot follow the plays of the game using the rules, much less tell what is going to happen next. We must, therefore, limit ourselves to the more basic question of the rules of the game. If we know the rules, we consider that we 'understand' the world" - **Richard Feynman [1]**

Chapter 1

Introduction

1.1 Electronic excitations in materials

When an incident photon is absorbed by a material, an electron is excited from the valence to the conduction band and leaves behind a positively charged vacancy, a hole. The attractive Coulomb interaction between the excited electron and the hole binds them together to form a bound neutral compound system of the two charge carriers, reminiscent of a hydrogen atom. This coupled excited electron-hole pair is called an *exciton*. An exciton can also be formed by different processes, e.g., from the injection of free electrons and holes into the material. Excitons play a pivotal role in many different phenomena in materials. They determine their optical properties, such as absorption but also emission via fluorescence or phosphorescence [2]. Strongly or weakly coupled electron-hole pairs are not only static objects: they can diffuse through a material, thereby transporting energy with zero net charge [3, 4, 5]. Excitons can also play a role in chemical reactions [6], be intermediates to the generation of free charges in devices [7], and drive biological processes [8], such as photosynthesis. The initial step in these processes of providing chemical energy for plants, algae, and bacteria involves the capture of energy from sunlight. Specialized pigment-protein complexes, called light-harvesting antenna complexes, consist of light-absorbing chromophores, typically attached to a protein structure that holds them in place. Before the molecule can relax, the electronic excitation must be harvested. That is, the excitation is transferred through space among the chromophores until it eventually reaches a reaction center where it initiates charge separation.

Technological applications often exploit the static and dynamic properties of excitons in a similar fashion. Considerable effort is directed at designing either pure or composite materials with target properties to enhance device characteristics, such as optimizing the color of emitted light and increasing stability in organic light-emitting diodes (OLEDs) [9, 10, 11], or boosting the power conversion efficiency in solar cells, to name only a few. A rational design of materials fulfilling these goals relies on the understanding of how the excitonic properties are related to material attributes, e.g., composition, chemical bonding, structural order, etc.

Beside the neutral excitations formed by the electron-hole pair, charged excitations can arise when excited electrons interact with the surrounding medium. For example, in OLEDs, charged excitations play a crucial role in the process of light emission. To optimize light emission and efficiency, OLEDs typically consist of multiple layers, including an emissive layer where the exciton formation and radiative recombination occur. The layers can include charge transport layers, which facilitate the movement of electrons and holes to the emissive layer, as well as electrode layers to apply the necessary voltage. When a voltage is applied across the OLED structure, an electric current flows through the device. This current causes electrons to move from a lower-energy level (called the highest occupied molecular orbital or HOMO) to a higher-energy level (lowest unoccupied molecular orbital or LUMO) in the organic material. This excited state can be intuitively interpreted by looking at the difference with the initial configuration, known as ground-state. In this picture, promotion of an electron to higher energy state can be described as an electron-like excitation, lacking of electrons in a lower energy state as a hole-like excitation whereas the Coulomb interaction between these two charged excitations is the aforementioned exciton. The interplay of the excited electrons and the surrounding is thus embedded in the charged excitation properties. Alongside their application in opto-electronic devices (e.g., charge carrier diffusion or extraction, more on this later), charged single-particle excitations measured in photoelectron spectroscopy (PS). In PS, electrons are ejected from a material upon irradiation with light (technical details explained in later sections, see Section 3.1, Section 5 and Section 6). Which electronic states are probed exactly, depends on the wavelength of the incident radiation. The most common ones use ultraviolet light (UPS) for valence states or X-rays (XPS) for core-level states. These experiments can help to reconstruct the energy profile of occupied states. An important quantity probed with this experiment is the first Ionization Potential (IP), defined as the energy needed to remove an electron from a bound state in a neutral sample. A complementary technique, known as inverse photoelectron spectroscopy, where an incident electron is scattered towards a sample,
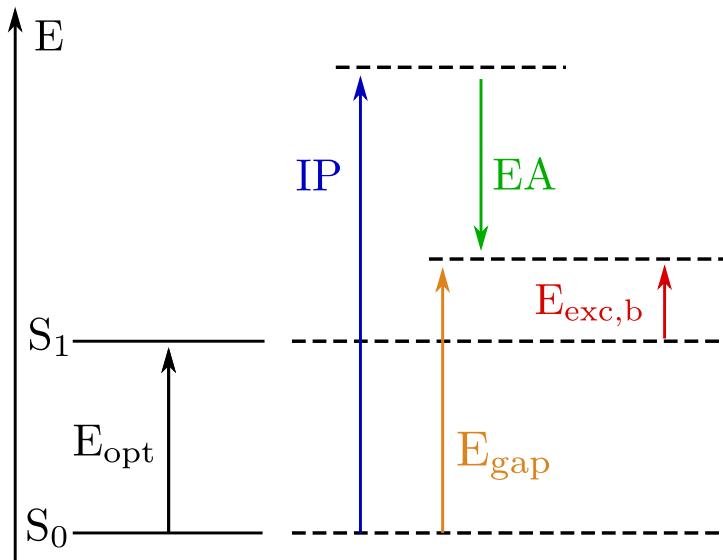
Figure 1.1: Energy diagram of useful quantities in the area of organic semi-conductors: E_{opt} is the energy of the first exciton state. E_{gap} is the difference between the Ionization Potential (IP) and the Electron Affinity (EA). The difference between E_{gap} and E_{opt} is the exciton binding energy, $E_{exc,b}$.

help deducing the spectrum of unoccupied states. In particular, the Electron Affinity (EA), defined as the energy needed to detach an electron from a negatively charged molecule, is often probed with this technique. Summarizing these different excitation energies, as it is often done in opto-electronic devices, it is interesting to look at a single molecule energy diagram depicted in Figure 1.1.

The nature of the excited electronic states is of great interest as it is directly related to processes such as light absorption and emission, photoconductivity, and electroluminescence. Among all the possible key parameters describing the physics of electronic devices such as OLEDs and OPVs, the exciton binding energy plays a pivotal role (as described later in Section 6). Exciton binding energy is defined as

$$E_{exc,b} = E_{gap} - E_{opt} = IP - EA - E_{opt}, \tag{1.1}$$

with E_{gap} being the HOMO-LUMO (or IP-EA) transport gap and E_{opt} the optical

gap. The optical gap can be seen as the energy threshold for photons to be absorbed (or the energy of the first excitonic state), while the transport gap is the threshold for creating an electron-hole pair that is not bound together.

The exciton binding energy can be determined only if a correct description and measurement of both neutral- and charged-excitations is provided. This is sought, for example, by combining both computational and laboratory experiments. Understanding the binding properties of excitons in materials and eventually manipulating them could lead to new applications or to better engineering of already-existing technologies. However, directly or indirectly measuring the required properties is hard to achieve as physical properties like size, shape, composition and arrangement of the molecules in materials under investigation strongly influence the nature and dynamics of the electronic excitation. This makes hard to draw general conclusions or unique interpretation about the behavior of electronic excitations in different materials. For this reason, ab-initio modeling has become appealing to infer information about the excited states when experimental interpretation is hindered by above factors. Computational experiments can be seen as complementary to the experimental ones when in need of quantitative and accurate predictions.

Beside the interest in understanding the underlying physics governing these excitations, quantitative predictions of properties of the different components that constitute the device can serve as input to large-scale simulation where the behavior of devices is reproduced (see [12, 13]). These models, used in lieu of experimental setups by researchers and industries, can help speeding up the engineering and tailoring of new opto-electronic devices. Several parameter-free models have demonstrated notable success in the prediction of crucial device properties such as current-voltage characteristics, charge density, and current density distribution [14, 15, 16]. A simplified example of a multiscale approach, encompassing both spatial and temporal dimensions, can be discerned in Figure 1.2. Starting at the molecular level, denoted as step (a) in the figure, pivotal parameters can be calculated. These parameters encompass the ground-state and excited-state geometries, polarizabilities, multipoles representation of the molecule, force-field parameters, reorganization energies, IP, EA, and $E_{exc,b}$. These quantities constitute a fundamental basis for subsequent stages of the workflow. In the next step of the workflow (b), these computed parameters are employed to construct a microscopic-scale system. This system enables the computation of additional critical quantities, including the microscopic morphology, site energies, electronic coupling elements, and transfer rates. Advancing to an elevated scale in step (c), macroscopic models are employed. These models solve the master equation, allow-

ing for the determination of excitation mobility and the diffusion tensor. These quantities provide valuable insights into the transport of excitations within the system, which is pivotal for understanding charge and energy transfer processes. Finally, in step (d), the knowledge gained from the previous stages is harnessed to develop realistic device models. These models are instrumental in assessing and predicting the device properties mentioned earlier, such as current-voltage characteristics, charge density, and current density distribution. The accuracy of each
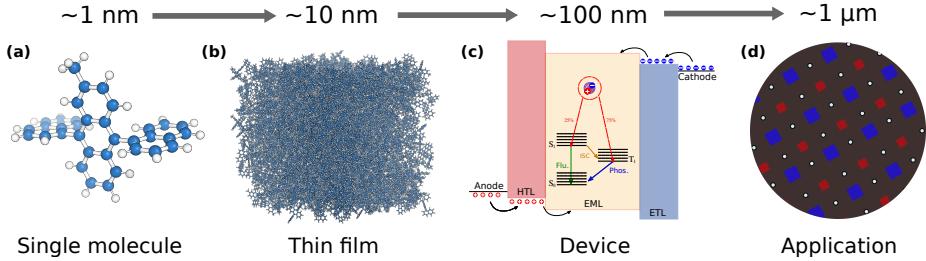
Figure 1.2: Example of multiscale workflow for parameter-less computation of macroscopic properties (a), passing through microscopic models (b) and macroscopic

step affects the goodness of estimate of the next one. Uncertainties trickle up to the next step in the workflow affecting the predictive power. For example, it has been shown [17] that the exciton binding energy must be known accurately when performing OLED simulations (equivalent of step (c) mentioned before) of the efficiency and its roll-off, which are highly sensitive to the input value for exciton binding energy use. Anticipating one of the objective of this thesis, estimate of the input parameters of macroscopic models, must not overlook where a molecule is in the system (bulk or surface) and its environment (i.e., distribution of surrounding molecules). Furthermore, accurate and correct methods must be employed to reduce uncertainties. This thesis aims at providing a reliable framework where inputs for macroscopic models can be computed with high accuracy at a reasonable computational cost.

1.2 Relation between materials properties and characteristics of electronic excitations

Details of the static and dynamic properties of electronic excitations depend on the material in which they form. Materials are in broad terms classified as either inorganic or organic as they differ in their chemical bonding and electronic characteristics. Focusing on excitons as an example, we illustrate the different materials and types of excitons schematically in Figure 1.3. *Inorganic materials* are often well-ordered systems with atoms arranged in regular crystal structures, with either covalent or ionic bonds. As a result, they are structurally rigid and allow very little room for modifications. Traditional inorganic semiconductors such as silicon, germanium, and Gallium arsenide (GaAs) have low band gaps (0.67 eV, 1.11 eV, and 1.43 eV respectively [18]). The dielectric constant in these materials can be large ($\epsilon_r > 10$) so that Coulomb effects between electrons and holes are small due to dielectric screening, with exciton binding energies of only several meV. The excitonic wave function typically extends over several lattice spacings, as indicated in Figure 1.3(a). This is known as a *Wannier–Mott exciton* [19]. For larger bandgap and/or lower dielectric constant, the screening effects become smaller, the exciton binding energy increases to the order of 0.1-1 eV as the excitonic wave function becomes more localized in space, e.g., in alkali halide crystals. Typically, such small-radius excitons are referred to as *Frenkel excitons* [20]. It should be noted, however, that in many situations, the distinction between Wannier–Mott and Frenkel excitons, or Frenkel excitons of different localization lengths, is not sharp, in particular in disordered materials without any clear lattice spacing. *Organic materials* are formed from molecular building blocks and can host Frenkel excitons of vastly varying localization character [21]. While the *intra-molecular* bonding is determined by covalent and ionic interactions, weak cohesive electrostatic and van-der-Waals interactions are responsible for the *inter-molecular* structure formation. As a result, there is in general a plethora of different material structures, ranging from well-ordered organic crystals (mostly at low temperature) to statically and/or thermally disordered structures with varying dimensionality. Often, there are even multiple phases present in the same organic material or material composite as technologically relevant materials are often created from solution processing [22, 23]. Organic materials combine chemical and mechanical benefits of organic compounds, such as tailoring of electronic properties by a modification by chemical synthesis, their light-weight, and flexibility with peculiar properties of semiconductor materials, e.g., the absorption/emission of light in the visible spectral range and conductivity that is sufficient for the operation of devices
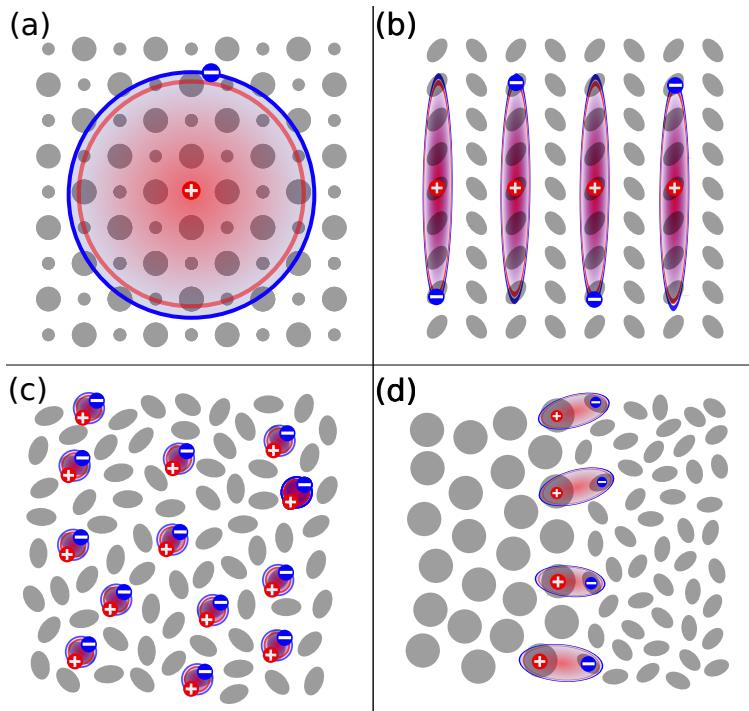
Figure 1.3: Illustration of different kind of excitons in different materials: (a) Small and large circles indicate the positions of atoms on a regular lattice as, e.g., in an MgO bulk crystal, and blue and red show the extension of a weakly bound Wannier–Mott exciton, typical for inorganic semiconductors. (b) Highly ordered molecular crystal structure where each oval represents a molecular unit. The exciton is delocalized over several molecules due to strong inter-molecular excitonic coupling. (c) Disordered (amorphous) molecular material, with Frenkel excitons strongly localized on single molecules. (d) Interface of a donor-acceptor heterostructure of two disordered molecular materials with bimolecular charge-transfer excitons.

such as light-emitting diodes (LEDs), solar cells, and field-effect-transistors. As a consequence of the intrinsically weak inter-molecular interactions and resulting

disorder, electronic states are typically localized on one or several molecular build-ing blocks, leading to low values of the dielectric constant usually in the region of $\epsilon_r = 3 - 4$. In Solar cells and OLEDs, absorption and emission take place mostly in the range of $2 - 3\,\mathrm{eV}$, hindering any significant charge-carrier concen-tration by thermal excitation at room temperature. As mentioned above, the low dielectric constant implies large exciton binding energies and small exciton radii. How small depends on the structural details of the material. Figure 1.3(b) schem-atically depicts a highly ordered molecular crystal. Tight and regular packing motifs can lead to high π-orbital overlap and strong excitonic coupling between the molecules and as a result, the exciton can extend over several units. With increasing disorder in the system as depicted in Figure 1.3(c), the inter-molecular coupling is weak, and typically single-molecule Frenkel excitons can be observed. In *multicomponent materials*, as shown in Figure 1.3(d), one can often find an-other type of exciton that extends over two molecules. Unlike an extended Frenkel exciton in ordered organic morphologies as in Figure 1.3(b), where both electron and hole part delocalize similarly over the molecular building blocks, the so-called *charge-transfer (CT) exciton* [21] is characterized by separation of the two charges on donor and acceptor parts. Due to the increased distance between electron and hole, the exciton binding energy is reduced compared to the Frenkel excitons in the bulk phase. As we will discuss in Section 1.3, the details of the conversion process between localized Frenkel and these bi-molecular CT excitons is a significant step, e.g., in the generation of free charges in organic solar cells. We emphasize that the above distinction between inorganic and organic materials, as well as between Wannier–Mott, Frenkel, and charge-transfer excitons is simplified for the sake of a compact presentation and therefore far from exhaustive. In fact, there are many examples of materials with mixed characteristics. These include perovskites or perovskite-like structures with embedded molecules, such as $CH_3NH_3PbX_3$ with X= I, Br, Cl, in which a $CH_3NH_3^+$ is surrounded by PbX_6 octahedra [24]. Other examples are organic-inorganic hybrids like metal or semiconductor nanoparticles functionalized by organic ligands, or dye-sensitized solar cell materials (e.g., TiO_2 with perylene-based dyes [25]). Furthermore, in soft conjugated polymers, elec-tronic states and thereby also excitons can be subject to changes in localization due to dynamical or static variations in conformations of the π-conjugated backbone, such as torsion angles between repeat units [26, 27, 28].

Figure 1.4: Examples for two applications driven by excitons in organic heterostructures: (a) Layer schematics of an organic light-emitting diode (OLED). Holes (electrons) are injected from the anode (cathode) in hole (electron) transport layers (HTL/ETL) ①, and drift-diffuse into the emission layer (EML) ②. There they form an exciton on one of the emitter molecules ③, which can emit light either by fluorescence of phosphorescence depending on the mechanism. (b) Illustration of the cascade of processes in charge generation at the donor-acceptor interface in an organic photovoltaic cell. Upon excitation by light, a strongly bound Frenkel exciton is formed in the donor phase, which then needs to diffuse toward the interface, where it converts into an intermediate bi-molecular charge transfer exciton. From here separated charges can drift-diffuse to the electrodes.

1.3 Role of electronic excitations in devices

The nature of the different electronic excitations as determined from material properties also has immediate consequences for dynamical processes involving the electron-hole pairs, and their exploitation in device applications [29]. While the binding energy of Wannier–Mott excitons in, e.g., silicon is comparable to the thermal energy, and it is hence possible to generate free charge carriers after photon absorption in silicon solar cells, more complex processes need to be considered in disordered, organic materials. Figure 1.4 illustrates two examples for the vital role involving both single-particle excitations and excitons play in opto-electronic

device applications based on organic heterostructures: organic light-emitting diodes (OLEDs, Figure 1.4(a)) and organic solar cells (Figure 1.4(b)). An OLED device typically consists of several layers, each of which contributes a specific task to the overall device functionality. The schematic in Figure 1.4(a) shows a simple case, in which an emission layer is sandwiched between hole and electron transporting layers, respectively, both contacted to electrodes. The electronic processes needed for actual light emission to occur comprise injection of charge carriers from the electrodes into the transport layers, their drift-diffusion through the transport into the emission layer. Careful tuning of electron and hole transport level, as well as the energies of singlet and triplet excitons is required to ensure that the excitons are formed, and they efficiently emit light via fluorescence or phosphorescence. Significant effort is currently directed at optimizing materials for thermally activated delayed fluorescence, a process in which a molecule is initially in a non-emitting excited state before thermal energy of the surrounding allows it to change to an emissive state, or exciplex emission, i.e., emission from a bi-molecular charge-transfer exciton. The active layer of an organic solar cell is usually a mix of donor and acceptor materials, and the interface between them, as depicted in Figure 1.4(b), plays a prominent role in the charge generation process. As mentioned before, the excitons created upon light absorption in either of the two layers are strongly bound with an exciton binding energy on the order of several tens of eV. Thermal energy alone is therefore not sufficient to separate the excited electron and hole. Instead, the Frenkel excitons diffuse towards the interface at which they can, ideally, undergo a conversion process to a bi-molecular CT exciton with reduced binding energy. This conversion combined with electrostatic energy profiles near the interface, eventually allow the charges to separate and to transfer through the bulk material to the electrodes. In both application examples, the device functionality is directly linked to the static (absorption/emission, recombination) or dynamic (diffusion, conversion, separation) processes involving electronic excitations of various types. Also in more general cases, optimizing the device performance therefore targets to a significant extent the design of materials and material combinations with tailored and well-controlled electronic properties.

1.4 Multi-scale modelling approach at microscopic scale

Controlled use of electronic excitations within materials has paved the way for technological advancements, from the design of cutting-edge opto-electronic devices to

the development of energy-efficient materials. A comprehensive understanding of electronic excitations is hence required for harnessing the full potential of materials. As mentioned above, modeling can be a very powerful tool in this rational design of materials. At the microscopic scale, electron-electron correlations and localized excitations influence the fundamental electronic structure and energy levels of the material. *Ab initio* methods ideally provide some insight into these quantum-level processes without any experimental input. Different theories and computational methods are available nowadays, each with its pros, cons and range of suitable application cases. However, as materials grow in complexity, encompassing thousands or millions of atoms, and real-world conditions arise, the computational burden of simulating such systems with high accuracy becomes overwhelming.

Macroscopic phenomena including optical absorption, luminescence, electrical conductivity, and other bulk or surface material properties cannot be captured with microscale models alone because of the interplay of numerous interactions across large length and time scales. As a consequence, the study of electronic excitations in complex disordered systems remains a challenge for ab-initio computational methods. A solution towards a methodology that bridges the gap between microscopic and macroscopic realms, unlocking new insights into electron excitations with materials, is thus required. In the specific, an important realization revolved around the fact that electronic excitations strongly localize on single molecules (or a limited number of molecules) due to the disorder of the large-scale morphology, and thus the interaction of this active exciton with the surrounding can be described with lower-level (i.e, less expensive) methods. Multiscale modelling has provided a mitigating solution to this conundrum, offering a coherent framework to reconcile the microscopic and macroscopic perspectives. By combining different quantum mechanical approaches (with different levels of accuracy and computational costs) or quantum mechanical approaches with classical and semi-classical methods, multiscale modelling enables the exploration of electron excitations across a wide range of length and time scales.

Various strategies have been proposed throughout the years to split the system into an 'active' portion of space, where the highest desired level of Quantum Mechanical (QM) treatment is performed, and an 'environmental' surrounding medium (a solvent, a metallic nanoparticle, a disordered (polymeric phase), etc.) that is considered at a lower level of theory. This lower level can be either a simplified QM model (QM/QM') (Dvorak et al. [30] explored embedding of wave function theories with Green's functions as Manby et al. [31] proposed a generalized and flexible QM-in-QM embedding scheme used to explore excited states [32, 33]), a molecular mechanics (MM) approach (QM/MM) [34, 35, 36, 37], or a continuum model [38]

representing the environment as a structure-less material having realistic macro-scopic dielectric properties. The combination of high-level quantum mechanical calculations and accurate MM electrostatics enables the study of complex systems where electronic excitations and solvent effects are critical. What set the QM/MM method apart is its ability to provide accurate descriptions of electronic excitations, account for complex interactions with the environment, and balance computational efficiency and accuracy. This makes it well-suited for investigating systems with challenging electronic structures, solvent effects, and intricate molecular arrangements, ultimately leading to a deeper understanding of a wide range of chemical and biochemical processes. Nevertheless, challenges and limitations stay and different approaches must be tailored to answer specific scientific objectives.

One of the objective of this thesis is the potential for predictive insights with a reasonable computational cost: the integration of multiple advanced computational techniques provides a platform for generating predictive insights into various chemical and physical phenomena. In other words, the aim of this work was not only understanding qualitatively the dynamics of a process influenced by environmental effects but also the ability to give accurate prediction that can help, for example, accurate extrapolation of quantity of interest from experimental measurements and provide reliable input quantities to be used in higher scale models (e.g., kinetic models). Whether it is predicting spectroscopic properties, or material behavior, the method proposed in this thesis allows to gain a comprehensive understanding of complex systems and phenomena keeping the computational cost on budget.

In this specific work, this objective is sought by combining high-level quantum mechanical treatment of the active zone by the GW-BSE method (based on the many-body perturbation theory) with the treatment of the environmental effects treated via a multipole representation. The GW-BSE method is a sophisticated and computationally intensive approach that goes beyond the limitations of standard density functional theory (DFT) methods (see Section 2.5 and Section 3). It provides a more accurate description of electronic excited states, which are crucial for studying properties like emission spectroscopy, optical absorption, charge transfer, and excited-state dynamics. The environment is instead described via a multipole representation: Molecular mechanics (MM) force fields often use atom-centered point charges to represent electrostatic interactions. However, these charges might not adequately capture long-range interactions and polarization effects. By using a multipole representation, which considers higher-order moments of charge distributions, more accurate treatment of electrostatics becomes pos-

sible. This is particularly valuable in cases where electrostatic interactions play a significant role, such as in studying solvent effects. Furthermore, developing and implementing an effective QM/MM approach (see Section 4.2) that incorporates GW-BSE calculations and a multipole MM representation requires innovation in both theoretical methodologies and computational software. Working on this integration contribute to the advancement of computational chemistry methods, expanding the capabilities of the field.

1.5 Thesis objectives and addressed questions

This thesis aims to address the multifaceted challenges in the field of electronic excitations in complex materials, with three distinct objectives:

1. **Method Objective**:
   The primary methodological objective of this research is to explore the feasibility of combining classical and quantum mechanics to get comprehensive insights into the behavior of realistic organic materials. Traditional classical mechanics offers efficient and computationally inexpensive tools for simulating large-scale systems, while quantum mechanics provides the necessary accuracy to describe the intricate electronic interactions at the atomic/molecular level. By devising a hybrid approach that seamlessly integrates these two realms, we seek to develop a powerful framework that can accurately capture both the macroscopic properties of materials and the microscopic intricacies of their electronic excitations. Quantum Mechanics/Molecular Mechanics (QM/MM) simulations are a powerful class of computational methods used to study complex molecular systems that involve both quantum mechanical and classical mechanical interactions. The basic idea behind QM/MM is to treat a part of the system (usually the active region of interest) using accurate quantum mechanical methods, while treating the remaining part with a faster and less computationally demanding classical force field. The use of GW-BSE calculations in the QM region allows for a highly accurate description of electronic excitations, such as optical transitions and charge transfer processes. Many traditional methods, including standard DFT, struggle to provide reliable predictions for these excited states. Thus, the inclusion of GW-BSE within a QM/MM framework is advantageous when studying systems where excited-state properties are crucial. The MM treatment should adequately capture long-range interactions and polarization effects. By using a multipole representation, which considers higher-order

moments of charge distributions, more accurate treatment of electrostatics becomes possible. This is particularly valuable in cases where electrostatic interactions play a significant role. The successful realization of this objective will improve our ability to study complex materials under realistic conditions for innovative advancements in material science and device engineering.

2. **Material Objective**:
Localized and delocalized (in the sense of bi-molecular) electronic excitations are addressed in this thesis. We selectively choose materials that have already demonstrated intriguing characteristics and properties, making them an ideal playground to test and validate our computational techniques. In the specific, for the former type of excitation, we focus on breaking down the underlying process governing photoelectron spectroscopy measurements of molecular thin films. As prototypical systems, we study the UPS spectrum for thin films of the α and β isomers of 2-methyl-9,10-bis(naphthalen-2-yl)anthracene (MADN). MADN is a morphologically stable amorphous wide-gap semiconductor that is used extensively as an ambipolar host material in OLEDs containing deep blue fluorescent emitter molecule. The interest for these materials lies in the fact that the measured spectra for these two materials show that the peak full width at half maximum is significantly smaller than for many other often-used hole transporting and emitting materials in OLEDs. Furthermore, the HOMO state is well-separated from the deeper levels. The selection of the two isomers enables us to study the effects of morphology differences and the related effects on energy level shifts due to the small molecular dipole moments. The success of a quantitative reproduction of the HOMO spectrum (UPS) motivate us to investigate the possible application of our technique also for unoccupied state (IPS) and absorption spectra. For bi-molecular excitations, we study an amorphous morphology with low-donor content composed of fullerene (C_{60}) and 5,6,11,12-tetraphenyltetracene (rubrene). Because of the low-donor content, a C_{60} cluster will surround the donor molecule, making the interaction between the single donor molecule with a close shell of neighboring C_{60} acceptors representative of the properties of the system as a whole. These complexes are therefore meaningful candidates for a computational analysis of the influence of donor-acceptor conformations and environment polarization effects. A GW-BSE based non-adiabatic coupling description has been employed to produce a rate-based model that describes the conversion dynamic between localized and charge transfer excitations. These selected

materials serve as excellent testbeds for our innovative methods, allowing us to rigorously assess the efficacy and accuracy of our computational models.

3. **Theoretical and Computational Objective**:
   The third objective of this thesis centers on contributing to the field of computational materials' science by implementing multi-scale methods and other innovative techniques into an open-source code. As mentioned before, computational tools play an increasingly pivotal role in studying electronic excitations, but their efficacy largely depends on the efficiency and scalability of the underlying algorithms. By integrating multiscale methods, such as quantum-mechanical simulations, molecular dynamics, and other approaches, we aim to create a versatile computational platform that can accurately model diverse materials and phenomena. Additionally, ensuring the code's open-source nature will foster collaboration, transparency, and wider dissemination of our findings within the scientific community. By achieving this computational objective, we aim to provide researchers with an accessible and efficient tool that empowers the exploration of electronic excitations in materials and accelerates the discovery of new materials with tailored properties.

These objectives can be summarized into questions that have been addressed throughout the thesis, namely:

1. How to combine GW-BSE with classical methods, taking into account thin-film and bulk morphologies?

2. Is it possible to provide quantitative predictions of experimental spectra (UPS, IPS and Absorption)? Can device models be informed from such first-principle analyses?

3. Is it possible to compute GW-BSE/MM based non-adiabatic coupling elements to be used in rate-based model to describe conversion dynamic between localized and charged transfer excitations?

Multiscale simulation approaches, in which the transport of excitations across a material is modeled as a series of bi-molecular transfer events, each of them described by an effective transfer rate.

1.6 Thesis outline

This work is structured in the following way: In Ch. 2 an overview of the theoretical background underlying the work of this thesis is presented. A brief introduction to quantum mechanics and the description of the many-electron problem is presented. An overview of the most common mean-field theories Hartree-Fock and Density Functional theory respectively, are illustrated. A short summary of wavefunction-based methods is also presented. In Ch. 3 a really brief introduction to Green's Functions including some definitions useful to understand the theoretical discussion about ab-initio mehtods to compute excited state properties of materials. In Ch. 4 details of the implementation of the aforementioned techniques are presented. A broad introduction to localized basis-expansion is given followed by a detailed description of its implementation in VOTCA-XTP. It follows an overview of some applications and results using the theory and the computational methods described in the previous part is presented. Ch. 5 and Ch. 6 chapters show how ab-initio many-particles theories, with the inclusion of a classical polarizable embedding and their computational implementations help bridging the gap with experimental spectroscopy and the underlying physics of these experiments. Spectroscopy experiments are used to measure quantities like ionization potential, electron affinity and optical gap. These are useful ingredients to get another meaningful quantity that cannot be measured directly, like the exciton binding energies. The computational methods that we developed helped deconvolving the uncertainty behind the interpretation of experimental spectra, becoming a useful tool towards a more controlled engineering of opto-electronic devices. The same theoretical and computational methods are not only useful in understanding single particle excitations but also two-particles excitations. In Ch. 7, the dynamic between localized and charge-transfer excitations are studied for a prototypical solar cell material in which there is a low-donor content, an ideal experimental setup where to prove the methods described above. Other than the computation of localized and charge-transfer excitons in a polarizable environment, non-adiabatic coupling has been studied comparing different diabatization methodologies providing qualitative and quantitative predictions. A minimal kinetic model of the conversion from localized excitation and charge-transfer state population stability based on Marcus rates is presented. The thesis is wrapped up in the conlclusion chapter (Ch. 8).

Chapter 2

Electronic Structure Theory

> All models are wrong. Some of them are useful
>
> ——————————————
>
> George Box

In this chapter an overview of the theoretical background underlying the work of this thesis is presented. The scope is to give a comprehensive summary to guide the reader throughout the rest of the thesis, in particular towards the description of excited state calculation presented in the next chapter. A brief introduction to quantum mechanics and the description of the many-electron problem is presented. An overview of the most common mean-field theories, Hartree-Fock and Density Functional theory respectively, are illustrated. A short summary of wavefunction-based methods is also presented. In the following the Dirac notation will be used, whenever comes handy, interchangeably with the real space representation of wavefunctions and operators.

2.1 Quantum Mechanics Theory

2.1.1 Classical Hamiltonian Dynamics

Any real physical system can be reduced, in its essence, to the study of the dynamics of interacting particles. Classically, a system of N particles can be described

using Hamiltonian mechanics [39]. For the purpose of this work the non-relativistc Hamiltonian function for a system of N particles is considered.

The time-dependent Hamiltonian depends on the spatial coordinates ($\mathbf{q}(t)$) of the N particles and their momenta ($\mathbf{p}(t)$). Labeling the mass of the i-th particle with m_i moving in a potential $V(\mathbf{q}(t), t)$, the Hamiltonian reads as

$$\mathcal{H}(\mathbf{q}(t), \mathbf{p}(t), t) = \sum_{i=1}^{N} \frac{\mathbf{p}_i(t) \cdot \mathbf{p}_i(t)}{2m_i} + V(\mathbf{q}(t), t) \tag{2.1}$$

with

$$\begin{aligned} \mathbf{q}(t) &= (\mathbf{q}_1(t), \ldots, \mathbf{q}_i(t), \ldots, \mathbf{q}_N(t)), \\ \mathbf{p}(t) &= (\mathbf{p}_1(t), \ldots, \mathbf{p}_i(t), \ldots, \mathbf{p}_N(t)). \end{aligned} \tag{2.2}$$

Eq. (2.1) states that the total energy of the system is given by the sum of the kinetic contribution and the potential energy. The interplay between these two contributions is what drives the system over time.

In classical mechanics the state of a system is given by a point ($\mathbf{q}$,$\mathbf{p}$) in the N dimensional space of coordinates and momenta. Choosing the initial positions and momenta of a collection of particles allows to describe the evolution of the system at any given time. $\mathbf{q}(t)$ and $\mathbf{p}(t)$ evolve following the equations of motion known as Hamilton's equations. For a system made of a single particle, the Hamilton's equation reads

$$\begin{aligned} \frac{dq_\alpha}{dt} &= \frac{\partial \mathcal{H}}{\partial p_\alpha}, \\ \frac{dp_\alpha}{dt} &= -\frac{\partial \mathcal{H}}{\partial q_\alpha}. \end{aligned} \tag{2.3}$$

with α a generic component of position and momentum vectors.

2.1.2 Quantum Mechanics and the Schrödinger Equation

In the realm of quantum mechanics, the *position-momentum uncertainty principle* [40] prevents from precisely predicting a system's dynamics using specific position and momentum values. Indistinguishable particles and experimental evidences [1] also challenge determinism. *Quantum mechanics*[1] introduces a paradigm shift with the wavefunction concept, replacing the classical $\mathbf{q}$ and $\mathbf{p}$ description. The state of a system is described by an object called wavefunction $\Phi(t)$. There is

---

[1]For a detailed understanding on the basic principles of quantum mechanics, refer to Appendix C.

no physical interpretation for this function. However, its squared absolute value, $|\Phi(t)|^2$, is interpreted as the *probability amplitude* of finding the system in that state. Measurements of physical observables, such as energy, position, and momentum, are described by operators that act on the wavefunction. The wavefunction $\Phi(t)$ provides probabilities for various measurement outcomes by encapsulating the potential results of an experiment. After measurement, $\Phi(t)$ transforms into a probability distribution for specific outcomes. This measurement process introduces non-deterministic effects, yet these effects are statistically predictable. The time evolution of the wavefunction is determined via the *Schrödinger equation.* The non-relativistic Schrödinger equation reads:

$$\hat{H}\Phi(t) = i\frac{\partial}{\partial t}\Phi(t). \tag{2.4}$$

$\hat{H}$ is the Hamiltonian operator of the system corresponding to the total energy of that system, including both kinetic energy and potential energy. Its spectrum, the system's energy spectrum or its set of energy eigenvalues, is the set of possible outcomes obtainable from a measurement of the system's total energy. Once $\hat{H}$ is known, the evolution of the system is in principle known by solving Eq. (2.4).

2.2   The many-electron problem

Atoms, molecules and solid are systems composed of charged atomic cores (nuclei) and electrons that mutually interact.
The Hamiltonian in this case is defined as

$$\hat{H} = -\frac{1}{2}\sum_{i=1}^{N}\nabla_i^2 - \frac{1}{2}\sum_{I=1}^{K}\frac{\nabla_I^2}{M_I} + \sum_{I=1}^{K}\sum_{J>I}^{K}\frac{Z_I Z_J}{|\mathbf{R}_I - \mathbf{R}_J|} - \sum_{i=1}^{N}\sum_{I=1}^{K}\frac{Z_I}{|\mathbf{r}_i - \mathbf{R}_I|} \tag{2.5}$$

where the first two terms are kinetic energy contributions for electrons and nuclei respectively (from now on called $\hat{K}_e$ and $\hat{K}_{nucl}$). The remaining terms originate from the electron-electron ($\hat{H}_{e-e}$),nuclei-nuclei ($\hat{H}_{nucl-nucl}$) and electron-nuclei Coulomb interaction ($\hat{H}_{e-nucl}$), respectively. For these systems, the stationary (time-independent) Schrödinger equation is

$$\hat{H}\Psi(\mathbf{x}, \mathbf{R}) = E\Psi(\mathbf{x}, \mathbf{R}). \tag{2.6}$$

This equation stems from Eq. (2.4) assuming that the Hamiltonian $\hat{H}$ does not explicitly depend on time and expressing its solution as $\Psi(\mathbf{x}, \mathbf{R}, t) = \exp\{-iEt\}\Psi(\mathbf{x}, \mathbf{R})$.

In this context $\Psi(\mathbf{x}, \mathbf{R})$ is the many-body wavefunction with energy E. This energy depends on the spatial coordinates $\mathbf{R} = \{\mathbf{R}_1, \ldots, \mathbf{R}_K\}$ of K nuclei with nuclear charges $\{Z_1, \ldots, Z_K\}$. The electronic spatial coordinates $\mathbf{r} = (\mathbf{r}_1, \ldots, \mathbf{r}_N)$ and their spin coordinates $\{s_i\}$ of the N electrons are conveniently condensed in one generalized coordinate $\mathbf{x}$.

Having set the problem in Eq. (2.6), with the Hamiltonian defined Eq. (2.5), is far from being the end of the story. The complexity of the interaction terms in Eq. (2.5) does not allow for analytic solutions in most of the problems of interest. The formulation's historical success enabled solving Hydrogen-like systems analytically, e.g., one electron with one nucleus. These, along with the particle in a box and harmonic oscillator, are explicit in quantum mechanics [41]. On the other hands, systems like helium, with two electrons, lacks an analytical solution due to the unsolvable three-body problem in both classical and quantum mechanics [41]. This is due to the electron-electron Coulomb interaction term in Eq. (2.8) is a two-particle operator, correlating the motion of the electrons.

With no analytic solution available, a possible alternative might be to solve the Schrödinger equation numerically. This has proven to be impractical as well. When looking at a system of N particles (both electrons and nuclei), the wave function Φ depends on $3N$ coordinate, ignoring the spin and time for the sake of simplicity. A naive attempt could involve the discretization of the wavefunction on a spatial grid. Even when choosing a very coarse grid, let us say of 10 grid points in each spatial direction, 10^{3N} values are needed to be stored in order to describe the wave function on the grid. As a proxy one might consider a water molecule. This molecule has 10 electrons and 3 nuclei. Therefore, 10^{39} values need to be stored. This corresponds to a memory occupation of 10^{30} Gb. This memory requirement is just to store the wavefunction: the operations involved in applying the Hamiltonian and solving Eq. (2.6) make de facto this approach unfeasible, even for the most powerful computers. These difficulties motivate the search of alternative approaches with more favorable scaling properties.

2.3 Born-Oppenheimer Approximation

A first step towards the solution of the many-body problem relies on the Born-Oppenheimer approximation [42]. Within this approximation the motion of nuclei and electrons can be decoupled. Since the typical mass M of nuclei is larger than the electronic mass m_e ($\frac{m_e}{M} \sim 10^{-3} - 10^{-4}$), the velocity of the nuclei is much smaller and one supposes that electrons adjust instantly to changes in the nuclei

positions. Electrons during their dynamics 'see' the nuclei fixed in their position. In the Born-Oppenheimer approximation the total wavefunction Ψ in Eq. (2.6) and Eq. (2.5) is expressed as the product of an electronic wavefunction and a nuclear one ($\Psi^{el}(\mathbf{x}; \mathbf{R})$ and $\Phi(\mathbf{R})$ respectively). This enables a separation of the Hamiltonian operator into electronic and nuclear terms, where cross-terms between electrons and nuclei are neglected. In this way it is possible to define a simpler coupled system of equations:

$$\hat{H}_{el}(\mathbf{R}) \equiv \hat{K}_{el} + \hat{H}_{e-e}(\mathbf{R}) + \hat{H}_{e-nucl}(\mathbf{R}) \tag{2.7}$$

$$\hat{H}_{el}(\mathbf{R})\,\Psi^{el}(\mathbf{x}; \mathbf{R}) = E_{el}(\mathbf{R})\Psi^{el}(\mathbf{x}; \mathbf{R}) \tag{2.8}$$

$$\left[\hat{K}_{nucl} + E_{el}(\mathbf{R})\right]\Phi(\mathbf{R}) = E\,\Phi(\mathbf{R}) \tag{2.9}$$

In other words, any electronic rearrangement happens in an environment of fixed nuclei in the position $\mathbf{R}$. Once electrons are relaxed (Eq. (2.8)), nuclei move in an effective electronic potential (Eq. (2.9)). Nuclei position enters in Eq. (2.8) only as parameters. The parametric dependence of Ψ^{el} and E_{el} on $\mathbf{R}$ means that for different sets of fixed nuclear coordinates $\mathbf{R}$ we have different electronic Schrödinger equations with different solutions Ψ^{el} and E_{el}, or, in other words, that the electronic Schrödinger equation written above is a family of equations parametrized by $\mathbf{R}$, rather then one equation. This approximation is just the first step towards a computational affordable solution of a many-electron problem. The numerical solution is still too expensive for the same argument used in the previous paragraph. Analytical solutions are not possible as well because the electron-electron Coulomb interaction term in Eq. (2.8).

In Section 7.1.3 we will discuss how to go further the Born-Approximation and its importance in applications. This is important for those cases in which the adiabatic approximation breaks down. Figure 2.1 shows a ficticious example of two adiabatic potential energy surfaces for the ground state and first excited state of a two coordinate molecular system. As long as the nuclei moves away from the close-contact point the adiabatic approximation is valid. Close to the contact-point the adiabatic approximation breaks down. To alleviate the computational demand *mean-field theories* can be beneficial. In these theories the many-body system is reduced to the problem of independent electrons moving in an effective potential that includes all the correlations coming from the remaining electrons. The two most important ones are the Hartree-Fock (HF) Theory and Density Functional Theory (DFT).
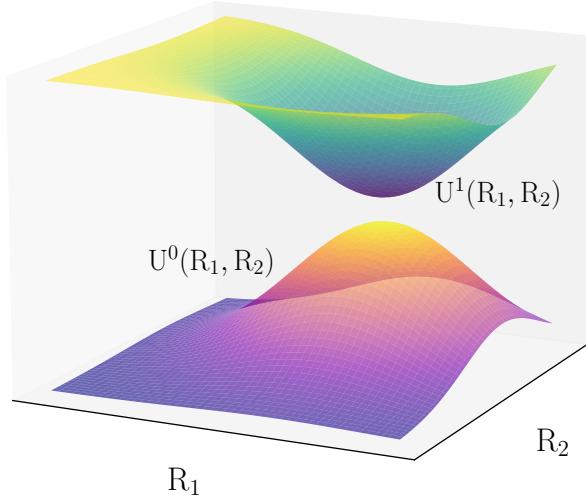
Figure 2.1: Adiabatic potential energy surface for the ground state and first excited state of a two coordinate molecular system. In the point where they approach each other, the adiabatic approximation is not longer valid to describe the dynamics.

2.4   Hartree-Fock Theory

2.4.1   Variational principle

Solving fully Eq. (2.8) is unfeasible for a realistic system, such as small molecules or crystal structure. Nevertheless, one can adopt strategies to compute at least the ground state (state of minimal energy) wave function Ψ_0 and energy E_0. To this end, one might use the so-called *variational principle* [43]. Let us choose an arbitrary trial many-body wave function Ψ^{trial} as ansatz for the the ground-state

wavefunction. The variational principle states that the corresponding energy is always larger than the ground state energy except when Ψ^{trial} equals the real ground state. In math,

$$E_{\text{trial}} = \langle \Psi_{\text{trial}} | \hat{H}_{\text{el}} | \Psi_{\text{trial}} \rangle, \tag{2.10}$$

$$E_0 = \langle \Psi_0 | \hat{H}_{\text{el}} | \Psi_0 \rangle, \tag{2.11}$$

$$E_{\text{trial}} \geq E_0 \tag{2.12}$$

The ground-state energy and wavefunctions can be systematically found searching all the admissible trial many-body wave functions such that

$$E_0 = \min_{\Psi^{\text{trial}}} E[\Psi^{\text{trial}}]. \tag{2.13}$$

Varying over the entire Hilbert space is usually too complicated, and a subspace of it is chosen. This is achieved by parametrizing the trial wavefunction by some (real) differentiable parameters α_i with $i = 1, \ldots, n$. The choice of the subspace is called the ansätz. Some choices of ansatzes lead to better approximations than others, therefore the choice of ansatz is important.

There is no general rules to chose the ansatz. However, since we are dealing with a system of many electrons, there are some physical constraints to be satisfied. One of those is the *Pauli exclusion principle*. Briefly this principle states that N electrons are forbidden to occupy the same quantum state. This reflects in the following mathematical property.

$$\Psi(\mathbf{x}_1, \ldots, \mathbf{x}_i, \mathbf{x}_j, \ldots, \mathbf{x}_N) = -\Psi(\mathbf{x}_1, \ldots, \mathbf{x}_j, \mathbf{x}_i, \ldots, \mathbf{x}_N) \tag{2.14}$$

In other words, the many-electrons wavefunction must be antisymmetric under exchange of electronic coordinates. This allows the system wavefunction to be zero in case two particles share the same quantum state properties.

The second physical constraint concerns the number of electrons in the system. Assuming the many-electron wavefunction to be known, it is possible to define a charge density $n(\mathbf{r})$ as

$$n(\mathbf{r}) = N \sum_{s_1} \cdots \sum_{s_N} \int \cdots \int |\Psi(\mathbf{x}_1, \ldots, \mathbf{x}_N)|^2 \sum_{i=1}^{N} \delta(\mathbf{r} - \mathbf{r}_i) \, d\mathbf{r}_1 \ldots d\mathbf{r}_N. \tag{2.15}$$

Integrating the density over a volume encompassing the whole system we obtain the number of electrons in the system. In formula,

$$\int n(\mathbf{r}) \, d\mathbf{r} = N. \tag{2.16}$$

Good ansätze must satisfy this condition. In the following some possible ansätze are presented.

Example of variational principle: the Helium atom

The electronic Hamiltonian for the Helium atom (1 nucleus of charge $Z = 2$ and 2 electrons) is defined as (leaving the spin variables aside for simplicity) [41]

$$\left[-\frac{\nabla_1^2}{2} - \frac{\nabla_2^2}{2} - \frac{Z}{\mathbf{r}_1} - \frac{Z}{\mathbf{r}_2} + \frac{1}{|\mathbf{r}_1 - \mathbf{r}_2|} \right] \psi(\mathbf{r}) = \mathrm{E}\,\psi(\mathbf{r}) \tag{2.17}$$

The five terms in the Hamiltonian represent, respectively, the kinetic energies of electrons 1 and 2, the nuclear attractions of electrons 1 and 2, and the repulsive interaction between the two electrons. The last contribution of Eq. (2.17) makes this problem analytically unsolvable. Let us assume for a moment that this term is not there. In this case the resulting Hamiltonian is fully solvable, and the two electron coordinates can be separated, reducing the problem to two independent hydrogen-like systems. The solution for the ground state (gs) in this special case is the product of two hydrogen-like system ground state system wavefunctions $\psi_{gs}(\mathbf{r}_1, \mathbf{r}_2) \propto \exp\{-Z|\mathbf{r}_1 - \mathbf{r}_2|\}$ [44]. This would correspond to a ground-state energy of -4 Hartree. This value is very different form the experimental value of -2.90372 Hartree. This is not surprising since no correlation/interaction among electrons was considered. Guided by this result, the variational principle can be used. If a trial ground-state wavefunction is used $\psi_{\mathrm{trial}}(\mathbf{r}_1, \mathbf{r}_2) \propto \exp\{-\alpha|\mathbf{r}_1 - \mathbf{r}_2|\}$, with α a parameter to be tuned. If this ansätz is used in Eq. (2.10), a parametric equation for the ground state energy is found. In the specific

$$\mathrm{E}(\alpha) = \alpha^2 - 2Z\alpha + \frac{5}{8}\alpha \tag{2.18}$$

minimizing respect to α, the lowest ground-state energy given the ansatz is obtained for $\alpha = Z - \frac{5}{16}$. A physical interpretation can be given, noting that the parameter α in the approximate wavefunction represents an effective nuclear charge. Each electron partially shields the other electron from the positively-charged nucleus by an amount equivalent to $\frac{5}{16}$ of an electron charge. This provides an energy of -2.84765 Hartee, differing from the experimental value of about 2%. This example shows how Eq. (2.11) holds, as expected by the variational principle. All in all this simple example showed the power of the variational principle as a tool to overcome the difficulties of the Schrödinger equation. Furthermore, the independent-electrons ansatz worked to be a successful starting point for the quest
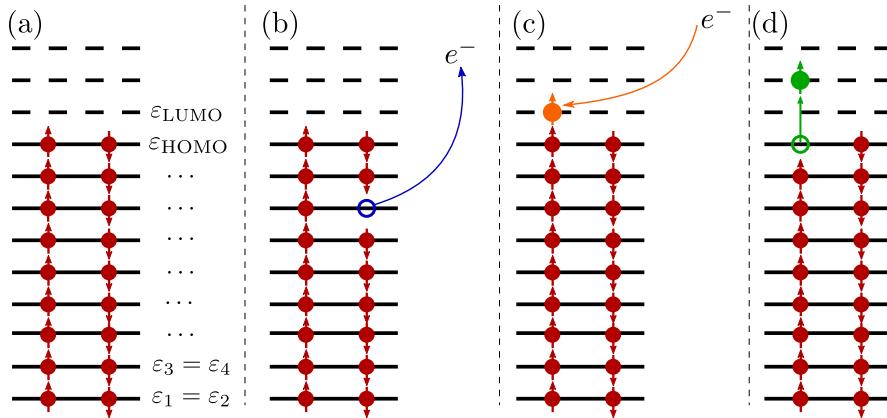
Figure 2.2: (Schematic representation of the single-electron occupation of molecular energy levels. As explained in the main text electrons occupy, starting from the bottom, all the energy levels until no more electrons are available. Only two electrons, with opposite spin, can share the same energy level (Pauli's exclusion principle). In (a) the ground-state configuration is depicted. Here is possible to define the HOMO and LUMO energies. In (b) the electron removal case is depicted, in (c) the electron addition as in (d) the case of electron promotion. All these scenarios are described within the independent-particle picture.

of an approximate solution inspiring powerful methods like the Hartree, Hartree-Fock and Density Functional Theory as we are about to show in the coming sections.

2.4.2 Independent particles approximation

As shown in the previous example, the simplest possible approximation that one can make is the limit of vanishing Coulomb interactions, or non-interacting single-particles. Despite this being a very crude approximation, this approach allows for a simple intuition of some complex concepts of pivotal importance for understanding material properties. It also allows a simple way to introduce the proper terminology that will be used throughout the whole manuscript.

The N non-interacting electrons Hamiltonian can be expressed as the sum of single-electron Hamiltonians $\hat{h}_i$

$$\hat{H}_{el}(\mathbf{R}) \approx \hat{K}_{el} + \hat{H}_{e-nucl}(\mathbf{R}) = \sum_{i=1}^{N} \hat{h}_i \tag{2.19}$$

and the corresponding N electron wave function $\Phi^0(\mathbf{r}; \mathbf{R})$ is simply a product of single-particle functions

$$\Phi^0(\mathbf{r}; \mathbf{R}) = \prod_{i=1}^{N} \phi_{\nu_i}^0(\mathbf{r}_i). \tag{2.20}$$

These single-particle functions are solutions to the single-particle Schrödinger equation

$$\hat{h}_i \phi_{\nu_i}^0(\mathbf{r}_i) = \varepsilon_{\nu_i}^0 \phi_{\nu_i}^0(\mathbf{r}_i) \tag{2.21}$$

where $\varepsilon_{\nu_i}^0$ is a single-particle energy. The total energy of the non-interacting particle system is given by

$$E_\nu^0 = \sum_{i=1}^{N} \epsilon_{\nu_i}^0, \tag{2.22}$$

i.e., a sum of the respective single-particle energies. Note that ν_i denotes a set of single-particle quantum-numbers.

The configuration of minimal $E_\nu^0 = E_0^0$, i.e. the ground state energy can be obtained by sorting all ϵ_{ν_i} according to their value and the filling up each energy level starting from the bottom with two electrons of opposite spin (as consequence of the *Pauli's exclusion principle*). This picture, is a useful visual tool when dealing with addition/removal of electron or promotion of an electron to higher energy levels, as shown in Figure 2.2.

It is often convenient to stress the importance of two distinctive orbitals. The single-particle function $\phi^0(\mathbf{r}_i)$ of the last filled energy level is called the highest occupied molecular orbital (HOMO), the one of the first empty level the lowest unoccupied molecular orbital (LUMO). These frontier orbitals are relevant when designing an opto-electronic device. When an organic molecule is excited by a light beam, it may absorb a photon. By the absorption of a photon, an electron-hole pair forms. Such an excitation represents the passage of an electron from the base state (HOMO) to a higher-energy orbital (LUMO). The interaction between an electron of the LUMO and a hole of the HOMO leads to the formation of what is known as an exciton. HOMO and LUMO are also crucial in the design of Organic LED (OLED). Applying a voltage across the OLED, a current of electrons begins

to flow through the device from the cathode to the anode. During this process, electrons are injected into the LUMO of the cathode and ejected to the HOMO of the anode (holes are injected). The ejected electron from the anode is now an electron-hole. Afterward, electrostatic forces within the OLED bring the electrons and the electron holes together to form an exciton near the so-called emissive layer. The decay of the singlet state exciton produces light. In other words, tuning the HOMO-LUMO gap between two material is fundamental for a the rational design of new opto-electronic devices.

Far from being the final solution, the non-interacting single-particle pictures can be useful to show qualitatively the nature of these frontier orbitals. If we remove the $l-$th electron, the energy of the $n - 1_l$ electron system is

$$E^0(n - 1_l) = \sum_{i=1}^{n} \epsilon_i^0 - \epsilon_l = E^0(n) - \epsilon_l \tag{2.23}$$

$$\Rightarrow E^0(n - 1_l) - E^0(n) = -\epsilon_l = \text{IP}_l \tag{2.24}$$

The occupied single-particle energies are therefore the negative of the respective ionization energy IP_l. If an electron is added to the $k-$th energy level, the energy of the $n + 1_k$ electron system is

$$E^0(n + 1_k) = \sum_{i=1}^{n} \epsilon_i^0 + \epsilon_k = E^0(n) + \epsilon_k \tag{2.25}$$

$$\Rightarrow E^0(n + 1_k) - E^0(n) = \epsilon_k = -\text{EA}_k \tag{2.26}$$

The unoccupied single-particle energies are therefore the negative of the respective electron affinities, although the definition of the sign may differ. For the electron promotion, if an electron is promoted from an occupied level l to the previously empty k-th energy level (e.g. by optical excitation), the total energy of is

$$E^0(n - 1_l + 1_k) = E^0(n) + \epsilon_k - \epsilon_l$$

So the, e.g. energy of absorption, is equal to the difference in single-particle energies.

Often, basic details of the electronic structure of molecules related to charge and energy transfer processes are discussed in terms of this single-particle picture. However, the downside is that, of course, the electrons of realistic molecular systems do interact. Still, one can stay within this framework taking the interactions of the electrons into account by transforming the full-interacting problem into what is called an effective (mean-field) single-particle problem, as will be shown in the following.

2.4.3 Hartree approximation

As in the case of the Helium atom, a possible ansatz for the many-electron wavefunction could be the product of orthonormal single-orbitals:

$$\Psi(\mathbf{x}_1, \ldots, \mathbf{x}_N) \approx \phi_1(\mathbf{x}_1) \ldots \phi_N(\mathbf{x}_N) \tag{2.27}$$

Despite this not being anti-symmetric (and thus not a perfect candidate for the right wavefunction) the simplicity of the approximation allows for the application of the mentioned minimization scheme. The varying degrees of freedom are the N single-electron orbitals, with the orthonormality constraint. Using Lagrange multipliers ε_i, the result is

$$\left[\hat{H}_0 + \hat{V}_H[n_i] \right] \phi_i(\mathbf{r}) = \varepsilon_i \phi_i(\mathbf{r}) \tag{2.28}$$

with $\hat{H}_0 = \hat{K} + V_{\text{ext}}$ and the so-called Hartree operator

$$\hat{V}_H[n_i](\mathbf{r}) = \int \frac{n_i(\mathbf{r}')}{|\mathbf{r} - \mathbf{r}'|} \mathrm{d}\mathbf{r}' \tag{2.29}$$

which is a state-dependent operator corresponding to the classical electrostatic potential at point $\mathbf{r}$ generated by density $n_i(\mathbf{r}') = \sum_{j \neq i}^{n_{occ}} |\phi_j(\mathbf{r}')|^2$, with $n_{occ} = N/2$ being the number of occupied electronic states. The total energy of the ground-state is defined as

$$E_0 = \sum_i^N \varepsilon_i - \sum_i^N \int \phi_i^*(\mathbf{r}) \hat{V}_H[n_i] \phi_i(\mathbf{r}) \, \mathrm{d}\mathbf{r} \tag{2.30}$$

Despite its simplicity and lack of physical interpretation, the Hartree approximation leads to two important aspects of mean-field theory. The first one is that the many-body problem can be reduced, with the right ansatz for the wavefunction, to subproblems in which a single particle moves in an effective field. The other aspect is that the solution must be sought self-consistently. The Hartree potential is unknown a priori because V_H depends on n_i, hence the orbital ϕ_i. This problem must be solved self-consistently: starting with an initial guess for the orbitals, solve Eq. (2.28), calculate n_i, update $V_H[n_i]$ and repeat till convergence.

2.4.4 Hartree-Fock approximation

In order to enforce the wavefunction to be antisymmetric, we can define (with an abuse of ntation) the new ansätz as a determinant of orthonormal single-orbitals

wavefunctions, known as Slater determinant (SD). This is mathematically defined as

$$\Psi(\mathbf{x}_1, \ldots, \mathbf{x}_N) \approx \Psi^{\mathrm{SD}}(\mathbf{x}_1, \cdots, \mathbf{x}_N) = \frac{1}{\sqrt{N!}} \begin{vmatrix} \phi_1(\mathbf{x}_1) & \cdots & \phi_N(\mathbf{x}_1) \\ \vdots & \ddots & \vdots \\ \phi_1(\mathbf{x}_N) & \cdots & \phi_N(\mathbf{x}_N) \end{vmatrix}. \tag{2.31}$$

This is the Hartree-Fock ansatz. This is an improvement upon the Hartree ansatz since the Pauli exclusion principle is satisfied. The drawback lies in the complexity of the mean-field operators. Using the variational principle with this ansatz one obtains a set of equations, one for each single-orbital wavefunction

$$\left[\hat{h}_0 + \hat{V}_{\mathrm{H}}[n(\mathbf{r})] + \sum_{j=1}^{N} \hat{V}_{\mathrm{F}}[\phi_j] \right] \phi_i(\mathbf{x}) = \varepsilon_i \phi_i(\mathbf{x}). \tag{2.32}$$

with the electron density being

$$n(\mathbf{r}_1) = N \int |\Psi^{\mathrm{SD}}(\mathbf{x}_1, \cdots, \mathbf{x}_N)|^2 \mathrm{d}\mathbf{x}_2 \ldots \mathrm{d}\mathbf{x}_N = \sum_{j=1}^{N} |\phi_j(\mathbf{r}_1)|^2 \tag{2.33}$$

and with $\hat{V}_{\mathrm{H}}[n]$ and $\hat{V}_{\mathrm{F}}[\phi_j]$ the Hartree and Fock potential contribution defined as

$$\hat{V}_{\mathrm{H}}[n](\mathbf{r}) = \int \sum_{j=1}^{N} \frac{|\phi_j(\mathbf{r}')|^2}{|\mathbf{r} - \mathbf{r}'|} \mathrm{d}\mathbf{r} = \int \frac{n(\mathbf{r}')}{|\mathbf{r} - \mathbf{r}'|} \mathrm{d}\mathbf{r}, \tag{2.34}$$

$$\hat{V}_{\mathrm{F}}[\phi_j]\phi_i(\mathbf{r}) = \int \phi_j^*(\mathbf{r}')\phi_i(\mathbf{r}') \frac{1}{|\mathbf{r} - \mathbf{r}'|} \mathrm{d}\mathbf{r}' \, \phi_j(\mathbf{r}) \tag{2.35}$$

The first term is the Hartree potential which represents the classical potential felt by one electron due to repulsion of the electron density. The second one is called exchange contribution with no classical analogue being a peculiarity of the fermionic nature of electrons.

Once Eq. (2.32) are solved, the ground state energy can be written as

$$\mathrm{E}_{\mathrm{HF}} = \sum_{i=1}^{N} \langle \phi_i | \hat{h}_0 | \phi_i \rangle + \sum_{i=1}^{N} \sum_{j=1}^{N} [\mathrm{J}_{ij} - \mathrm{K}_{ij}] \tag{2.36}$$

with

$$\mathrm{J}_{ij} = \frac{1}{2}(ii|jj) = \frac{1}{2}\int\int \frac{|\phi_i(\mathbf{x})|^2|\phi_j(\mathbf{x}')|^2}{|\mathbf{r}-\mathbf{r}'|}\mathrm{d}\mathbf{r}\,\mathrm{d}\mathbf{r}' \qquad (2.37)$$

$$\mathrm{K}_{ij} = \frac{1}{2}(ij|ji) = \frac{1}{2}\int\int \frac{\phi_i(\mathbf{x})\phi_j^*(\mathbf{x})\phi_j(\mathbf{x}')\phi_i^*(\mathbf{x}')}{|\mathbf{r}-\mathbf{r}'|}\mathrm{d}\mathbf{r}\,\mathrm{d}\mathbf{r}'\,. \qquad (2.38)$$

The first term in Eq. (2.36) is the contribution from the kinetic energy and the external potential. The second term, $\mathrm{J}_{ij} = \frac{1}{2}(ii|jj)$ is known as *Hartree* energy and stands for the classical averaged electrostatic repulsion energy of all the particles in the system. The last term $\mathrm{K}_{ij} = \frac{1}{2}(ij|ji)$ is known as *Fock* energy term or *exchange* term. This term has no classical analogue since it stems from the fermionic nature of electrons. When $i = j$, the Hartree and exchange terms cancel out since $(ii|jj) = (ij|ji)$. In this way the HF theory avoids unphysical self-interaction (i.e an electron cannot interact with itself).

2.4.5 Beyond HF approximation: Electronic correlation

As we already discussed, a single Slater determinant is only an approximation of the real many-body wavefunction. In literature HF failures are called correlation effects. We can formally define the correlation energy as the difference between the exact ground state energy and the Hartree-Fock energy

$$\mathrm{E}_{\mathrm{corr}} = \mathrm{E}_{\mathrm{GS}}^{\mathrm{exact}} - \mathrm{E}_{\mathrm{HF}} \qquad (2.39)$$

Deviations from the exact solution of the Schrödinger equation stem from the so-called static and dynamical correlation effects. The former reflects the inadequacy of a single determinant in describing a given molecular state, and is due to nearly degenerate states or rearrangement of electrons within partially filled shells. In layman's terms, there are situations in which the ground state is well described only with more than one (nearly-)degenerate determinant. In this case the Hartree–Fock wavefunction (single determinant) is qualitatively wrong. The latter, on the other hand, arise because Hartree-Fock replaces the instantaneous electron-electron repulsion with the repulsion of each electron with an average electron charge cloud of the remaining electrons. What is unphysical about this is that it does not take into account the fact that the electron will push away the other electrons as it moves around. This tendency for the electrons to stay apart diminishes the repulsion energy

In order to account for correlation effects beyond the exchange interaction, an approach based on a single ground-state Slater determinant is not sufficient. To

cope with this, an infinite sum of Slater determinants, including determinants describing one, two, three, etc. electrons excitations is required.

$$\Psi(\mathbf{x}_1, \ldots, \mathbf{x}_N) = \sum_{i=1}^{\infty} \Psi_i^{\mathrm{SD}} \tag{2.40}$$

this method is known as *Full Configuration Interaction Method* (Full CI). Upon this idea other methods have been developed. For a brief overview we redirect the reader to Appendix F.

2.5 Density Functional Theory

Density Functional Theory (DFT) is considered one of the most important and successful developments in theoretical physics in the last 100 years. In this method the main character is the electron density $n(\mathbf{r})$ instead of the wavefunction. This brings the advantage of condensing the many-body information, usually stored in the complicated many-body wavefunction depending on $3N$ spatial variables into a simple 3-dimensional object.

2.5.1 The Hohenberg-Kohn theorems

The theoretical basis of DFT has been set by Hohenberg and Kohn [45] in two theorems. The first theorem states that the external potential $V_{\mathrm{ext}}(\mathbf{r})$, which is the only system-specific ingredient to form the electronic Hamiltonian, is uniquely defined within an additive constant by the ground state density $n_0(\mathbf{r})$. In other words, two external potential differing by more than a constant cannot give the same ground state density. Accordingly, the ground-state density uniquely determines the full many-body Hamiltonian and hence the exact total ground state energy

$$n_0(\mathbf{r}) \rightarrow V_{\mathrm{ext}}(\mathbf{r}) \rightarrow \hat{\mathrm{H}} \rightarrow \mathrm{E}_0 \tag{2.41}$$

A pictorial description of the first Hohenberg-Kohn theorem is given in Figure 2.3 to help the reader understand this theorem. The usual way of solving the Schrödinger equation would require selecting an external potential (and thus fully determine the system Hamiltonian), then solve the equation calculating the system wavefunction and eventually get the electron density. The Hohenberg-Kohn theorem shift all the attention on the electron density first. The ground state energy is
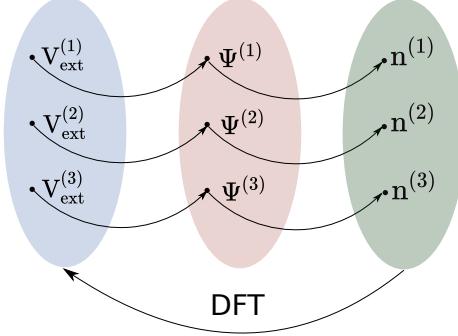
Figure 2.3: Pictorial description of the Hohenberg-Kohn theorem. Following the Schrödinger approach once an external potential $V_{\mathbf{ext}}$ is defined a wavefunction can be computed and thus the electron density is uniquely defined. According to the H-K theorem for the ground-state there is a correspondence between the electron density and the external potential (V). Therefore, the electron density uniquely define the Hamiltonian of the system (the Hamiltonian is a functional of the ground-state density) making the wavefunctions functionally dependent on the density as well.

thus a functional of the ground-state density and can be expressed as

$$E[n_0] = F_{HK}[n_0] + \int V_{ext}(\mathbf{r})n_0(\mathbf{r})d\mathbf{r} \qquad (2.42)$$

$$F_{HK}[n_0] = T[n_0] + E_{e-e}[n_0]. \qquad (2.43)$$

with $F_{HK}[n_0(\mathbf{r})]$ the so-called Hohenberg-Kohn functional, independent from the system under analysis, $T[n_0]$ the kinetic energy functional and $E_{e-e}[n_0]$ is the electron-electron interaction functional. The latter can be further split into an electrostatic contribution, usually called Hartree term E_H, and a non-classical contribution accounting for exchange and correlation (xc) effects

$$E_{e-e}[n_0] = \frac{1}{2} \int \frac{n_0(\mathbf{r})n_0(\mathbf{r}')}{|\mathbf{r}-\mathbf{r}'|} d\mathbf{r}\, d\mathbf{r}' + E_{xc} \qquad (2.44)$$

The explicit form of the non-classical term, and thus the Hohenberg-Kohn functional, is not known.

The second Hohenberg-Kohn theorem introduces the variational principle for the energy functional with respect to the charge density. It states that $E[n]$ has its minimum at the ground state equilibrium density $n_0(\mathbf{r})$,

$$E_0 = \min_n E[n] \doteq E[n_0] \tag{2.45}$$

This theorem provides a systematic way to obtain the ground state energy from trial densities. As in the case of the variational principle for wavefunctions, also in this case it would be impossible to span the whole space of densities and select the one to minimize the ground-state energy functional. Despite their pivotal importance, these theorems do not provide any practical recipe to calculate the density and no information about the Hohenberg-Kohn function F_{HK} is given as well.

2.5.2 Kohn-Sham equations

The big breakthrough for DFT came with the so-called Kohn-Sham ansatz [46]. The idea is to introduce an auxiliary reference system of N independent (i.e., non-interacting) electrons whose density $n_s(\mathbf{r})$ equals the density $n(\mathbf{r})$ of the corresponding interacting system.

Since for a non-interacting system of electrons the many-body wavefunction is a single Slater determinant, the density $n_s(\mathbf{r})$ is completely determined by single-electron orbitals, from now on called Kohn-Sham functions $\phi_i^{KS}(\mathbf{r})$

$$n_s(\mathbf{r}) = \sum_i^N |\phi_i^{KS}(\mathbf{r})|^2 \equiv n(\mathbf{r}), \tag{2.46}$$

their kinetic energy reads as

$$\hat{K}_s[n] = -\sum_i^N \int \phi_i^{KS*}(\mathbf{r}) \frac{\nabla^2}{2} \phi_i^{KS}(\mathbf{r}) d\mathbf{r} \tag{2.47}$$

These two definitions can help with the unknown Hohenberg-Kohn functional. We can define F_{HK} as

$$F_{HK} = \hat{K}_s[n] + E_H[n] + E_{xc}[n] \tag{2.48}$$

with

$$E_{xc} = (\hat{K}[n] - \hat{K}_s[n]) + (E_{el-el} - E_H). \tag{2.49}$$

We call this the exchange-correlation functional. It contains all the unknown contributions coming from the residual part of the kinetic energy stemming from using Eq. (2.47) in lieu of the many-body counterpart, the repulsive exchange interactions due to Pauli's exclusion principle and correlation effects. This new definition is nothing but shuffling terms around and coalescing all our ignorance about the many-body system on to the exchange-correlation term. This term is unknown though approximations can be found. Finding a universal and silver-bullet exchange-functional is a vivid research field still to be explored. Let's put aside for a moment the exact form of E_{xc} and go back to how the Kohn-Sham functional might lead to a practical way of solving DFT.

We can minimize the energy functional Eq. (2.43) with respect to the density leads to a density-only Euler eigenvalue equation

$$\frac{\delta F[n]}{\delta n(\mathbf{r})} + V_{ext}(\mathbf{r}) = \mu \tag{2.50}$$

with μ the chemical potential. If, instead, the one-particle Kohn-Sham orbitals ϕ_i^{KS} is used as variational parameters gives the Kohn-Sham (KS) equations:

$$\left[-\frac{1}{2}\nabla^2 + V_{eff}(\mathbf{r}) \right] \phi_i^{KS}(\mathbf{r}) = \varepsilon_i^{KS} \phi_i^{KS}(\mathbf{r}), \tag{2.51}$$

with the effective potential defined as

$$V_{eff}(\mathbf{r}) = V_H(\mathbf{r}) + V_{ext}(\mathbf{r}) + V_{xc}(\mathbf{r}) \quad \text{with} \quad V_{xc}(\mathbf{r}) = \frac{\delta E_{xc}[n]}{\delta n(\mathbf{r})} \tag{2.52}$$

Equation (2.51) is a single-particle problem in which electrons move in an effective (mean-field) potential V_{eff}. This potential depends on the density and so on the solution of the problem itself. A self-consistent field scheme starting from an initial guess density ought to be use in order to solve KS eigenvalue problem.

At first glance KS Eq. (2.51) and HF Eq. (2.32) look similar. It is important at this point drawing the differences between the two. Hartree-Fock theory is based on the goal of looking for the best approximation for the many-electrons wavefunction. DFT, on the other hand, is an exact ab-initio theory (i.e. no assumption about the many-electron wavefunction) provided the exchange-correlation potential. The effective potential in the DFT-KS is local in space, compared to the non-local Fock exchange term in the HF equations. This simplicity is however cancelled in some sense by the fact that the exact form of this potential is not known and that it is supposed to show a very complicated non-local dependence on the electron density.

2.5.3 Exchange correlation potential approximation

> The exchange-correlation energy is the name we give to the part of the energy functional that we do not know how to calculate otherwise. For this reason, it has been named the *stupidity energy* by Feynman (1972).
>
> Baroni et al. [47]

As mentioned before there is no exact form for the exchange-correlation functional. For this reason a number of approximations are available and new ones are developed. In fact the reliability of the Kohn–Sham method depends on the validity of this approximated functional. Different criteria must be fulfilled such as satisfying physical limits and properties, simplicity (i.e., few parameters should be involved, ideally none) and universality (i.e the functional should reproduce the correct properties accessible with DFT for numerous large number of materials, ideally for all of them). In the following the reader is guided through the most common types of functionals used in quantum chemistry. A thorough discussion is beyond the scope of this work, but it is suggested to read [48] for a technical and historical journey through different families of functionals.

Local Density Approximation (LDA)

The simplest of these approximations is the *local density approximation* (LDA). The assumption behind this approximation is that the charge density of the system, not homogeneous overall, is locally similar to the one of the homogeneous electron gas (HEG), whose exchange-correlation energy is known. The functional can be written as

$$E_{xc}^{LDA}[n(\mathbf{r})] = \int n(\mathbf{r})\, \epsilon_{xc}^{HEG}[n(\mathbf{r})]\mathrm{d}\mathbf{r} \tag{2.53}$$

the exchange and correlation contribution can be split into $\epsilon_{xc}^{HEG} = \epsilon_{x}^{HEG} + \epsilon_{c}^{HEG}$. The exchange part have an analytical form of the kind:

$$\epsilon_{x}^{HEG}[n(\mathbf{r})] = -\frac{3}{4}\left(\frac{3}{\pi}\right)^{1/3} \int n(\mathbf{r})^{1/3}\mathrm{d}\mathbf{r}\,. \tag{2.54}$$

The correlation part, on the other hand, is known only in the high- and low-density limit. In formula,

$$\epsilon_c^{\text{HEG}}[n(\mathbf{r})] = \begin{cases} A \ln{(r_s)} + B + r_s(C \ln{(r_s)} + D) & \text{in the High-density limit} \\ \frac{1}{2} \left(\frac{g_0}{r_s} + \frac{g_1}{r_s^{3/2}} + \cdots \right) & \text{in the Low-density limit} \end{cases}$$

(2.55)

with r_s the dimensionless Wigner-Seitz parameter defined as the radius of a sphere which encompasses exactly one electron, divided by the Bohr radius. The Wigner-Seitz parameter is related to the density as

$$\frac{4\pi}{3} r_s^3 = \frac{1}{n(\mathbf{r})}.$$

(2.56)

The intermediate values for the correlation energy density are computed using accurate quantum Monte Carlo simulations for the energy of the HEG. These have been performed for several intermediate values of the density, in turn providing accurate values of the correlation energy density.

Generalized gradient approximation (GGA)

The uniform electron gas is intuitively not such a great model for those systems whose electron density can vary rapidly over a small region of space, such as in the case of molecules. An improvement upon the LDA can hence be obtained by Generalized Gradient Approximation (GGA) functionals. These depend not just on the value of the density at a point (as in the LDA case) but also on its gradient. This should account for truly non-local density dependencies. These functionals are formally defined as

$$\mathrm{E}_{\text{xc}}^{\text{GGA}}[n(\mathbf{r})] = \int n(\mathbf{r})\, \epsilon_{\text{xc}}^{\text{GGA}}[n(\mathbf{r}), |\nabla n(\mathbf{r})|]\mathrm{d}\mathbf{r}.$$

(2.57)

Unlike LDA, there is no single universal form. Most GGA functionals are constructed in the form of a correction term which is added to the LDA functional

$$\epsilon_{\text{xc}}^{\text{GGA}}[n(\mathbf{r}), |\nabla n(\mathbf{r})|] = \epsilon_{\text{xc}}^{\text{HEG}}[n(\mathbf{r})] + \Delta_{\text{xc}} \left[\frac{\nabla n(\mathbf{r})}{n(\mathbf{r})^{4/3}} \right]$$

(2.58)

Although various forms of GGA exchange functionals have been developed, the differences in the best-known functionals are found only in the dependence on the dimensionless parameter $\frac{\nabla n(\mathbf{r})}{n(\mathbf{r})^{4/3}}$. In particular GGA functionals are characterized

by their differences in the region of low electron density and/or high density gradient. This is attributed to the lack of fundamental physical conditions for exchange energy in the low density/high density gradient region. The exchange functional forms in these regions have been determined to improve the reproducibility of properties. Popular GGAs include PBE [49] and BLYP [50, 51].

Hybrid Functionals

Hybrid functionals mix the Hartree–Fock exchange integral with GGA exchange functionals at a constant ratio, based on the concept of the adiabatic connection, which makes the Kohn–Sham energies of the independent electron model link to those of the fully interacting electron one. Hybrid functionals are based on the ansatz that the exact exchange energy is situated between the GGA exchange energy functional and the Hartree–Fock exchange integral. De facto, they include fractions of exact Hartree-Fock exchange energy, calculated as a functional of the Kohn-Sham molecular orbitals

$$E_x^{HF}[\{\phi_i^{KS}\}] = \iint \frac{\phi_i^{KS}(\mathbf{x})\phi_j^{KS,*}(\mathbf{x})\phi_j^{KS}(\mathbf{x}')\phi_i^{KS,*}(\mathbf{x}')}{|\mathbf{r} - \mathbf{r}'|} d\mathbf{r}\, d\mathbf{r}'. \tag{2.59}$$

These functionals have the following general form

$$E_{xc} = (1 - a)E_x^{GGA} + aE_x^{HF} + E_c^{GGA} \tag{2.60}$$

Different hybrid functionals differ in the choice of the mixing parameters and the terms to be mixed. The most popular functionals of this family are the B3LYP hybrid functional [52], the PBE0 hybrid functional [53], and the Heyd–Scuseria–Ernzerhof (HSE) hybrid functional [54].

2.5.4 Physical interpretation of DFT-KS orbitals and energies and their application beyond ground-state properties

It is often debated what is the physical meaning of the DFT-KS energies [55]. By construction, these are the energies of independent electrons in the fictitious system with the same density as the original interacting electrons system in its ground state. The entailed question could be "Do these energies are the real electron energies?". The answer to this question is important since DFT is a relative cheap tool to infer material properties. Having access not only to ground-state

properties but also excited state properties it is of pivotal importance in understanding exotic material properties that potentially could lead to a new generation of optoelectronic devices, aside with the intellectual challenge leading to this discovery. Kohn-Sham eigenvalues enter the equation as Lagrange multipliers to ensure orthogonality of the Kohn-Sham wavefunctions in the energy functional minimization. This is equivalent to the HF scheme in which HF eigenvalues allows the single-particle HF wavefunctions to be orthogonal among each other. In HF, it is possible to give a physical interpretation to these energies. We cannot say the same about the DFT-KS ones. Because of the similarities between HF and DFT-KS, one would be tempted to extend the Koopman's theorem in the DFT-KS realm. In DFT-KS, however, because of the exchange-correlation potential there is no mapping between excitation energies and KS eigenvalues. One could say that KS orbitals are nothing but a mathematical tool to obtain the correct ground-state density, thus the correct ground-state properties. Whatever is outside this frame doesn't have a clear interpretation. It is possible to extend upon this subject, showing that the problem roots in the approximation of the exchange-correlation potential [56]. In the DFT realm there is a theorem called *Janak's theorem*. This theorem connects DFT-KS eigenvalues to the derivative of the total energy with respect to the *fractional* occupation number $f_i \in [0, 1]$. In math

$$\varepsilon_i^{\text{KS}} = \left. \frac{\partial \text{E}_{\text{KS}}^{N_0}}{\partial f_i} \right|_{f_i = 1} \tag{2.61}$$

Moreover it can be shown that the ground-state energy for a system of fractional number of electrons ($N = N_0 + \alpha$) with $\alpha \in [0, 1]$ is a linear combination of the ground state energies at the closest integer values [56]

$$\text{E}(N) = (1 - \alpha)\text{E}(N_0) + \alpha\text{E}(N_0 + 1) \tag{2.62}$$

this implies that the total energy $\text{E}(N)$ is piecewise linear. For the exact KS-DFT, this piecewise linearity must be fulfilled. Only if this property is fulfilled, the KS eigenvalues can be interpreted as excitation energy. This property is stronger than the Koopman's theorem because relaxation effects (i.e., rearranging of electrons due to addition/removal of electrons) are included. This theoretical results, crumble down when actual calculation are performed. At the moment, a substantial group of approximations for the exchange-correlation potential does not satisfy the piecewise linearity aforementioned and thus one cannot interpret the KS-DFT eigenvalues as excitation energies. Nevertheless, many efforts and attempts to reconciliate KS-DFT eigenvalues with their interpretation as excitation

energies have been published [57, 58, 59, 60]. Despite many works ignores this fact (whether with awareness or not it depends on the specific work) and use naively the DFT-KS to estimate the excitation energies, this shows the need to be careful when interpreting results. Another option is pursuing a different approach to better embrace the excitation properties of a material. In the following the many-body Green's function perturbation theory is described to this end. The reader should keep in mind that there are other successful approaches as TDDFT and Koopman's compliant methods [61]. An overview of these methods is beyond the scope of this thesis.

Chapter 3

Many-body Perturbation Theory (GW-BSE)

All properties of materials can, in principle, be calculated from the many-body wavefunction of the interacting many-particle system as introduced in Ch. 2. In practice, this is not possible for most systems due to the large number of particles. Most physical properties, however, do not require the full information of the many-particle wave function anyway, but can be described by response functions that involve the physics of only a few (effective) particles instead of all particles in the system. The key idea of many-body perturbation theory (MBPT) is to transform the many-particle problem into an effective equation of motion for such response functions, which then has the form of a few-particle problem. In the following we will give a really brief introduction to Green's Functions including some definitions useful to understand the theoretical discussion about ab-initio mehtods to compute excited state properties of materials.

3.1 Interpretation of spectroscopy experiments: a genuine many-body problem

Spectroscopy techniques are the most established and used experimental methods for probing the electronic structure of materials. Different techniques share the common aspect of perturbing and thus promoting the system into an excited
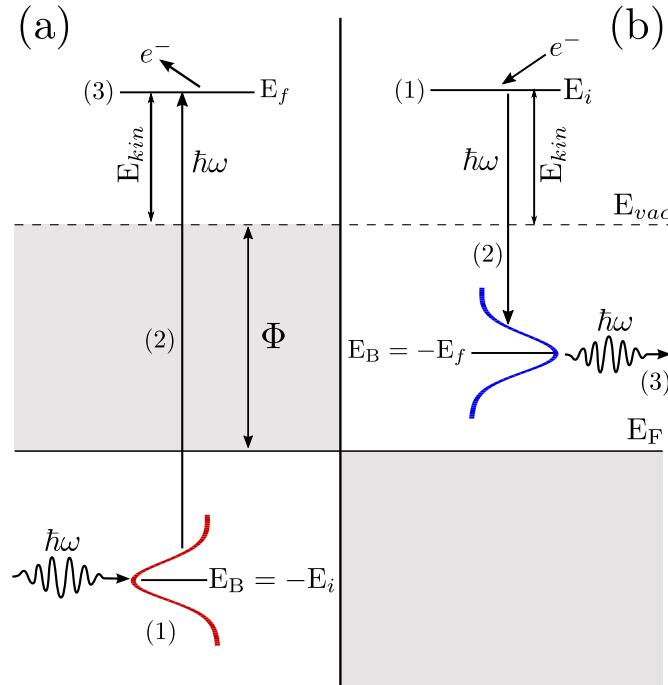
Figure 3.1: A schematic of different photoelectron spectroscopy. In (a) the
direct Photoelectron Spectroscopy (PS) is presented. In this case a beam of
light of energy $\hbar\omega$ hitting a specimen (1), promotes an electron from some
occupied state density of state (2). If the energy of the electron is bigger
than the work function the electron is released in the vacuum (3) with some
kinetic energy E_{kin}. Probing the distribution of the kinetic energy of outing
electrons allows to have information about the initial occupied density of
state (DOS). In (b) the inverse of the process described in (a), usually de-
noted as Inverse Photoelectron Spectroscopy (IPS). In this case unoccupied
levels are probed filling these states with electrons of fixed kinetic energy.
This excited state relaxes with the emission of some photon allowing for
retrieving info about the unoccupied state.

state. The system's response is proportional to its electronic structure. Access
to the electronic structure is not interesting only per se, but it paves the way to
measure quantities and understand fundamental processes of great importance in
solid-state physics, chemistry, and material science. In this context, the most used
techniques are the Photoelectron spectroscopy (PES) [62, 63, 64] and its comple-
mentary, the Inverse Photoelectron spectroscopy (IPES) or Bremsstrahlung Iso-
chromat Spectroscopy (BIS) [65, 66]. In the former, electrons are ejected from
a sample upon irradiation with visible or ultraviolet light (UPS) or with X-rays
(XPS). In the latter, electrons are injected into the system measuring the out-
ward photons are eventually detected. The relation between PES and IPES with
electronic structure is often explained within a *single-particle* picture in which we
assume that only a single electron is involved in the PES and IPES processes. A
schematic of the process is depicted in Figure 3.1. Furthermore, the electronic
structure of the initial N-particle ground state and the final (ionized) system are
the same. In other words, the ejection (injection) of the electron and the related
creation of a positive (negative) potential is assumed to have no influence on the
remaning electrons.

Regarding the PES, the measured kinetic energy E_{kin} of the photoelectron and the
orbital energy ε_i are related, according to energy conservation

$$-\varepsilon_i + E_{kin} = \hbar\omega \qquad (3.1)$$

this is also known as *frozen-orbital approximation*. We can thus define the bind-
ing energy, i.e the energy needed to eject and electron from the system as $E_b =
\hbar\omega - E_{kin} = -\varepsilon_i$. Since in this approximation the ground and excites states are
equal, the binding energy is given by a single-particle ground-state property. Des-
pite performing qualitatively good, this approach has been proved to be quantitat-
ively poor in many cases since the interaction among the electrons plays a crucial
role in these kind of processes. In other words, ground-state properties cannot be
used to describe excited states of a system as microscopic processes underlying
spectroscopy experiments constitute a manifold of complicated many-particle in-
teractions. All the N particles are involved and coupled through interactions. In
the PES, the created positive hole potential influences the ionized $(N-1)$ electron
system leading to differences between the initial and the final state. Reorganiza-
tion of electronic levels, formation of neutral excitations (electron-hole pairs also
known as excitons), collective electronic oscillations (plasmons) or atomic vibra-
tions (phonons) are responsible for these differences. In a general and thus formally
correct framework, PES accesses the energy difference between the total energy of
a system of N interacting electrons in the ground state (with energy E_0^N) and the

total energy of a $(N-1)$ electrons system in which an electron has been ejected from state i (with energy E_i^{N-1})). Accordin to energy conservation,

$$\hbar\omega + E_0^N = E_{kin} + E_i^{N-1}, \qquad (3.2)$$

$$E_b = \hbar\omega - E_{kin} = E_i^{N-1} - E_0^N \qquad (3.3)$$

The binding energy for occupied states is the energy needed to extract an electron from a system of N interacting electrons in which the creation of a hole (i.e abscence of an electron) and its influence on the electronic structure of the remaining electrons is taken into account. It is not difficult to apply the same reasoning for unoccupied states and hence the IPES spectrum. In IPES and electron with fixed kinetic energy E_{kin} is inserted into the i-th unoccupied state of the N electron system, which relaxes to a charged (N+1) ground state after emitting a photon. The energy needed to insert this electron in the i-th state of a system of N interacting electrons is according to energy conservation,

$$E_{kin} + E_0^N = \hbar\omega + E_i^{N+1}, \qquad (3.4)$$

$$E_b = \hbar\omega - E_{kin} = E_0^N - E_i^{N+1}. \qquad (3.5)$$

In view of these consideration, two important experimental quantities can be extrapolated from the system's response: the Ionization Potential and the Electron Affinity. The former is defined as the energy needed to eject and electron from the highest occupied (HO) state as the latter is the energy to fill the lowest unoccupied (LU) state of the system. In formula,

$$IP = E_{HO}^{N-1} - E_0^N \qquad (3.6)$$

$$EA = E_0^N - E_{LU}^{N+1}. \qquad (3.7)$$

Anticipating a bit the discussion of Section 5, it is sometimes hard to interpret experimental results and thus extrapolating IP and EA from the data. This is because of the interplay of different phenomena that in some cases hinder the interpretation of the experimental evidences. Excitation processes in organic semiconductors, because their localized nature, give rise to strong structural reorganization (polaron formation) and electron-vibration coupling, which leads to shifts, broadening and additional features that make a direct extrapolation of IP and EA from spectra not straightforward.

Computational methods that allows for an easier interpretation of these spectra cannot rely on DFT only. As already stated Section 2.5.4, DFT is not the right

theory to describe excited states. Therefore in the next sections an overview of MBPT is presented. This theory is perfectly built to take into account excited states.

3.2 Green's Functions as time-evolution propagators

For the sake of simplicity, we consider for the moment a single particle in free space (quantum vacuum) described by a single particle Hamiltonian $\hat{H}_1$. Its stationary eigenstates and eigenenergies are given by

$$\hat{H}_1 |\psi_n\rangle = \varepsilon_n |\psi_n\rangle \tag{3.8}$$

Imagine now to prepare the system in an arbitrary trial state instead and then follow its time evolution. If the trial state $|\psi_{\text{tr}}\rangle$ is created at time $t = 0$, the wavefunction at a later time t is given by

$$|\psi(t)\rangle = \exp\left(-i\hat{H}_1 t\right) |\psi_{\text{tr}}\rangle = \sum_n |\psi_n\rangle \exp(-i\varepsilon_n t) \langle\psi_n|\psi_{\text{tr}}\rangle . \tag{3.9}$$

Knowledge of the $\hat{H}_1$ spectrum is thus necessary to calculate the time evolution of a trial state. Eventually, at time t, we want to know the probability amplitude that a measurement would find the particle at position $\mathbf{r}$

$$\langle\mathbf{r}|\psi(t)\rangle = \langle\mathbf{r}| \exp\left(-i\hat{H}_1 t\right) |\psi_{\text{tr}}\rangle = \int d\mathbf{r}' \langle\mathbf{r}| \exp\left(-i\hat{H}_1 t\right) |\mathbf{r}'\rangle \langle\mathbf{r}'|\psi_{\text{tr}}\rangle \tag{3.10}$$

using the completeness of the eigenstates $\{|\psi_n\rangle\}$

$$\langle\mathbf{r}|\psi(t)\rangle = \int d\mathbf{r}' \sum_n \langle\mathbf{r}|\psi_n\rangle \exp(-i\varepsilon_n t) \langle\psi_n|\mathbf{r}'\rangle \langle\mathbf{r}'|\psi_{\text{tr}}\rangle =$$
$$\int d\mathbf{r}' G_{\text{free}}(\mathbf{r}, \mathbf{r}', t) \langle\mathbf{r}'|\psi_{\text{tr}}\rangle \tag{3.11}$$

where we have introduced the free particle propagator

$$G_{\text{free}}(\mathbf{r}, \mathbf{r}', t) = \sum_n \langle\mathbf{r}|\psi_n\rangle \exp(-i\varepsilon_n t) \langle\psi_n|\mathbf{r}'\rangle . \tag{3.12}$$

Transforming $G_{\text{free}}(\mathbf{r}, \mathbf{r}', t)$ from the time to the energy domain one obtains

$$G_{\text{free}}(\mathbf{r}, \mathbf{r}', E) = \sum_n \frac{\langle \mathbf{r} | \psi_n \rangle \langle \psi_n | \mathbf{r}' \rangle}{E - \varepsilon_n + i\eta} = \langle \mathbf{r} | \, G_{\text{free}}(E) \, | \mathbf{r}' \rangle \tag{3.13}$$

with $\eta = 0^+$ as $G_{\text{free}}(E) = \sum_n \frac{|\psi_n\rangle\langle\psi_n|}{E-\varepsilon_n+i\eta}$ being the Green's function operator for the free particle problem. This can be made more clear rewriting it as

$$(H_1 - E + i\eta) \, G_{\text{free}}(\mathbf{r}, \mathbf{r}', E) = -\delta(\mathbf{r}, \mathbf{r}'). \tag{3.14}$$

In other words, propagators and Green's functions are strictly correlated. The interesting thing is that there is more information in the propagator than the possibility of calculating the evolution of any initial state but it can be seen as a gateway to the Hamiltonian spectrum. In fact it can be shown that the density of state (DOS) can be computed as

$$\sum_n \delta(E - \varepsilon_n) = -\frac{1}{\pi} \, \text{Im}\{\text{Tr}\{G_{\text{free}}(E)\}\}, \tag{3.15}$$

with $\text{Tr}\{G_{\text{free}}(E)\} = \sum_m \langle \psi_m | \, G_{\text{free}}(E) \, | \psi_m \rangle$. On top of that, $G_{\text{free}}(\mathbf{r}, \mathbf{r}', E)$ is a function with poles at the particle excitation energies (in this case the particle spectrum) as the residues are the excitation amplitudes. In other words, the propagator contains the information of both the spectrum and the eigenfunctions of the problem under analysis. In the quest of reducing the computational cost for the excitation problem the Green's function works as a good trade-off between information load and reduced degrees of freedom.

This analysis does not apply only to the free-particle case. The same idea and framework can be applied to see what one can learn by either addition or removal of a particle in an environment when many others are present. This information is vital in many physical application and in the specific of this work for the study of electronic excitation in complex materials. The only difference can be in the role played by the physical vacuum showed in the above example. For a system of many particles the vacuum state should be replaced by a many-body state, usually its ground state. Only in this way this formalism helps understanding how to probe the system by adding/removing particles or creating neutral excitations.

3.3 One- and two-particles Green's function

Before discussing the one- and the two-particles Green's function, it is important to introduce some quantities and notations useful for the following discussion.

These belong to the so-called *field operator* and *second quantization* formalism. A comprehensive summary and a link between these two descriptions is given in Appendix D. What it is important to know at this stage is how to describe the creation of particles at time t at position $\mathbf{r}$. This is achievable in the Heisenberg picture (see Appendix E) via the definition of the creation field operator

$$\psi^\dagger(\mathbf{r}, t) = \exp(i\mathrm{H}t)\psi^\dagger(\mathbf{r})\exp(-i\mathrm{H}t). \tag{3.16}$$

Its equivalent in the second quantization formalism reads as

$$c_\alpha^\dagger(t) = \exp(i\mathrm{H}t)c_\alpha^\dagger(t)\exp(-i\mathrm{H}t). \tag{3.17}$$

For the annihilation it is sufficient to take the adjoint of the previous expressions. For the sake of simplicity we dropped the $\hat{}$ symbol for indicating operators.

As the chapter title suggests, many-body perturbation theory deals with the perturbation of a known, solvable Hamiltonian. Given any Hamiltonian H, it is in principle possible to split it into two parts: A solvable part H_0 (for solvable we mean that we can find eigenvalues and eigenvectors) and the remaining part that is defined as a perturbation V.

$$\mathrm{H} = \mathrm{H}_0 + V. \tag{3.18}$$

Let us define the *N-body* wavefunction that solves H with $\left|\Psi_n^N\right\rangle$ while the wavefunction that solves H_0 (the unperturbed system wavefunction) with $\left|\Phi_n^N\right\rangle$. In formula,

$$\begin{aligned} \mathrm{H}\left|\Psi_n^N\right\rangle &= \mathrm{E_n}(N)\left|\Psi_n^N\right\rangle \\ \mathrm{H}_0\left|\Phi_n^N\right\rangle &= \mathrm{E_n^0}(N)\left|\Phi_n^N\right\rangle \end{aligned} \tag{3.19}$$

The definitions given in the following are general and do not depend on the type of interaction used. Thus, most properties of Green's functions result from general principles of quantum mechanics and are valid for any system.

3.3.1 One-particle Green's function

The one-body (often called the two-points) Green's function is defined as

$$G(\mathbf{r}, t; \mathbf{r}', t') = -i\left\langle\Psi_0^N\right|T\left(\psi(\mathbf{r}, t)\psi^\dagger(\mathbf{r}', t')\right)\left|\Psi_0^N\right\rangle, \tag{3.20}$$

with Ψ_0^N the N-body ground-state and with $T(\dots)$ being the time-ordering operator that imposes a change of sign for each exchange of two fermion field operators

$$T\left(\psi(\mathbf{r}, t)\psi^\dagger(\mathbf{r}', t')\right) = \begin{cases} \psi(\mathbf{r}, t)\psi^\dagger(\mathbf{r}', t'), & t > t' \\ \pm\psi^\dagger(\mathbf{r}', t')\psi(\mathbf{r}, t), & t < t' \end{cases} \tag{3.21}$$

where the upper (lower) sign is for bosons (fermions). G describes the propagation of one particle or one hole on top of the ground state for different space-time points. A similar definition can be given for the non interacting state Φ_n^N where the Heisenberg operators must evolve according to H_0 only. This Green's function is called G^0.

If the Hamiltonian does not depend explicitly on time, we can just consider the time difference $t - t'$. The propagator Eq. 3.20 will read

$$G(\mathbf{r}, \mathbf{r}'; t - t') = -i\theta(t - t') \left\langle \Psi_0^N \right| \psi(\mathbf{r}) e^{-i(H - E_0)(t - t')} \psi^\dagger(\mathbf{r}') \left| \Psi_0^N \right\rangle +$$
$$\mp i\theta(t' - t) \left\langle \Psi_0^N \right| \psi^\dagger(\mathbf{r}') e^{-i(H - E_0)(t - t')} \psi(\mathbf{r}) \left| \Psi_0^N \right\rangle \quad (3.22)$$

if we Fourier transform this expression we obtain

$$G(\mathbf{r}, \mathbf{r}'; \omega) = G^{\text{particle}}(\mathbf{r}, \mathbf{r}'; \omega) + G^{\text{hole}}(\mathbf{r}, \mathbf{r}'; \omega) =$$
$$= \left\langle \Psi_0^N \right| \psi(\mathbf{r})(\omega - (H - E_0) + i\eta)^{-1} \psi^\dagger(\mathbf{r}') \left| \Psi_0^N \right\rangle + \quad (3.23)$$
$$\mp \left\langle \Psi_0^N \right| \psi^\dagger(\mathbf{r}')(\omega + (H - E_0) - i\eta)^{-1} \psi(\mathbf{r}) \left| \Psi_0^N \right\rangle$$

G^{particle} propagates a particle from r to r'. On the contrary G^{hole} propagates a hole from $\mathbf{r}'$ to $\mathbf{r}$. Note that the interpretation is that a particle is added at $\mathbf{r}$, and later on some (indistiguishable) particle is removed from $\mathbf{r}'$ (and similarly for holes). In the mean time, it is the fully correlated $(N \pm 1)$-body system that propagates.

Of course the same definitions hold for any orthonormal single-particle basis

$$G_{\alpha\beta}(t, t') = -i \left\langle \Psi_0^N \right| T\left(c_\alpha(t) c_\beta^\dagger(t') \right) \left| \Psi_0^N \right\rangle \quad (3.24)$$

where

$$G(\mathbf{r}, t; \mathbf{r}', t') = \sum_{\alpha\beta} u_\alpha(r) G_{\alpha\beta}(t, t') u_\beta^*(r') \quad (3.25)$$

and

$$G_{\alpha\beta}(\omega) = \left\langle \Psi_0^N \right| c_\alpha(\omega - (H - E_0) + i\eta)^{-1} c_\beta^\dagger \left| \Psi_0^N \right\rangle$$
$$\mp \left\langle \Psi_0^N \right| c_\beta^\dagger(\omega + (H - E_0) - i\eta)^{-1} c_\alpha \left| \Psi_0^N \right\rangle \quad (3.26)$$

Despite the abstract look of these expressions, the second quantization formalism allows for a generic definition regardless of any orthonormal basis, i.e., without restricting oneself to coordindate space.
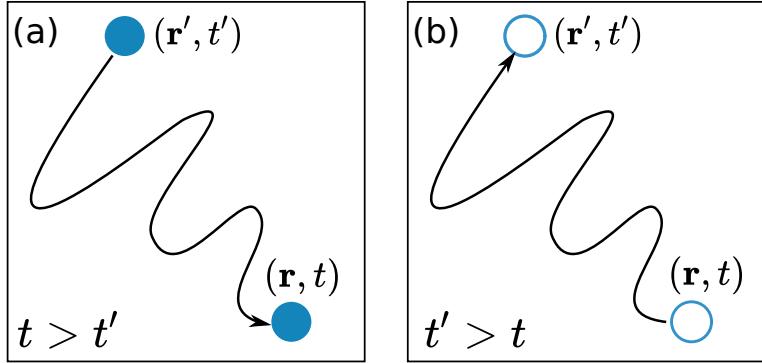
Figure 3.2: Schematic of single particle/hole dynamic represented by single particle Green's functions. (a) G^{particle} holds for $t > t'$, time at which an electron is created at $(\mathbf{r}, t)$, it propagates until annihilation at $(\mathbf{r},' t')$ occour. (b) G^{hole} holds for $t' > t$, time at which an hole is created at $(\mathbf{r}, t)$, it propagates until annihilation at $(\mathbf{r}', t')$ occours '.

3.3.2 Lehmann representation

Let us insert a completeness for the intermediate states $\left|\Psi_n^{N\pm1}\right\rangle$ in Eq. 3.26

$$
\begin{aligned}
G_{\alpha\beta}(\omega) = &\sum_n \frac{\left\langle \Psi_0^N \middle| c_\alpha \middle| \Psi_n^{N+1} \right\rangle \left\langle \Psi_n^{N+1} \middle| c_\beta^\dagger \middle| \Psi_0^N \right\rangle}{\omega - (E_n^{N+1} - E_0^N) + i\eta} \\
&\mp \sum_k \frac{\left\langle \Psi_0^N \middle| c_\beta^\dagger \middle| \Psi_k^{N-1} \right\rangle \left\langle \Psi_k^{N-1} \middle| c_\alpha \middle| \Psi_0^N \right\rangle}{\omega + (E_k^{N-1} - E_0^N) - i\eta}
\end{aligned}
\tag{3.27}
$$

known as the Lehmann repressentation of a many-body Green's function. Here, the first and second terms on the left hand side describe the propagation of a (quasi)particle and a (quasi)hole excitation. The poles are the energies relatives to the $\left|\Psi_0^N\right\rangle$ ground state. Hence they give the energies actually released in a capture reaction experiment to a bound state of $\left|\Psi_n^{N+1}\right\rangle$. The residues are transition amplitudes for the addition of a particle and take the name of spectroscopic amplitudes. In fact these energies and amplitudes are solutions of a Schrödinger-like equation: the Dyson equation. The hole part of the propagator gives instead
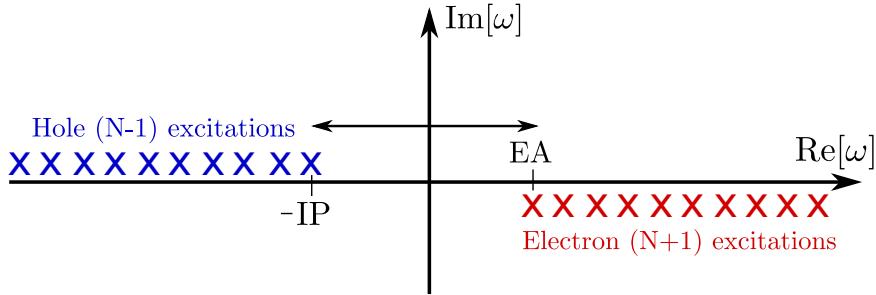
Figure 3.3: Schematic representation of the location of the poles of the one-particle Green's function. The difference between IP and EA is usually called transport or fundamental gap.

information on the process of particle emission, the poles being the exact energy absorbed in the process. The location of the poles, as reported in Figure 3.3, of the Green's function in the complex plane provides the information needed to interpret those processes measured in experiments in which a single electron is inserted to or removed from the system.

3.3.3 Spectral function and dispersion relations

By using the relation

$$\frac{1}{x \pm i\eta} = P\left(\frac{1}{x}\right) \mp i\pi\delta(x) \tag{3.28}$$

it is possible to derive the one-body spectral function from Eq. 3.24. In math,

$$S_{\alpha\beta}(\omega) = S_{\alpha\beta}^{\text{particle}}(\omega) + S_{\alpha\beta}^{\text{hole}}(\omega), \tag{3.29}$$

where the particle and hole components are

$$S_{\alpha\beta}^{\text{particle}}(\omega) = -\frac{1}{\pi} \text{Im}\left\{G_{\alpha\beta}^{\text{particle}}(\omega)\right\} =$$
$$= \sum_n \left\langle \Psi_0^N \middle| c_\alpha \middle| \Psi_n^{N+1} \right\rangle \left\langle \Psi_n^{N+1} \middle| c_\beta^\dagger \middle| \Psi_0^N \right\rangle \delta(\omega - (E_n^{N+1} - E_0^N)) \tag{3.30}$$

$$S_{\alpha\beta}^{\text{hole}}(\omega) = -\frac{1}{\pi}\,\text{Im}\big\{G_{\alpha\beta}^{\text{hole}}(\omega)\big\} =$$

$$= \sum_k \big\langle \Psi_0^N \big| c_\beta^\dagger \big| \Psi_k^{N-1}\big\rangle \big\langle \Psi_k^{N-1}\big| c_\alpha \big|\Psi_0^N\big\rangle\, \delta(\omega + (E_k^{N-1} - E_0^N)) \quad (3.31)$$

The diagonal part of the spectral function is interpreted as the probability one particle in the state α leaving or removing of adding the residual system in a state of energy ω.

3.3.4   Two particle Green's function

The Green's function definition can be extended to Green's functions for the propagation of more than one particle. In general, for each additional particle it will be necessary to introduce one additional creation and one annihilation operator. The two-particle $L^{(2)}$ (also called four-points propagator) Green's function is

$$L_{\alpha\beta\gamma\delta}^{(2)}(t_1, t_2, t_1', t_2') = -i\,\big\langle \Psi_0^N \big| T\left(c_\beta(t_2) c_\alpha(t_1) c_\gamma^\dagger(t_1') c_\delta^\dagger(t_2') \right) \big| \Psi_0^N\big\rangle \qquad (3.32)$$

It should be noted that the actual number of particles that are propagated by these objects depends on the ordering of the time variables. Therefore the information on transitions between eigenstates of the systems with N, $N\pm 1$ and $N\pm 2$ bodies are all encoded in the previous equation. Obviously, the presence of so many time variables makes the use of these functions extremely difficult (and even impossible, in many cases). However, it is still useful to consider only certain time orderings which allow to extract the information not included in the one-body propagator. The two-particle correlation is defined [67] as

$$L(12; 1', 2') = G(1, 1')G(2, 2') - L^{(2)}(1, 2; 1', 2'). \qquad (3.33)$$

If one imagines to apply a one-particle potential

$$u(\mathbf{x}_1, t_1; \mathbf{x}_2, t2) = u(\mathbf{x}1, \mathbf{x}2; t_2)\delta(t_1 - t_2), \qquad (3.34)$$

it is possible to show [68] that

$$L(12; 1'2') = \frac{\delta G(1, 1')}{\delta u(2, 2')}. \qquad (3.35)$$

Massaging this expression, one can arrive to the important result

$$L(12; 1'2') = -\int G(1, 3)\frac{\delta G^{-1}(3, 3')}{\delta u(2', 2)}G(3', 1)d(3, 3'). \qquad (3.36)$$

This formula is central for the evaluation of electron-hole interaction. It requires information about the single-particle Green's function in an interacting system. The next section is devoted to the computation of this quantity.

3.4 Hedin's equations and GW approximation

With the help of the definition given above, it is possible to discuss the theoretical framework to evaluate single particle charged excitations.
The system Hamiltonian can be written in second quantization as

$$H = \int \hat{\psi}^\dagger(\mathbf{x}) H_0(\mathbf{r}) \hat{\psi}(\mathbf{x}) \mathrm{d}\mathbf{r} + \frac{1}{2} \int \hat{\psi}^\dagger(\mathbf{x}) \hat{\psi}^\dagger(\mathbf{x}') v_c(\mathbf{r}, \mathbf{r}') \hat{\psi}(\mathbf{x}) \hat{\psi}(\mathbf{x}') \mathrm{d}\mathbf{x} \, \mathrm{d}\mathbf{x}' \quad (3.37)$$

with H_0 the single particle Hamiltonian operator in real space and $v_c(\mathbf{r}, \mathbf{r}') = |\mathbf{r} - \mathbf{r}'|^{-1}$ the Coulomb potential.
In the Heisenberg picture, the equation of motion for the field operators is

$$i \frac{\partial}{\partial t} \hat{\psi}(\mathbf{x}, t) = [\hat{\psi}(\mathbf{x}, t), H] \quad (3.38)$$

with $[\cdot, \cdot]$ a commutator.
From this it is possible to derive an equation of motion for the single-particle Green's function

$$\left(\frac{\partial}{\partial t} - H_0 \right) G(\mathbf{x}, t; \mathbf{x}', t') + i \int v_c(\mathbf{r}, \mathbf{r}'') L^{(2)}(\mathbf{x}'', t; \mathbf{x}', t'; \mathbf{x}', t'; \mathbf{x}, t) \mathrm{d}\mathbf{x}'' =$$
$$\delta(\mathbf{x} - \mathbf{x}') \delta(t - t') \quad (3.39)$$

This expression shows that solving for the single-particle Green's function requires the knowledge of the two-particle Green's function. It is not hard to understand that the same situation holds for the two-particle Green's function, whose solution depends on the knowledge on the three-particle Green's function and so on for a system of infinite number of equations. In order to find a closed system of equations it can be useful introducing the *Self-Energy* $\Sigma(\mathbf{r}, t; \mathbf{r}', t')$. This is formally defined as

$$i \int v_c(\mathbf{x}, \mathbf{x}'') L^{(2)}(\mathbf{x}'', t; \mathbf{x}', t'; \mathbf{x}', t'; \mathbf{x}, t) \mathrm{d}\mathbf{x}'' =$$
$$- \int \Sigma(\mathbf{x}, t; \mathbf{x}', t') G(\mathbf{x}'', t''; \mathbf{x}, t) \mathrm{d}\mathbf{x}'' \, \mathrm{d}t'' . \quad (3.40)$$

this simplifies Eq. (3.39) as

$$\left(\frac{\partial}{\partial t} - H_0\right) G(\mathbf{x}, t; \mathbf{x}', t') - \int \Sigma(\mathbf{x}, t; \mathbf{x}', t') G(\mathbf{x}'', t''; \mathbf{x}, t) \mathrm{d}\mathbf{x}'' \, \mathrm{d}t'' =$$
$$\delta(\mathbf{x} - \mathbf{x}')\delta(t - t') \quad (3.41)$$

reducing the solution of the problem to find the self-energy operator. This operator is a not-so-nice object, being non-local and non-hermitian. The self-energy operator is part of a closed set of coupled equations. Solving this set allows to find the self-energy and thus solving the many-body problem for the one particle excitation. This set of equation is called *Hedin's equations*. A derivation can be found in[69]. Introducing the set of variables $(i) = (\mathbf{x}_i, t_i) = (\mathbf{r}_i, s_i, t_i)$ for the collecting variables for position, spin and time the Hedin's equation have the form

$$G(1, 2) = G_0(1, 2) + \int G_0(1, 3)\Sigma(3, 4)G(4, 2) \, d(3, 4) \tag{3.42}$$

$$\Sigma(1, 2) = i \int G(1, 3)W(1, 4)\Gamma(4, 2, 3) \, d(3, 4) \tag{3.43}$$

$$\Gamma(1, 2, 3) = \delta(1, 2)\delta(1, 3) + \int \frac{\delta\Sigma(1, 2)}{\delta G(4, 5)}G(4, 6)G(5, 7)\Gamma(6, 7, 3) \, d(4, 5, 6, 7) \tag{3.44}$$

$$P(1, 2) = -i \int G(1, 3)G(4, 1)\Gamma(3, 4, 2) \, d(3, 4) \tag{3.45}$$

$$W(1, 2) = v(1, 2) + \int v(1, 3)P(3, 4)W(4, 2) \, d(3, 4) \tag{3.46}$$

Here Γ is the vertex correction, P the polarization, W the screened Coulomb interaction and ν the bare Coulomb interaction.

Evaluating this system of coupled equations poses severe computational problems, especially the calculation of the functional derivative in Eq. (3.44). In order to simplify the problem some approximation is needed. If one imposes the condition on the vertex correction

$$\Gamma(1, 2, 3) \approx \delta(1, 2)\delta(1, 3) \tag{3.47}$$

the final set of equations simplify in the so-called *GW approximation*. Before writing the new set of equations is useful to rewrite Eq. (3.46) in terms of the

microscopic dielectric function ϵ using the following definitions

$$\epsilon(1,2) = \delta(1,2) - \int v(1,3)P(3,2)d(3) \tag{3.48}$$

$$\delta(1,2) = \int \epsilon(1,3)\epsilon^{-1}(3,2)d(3) \tag{3.49}$$

$$W(1,2) = \int \epsilon^{-1}(1,3)v(3,2)\,d(3) \tag{3.50}$$

This set of equations show the physical meaning of the screened Coulomb interaction. It is common knowledge that electrostatic interaction is not the same in vacuum as in a dielectric medium. At a macroscopic level this difference is measured by the dielectric constant of the medium. Eq. (3.50) is the equivalent definition on a microscopic scale. Electrons act as a dielectric medium that reduces the interaction between any pair. The effective interaction between electrons is thus decreased from v_c. Another aspect of the screened Coulomb interaction is dynamical nature. The screening effect is more effective for some frequencies than for others. The frequency dependence of W is what allows the system to relax and screen the quasiparticle. How to treat this frequency dependence will be discussed in Section 4.2.3.

The GW approximation thus reads as

$$G(1,2) = G_0(1,2) + \int G_0(1,3)\Sigma(3,4)G(4,2)\,d(3,4) \tag{3.51}$$

$$\Sigma(1,2) = iG(1,2)W(1,2) \tag{3.52}$$

$$P(1,2) = -iG(1,2)G(2,1) \tag{3.53}$$

$$\Gamma(1,2,3) = \delta(1,2)\delta(1,3) \tag{3.54}$$

$$W(1,2) = \int \epsilon^{-1}(1,3)v(3,2)\,d(3) \tag{3.55}$$

The GW self-energy is similar to the bare exchange in Eq. (2.38) in Hartree-Fock theory . Given the similarity between the GW self-energy and bare exchange, GW can be thought of as a dynamically screened version of Hartree-Fock. Eq. (3.53) shows that the irreducible polarizability is just a simple product of two Green's functions. This is the well known Random-Phase Approximation (RPA) to the dielectric matrix.

The GW equations must be solved self-consistently since all four quantities are coupled to each other. As with other nonlinear equations, including the equations

of mean-field theories like Kohn-Sham DFT or Hartree-Fock theory, the GW equations can be solved by iteration. The algorithm is the following: starting from a given G_0 and iterate to self-consistency as can be shown in Figure 3.4. To proceed we express G in its spectral representation, with E a complex number
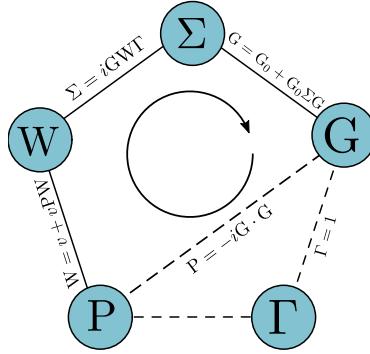
Figure 3.4: Pictorial description of the Hedin's equations, often called Hedin's pentagon. All the linked quantities are depicted as the vertexes of a pentagon. Each side of the pentagon represents one of the Hedin's equation. Starting from an initial guess for one of the quantities, e.g. G, it is possible to "solve the pentagon" self-consistently. The GW approximation can also be depicted using this pentagon, skipping the Γ vertex.

3.4.1 Solving for quasiparticle excitations

Using DFT, the ground state $|N, 0\rangle$ is determined from the solutions of the Kohn–Sham (KS) equations in Eq. (2.51). Charged excitation can be found as stated before using the GW approximation, in which the self-energy takes the form

$$\Sigma(\mathbf{x}, \mathbf{x}', \omega) = \frac{\mathrm{i}}{2\pi} \int \mathrm{d}\omega' \, G_1(\mathbf{x}, \mathbf{x}', \omega + \omega') \, W(\mathbf{x}, \mathbf{x}', \omega), \qquad (3.56)$$

i.e., it is a convolution of G_1 with the screened Coulomb interaction $W = \epsilon^{-1} v_\mathrm{c}$, where $v_\mathrm{c}(\mathbf{r}, \mathbf{r}') = |\mathbf{r} - \mathbf{r}'|^{-1}$ is the bare Coulomb interaction and $\epsilon^{-1}(\mathbf{r}, \mathbf{r}', \omega)$ is the inverse dielectric function calculated in the Random-Phase Approximation (RPA) [70]. A pictorial example of this approximation is depicted in Figure 3.5.
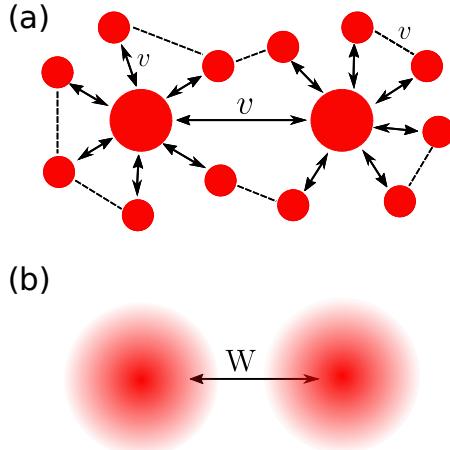
Figure 3.5: In (a) a schematic of an interacting many-particles system with electrostatic interaction v. The two particles depicted with bigger red dots, experience the interaction among each other plus the interaction with all the other surrounding particles. In (b) the electrostatic interaction between the bigger red dots is substituted with the screened interaction $W = \epsilon^{-1}v$. This is called quasiparticle approximation. The screening includes the effect of the interaction with the surrounding particles. The Random-Pahse-Approximation (RPA) screening is obtained when the interaction depicted in (a) with dashed line is neglected.

Using this approximation, Eq. (2.51) is converted into a Dyson-type equation of motion for the quasiparticles (i.e., the QP electron and hole states) [71, 72]:

$$\left[\widehat{H}_0 + \widehat{\Sigma}(\varepsilon_i^{\mathrm{QP}})\right]\left|\phi_i^{\mathrm{QP}}\right\rangle = \varepsilon_i^{\mathrm{QP}}\left|\phi_i^{\mathrm{QP}}\right\rangle , \tag{3.57}$$

where $\varepsilon_i^{\mathrm{QP}}$ are the one-particle excitation energies of the system, and $\left|\phi_i^{\mathrm{QP}}\right\rangle$ are the QP wave functions.

In practice, the QP wave functions are expressed in a basis of KS states, i.e.,

$$\left|\phi_i^{\mathrm{QP}}\right\rangle = \sum_j a_j^i \left|\phi_j^{\mathrm{KS}}\right\rangle . \tag{3.58}$$

With $\widehat{H}_0 = \widehat{H}^{\mathrm{KS}} - \widehat{V}_{\mathrm{xc}}$, diagonalizing the energy-dependent QP Hamiltonian in this basis as

$$H_{ij}^{\mathrm{QP}}(E) = \varepsilon_i^{\mathrm{KS}}\delta_{ij} + \left\langle \phi_i^{\mathrm{KS}} \right| \widehat{\Sigma}(E) - \widehat{V}_{\mathrm{xc}} \left| \phi_j^{\mathrm{KS}} \right\rangle s \tag{3.59}$$

yields the QP states and energies.

If the off-diagonal elements of Eq. (3.59) are small, i.e. $\left| \phi_i^{\mathrm{QP}} \right\rangle \approx \left| \phi_i^{\mathrm{KS}} \right\rangle$, the quasiparticle energies can be evaluated perturbatively according to

$$\varepsilon_i^{\mathrm{QP}} = \varepsilon_i^{\mathrm{KS}} + \Delta\varepsilon_i^{GW} = \varepsilon_i^{\mathrm{KS}} + \left\langle \phi_i^{\mathrm{KS}} \right| \widehat{\Sigma}(\varepsilon_i^{\mathrm{QP}}) - \widehat{V}_{\mathrm{xc}} \left| \phi_i^{\mathrm{KS}} \right\rangle. \tag{3.60}$$

Computing $\varepsilon_i^{\mathrm{QP}}$ requires determination of $\Delta\varepsilon_i^{GW}$, which consequently leads to self-consistently solving Eq. (3.60). This can be achieved by first identifying an interval containing a solution on a grid and then refining this using a bisection (graphical solution). As an alternative, Newton fixed-point iterations can be performed. Conventionally this is referred to as the G_0W_0 approximation. To improve upon this one-shot approach, the evGW procedure can be used instead: QP energies are updated both in the calculation of the non-local, energy-dependent microscopic dielectric function determined within the RPA and in the Green's function until eigenvalue (ev) self-consistency is reached.

3.5 Electron-Hole excitations with Bethe-Salpeter equation

Neutral excitations with a conserved number of electrons and a change in their configuration S ($|N, 0\rangle \rightarrow |N, S\rangle$) rely instead on the two-particle Green's function [73]. This can be obtained from another Dyson-like equation of motion, known as the Bethe–Salpeter Equation (BSE) [74]. The 2-bodies correlation function of Eq. (3.33), with the help of Eq. (3.36) and Eq. (3.51), satisfy the following Dyson-like equation

$$L(1, 2, 1', 2') = L_0(1, 2, 1', 2') +$$
$$+ \int L_0(1, 4, 1', 3)\Xi(3, 5, 4, 6)L(6, 2, 5, 2')d(3, 4, 5, 6) \tag{3.61}$$

with the interaction kernel being

$$\Xi(3, 2, 3', 2') = -i\delta(3, 3')\delta(2', 2)v_c(3, 2) + \frac{\delta\Sigma(3, 3')}{\delta G(2', 2)}. \tag{3.62}$$

The uncorrelated $L_0(1, 2, 1', 2') = G(1, 2')G(2, 1')$ contains the Green function G, solution of Eq. (3.51).

L depends on four time variables, related to two creation processes (electron and hole) and two annihilation processes. We restrict ourselves to simultaneous creation and to simultaneous annihilation, so only two of the four time variables are independent. Due to time homogeneity in the absence of external fields, only the difference of these two time variables is relevant for Eq. (3.61) and is used to carry out a one-dimensional time-energy Fourier transform into $L(1, 2, 1', 2', \omega)$, where (1), (2), etc. now contain only position and spin degrees-of-freedom.

If the self-energy is determined within the GW approximation the electron-hole kernel is written as:

$$\Xi^{GW}(3, 2, 3', 2') \approx -i\delta(3, 3')\delta(2', 2)v_c(3, 2) + \delta(3, 2')\delta(3', 2)W(3, 2). \qquad (3.63)$$

In principle, having a form for the interaction kernel, the Bethe-Salpeter equation can be solved. Now we will use a non rigorous argument to show one possible way to solve it. The idea is transform the Bethe-Salpeter equation into an effective two-particle Hamiltonian that is then diagonalized. To this end we can write the equation in the basis of the orthonormal orbitals that diagonalize G_0. L_0 can be written as

$$L_0(1, 2, 1', 2', \omega) = i \sum_{v,c} \Big[\frac{\phi_c(\mathbf{x}_1)\phi_v(\mathbf{x}_1')\phi_v(\mathbf{x}_2)\phi_c(\mathbf{x}_2')}{\omega - (E_c - E_v)} - $$
$$\frac{\phi_v(\mathbf{x}_1)\phi_c(\mathbf{x}_1')\phi_c(\mathbf{x}_2)\phi_v(\mathbf{x}_2')}{\omega - (E_c + E_v)} \Big] \qquad (3.64)$$

with v running over the occupied and c over the empty states.

Eq. (3.61) can be rewritten as

$$L(\omega) = \left[L_0^{-1} + \Xi \right]^{-1} = \left[H^{BSE} - \mathbb{1}\omega \right]^{-1}. \qquad (3.65)$$

Assuming that the electron-hole excitations are long-lived (the excitations correspond to peaks in L) we can write L similarly to the one-particle Green's function in Eq. (3.27). In other words electron-hole excitations can be sought solving a Green's function problem of the kind (abusing the notation) $[H^{BSE} - \omega]\chi_S = -\delta$. The electron-hole Green's function can be expressed as

$$L(1, 2, 1', 2', \omega) = i \sum_S \left[\frac{\chi_S(\mathbf{x}_1, \mathbf{x}_1')\chi_S(\mathbf{x}_2', \mathbf{x}_2)}{\omega - \Omega_S} - \frac{\chi_S(\mathbf{x}_2, \mathbf{x}_2')\chi_S(\mathbf{x}_1', \mathbf{x}_1)}{\omega + \Omega_S} \right]. \qquad (3.66)$$

S denotes the correlated electron-hole excitations of the system with corresponding excitation energies Ω_S. The electron-hole amplitudes are given by

$$\chi_S(\mathbf{x}, \mathbf{x}') = -\langle N, 0| \hat{\psi}^\dagger(\mathbf{x}')\hat{\psi}(\mathbf{x}) |N, S\rangle. \tag{3.67}$$

In the specific case of optical excitations, one can employ a product basis of QP wave functions for coupled electron-hole amplitudes, i.e.,

$$
\begin{aligned}
\chi_S(\mathbf{r}_\mathrm{e}, \mathbf{r}_\mathrm{h}) = \sum_v^\mathrm{occ} \sum_c^\mathrm{unocc} \sum_{\sigma\sigma'} & A^S_{vc,\sigma\sigma'}\phi_{c,\sigma'}(\mathbf{r}_\mathrm{e})\phi^*_{v,\sigma}(\mathbf{r}_\mathrm{h}) \\
& + B^S_{vc,\sigma\sigma'}\phi_{v,\sigma'}(\mathbf{r}_\mathrm{e})\phi^*_{c,\sigma}(\mathbf{r}_\mathrm{h}),
\end{aligned}
\tag{3.68}
$$

where $\mathbf{r}_\mathrm{e}$ ($\mathbf{r}_\mathrm{h}$) is for the electron (hole) coordinate, and we drop the label QP for clarity. Here, $A_{vc,\sigma\sigma'}$ ($B_{vc,\sigma\sigma'}$) are the expansion coefficients of the excited state wave function in terms of resonant (anti-resonant) transitions between QP occupied (occ.) states v and unoccupied (unocc.) c with spin σ and σ', respectively. So the effective two-particle Hamiltonian H^BSE is of the form

$$
\begin{pmatrix} \mathbf{H}^\mathrm{res} & \mathbf{K} \\ -\underline{\mathbf{K}} & -\underline{\mathbf{H}}^\mathrm{res} \end{pmatrix} \begin{pmatrix} A^S \\ B^S \end{pmatrix} = \Omega_S \begin{pmatrix} A^S \\ B^S \end{pmatrix}. \tag{3.69}
$$

Assuming that spin-orbit coupling is negligible, this Hamiltonian has block structure in terms of the spin combinations [75]. It can be decoupled into singlet and triplet Hamiltonians, allowing us to drop the explicit spin variables. Then, the matrix elements of $\underline{\mathbf{H}}^\mathrm{res}$ and $\underline{\mathbf{K}}$ are calculated as

$$H^\mathrm{res}_{vc,v'c'} = D_{vc,v'c'} + \kappa K^\mathrm{x}_{vc,v'c'} + K^\mathrm{d}_{vc,v'c'} \tag{3.70}$$

$$K_{cv,v'c'} = \kappa K^\mathrm{x}_{cv,v'c'} + K^\mathrm{d}_{cv,v'c'}, \tag{3.71}$$

where $\kappa = 2$ (0) for spin singlet (triplet) excitations, and

$$D_{vc,v'c'} = (\varepsilon_c - \varepsilon_v)\delta_{vv'}\delta_{cc'} \tag{3.72}$$

$$K^\mathrm{x}_{vc,v'c'} = \int \mathrm{d}^3\mathbf{r}_\mathrm{e}\, \mathrm{d}^3\mathbf{r}_\mathrm{h}\, \phi^*_c(\mathbf{r}_\mathrm{e})\phi_v(\mathbf{r}_\mathrm{e})v_\mathrm{c}(\mathbf{r}_\mathrm{e}, \mathbf{r}_\mathrm{h})\phi_{c'}(\mathbf{r}_\mathrm{h})\phi^*_{v'}(\mathbf{r}_\mathrm{h}) \tag{3.73}$$

$$K^\mathrm{d}_{vc,v'c'} = -\iint \mathrm{d}^3\mathbf{r}_\mathrm{e}\, \mathrm{d}^3\mathbf{r}_\mathrm{h}\, d\omega\, \phi^*_c(\mathbf{r}_\mathrm{e})\phi_{c'}(\mathbf{r}_\mathrm{e}\phi_v(\mathbf{r}_\mathrm{h})\phi^*_{v'}(\mathbf{r}_\mathrm{h}))$$
$$\times W(\mathbf{r}_\mathrm{e}, \mathbf{r}_\mathrm{h}, \omega)f(\omega, \Omega_S) \tag{3.74}$$

$$f(\omega, \Omega_S) = \frac{i}{2\pi}\frac{1}{\Omega_S - \omega - (E_{c'} - E_{v'} + i0^+)} - \frac{1}{\Omega_S + \omega - (E_c - E_v + i0^+)} \tag{3.75}$$

The exchange interaction K^{x} originates from the bare interaction v_{c}, and is responsible for the singlet-triplet splitting. The direct interaction K^{d} contains the attractive, but screened, interaction W between electron and hole. This interaction is responsible for the binding of the electron-hole pair. Furthermore, it is assumed here that the dynamic properties of $W(\omega)$ are negligible, and the computationally less demanding static approximation $\omega = 0$ is sufficient. This is true when in $K^{\mathrm{d}}_{vc,v'c'}$ the excitonic binding energies $\Omega_S - \omega - (E_{c'} - E_{v'})$ are much smaller than the characteristic screeening frequencies of $W(\omega)$. This approximation is often valid in many case since the binding energy is very large (several eV). For this reason in molecular application the static approximation is enforced simplyfing notably the implementation of the BSE. It is worth mentioning that in those case in which this approximation might not hold the possibility of going beyond the static approximation can be achievied computing a dynamical correction of the electron–hole screening thanks to a renormalized first-order perturbative correction to the static BSE excitation energies [76].

In systems for which the elements of the off-diagonal blocks $\underline{\mathbf{K}}$ in Eq. (3.69) are negligible, it is legitimate to use the Tamm–Dancoff Approximation (TDA) [77], in which the electron-hole amplitude is expressed as

$$\chi_S^{\mathrm{TDA}}(\mathbf{r}_{\mathrm{e}}, \mathbf{r}_{\mathrm{h}}) = \sum_v^{\mathrm{occ}} \sum_c^{\mathrm{unocc}} A_{\mathrm{TDA},vc}^S \phi_c(\mathbf{r}_{\mathrm{e}}) \phi_v^*(\mathbf{r}_{\mathrm{h}}), \qquad (3.76)$$

i.e., by resonant transitions from occupied v to unoccupied c states only. The effective Hamiltonian reduces to the upper diagonal block of Eq. (3.69):

$$\underline{\mathbf{H}}^{\mathrm{res}} A_{\mathrm{TDA}}^S = \Omega_S^{\mathrm{TDA}} A_{\mathrm{TDA}}^S. \qquad (3.77)$$

The TDA is known to reduce triplet instabilities [78, 79]. On the other hand, the coupling between resonant and anti-resonant parts is significant, and its neglect can cause deviations of several $0.1\,\mathrm{eV}$ from results obtained with the full approach [80], in particular for small molecules.

3.6 QM/MM embedding schemes for QP and excitons

When dealing with electronic excitations in complex molecular systems, properties of the individual molecules forming the system, are often not sufficient for

a complete and exhaustive description of these phenomena. The nature of excited states is in general a result of a convoluted interplay between the intrinsic quantum-mechanical properties of the basic units, i.e. isolated molecules, and the local and global morphology of the large-scale molecular system. As it would be clear in Ch. 4, a full quantum-mechanical treatment of such a complex system it is practically impossible. The $\mathcal{O}(N^4)$ scaling and overall cost of canonical GW-BSE implementations restrict the tractable system size and prohibit the study of many systems that are relevant in the chemistry and physics community, such as solid-liquid interfaces, molecules in solution, complex alloys, nanostructures or hybrid interfaces, that require large simulation cells with hundreds to thousands of atoms. A different approach capable of combining the predictive power of QM methods whilst keeping a reasonable computational scaling must be sought. Embedding strategies currently provide the best compromise between accuracy and computational cost in modeling properties and processes of large and complex molecular systems. In embedding theories a subsystem of interest is treated at a higher level of accuracy whilst the rest of the system is accounted for with a lower accuracy method. In this framework, different methods have been proposed all over the years, from the continuum embedding models [81, 82, 83, 84], the popular QM/MM approach [85, 36] to the more recent and very promising density matrix [86] and density functional embedding techniques [33, 87, 81, 38, 88, 89]. It is important to stress that a successful embedding method used for excited state evaluations must be able to model the polarization response of the environment to a charge fluctuation in the embedded region. For the sake of brevity in the following only the QM/MM approach, used to get results in this thesis, is discussed. It is important to stress in order to avoid any misunderstanding that in this thesis the QM/MM method has been employed *only* to evaluate the effect of the environment on the density of states of a system. Despite the fact that QM/MM could be employed to evaluate forces on molecules and trajectories of complex systems in solution, these things are beyond the scope of the thesis.

3.6.1 Hybrid quantum-classical embedding method (QM/MM)

The QM/MM framework is defined as the framework in which the quantum (excited) state is linked to a polarizable atomistic model for the environment. Assuming a weak coupling between the classical and the quantum region, the former affects the latter (and vice versa) via electrostatic interactions only. Static local-fields are associated with the distribution of static multipoles in the MM region. In addition to these static local-fields, the electron density of the QM region re-

arrange upon excitation and accordingly its electrostatic potential affecting the MM region is modified. These effects are called polarization effects. These are stronger in the region close to the active QM region and they are crucial in those cases involving charged excitations or larger modification of molecular dipole moments. QM/MM approaches can use either subtractive or additive schemes. To explain the difference, let us take into account a system split in two subregions, labeled with the indeces 1 and 2. In a subtractive scheme, three separate calculations are performed: One QM calculation with the QM region (subsystem 1) and two MM calculations, one for the entire system (subsystems 1 and 2) and one for the QM region (subsysem 1). The total QM/MM energy is then obtained as:

$$E_{QM/MM}^{sub} = E_1^{QM} + E_{12}^{MM} - E_1^{MM} \qquad (3.78)$$

The advantage with this approach is the simplicity: It automatically ensures that no interactions are double-counted and it can be set up for any QM and MM software. It is also easily extendable to those systems that require a special treatment of long-range effects, usually sought using Ewald summation techniques [90] et similia. The main drawback is the requirment for the MM parametrization of the QM region to evaluate E_{12}^{MM}. This can be a limiting aspect when dealing with excited states in terms of accuracy and predictiveness.
On the other hand, the additive scheme total energy reads

$$E_{QM/MM}^{add} = E_1^{QM} + E_2^{MM} + V_{12}^{QM/MM}. \qquad (3.79)$$

where the QM system is embedded within the larger MM system, and the energy of the whole system is the sum of QM, MM, and QM/MM coupling terms. The interaction between the two regions is explicity evaluated via the term $V_{12}^{QM/MM}$. In this work only the electrostatic embedding scheme was used. This implies that the electrostatic interactions between the two subsystems are handled during the computation of the electronic wave function. The MM multipoles enter the QM Hamiltonian as one-electron operators. A schematic of this approach is depicted in Figure 3.6. The main advantage of this scheme is the avoidance of parametrization of the QM region.

3.6.2 Multipole representation of molecules and classical energy contribution

Our scheme makes use of a distributed atomic multipole representation for molecules in the MM region, which allows treatment of both the effects of static
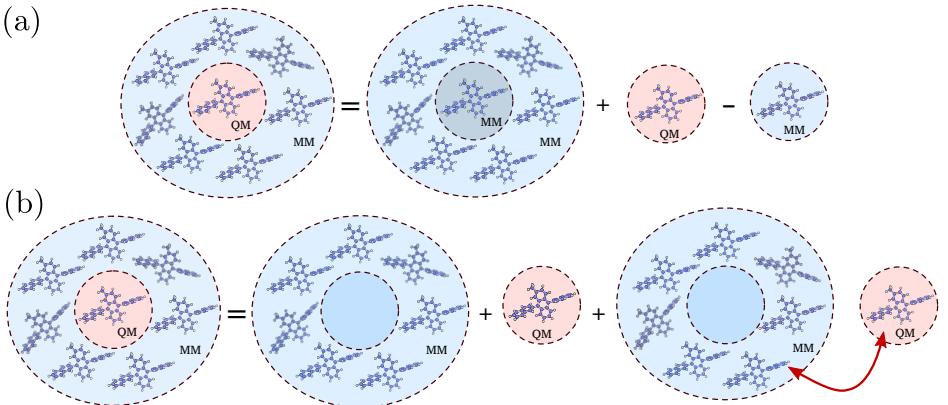
Figure 3.6: Schematic representation of different QM/MM embedding schemes. In (a) the subtractive QM/MM scheme. The QM part is replaced by a classical counterpart, and the interaction between the inner and outer region is treated purely classicaly. In order to avoid double counting the energy of the classicaly-treated QM part must be subtracted from the overall energy. In other words in the subtractive scheme the QM region energy is shifted with the help of the classical contribution. In (b) the additive scheme consist of evaluating the MM and QM region energy separately. The interaction between the QM and MM part is treated explicitly (in (b) it is represented with a red line). Usually the MM part enters in the QM Hamiltonian as an external field. Once the electron density of the QM region is obtained, this is let to interact with the MM part. This is repeated until self-consistency is reached.

electric fields and the polarization response as a self-consistent reaction field. Specifically, static atomic multipole moments [91] Q_t^m are employed, where t indicates the multipole rank and m the associated atom in the molecule M. The tensor $T_{tu}^{mm'}$ describes the interactions between the multipoles moments Q_t^m and $Q_u^{m'}$. To model the polarization effects, each atom can additionally be assigned a polarizability $\alpha_{tu}^{mm'}$ for the creation of induced moments ΔQ_t^m due to the field generated by moments u on a different atom m'.

To show how to evaluate the MM total energy contributions in Eq. (3.78) and Eq. (3.79) we can imagine splitting a purely classical MM system $\mathcal{S}$ in state s into regions $\mathcal{R}$ and $\mathcal{R}'$ with $\mathcal{S} = \mathcal{R} \cup \mathcal{R}'$, its total energy is given by

$$E_{\text{class}}^{(s)}(\mathcal{S}) = E^{(s)}(\mathcal{R}) + E^{(s)}(\mathcal{R}') + E^{(s)}(\mathcal{R}, \mathcal{R}'), \tag{3.80}$$

where

$$E^{(s)}(\mathcal{R}) = \frac{1}{2} \sum_{M \in \mathcal{R}} \sum_{\substack{M' \in \mathcal{R} \\ M' \neq M}} E_{MM'}^{(s)} + \frac{1}{2} \sum_{M \in \mathcal{R}} E_M^{(s)} \tag{3.81}$$

$$E^{(s)}(\mathcal{R}, \mathcal{R}') = \sum_{M \in \mathcal{R}} \sum_{M' \in \mathcal{R}'} E_{MM'}^{(s)} \tag{3.82}$$

with

$$E_{MM'}^{(s)} = \sum_{m \in M} \sum_{m' \in M'} \sum_{tu} (Q_t^{m(s)} + \Delta Q_t^{m(s)})$$
$$\times T_{tu}^{mm'} (Q_u^{m'(s)} + \Delta Q_u^{m'(s)}) \tag{3.83}$$

and

$$E_M^{(s)} = \sum_{m \in M} \sum_{\substack{m' \in M \\ m' \neq m}} \sum_{tu} \Delta Q_t^{m(s)} (\alpha^{-1})_{tu(s)}^{mm'} \Delta Q_u^{m'(s)}. \tag{3.84}$$

Eq. (3.80) follows a variational principle with respect to the induced moments, and a preconditioned conjugate gradient method is used to find the ΔQ_t^m, which give the minimum energy. Induced interactions are modified using Thole's damping functions [92, 93] to avoid overpolarization.

3.6.3 Interaction between the classical- and quantum-treated subsystems

The way the interaction between the classical- and quantum-treated subsystems is formulated hugely depends on the specific computational implementation of both

the classical and quantum algorithms. In the following we present how this inter-action is treated in the open-source VOTCA-XTP software [94, 37]. This software allows for the calculation of the excited-state electronic structure of molecules using many-body Green's functions theory in the GW approximation with the Bethe–Salpeter Equation (BSE). A distinctive feature of VOTCA-XTP is the cap-ability to couple the calculation of electronic excitations to a classical polarizable environment on atomistic level in a coupled quantum- and molecular-mechanics (QM/MM) scheme, where a complex morphology can be imported from Molecular Dynamics simulations.

If the additive scheme is used, the MM multipoles can interact with the QM region as an additional external potential, while the explicit electrostatic field from the QM density is used to polarize the MM region. In the GW-BSE framework, the density depends on the state of interest (s). If s is a quasiparticle excitation, we define

$$\rho_{\mathrm{QP}}^{(s)}(\mathbf{r}) = \rho_{\mathrm{DFT}}(\mathbf{r}) + f_s|\phi_s^{\mathrm{QP}}(\mathbf{r})|^2, \tag{3.85}$$

with $f_s = -1$ for occupied and $f_s = +1$ for unoccupied QPs. If s is an electron-hole excitation, its total density is evaluated as

$$\rho^{(s)}(\mathbf{r}) = \rho_{\mathrm{DFT}}(\mathbf{r}) + \rho_e^{(s)}(\mathbf{r}) - \rho_h^{(s)}(\mathbf{r}). \tag{3.86}$$

Here the electron (hole) contribution of the exciton to the density is computed by integrating the squared excited-state wavefunction χ_S with respect to the hole (electron) coordinates, i.e.,

$$\rho_{\mathrm{e}}^{(s)}(\mathbf{r}) = \rho_{\mathrm{e}}^{(s)}(\mathbf{r}_{\mathrm{e}}) = \int d\mathbf{r}_{\mathrm{h}}|\chi_S(\mathbf{r}_{\mathrm{e}}, \mathbf{r}_{\mathrm{h}})|^2$$
$$\rho_{\mathrm{h}}^{(s)}(\mathbf{r}) = \rho_{\mathrm{h}}^{(s)}(\mathbf{r}_{\mathrm{h}}) = \int d\mathbf{r}_{\mathrm{e}}|\chi_S(\mathbf{r}_{\mathrm{e}}, \mathbf{r}_{\mathrm{h}})|^2. \tag{3.87}$$

More specifically, VOTCA-XTP can partition a system into multiple active QM regions (possibly treated at different levels of theory) and multiple classical MM regions, in which static and polarizable multipoles of different orders can be defined, generalizing Eq. (3.80). In order to evaluate excitation energies within this QM/MM scheme, a self-consistent procedure is required if polarization is in-cluded in the MM region. Within a single iteration step p, a QM level calculation (DFT for the ground state $s = n$, DFT+GW-BSE for electron-hole excited $s = x$ states) is performed in the electric field generated by the total moments in the MM region. The resulting QM energy then reads

$$E_{\mathrm{QM}}^{(s),p} = E_{\mathrm{DFT}}^{(s),p} + \delta_{sx}\,\Omega_S^p. \tag{3.88}$$

The associated total electron density is then evaluated on a grid. In VOTCA-XTP, the default quadrature on a grid used for the numerical integration is an Euler–MacLaurin scheme for the radial components and a Lebedev scheme for the angular components, and the discretized density is then used to self-consistently determine new induced dipoles in the MM region. The minimized classical energy $E_{\text{class}}^{(s),p}$ is used to update the total energy of the coupled QM/MM system

$$E_{\text{QM/MM}}^{(s),p} = E_{\text{QM}}^{(s),p} + E_{\text{class}}^{(s),p},$$ (3.89)

an expression equivalent to Eq. (3.79) but state specific.

The whole procedure is repeated until the change of total energy is less then a preselected accuracy, typically 10^{-5} Ha. To obtain the excitation energy $\Omega^{(s)}$ of a
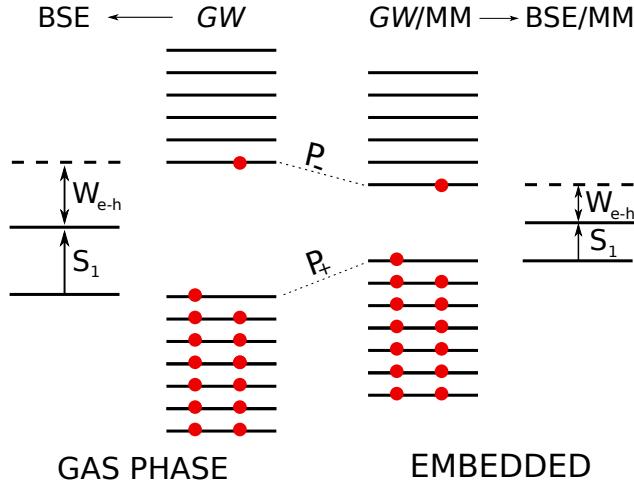
Figure 3.7: Effect of polarization on quasiparticle (treated using GW) and exciton energies (treated using BSE) in the QM/MM procedures.

complex in the polarizable environment, total energies of the combined QM/MM system are obtained self-consistently for both the ground and excited state, and their difference defines

$$\Omega^{(s)} = E_{\text{QM/MM}}^{(s)} - E_{\text{QM/MM}}^{(n)}.$$ (3.90)

An equivalent formulation for quasiparticle excitation energies uses the respective $\varepsilon^{\mathrm{QP}}$ instead of Ω_S in Eq. (3.88). Figure 3.7 shows a schematic representation of the effect of polarization on excitation energies (for both quasiparticles and excitons) in the QM/MM schema. The above QM/MM procedures rely on the representation of the molecules in the MM region by static atomic multipoles and polarizabilities. These can be taken from standard parameterizations, available for instance from the AMOEBA force field [95]. However, in many cases it is necessary to make custom parameterizations. VOTCA-XTP can either read fitted partial charges from one of the supported external DFT packages or obtain them with its internal CHELPG [96] module. Higher order static multipoles can be taken from the GDMA software [97]. VOTCA-XTP also provides a tool for the optimization of atomic polarizabilities after the static moments are defined. Starting from generic element-specific polarizabilities from AMOEBA, these are scaled atom-specific to reproduce the polarizable volume of the molecule as obtained from DFT.

Chapter 4

Numerical methods and practical realization for DFT, GW-BSE and QM/MM methods

> Sometimes one can improve the theories in the sense of discovering a quicker, more efficient way of doing a given calculation

> John Pople

In this chapter we address how DFT, *GW*-BSE and QM/MM methods are implemented for a numerical evaluation of electronic properties in the open-source code VOTCA-XTP. In the first section a brief review of the basis set expansion and a section on how to rewrite the equations of the previous chapter as linear algebra problems. This is followed by a focus on the differences between different choices of the basis set, stressing on their pros and cons. The last part is dedicated to the actual implementation in VOTCA-XTP with a review of different technical aspect

and computational strategies.

4.1 Basis set expansion

Computers gained popularity in theoretical physics studies and modelling due to the possibility of turning many problems into the linear-algebra language. Computers turned to be extraordinary tools for solving linear algebra. Even high dimensional problems can be solved in a reasonable amount of computational time using one of the many algorithms and the libraries developed so far. The possibility that computers can solve problems unthinkable to be solved by humans really pushed science and engineering into the computational scientific revolution we are all experiencing. To actually solve any of the problem presented in previous sections in any practical calculation, we have to describe the wavefunctions using a finite amount of information since we cannot describe an arbitrary continuous function on a computer. To do this, we define a finite set of functions that serves as a basis set for an approximate expansion of the exact orbitals. For the sake of brevity this idea is applied to Kohn-Sham equations only. The reader should be aware that the same way of thought works for other theories such as Hartree-Fock or GW-BSE as well. All these theories allow for the calculation of molecular orbitals (MOs), functions that represent a region in a molecule where an electron is likely to be found. These are often sought expanding them via Atomic Orbitals (AOs). These are atom-centered functions. The main idea is that the electron distribution in molecules is not so different from the electron distribution in the component atoms. This means that the orbitals of the separate atoms is a good starting point for the expansion of the MOs. HF and DFT are often used to get AOs whilst MOs are obtained via GW-BSE. Let us start expanding KS wavefunctions as

$$\phi_i^{\mathrm{KS}}(\mathbf{r}) = \sum_\mu c_\mu^i \, \chi_\mu(\mathbf{r}) \tag{4.1}$$

with $\{\chi_\mu(\mathbf{r})\}$ a set of basis elements and $\{c_\mu^i\}$, the expansion coefficients. For the sake of generality the basis is taken to be non-orthonormal with overlap matrix elements defined as

$$\mathrm{S}_{\nu\mu} = \int \chi_\nu(\mathbf{r})\chi_\mu(\mathbf{r})\mathrm{d}\mathbf{r} \,. \tag{4.2}$$

Using Eq. (4.1) allows to rewrite all orbitals derived properties. For instance, the

electron density can be expressed as:

$$n(\mathbf{r}) = \sum_i^N |\phi_i^{\mathrm{KS}}(\mathbf{r})|^2 = \sum_i^N \sum_{\mu\nu} c_\nu^{i*} c_\mu^i \, \chi_\nu^*(\mathbf{r})\chi_\mu(\mathbf{r}) = \sum_{\mu\nu} \mathrm{D}_{\nu\mu}\chi_\nu^*(\mathbf{r})\chi_\mu(\mathbf{r}) \qquad (4.3)$$

with the definition of the density matrix

$$\mathrm{D}_{\nu\mu} = \sum_i^N \sum_{\mu\nu} c_\nu^{i*} c_\mu^i \qquad (4.4)$$

All the spatial dependent parts can be integrated leading to vector/matrix expressions solvable using standard linear algebra procedures. As an example, using Eq. (4.1) in Eq. (2.51), followed by multiplication from the left of $\phi_j(\mathbf{r})$ and integration, we obtain a generalized eigenvalue problem

$$\sum_\mu \mathrm{F}_{\nu\mu}^{\mathrm{KS}} c_\mu^i = \sum_\mu \mathrm{S}_{\nu\mu} c_\mu^i \varepsilon_i^{\mathrm{KS}} \qquad (4.5)$$

with the Fock matrix defined as:

$$\mathrm{F}_{\nu\mu}^{\mathrm{KS}} = -\frac{1}{2}\int \chi_\nu^*(\mathbf{r})\nabla^2\chi_\mu(\mathbf{r})\mathrm{d}\mathbf{r} - \int \chi_\nu^*(\mathbf{r})V_{ext}(\mathbf{r})\chi_\mu(\mathbf{r})\mathrm{d}\mathbf{r} +$$
$$+ \sum_{\eta\delta}\int \frac{\chi_\nu^*(\mathbf{r})\chi_\mu(\mathbf{r})\chi_\eta(\mathbf{r}')\chi_\delta(\mathbf{r}')}{|\mathbf{r}-\mathbf{r}'|}\mathrm{d}\mathbf{r}\,\mathrm{d}\mathbf{r}'\,\mathrm{D}_{\eta\delta} + \int \chi_\nu^*(\mathbf{r})V_{\mathrm{xc}}(\mathbf{r})\chi_\mu(\mathbf{r})\mathrm{d}\mathbf{r}\,. \quad (4.6)$$

This implies that it is possible to determine all the integrals in this equation. For the sake of brevity we can define the first term arising from the kinetic-energy definition with matrix elements $T_{\nu\mu}$ as for the external potential and the exchange-correlation one we use the labelling $V_{\nu\mu}^{\mathrm{ext}}$ and $V_{\nu\mu}^{\mathrm{xc}}$. Eq. (4.6) are actually dependent (via n and $V_{\nu\mu}^{\mathrm{xc}}$) on yet unknown coefficients determined with Eq. (4.5).
In literature it is common to define the 4-center Coulomb integral, arising from the Hartree term, as

$$(\nu\mu|\eta\delta) = \int \frac{\chi_\nu(\mathbf{r})\chi_\mu(\mathbf{r})\chi_\eta(\mathbf{r}')\chi_\delta(\mathbf{r}')}{|\mathbf{r}-\mathbf{r}'|}\mathrm{d}\mathbf{r}\,\mathrm{d}\mathbf{r}' \qquad (4.7)$$

These kind of integrals are recurring also in GW-BSE and are by far the most expensive type of integral to determine in practical calculation. The formal scaling for these integrals, given N basis elements, is $\mathcal{O}(N^4)$. How to curb the expenses

of these integrals is discussed in Section 4.2. The homogeneous linear system Eq. (4.5) admits non zero solutions for the unknown coefficients c_μ^i only if the determinant of the matrix in square bracket is null, i.e.

$$\det\left(\underline{\mathbf{F}}^{\text{KS}} - \varepsilon_i^{\text{KS}}\underline{\mathbf{S}}\right) = 0 \qquad (4.8)$$

Therefore, the problem of solving the KS equations for each orbital is transformed into a problem of linear algebra, which can be solved by standard diagonalization techniques.

In principle Eq. (4.6) is exact assuming that one has access to a infinite basis and can perform all the integrals exactly. However this is seldom the case. The first problem reflects the fact that no exact basis can be employed. A finite basis (i.e with a finite number of basis elements) is often employed instead. This implies that results and predictions might be strongly dependent on the choice of the basis set. A good practice should entails checking the convergence towards the exact complete basis set (CBS) limit. Nevertheless, this is not always possible, in particular in those situations in which calculations are prohibitively expensive and convergence checks can be hard to test. Attempts to address the CBS limit problem have led to the emergence of a wide variety of the extrapolation schemes [98, 99, 100, 101, 102, 103, 104] where the infinite basis set calculations are realized by extrapolation to the CBS limit. These extrapolations are often based on formulas for the asymptotic convergence of energies and other properties to their CBS limit. A very simple example of this procedure is in Figure 4.2. Any particular choice of a basis set affects the way integrals are computed in Eq. (4.6). Sometimes the choice is made base on how fast integrals can be computed, even with the possibility of getting analytical results, e.g. the choice of localized gaussian basis set. There are other times in which is nature of the problem that requires a privileged choice, e.g. plane waves expansion for crystal systems. Another cumbersome aspect deals with the exchange-correlation term of Eq. (4.6) which is usually known only on a discrete spatial grid. A numerical integration should be performed leading to potential efficiency and accuracy issues. All these examples warn the reader about the importance of following some guidelines when selecting a basis set. We will discuss some common basis set used in computational chemistry in the following section.

4.1.1 Atomic Orbitals

The choice of the basis set to employ in the calculation highly depends on the problem under study. In computational chemistry and in the specific of the study

of molecular systems *atomic orbitals* (AOs) are often employed. These kind of orbitals are centered on the nuclei, and can be represented in terms of basis function with different functional forms, or can be given numerically on a grid. A suitable basis set should allow for a systematic improvement of its quality when the number of basis functions are required to achieve a reasonable accuracy in the electronic distribution. In the case of analytic expressions, the basis functions should be simple enough that the Hamiltonian matrix elements can be easily evaluated, preferably also analytically. For molecular system using linear combinations of solutions to the hydrogen atom, so called **Slater Type Orbitals** or STOs are useful. They, as the real wave function, decay as $\approx \exp(-|\mathbf{r}|)$ and have a cusps at the atomic nuclei. Their functional form is

$$\chi(\mathbf{r}) = N_{l,\alpha} Y_{lm}(\nu, \theta) |\mathbf{r}|^l \exp\{-\alpha|\mathbf{r}|\} \tag{4.9}$$

with normalization constant $N_{l,\alpha}$ and spherical harmonic $Y_{lm}(\nu, \theta)$. Due to their similarity to the orbitals of the hydrogen atom, these functions are also named as $s,p,d,f \ldots$ depending on the value of l $(0,1,2,3,\ldots)$. All functions with the same l and α are collectively referred to as a shell. The exponential form does not lead to easy evaluation of integrals, in particular the computation of four-center Coulomb integrals in Eq. (4.7) and the three-center Coulomb integrals in Eq. (4.17) that will be presented in Section 4.2. STO basis is only practical for atoms and linear molecules [105]. An alternative to STOs that is both atom-centered and that allows for tractable integrals evaluation **Gaussian Type Orbitals** or GTOs. Their functional form in polar coordinates is

$$\chi(\mathbf{r}) = N_{l,\alpha} Y_{lm}(\nu, \theta) |\mathbf{r}|^l \exp\{-\alpha|\mathbf{r}|^2\}. \tag{4.10}$$

This form allows for a massivly faster way to evaluate matrix elements of Eq. (4.5), except for the exchange-correlation part. Sometimes it is convenient to employ for the computation of the Hamiltonian matrix elements the *Cartesian* GTOs, given by

$$\phi_{ijk}(\mathbf{r}) = \chi_i(x)\chi_i(y)\chi_i(z) \tag{4.11}$$

with

$$\chi_i(x) = M_{i\alpha} x^i \exp\{-\alpha x^2\} \tag{4.12}$$

and analogous expressions for the y and z components. The main advantage of Cartesian GTOs is that the molecular integrals factorize into the three Cartesian variables [105].

As they do not really resemble real atomic orbitals, linear combination of GTOs are used to approximate STOs. A single GTO basis function has significant errors

when compared to a STO (see Figure 4.1), especially near the nucleus. These linear combinations are referred to as contractions. Their functional form is

$$\chi(\mathbf{r}) = \sum_i c_i \, \mathrm{N}_{l,\alpha_i} Y_{lm}(\nu, \theta) |\mathbf{r}|^l \exp\{-\alpha_i |\mathbf{r}|^2\} \qquad (4.13)$$

with c_i being one contraction coefficient. Due to the contractions, GTOs implementations have to evaluate many more integrals than STO codes but even then GTO evaluation is still much faster than numerical integration over positions. GTOs are not able to reproduce the cusp at the nuclei positions nor the correct exponential asymptotic decay of the wavefunction, as shown in Figure 4.1. To show an example how this contraction works, one can consider a basis set named def2-svp [106], which for carbon has 3 contracted s-shells, 2 contracted p-shells and 1 simple d-shell for a total of 14 variables coefficients for carbon. The functions of the d-shell are referred to as polarization functions, as they are not needed for the isolated atom, but add more degrees of freedom to allow the electron cloud to be polarized in a molecular environment. For a better understanding of how integ-
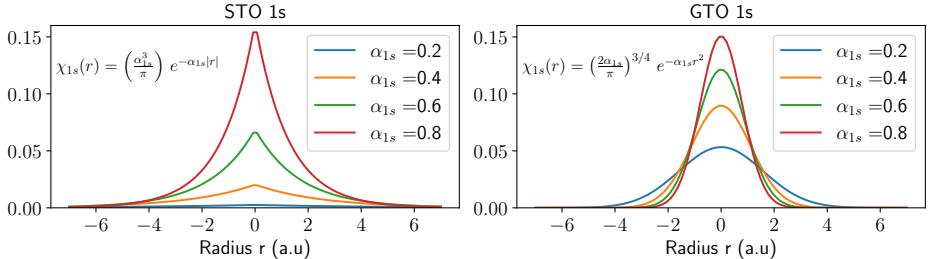
Figure 4.1: Example for the difference between STOs and GTOs. In the specific the picture report the $1s$ orbital in the two cases. The functional form is reported in the insight. It is clear how these two basis sets are different in terms of tails and peak cusps.

rals are performed and other kind of basis sets the reader can go through work of Kohanoff [110]. A disadvantage of basis set methods is that, although the basis set (chosen by physical motivation) often yields acceptable results for a small number of basis functions, precise calculations can be rather costly because they may require a large number of basis functions. Due to these limitations, in recent years purely numerical methods have been developed to solve the Kohn-Sham equation,

Figure 4.2: DFT@PBE/cc-pVnZ energies [in Hartree] for water as a function of basis set size. The basis sets employed [107, 108, 109] it is commonly abbreviated as cc-pVnZ, where $n = D, T, Q, 5, 6, \ldots$ is the *cardinal number*. The higher the cardinal number the higher the basis set. The dotted line marks the Etot(DFT/CBS) energy predicted through limit extrapolation. The red curve represents Etot(DFT) as a continous function of cardinal number n.

for instance by using numerical orbitals [111, 112, 113], finite differences and finite elements [114, 115, 116], multigrid [117, 118] or wavelet methods [119, 120].

4.2 Technical implementation of DFT and GW-BSE in VOTCA-XTP

An open-source implementation of *GW*-BSE can be the one of the VOTCA-XTP package [94, 37] that expresses the electronic states using atom-centered Gaussian-type orbitals (GTOs). VOTCA-XTP is part of the VOTCA software suite [121, 122, 123], written in C++, and freely available on GitHub. It contains an internal module for calculating the DFT ground state mostly for development purposes, and additionally provides extensible interfaces to the standard package

Orca [124]. One distinct feature of the *GW*-BSE implementation in VOTCA-XTP is that it comes in two modes. The standalone mode operates like any common quantum-chemistry software, and requires only the atom coordinates of the molecule and calculation parameters as input. In the second mode, a complex molecular morphology of, e.g., a solute-solvent mixture or a donor-acceptor blend, is first simulated by Molecular Dynamics (MD) or similar techniques, and then translated as a whole into an internal data structure. This morphology mode facilitates the evaluation of the excited-state electronic structure in a complex environment [87, 125, 123, 36, 126] in a hybrid quantum- and molecular-mechanics *GW*-BSE/MM scheme [123], and is linked to a multiscale framework for the determination of dynamical electronic properties. Additional features of this framework include, i.a., the calculation of electronic [127] and excitonic [128] intermolecular coupling elements (transfer integrals), the prediction of ultraviolet photoelectron spectra including carrier-vibration coupling [126], the simulation of optical absorption and emission spectra from coupled solute-solvent relaxation [129], and the determination of charge-carrier mobilities [122] and exciton diffusion lengths [130] via kinetic Monte Carlo.

4.2.1 DFT implementation computational cost

The overview on the basis set expansion of Sec. 4.1 already shows the main ideas for a standard DFT implementation as the one present in VOTCA-XTP. What is important stress is estimating to which extent the computational cost of DFT scales with respect to the number of atoms N of the system under investigation. If we analyze the cost for each step leading to the solution of the eigenvalue problem Eq. (4.5)

- Formation of $\underline{F}^{KS}$: $O(N^3)$

- Formation of $\underline{S}$: $O(N^3)$

- Formation of $(\mu\nu|\eta\delta)$: $O(N^4)$

- Formation of K (Hybrid only): $O(N^4)$

- Eigendecomposition: $O(N^3)$

The overall scaling for a standard implementation of DFT is $O(N^4)$. Despite this being a better scaling behaviour when compared to other methods as the wavefunctions ones briefly described in Appendix F the computational cost is still high.

If it is possible to state that ground-state properties are feasible to compute due to improvements in DFT implementations for almost all the implementations, the same cannot be said about excited state. Calculating the excited state requires special treatments that typically add extra costs when compared to DFT. In the following an overview of the implementation of GW-BSE in VOTCA-XTP is given.

4.2.2 GW-BSE with Gaussian orbitals

VOTCA-XTP uses Gaussian-type orbitals (GTOs)

$$\chi_\alpha(\mathbf{r}) = \chi_{\{l,m_\ell,\gamma,I\}}(\mathbf{r}) = N_{l\gamma} Y_{lm_l} |\mathbf{r} - \mathbf{R}_I|^l \exp\left(-\gamma |\mathbf{r} - \mathbf{R}_I|^2\right) \tag{4.14}$$

with decay constant γ centered around atom position $\mathbf{R}_I$, where Y_{lm_l} are spherical harmonics with angular momentum number l and magnetic quantum numbers m_l, and $N_{l\gamma}$ is a normalization constant, to expand the one- and two-point quantities involved in both DFT and GW-BSE steps. Specifically, the KS states in Eq. (2.51) are expressed using these basis functions in real space turning Eqs. 2.51, 3.59, and 3.69 into (generalized) eigenvalue problems in matrix form. See also the discussion about efficient solvers for the BSE in Sec. 4.3.2. VOTCA-XTP evaluates the integrals of the respective operators over the Gaussian basis functions using the modified recursive algorithms by Obara and Saika [131, 132] for contracted Gaussian basis functions with $l \leq 4$.

Of particular importance is the computation of 4-center repulsion integrals of Eq. (4.7) over the GTOs. This computation scales with N_{b}^4 (with N_{b} the number of basis functions) and occurs in the KS Hamiltonian term $\widehat{V}_{\mathrm{H}}$ and in the self-energy of GW. The set of N_{b}^2 unique product functions $\chi_\alpha(\mathbf{r})\chi_\beta(\mathbf{r})$ can be approximated by a smaller auxiliary basis containing only $N_{\mathrm{aux}} = 3N_{\mathrm{b}}$ to $5N_{\mathrm{b}}$ functions ξ_μ. This reduces the scaling from N_{b}^4 to N_{b}^3 by rewriting the 4-center integrals as a combination of 3-center and 2-center repulsion integrals [133]:

$$(\alpha\beta|\alpha'\beta') \approx \sum_{\mu,\nu} (\alpha\beta|\mu)(\mu|\nu)^{-1}(\nu|\alpha'\beta'), \tag{4.15}$$

where $(\mu|\nu)^{-1}$ is an element of the inverse of the 2-center repulsion matrix

$$(\mu|\nu) = \iint \mathrm{d}^3\mathbf{r}\, \mathrm{d}^3\mathbf{r}'\, \xi_\mu(\mathbf{r}) \frac{1}{|\mathbf{r} - \mathbf{r}'|} \xi_\nu(\mathbf{r}') \tag{4.16}$$

and $(\alpha\beta|\mu)$ is an element of the 3-center repulsion tensor

$$(\alpha\beta|\mu) = \iint d^3\mathbf{r}\, d^3\mathbf{r}'\, \chi_\alpha(\mathbf{r})\chi_\beta(\mathbf{r})\frac{1}{|\mathbf{r} - \mathbf{r}'|}\xi_\mu(\mathbf{r}'). \qquad (4.17)$$

The expression in Eq. (4.15) appears formally as the insertion of a resolution-of-identity (RI) with metric $(\nu|\mu)^{-1}$.

Within the RI approximation, the elements of the QP Hamiltonian in the basis of KS states contain $\Sigma_{mn}(E) = \langle\phi_m^{\mathrm{KS}}|\,\widehat{\Sigma}(E)\,|\phi_n^{\mathrm{KS}}\rangle$ (Eqs. 3.59 and 3.60), which are determined as

$$\Sigma_{mn}(E) = \sum_{\mu,\nu}\sum_l I_\mu^{ml} I_\nu^{nl} \frac{i}{2\pi}\int d\omega\, \frac{e^{i\omega\theta}\epsilon_{\mu\nu}^{-1}(\omega)}{E + \omega - \varepsilon_l \pm i\eta}, \qquad (4.18)$$

where the factor with $\theta \to 0^+$ ensures convergence of the integral, and the imaginary perturbations $\pm\eta$ avoid singularities on the real axis, where the plus (minus) is taken when l is occupied (unoccupied). Further,

$$I_\mu^{ml} = \sum_\nu (\mu|\nu)^{-1/2}\sum_{\alpha,\beta} c_\alpha^m c_\beta^l (\alpha\beta|\nu) = \sum_\nu (\mu|\nu)^{-1/2} M_\nu^{ml} \qquad (4.19)$$

and

$$\epsilon_{\mu\nu}(\omega) = \delta_{\mu\nu} - 2\sum_m^{\mathrm{occ}}\sum_l^{\mathrm{unocc}} I_\mu^{ml} I_\nu^{ml} \left[\frac{1}{\omega - (\varepsilon_m - \varepsilon_l) + 2i\eta} \right.$$
$$\left. - \frac{1}{\omega + (\varepsilon_m - \varepsilon_l) - 2i\eta}\right]. \qquad (4.20)$$

is called the dielectric matrix. As described in Section 3.4.1, in the G_0W_0 approach, we take the KS energies $\varepsilon_i = \varepsilon_i^{\mathrm{KS}}$, whereas in the ev$GW$ approach, we take the QP energies $\varepsilon_i = \varepsilon_i^{\mathrm{QP}}$. Currently, VOTCA-XTP pre-calculates all integrals at the start of the calculation and keeps I_μ^{ml} in memory.

4.2.3   Frequency dependence of the self-energy

The frequency integration, in Eq. (3.56), is one of the major difficulties in a GW calculation. Although it is possible to perform a numerical integration, this is likely unstable, since the integrand needs to be evaluated in regions in which it is ill-behaved. VOTCA-XTP offers different alternatives for an approximate or exact

integration, summarized in the following. We present three methods: one that is exact yet takes too much computational effort, one that is exact and is reduced in scaling, and one that is approximate yet very well-scaled. In the GW approach, it is customary to separate the self-energy $\Sigma = iGW$ into its bare exchange part $\Sigma_{\mathrm{x}} = iGv_{\mathrm{c}}$ and its correlation part $\Sigma_{\mathrm{c}} = iG\widetilde{W}$, where $\widetilde{W} = W - v_{\mathrm{c}}$. In the following, several approaches to determine the correlation part of Eq. (4.18) are presented.

Fully Analytical Approach (FAA)

The integral in Eq. (4.18) can be evaluated analytically, yielding an exact expression of the correlation part of the self-energy. Its evaluation requires the calculation of the reducible polarizability $\widehat{P}$. We can express it in terms of an eigenvalue decomposition of the RPA Hamiltonian $\widehat{H}^{\mathrm{RPA}}$

$$\widehat{P}(\omega) = [\widehat{H}^{\mathrm{RPA}} - \omega]^{-1} = \sum_S \frac{|\chi_S\rangle \langle \chi_S|}{\Omega_S - \omega}, \qquad (4.21)$$

where the RPA Hamiltonian obeys a BSE as in Eq. (3.69) with $\kappa = -1$ and $K^{\mathrm{d}} = 0$ in Eqs. 3.70 and 3.71.

We can apply analytic continuation to the complex plane and contour deformation techniques to the convolution Eq. (3.56) [134, 135]. The resulting matrix entries of the correlation part of the self-energy are given by

$$\Sigma_{\mathrm{c},mn}(E) = 2 \sum_{l,S} \frac{R_{ml}^S R_{nl}^S}{E - \varepsilon_l \pm (\Omega_S - i\eta)}, \qquad (4.22)$$

where $\pm$ denotes $+ (-)$ for l occupied (unoccupied), and the factor 2 accounts for spin degeneracy. The residues R_{mn}^S are calculated as

$$R_{mn}^S = \sum_{\mu,\nu} \sum_v^{\mathrm{occ}} \sum_c^{\mathrm{unocc}} I_\mu^{mn} I_\nu^{vc} (A_{vc}^S + B_{vc}^S). \qquad (4.23)$$

While this approach is analytically exact, it is not feasible for large systems as the diagonalization of $\widehat{H}^{\mathrm{RPA}}$ scales as N^6 in computational effort and N^4 in memory required [136].
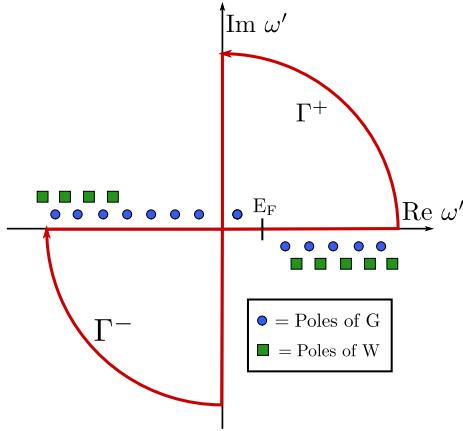
Figure 4.3: Schematic for the contour deformation technique. In read the integration paths in the complex plane to evaluate $\Sigma_c(E)$. Γ^+ and Γ^- are the integration contours. These are chosen to include only the poles of G, but not the poles of W.

Contour Deformation Approach (CDA)

To avoid the computational bottleneck due to the scaling of the FAA, an alternative approach, also involving analytic continuation of the integral over the real axis from Eq. (4.18) to the complex plane and contour deformation techniques, can be employed. It yields a different rewriting, containing an integral over the imaginary axis and residual contributions. The contour deformation and the poles of G and W is shown in Figure 4.3. Since the new integral is very peaked around the origin when $E \approx \varepsilon_\ell$ for some ℓ, we add a Gaussian function inside the integral and subtract its integral value on the outside. We then can calculate the matrix entries $\Sigma_{c,mn} = \Sigma_{c,mn}^{int}(E) + \Sigma_{c,mn}^{res}(E)$, with the integral term

$$
\Sigma_{c,mn}^{int}(E) = \frac{1}{\pi} \sum_{\mu,\nu,l} I_\mu^{ml} I_\nu^{nl} \int d\omega \, \frac{E - \varepsilon_l}{\omega^2 + (E - \varepsilon_l)^2} \times
$$
$$
\times \left[\kappa_{\mu\nu}(0) e^{-\alpha^2 \omega^2} - \kappa_{\mu\nu}(i\omega) \right],
$$

(4.24)

which can be numerically evaluated using a Gauss–Laguerre quadrature method, and the residual term

$$
\begin{aligned}
\Sigma_{\mathrm{c},mn}^{\mathrm{res}}(E) = \sum_{\mu,\nu,l} I_\mu^{ml} I_\nu^{nl} \Big[& \kappa_{\mu\nu}(E - \varepsilon_l \pm \mathrm{i}\eta)\Theta_l(E) - \\
& - \frac{1}{2}\kappa_{\mu\nu}(0)\mathrm{e}^{\alpha^2(E-\varepsilon_l)^2}\mathrm{sgn}(E-\varepsilon_l)\mathrm{erfc}(\alpha|E-\varepsilon_l|) \Big].
\end{aligned}
\tag{4.25}
$$

Here, $\underline{\kappa} = \underline{\epsilon}^{-1} - \mathbf{I}$, and α is a Gaussian scaling parameter adaptive to the numerical model to be used. [137, 138] Furthermore, for l occupied $\Theta_l(E)$ is -1 if $E < \varepsilon_l$ and $-1/2$ if $E = \varepsilon_l$; for l unoccupied it is 1 if $E > \varepsilon_l$ and $1/2$ if $E = \varepsilon_l$. By design, the FAA is in principle the most exact one, since it is parameter-free except for the dependence on the basis set. However, the same results can already be achieved with the CDA using a moderately-sized numerical integration grid for the Gauss–Laguerre quadrature, which reduces the scaling.

Plasmon-Pole Model (PPM)

Instead of a formally exact treatment of the frequency dependence, it can be approximated within a generalized plasmon-pole model (PPM) [139, 140]. The dielectric matrix can be expressed in terms of its eigenvalues $\lambda_{\mu'}$ and eigenvectors $\Phi_{\mu'}$ as

$$
\epsilon_{\mu\nu}(\omega) = \sum_{\mu'} \Phi_{\mu'}^\mu(\omega)\,\lambda_{\mu'}(\omega)\,\Phi_{\mu'}^\nu(\omega),
\tag{4.26}
$$

In the PPM, eigenvectors are assumed to be frequency-independent, so only the eigenvalues $\lambda_{\mu'}$ depend on ω. In particular, this approximate dependence reads

$$
\lambda_{\mu'}^{-1}(\omega) \approx 1 + \frac{z_{\mu'}\omega_{\mu'}}{2}\left[\frac{1}{\omega - (\omega_{\mu'} - \mathrm{i}\eta)} - \frac{1}{\omega + (\omega_{\mu'} - \mathrm{i}\eta)}\right].
\tag{4.27}
$$

Here, $z_{\mu'}$ denotes the plasmon-pole weight and $\omega_{\mu'}$ denotes the plasmon-pole frequency. These two model parameters are found by fitting the plasmon-pole model to the exact dielectric function [141], as shown in Eq. (4.20), for the frequencies $\omega = 0$ and $\omega = \mathrm{i}E_0$, with E_0 an additional model parameter, typically $E_0 = 0.5\,\mathrm{Ha}$. The correlation part of the self-energy results from the second term of Eq. (4.27), and its matrix entries are obtained as

$$
\Sigma_{\mathrm{c},mn}(E) = 2\sum_{l,\mu'} \frac{1}{4}\frac{z_{\mu'}\omega_{\mu'} I_{\mu'}^{ml} I_{\mu'}^{nl}}{E - \varepsilon_l \pm \omega_{\mu'}},
\tag{4.28}
$$

where $\pm$ denotes $+ (-)$ for l occupied (unoccupied), and the factor 2 accounts for spin.
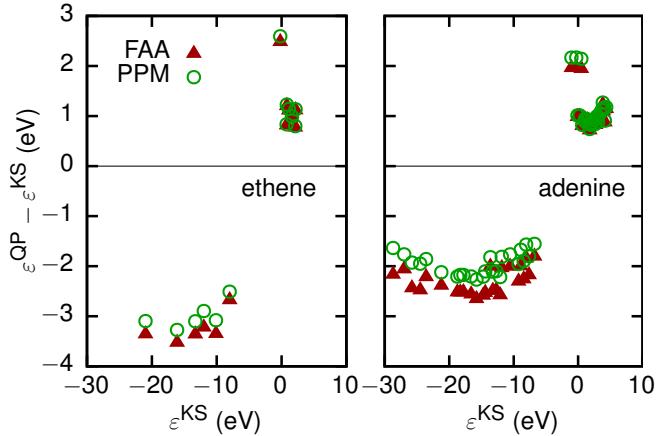
Figure 4.4: Comparison of the QP corrections $\varepsilon^{QP} - \varepsilon^{KS}$ vs the KS energies for ethene (left) and adenine (right), obtained with the frequency integration of Eq. (3.56) using the FAA (triangles) and the PPM (circles), respectively.

Comparison of FAA and PPM for QP excitations of ethene and adenine

Figure 4.4 illustrates the influence of the choice of technique for the frequency integration on the obtained QP corrections to the KS state energies for two small molecules: ethene and adenine. In both cases, the calculations have been performed using the aug-cc-pVTZ basis [142], an optimized RI basis [143] and the PBE0 [53] functional for the DFT ground-state calculation, with the whole range of states (121 for ethene, 399 of adenine) included in the RPA and QP steps. The corrections for all occupied levels and the same number of unoccupied levels is shown. Clearly, the QP corrections obtained with the PPM are slightly more positive (about $0.3\,\mathrm{eV}$) than with the exact method for the occupied and lowest unoccupied levels in both cases, whereas there is hardly any deviation for unoccupied levels at higher energy. It should be noted that, due to the nature of the

deviations, energy differences near the gap are very similar for both methods. In particular, the QP gap between HOMO and LUMO levels as predicted by the PPM and the exact method differs by only 0.05 eV for the two molecules considered here. It is also visible that the corrections, e.g., to the DFT LUMO level in ethene, are larger than for higher unoccupied states, leading to level switching in GW (LUMO+3). This behavior is the same for FAA and PPM. However, this close agreement is paralleled by a significant difference in computational cost: [1] while the use of Eq. (4.22) increases the computation time from 4 min to 12 min compared to the PPM in ethene, we find that for adenine the same causes an increase from 174 min to 2566 min.

Considering the above, we find that the PPM appears to be a suitable "low-cost" approximation to the exact frequency dependence of the self-energy when the main interest is in near-gap excitations such as HOMO and LUMO energies or HOMO-LUMO transitions in larger molecular systems. More significant deviations can be expected when mixed transitions involving other orbitals are investigated.

4.3 Software Development Strategies

VOTCA-XTP is written in C++ and mostly adheres to the C++14 standard [144]. It can be obtained on `github.com/votca/xtp`. We use the Git feature branch workflow combined with code review and continuous integration, which executes code formatting, static analyzers, debug and release builds and the test-suite. We use CMake as the build system, which also resolves the inclusion of external dependencies. The linear algebra is handled by Eigen [145], which can be accelerated by internally calling the Intel Math Kernel Library [146]. For serialization, the HDF5 format is used via the canonical libraries [147]. Exchange-correlation functionals are provided by the LIBXC package [148]. Various boost packages [149] are used for file system operations, file parsing and string operations. Doxygen is used to document the APIs of VOTCA-XTP and automatically deploys to `http://doc.votca.org`.

VOTCA-XTP is designed as a library, which is linked into very thin executables, which can execute a variety of calculators by adding keywords on the command line. Virtual interfaces and factory patterns make the addition of new calculators simple. The same architecture is used for external DFT and MD codes, making VOTCA-XTP easily extensible.

---

[1]Measured on a single thread of an Intel(R) Xeon(R) CPU E7-4830 v4 @ 2.00GHz

Molecule	N_b	N_aux	Time (s)	
			CPU	GPU
Benzene	174	774	21	9
Naphthalene	274	1228	68	28
Phenanthrene	374	1682	216	44
Coronene	600	2724	1421	266

Table 4.1: Comparison of calculation times for the convolution of the 3-center repulsion tensor with the molecular orbital coefficients on CPU (single thread of Intel(R) Xeon(R) Gold 5120) and GPU (Nvidia Titan Xp), respectively, for four polycyclic aromatic hydrocarbons with different numbers of functions in the basis (N_b) and auxiliary basis (N_aux).

4.3.1 GPU acceleration

The computation of the $M_\nu^{ml} = \sum_{\alpha,\beta} c_\alpha^m c_\beta^l (\alpha\beta|\nu)$ term in Eq. (4.19) requires the convolution of the 3-center repulsion tensor from Eq. (4.17) with the molecular orbital coefficients. These convolutions involve a large number of matrix-matrix multiplications that take a significant fraction of the computation time. In VOTCA-XTP, we have accelerated these operations by offloading them to a GPU, using the highly optimized CuBLAS library [150]. Moreover, due to the typically limited memory of the GPU and the latency required to copy the matrices back and forth from the device, there are limitations to the theoretical speedup for a given system size.

Tab. 4.1 illustrates the time trend for the 3-center integrals calculation on GPU (Nvidia Titan Xp) and single CPU thread (Intel(R) Xeon(R) Gold 5120) as the molecular size increases. For systems smaller than benzene the acceleration achieved by the GPU does not compensate for much of the communication latency, and consequently the reduction of calculation time is limited, albeit on an already overall low level. For benzene and naphthalene, we observe a GPU speedup of about 60 % compared to the respective single CPU thread values, while for the larger systems (phenanthrene and coronene) it increases to 80 %. For even larger systems, the speedup increases until it eventually plateaus due to limits in the GPU memory and hardware bandwidth. Even though the observed quantitative speedups depend on the given GPU/CPU hardware combination, a qualitatively similar behavior is expected in a general setting. Note that overall, best perform-

ance is obtained by combining all CPU threads and the GPU in a mixed hybrid OpenMP/Cuda mode, which is also implemented in VOTCA-XTP.

4.3.2 Iterative matrix-free eigensolvers for the BSE

The size of the BSE matrix in Eq. (3.69) increases rapidly with the number of occupied (N_{occ}) and unoccupied (N_{unocc}) states included in the product basis, with its dimension being $2N_{\mathrm{BSE}} \times 2N_{\mathrm{BSE}}$, where $N_{\mathrm{BSE}} = N_{\mathrm{occ}} \times N_{\mathrm{unocc}}$. Even if the TDA (Eq. (3.77)) is used, the dimension of $\underline{\mathbf{H}}^{\mathrm{res}}$ is still $N_{\mathrm{BSE}} \times N_{\mathrm{BSE}}$. This leads to a computational as well as a memory bottleneck for GW-BSE calculations. The Davidson algorithms [151, 152] form a family of subspace-iterative diagonalization schemes that are extensively used in large-scale quantum chemistry applications [153, 154]. These methods allow rapid computation of a selected numbers of eigenvalues of large matrices, while reducing memory requirements when compared to other methods.

For an eigenproblem $\underline{\mathbf{H}}\mathbf{X} = \Omega\mathbf{X}$, the Davidson method starts from a set of N guess eigenvectors $\underline{\mathbf{V}} = \{\mathbf{v}_1, \mathbf{v}_2, \ldots, \mathbf{v}_N\}$, where each $\mathbf{v}_i$ is a column vector. These vectors are used to obtain a small eigenvalue problem:

$$(\underline{\mathbf{V}}^T \underline{\mathbf{H}} \, \underline{\mathbf{V}})\mathbf{x} = \omega\mathbf{x}. \tag{4.29}$$

The Ritz eigenpairs of this problem ($\omega_i, \mathbf{y}_i = \underline{\mathbf{V}}\mathbf{x}_i$) are approximate solutions of the large eigenvalue problem. The residues of the Ritz eigenpairs, $\mathbf{r}_i = \underline{\mathbf{H}}\mathbf{y}_i - \omega_i\mathbf{y}_i$, are then used to construct additional basis vectors, $\mathbf{t}_i$, that are appended to the projector: $\underline{\mathbf{V}} = \{\mathbf{v}_1, \mathbf{v}_2, \ldots, \mathbf{v}_N, \mathbf{t}_1, \mathbf{t}_2, \ldots \mathbf{t}_n\}$. This new projector is then orthogonalized, using either a Gram-Schmidt or a QR approach, and used to obtain a better approximation of the large eigenpairs. This is repeated until the residues of all Ritz eigenpairs respect the condition $||\mathbf{r}_i|| \leq \epsilon$, where ϵ is a fixed threshold parameter. When the size of the projector $\underline{\mathbf{V}}$ becomes too large, it is reset to N Ritz eigenvectors.

In addition to considerably accelerating the diagonalization of the BSE matrix, these methods do not require the matrix to be stored in memory and only the action of this matrix on vectors is required. This matrix-free approach naturally decreases the memory requirement of the calculation. Different methods based on the general idea behind the Davidson algorithm have been developed. These methods differ in the way the correction vectors $\mathbf{t}_i$ are calculated and on which part of the spectrum is targeted. We briefly present the solutions we have implemented in VOTCA-XTP to solve the BSE equation using the TDA or the full matrix.

Molecule	N_{BSE}	Time (s)			Memory (GB)		
		DSYVEX	DPR	DPR-MF	DSYVEX	DPR	DPR-MF
Uracil	7743	83.44	1.33	32.63	1.08	1.20	0.71
Cytosine	8149	98.68	1.52	33.16	1.21	1.31	0.79
Thymine	10593	217.85	2.03	61.99	1.88	2.02	1.16
Adenine	11725	293.49	2.39	75.48	2.18	2.38	1.28

Table 4.2: Performance benchmark (computation time and memory requirements) of different diagonalization schemes implemented in VOTCA-XTP during the calculation of the 25 lowest singlet excitations of the $N_{\mathrm{BSE}} \times N_{\mathrm{BSE}}$ BSE matrices using the TDA on a single thread.

If the TDA is used, the Davidson method allows rapid computation of the lowest N eigenvalues and eigenvectors of the Hermitian matrix $\underline{\mathbf{H}}^{\mathrm{res}}$. The initial projector $\underline{\mathbf{V}}$ is then set to select the N transitions with the lowest energy difference. We have implemented different methods to compute the correction vectors. Following Davidson's original idea [151], the correction vectors can be obtained via

$$\mathbf{t}_i = -(\underline{\mathbf{D}}^{\mathrm{res}} - \omega_i \underline{\mathbf{I}})^{-1} \mathbf{r}_i, \qquad (4.30)$$

where $\underline{\mathbf{D}}^{\mathrm{res}}$ is the diagonal of the matrix $\underline{\mathbf{H}}^{\mathrm{res}}$. Note that $(\underline{\mathbf{D}}^{\mathrm{res}} - \omega_i \underline{\mathbf{I}})$ is a diagonal matrix and that therefore it is not necessary to explicitly diagonalize it. It is important to mention that the method outlined above requires only one evaluation of $\underline{\mathbf{H}}^{\mathrm{res}}\underline{\mathbf{V}}$ per iteration. This product can be calculated without having to form the complete $\underline{\mathbf{H}}^{\mathrm{res}}$ matrix, decreasing the memory requirement at the expense of a slight increase in computational time.

If the TDA is not used, the lowest transitions correspond to the interior eigenvalues of the non-Hermitian matrix in Eq. (3.69), as all its eigenvalues come in pairs $(-\Omega_S, \Omega_S)$. The procedure outlined above is optimal for exterior eigenvalues but often leads to spurious eigenvalues when applied to the calculation of interior eigenvalues. Following Morgan [155], the original Rayleigh–Ritz approach is modified to map the interior eigenvalues to the exterior of the spectrum of an inverted matrix. To this end, the small eigenvalue problem Eq. (4.29) is replaced by the generalized eigenvalue problem

$$(\underline{\mathbf{V}}^T \underline{\mathbf{H}} \underline{\mathbf{V}})\mathbf{x} = \omega(\underline{\mathbf{V}}^T \underline{\mathbf{H}}^2 \underline{\mathbf{V}})\mathbf{x}. \qquad (4.31)$$

Solving Eq. (4.31) gives the harmonic Ritz eigenpairs $(\omega_i, \mathbf{y}_i = \underline{\mathbf{V}}\mathbf{x}_i)$ with $\omega_i = \mathbf{x}_i^T \underline{\mathbf{V}}^T \underline{\mathbf{H}} \underline{\mathbf{V}} \mathbf{x}_i$. As before, the residues of these eigenpairs are used to construct

correction vectors using Eq. (4.30), which are then appended to the projector matrix $\underline{\mathbf{V}}$. It is worth noting that the generalized eigenvalue problem Eq. (4.31) requires two matrix-vector products per iteration to evaluate $\underline{\mathbf{H}}\,\underline{\mathbf{V}}$ and $\underline{\mathbf{H}}^2\underline{\mathbf{V}}$, which significantly increases the computational cost of the method.

To illustrate the performance of our implementation of the Davidson algorithm, we show in Tab. 4.2 the computation time and the memory requirement of the BSE calculations of 4 nucleobases. Here, the Davidson method (Diagonal-Preconditioned-Residue, DPR) using Eq. (4.30) to obtain the correction vectors, as well as its matrix-free implementation (DPR-MF), are compared to the highly-optimized Lapack routine DSYVEX, which also allows the calculation of the lowest part of the spectrum. As seen in Tab. 4.2, the DPR method is up to 2 orders of magnitude faster than DSYVEX, while having similar memory requirements. The matrix-free approach is faster than DSYVEX, but significantly reduces the memory requirement, hence enabling BSE calculations on much larger systems. The speed-up offered by the Davidson method over DSYVEX is most apparent when only a small number of eigenvalues are required. For example in the case of the adenine molecule, the calculations of the lowest 1000 eigenvalues of the BSE matrix required approximately the same amount of time using the DPR or DSYVEX methods while the DPR-MF was twice as slow. Note that the full diagonalization of the BSE matrix is not supported by VOTCA-XTP due to the high computational cost and memory load that it would require. As a consequence VOTCA-XTP is not suitable for computing the absorption spectrum of large systems far from the band-edge.

4.3.3 Conclusions

All in all, the design of VOTCA-XTP aims at striking a balance between performance, accuracy and implementation complexity. For instance, the RI approximation simplifies the implementation and speeds up the calculations. In particular, the N_b^3 scaling of the memory requirements of the RPA makes keeping the three-center integrals in memory feasible for moderate-sized molecules described by up to approximately 1500 basis functions, thus allowing GW-BSE calculations even on desktop hardware. As VOTCA-XTP is built with shared memory parallelization, large memory hardware is required for the treatment of larger systems. This could, in principle, be overcome either by calculating the necessary terms on the fly or by efficiently storing them on disk. Both would come with a noticeable drop in performance, and are currently not actively pursued. Instead, we consider as an alternative the inclusion of a framework for Density Functional Perturbation

Theory [47] (DFPT) into VOTCA-XTP. It has been shown before [156] that the explicit summation over unoccupied states in the RPA can be omitted, if the whole GW is rephrased in terms of a Sternheimer equation. In the same spirit, DFPT can also yield beneficial improvements in terms of speed and memory consumption for the BSE [157].

Besides the above limitations, the GW-BSE implementation in VOTCA-XTP currently supports only closed-shell calculations and thus systems with explicit spin, e.g., for the optical spectra of cations or anions cannot be treated. This restriction is planned to be lifted in future versions. Furthermore, VOTCA-XTP can only determine excited-state response properties such as atomic forces, excited-state vibrational modes, or polarization tensors via numerical derivatives due to the lack of analytic gradient expressions [158]. It is also known that while the GTO-based implementation is adequate for the representation of bound electronic states, it is less effective in describing delocalized electronic states close to or above the vacuum level. As a consequence, Rydberg excitations are not as reliably accounted for. Such states typically require the addition of very diffuse atomic basis functions, causing significant linear dependencies in the molecular basis set which require careful treatment [159].

In the GW-BSE/MM framework, classical polarization effects of the environment are currently modeled via atomic induced dipoles as described in Section 3.6. This model cannot be expected to yield an accurate description of the response, if the environment is strongly polarizable to the extent that charge flow effects are present. Furthermore, our GW-BSE/MM framework relies on the assumption that the environment response is single-reference in character, allowing for an unambiguous identification of the excited states in the self-consistent procedure required to evaluate Eq. (3.88). This can be achieved by analyzing excited-state characteristics, such as oscillator strengths for optical transitions or the amount of transferred charge between two molecules, or directly the density matrix of the excitation. Any of these state-tracking methods are not straightforwardly applicable, e.g., at or close to intersections where at least two states mix strongly. The inclusion of automatic solutions to this problem [160, 161] is left for future developments.

Results

In this part an overview of some applications and results using the theory and the computational methods described in the previous part is presented. The majority of the results presented has been published and a reference to the original paper is set on the beginning of the chapter. To make a coherent story, content of these papers have been condensed in three chapters. For those results without any reference the reader must be aware that they are not yet published and thus are still work in progress results. The first (Section 5) and the second (Section 6) chapters show how ab-initio many-particles theories, with the inclusion of a classical polarizable embedding and their computational implementations help bridging the gap with experimental spectroscopy and the underlying physics of these experiments. Spectroscopy experiments are used to measure quantities like ionization potential, electron affinity and optical gap. These are useful ingredients to get another meaningful quantity that cannot be measured directly, like the exciton binding energies. The computational methods that we developed helped deconvolving the uncertainty behind the interpretation of experimental spectra, becoming a useful tool towards a more controlled engineering of opto-electronic devices. The same theoretical and computational methods are not only useful in understanding single particle excitations but also two-particles excitations. In Section 7, the dynamic between localized and charge-transfer excitations are stud-

ied for a prototypical solar cell material in which there is a low-donor content, an ideal experimental setup where to prove the methods described above. Other than the computation of localized and charge-transfer excitons in a polarizable environment, non-adiabatic coupling has been studied comparing different diabatization methodologies providing qualitative and quantitive predictions. A minimal kinetic model of the conversion from localized excitation and charge-transfer state population stability based on Marcus rates is presented.

Chapter 5

Quantitative Predictions of Photoelectron Spectra in Amorphous Molecular Solids from Multiscale Quasiparticle Embedding

In this chapter we present a first-principles-based multiscale simulation framework for quantitative predictions of the high-energy part of the ultraviolet photoelectron spectroscopy (UPS) spectra of amorphous molecular solids. The approach combines a deposition simulation, many-body Green's function theory, polarizable film embedding, and multimode electron-vibrational coupling and provides a molecular-level view on the interactions and processes giving rise to spectral features. This insight helps bridging the current gap between experimental UPS and theoretical models as accurate analyses are hampered by the energetic disorder,

surface sensitivity of the measurement, and the complexity of excitation processes. In particular, this is relevant for the unambiguous determination the highest occupied molecular orbital energy (HOMO) of organic semiconductors, a key quantity for tailoring and engineering new optoelectronic devices. We demonstrate the capabilities of the simulation approach studying the spectrum of two isomers of 2-methyl-9,10-bis(naphthalen-2-yl)anthracene as archetypical materials showing a clearly separated HOMO peak in experiment. The agreement with experiment is excellent, suggesting that our approach provides a route for determining the HOMO energy with an accuracy better than 0.1 eV.

5.1 Introduction

Amorphous organic semiconductors are intensively applied in opto-electronic devices such as organic light-emitting diodes (OLEDs) [162, 163, 164, 165], photovoltaic cells [166, 167, 168] and photodetectors [169, 170, 171]. Device properties can be tuned by varying the chemical building blocks or the material processing conditions, and by combining different molecular materials in complex blends or layer stacks. A key parameter determining the functioning of a material in a device is the ionization energy, often termed the highest occupied molecular orbital (HOMO) energy, $\varepsilon_{\text{HOMO}}$. Relative changes of $\varepsilon_{\text{HOMO}}$ on the order of 0.1 eV can already significantly alter the charge transport through host-guest materials or across internal interfaces between layers. However, even when using the perhaps most direct method for measuring $\varepsilon_{\text{HOMO}}$, Ultraviolet Photoelectron Spectroscopy (UPS), this level of accuracy has so far not been accomplished.

Excitation processes in organic semiconductors are complex because their localized nature gives rise to strong structural reorganization (polaron formation) and electron-vibration coupling, which leads to shifts, broadening and additional features in the UPS spectrum [172, 173, 174, 175]. Combined with the energetic disorder originating from the amorphous structure and the surface-sensitivity of the measurement, this obstructs the unambiguous analysis of the spectra. As a result, the method used for deducing $\varepsilon_{\text{HOMO}}$ from the spectra (from the first peak energy or from an effective onset energy?) is a subject of debate [176, 177, 178]. This uncertainty hampers the use of UPS studies for the rational design of new devices, and the combined use of high-resolution UPS, inverse UPS and photoluminescence spectra for obtaining accurate exciton binding energies [179]. Qualitative understanding of the spectra is often sought via gas-phase single-molecule calculations based on density functional theory (DFT). However, the obtained energy levels

need to be artificially shifted and broadened due to the well-known underestimation of the single-particle energy gap by DFT [180, 181] and due to the effects of intermolecular interactions [182]. Those calculations lack an explicit link to the molecular morphology, cannot resolve surface and bulk contributions to the density of states (DOS), and do not account for the spectral consequences of the molecular ionization process resulting from the excitation of molecular vibrations. This lack of predictive power combined with the ambiguity in extracting the DOS from the experimental data is a big obstacle for the development of layer stacks for organic photovoltaics or next-generation OLEDs, for which the functioning and ultimate performance is already sensitive to energy level variations of only $100\,\mathrm{meV}$.

In this work, we present a first-principles-based multiscale simulation approach that bridges the current gap between experimental UPS and theoretical models by providing a quantitative prediction of the high-energy part of the UPS spectrum from which the ionization potential is derived. It consists of an accurate evaluation of (i) quasiparticle energy levels within the GW approximation and (ii) thin-film embedding effects, using a hybrid quantum-mechanics/molecular-mechanics (QM/MM) approach that takes the molecular polarizabilities and the long-range interactions due to partially ordered static multipole moments into account, (iii) the inclusion of surface sensitivity via the electron attenuation length (EAL), Λ, and (iv) a full-quantum treatment of electron-vibration coupling. We focus here on only one type of initial state (frontier orbital), and simulate the UPS spectrum for perpendicular emission as a weighted sum of individual molecular environment-dependent densities of states according to

$$S_{\mathrm{UPS}}(E) = \frac{1}{N_{\mathrm{m}}} \sum_{j=1}^{N_{\mathrm{m}}} S_{\mathrm{el\text{-}vib}}(E; \varepsilon_j) \exp\left(-\frac{z_0(x,y) - z_j}{\Lambda}\right), \qquad (5.1)$$

with ε_j the frontier orbital energy level of molecule j, z_j the distance of the molecule's center-of-mass (COM) to the corrugated surface at $z_0(x,y)$ [183], and $S_{\mathrm{el\text{-}vib}}(E; \varepsilon_j)$ the energy-dependent spectral shape due to electron-vibration coupling. N_{m} is the total number of molecules included in the summation, which is equal to the number of molecules for which from a vapour deposition simulation the atomistic morphology is obtained (see Sec. 5.2). In view of the large optical absorption depth, we neglect optical matrix element effects.

As prototypical systems, we study the UPS spectrum for thin films of the α and β isomers of 2-methyl-9,10-bis(naphthalen-2-yl)anthracene (MADN), whose chemical structures are shown as insets in Fig. 5.1. MADN is a morphologically stable amorphous wide-gap semiconductor [184] that is used extensively as

an ambipolar host material in OLEDs containing deep blue fluorescent emitter molecules [185, 186, 187, 188, 189, 190]. The methyl substituent disrupts the symmetry and stabilizes the material against crystallization. The type of coupling of the anthracene core and the naphtyl substituents (α or β) affects the planarity of the molecules, and thereby the frontier orbital energies and their distribution in a thin film. We regard MADN as particularly suitable for this study because it exhibits a HOMO peak that originates from a single non-degenerate state, located predominantly on the anthracene core. Experimental high resolution (low instrumental broadening) UPS measurements (see Fig. 5.1) were done in a multi-chamber VG EscaLab II system with a base pressure of the deposition and the analyzer chamber in the upper 10^{-6} and the lower 10^{-8} Pa range respectively. α- and β-MADN (Lumtec) were deposited by high-vacuum ($8 \cdot 10^{-6}$ Pa) thermal evaporation onto in situ sputter-cleaned Au-coated Si-substrates at a rate of about 1 nm/min. The deposited films were transferred under ultra high vacuum (UHV) between the deposition and the analyzer chamber. The UPS spectra were recorded at a -6 V bias voltage using HeI radiation, generated in a differentially-pumped discharge lamp.

Figure 5.1 show that the peak full width at half maximum (~ 0.4 eV) is significantly smaller than for many other often-used hole transporting and emitting materials in OLEDs. It is furthermore advantageous that the HOMO state is well-separated from the deeper levels. The selection of the two isomers enables us to study the effects of morphology differences and the related effects on energy level shifts due to the small molecular dipole moments.
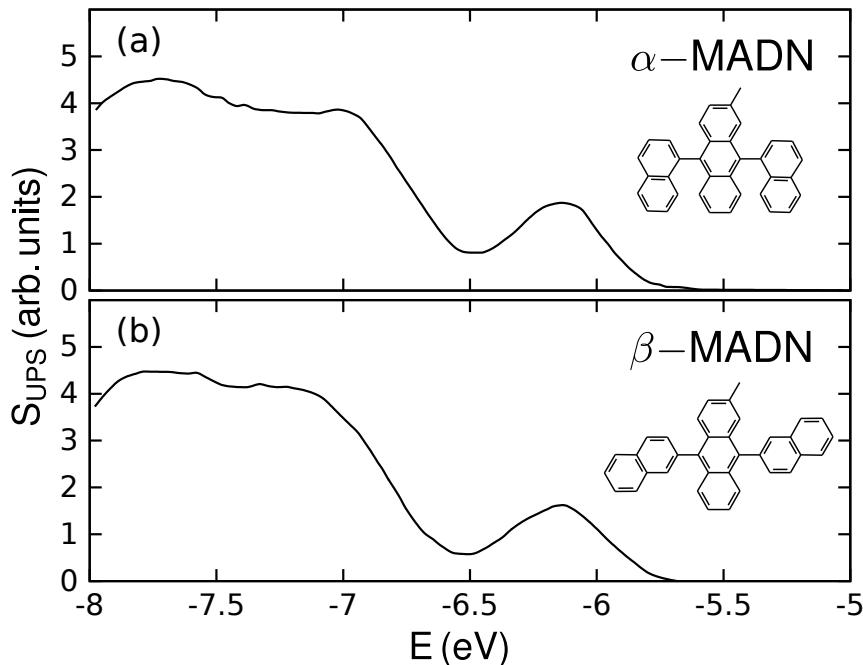
Figure 5.1: Experimental UPS spectra obtained using He-I radiation (21.2 eV) for (a) α-MADN and (b) β-MADN, respectively. For both systems, the peak associated to the HOMO, at about -6.1 eV, is clearly separated from the deeper levels. Experiments from C.H.L. Weijtens in collaboration with Prof. R. Coehoorn and his research team [191].

5.2 Atomistic thin-film morphologies

As a first step, realistic thin-film morphologies are obtained using the Metropolis Monte Carlo-based simulated annealing protocol DEPOSIT [192]. It mimics the vapor deposition (PVD) process and provides molecular morphologies that exhibit commonly observed PVD characteristic features [193, 194]. Each molecule was deposited using 32 simulated annealing cycles with 120000 Monte-Carlo steps each, with annealing temperatures decreasing from 4000 K to 300 K. Periodic boundary conditions were applied in the directions perpendicular to the growth direction with a side length equal to 10 nm. The deposition substrate is represented by a fixed dense layer of MADN. The energy at each simulation step was computed using customized force-fields generated using the Parametrizer module of the DE-POSIT code. These force-fields comprise Coulomb electrostatics based on partial charges obtained from an electrostatic potential fit [195], Lennard-Jones potentials to account for the van-der-Waals interaction and the Pauli repulsion, and compound-specific dihedral force-fields with quantum chemistry accuracy generated by the Dihedral Parametrizer of the DEPOSIT code. The final deposited morphologies contain 1000 molecules and are about 10 nm thick. For the following analysis, we remove the bottom 2 nm of the film to avoid spurious effects from the artificial substrate.

5.3 Quasiparticle Energies in the GW Approximation

The internal contributions to the HOMO energy of all individual molecules are calculated including quasiparticle corrections within the *GW* approximation of many-body Green's Functions theory [196, 197]. At this level, the calculations already include the effects of molecular deformations, obtained from the morphology simulations, but not yet the effects of embedding in the polarizable thin-film environment. These will be discussed in Section 5.4. The properties of a closed shell system of N electrons with spin singlet ground state can be calculated using DFT by solving the *Kohn–Sham* (KS) equation of Eq. (2.51) As described in Section 3.4.1, particle-like excitations, known as quasiparticles (QP), in which one electron is added to or removed from the N-electron ground state, are described by the one-body Green's function, in particular in the form of the *GW* approximation. As already described, the main ingredient of the *GW* approximation is the self-energy operator. As the self-energy is energy-dependent, and thus depends on

ε_i^{QP}, the solution to Eq. (3.59) or Eq. (3.60) need to be found self-consistently. Both the correction term $\Delta\epsilon_i^{GW}$ and the non-local, energy-dependent microscopic dielectric function calculated within the RPA depend on ε_i^{QP} [198, 199]. Within the GW method employed in this work, we iteratively solve the Hamiltonian by updating as well the energy-dependent non-local dielectric function, until self-consistency of the eigenvalues (ev) is obtained. In literature this is often referred to as evGW [200, 37, 136].

We have performed the KS-DFT and the GW steps using the ORCA [201] and VOTCA-XTP [200, 37] software packages, respectively.

All results reported in this chapter, are obtained using the PBE functional and the cc-pVTZ basis [202] with its optimized auxiliary basis set [203] for resolution-of-identity techniques.

The KS-DFT eigenvalues, and thus the quasiparticle energies, may depend strongly on the exchange-correlation functional used. However, for both MADN isomers, the final GW results show a negligible starting-point dependence. A comparison using the PBE functional [204] and the hybrid PBEh [205, 206] is given in the following.

In Tab. 5.1 we show a comparison of the calculated gas-phase energy levels for α-MADN and β-MADN, obtained using the PBE and PBEh exchange-correlation functionals with the cc-pVTZ basis (see the discussion and references above). In each case, the table gives the Kohn-Sham (KS) energy ε^{KS}, the perturbatively calculated GW energy $\varepsilon^{QP,pert}$, and the exact GW energy, ε^{QP}.

Note the difference in the results obtained for ε^{KS}, e.g., in the HOMO energy of α-MADN: -4.79 eV (PBE) and -5.55 eV (PBEh). This is a consequence of the spurious self-interaction in the functionals and the inadequacy of DFT to describe electronically excited states. Figure 5.2 shows the errors made by using the two different functionals to calculate the KS energies, as judged by comparing these energies with the perturbatively calculated or exact GW energies. The correction to the KS-levels is not constant, and is quite different for the occupied and unoccupied states. We can see that for the PBE functional the quasi-particle correction is more pronounced than for hybrid PBEh functional, which already contains part of the exchange contributions to the self-energy operator. In spite of the different energy-dependent corrections, the final quasi-particle energies (see Table 5.1) do not show a significant dependence on the exchange-correlation functional used. The exact GW HOMO energies, as obtained from both functionals, differ for α-MADN (β-MADN) only by about 0.01 eV (0.02 eV).

The numerical accuracy of the calculations depends on the convergence limit used, the number of levels included and the method for carrying out the frequency in-

Table 5.1: Comparison of the calculated gas-phase energy levels (in eV) for α-MADN and β-MADN, obtained using the PBE and PBEh exchange-correlation functionals with the cc-pVTZ basis set, within KS-DFT ($\varepsilon^{\mathrm{KS}}$), including perturbative quasiparticle corrections ($\varepsilon^{\mathrm{QP,pert}}$), and after diagonalization of the quasiparticle Hamiltonian ($\varepsilon^{\mathrm{QP}}$), respectively. All energies are given in units eV.

	α-MADN				**β-MADN**		
	$\varepsilon^{\mathrm{KS}}$	$\varepsilon^{\mathrm{QP,pert}}$	$\varepsilon^{\mathrm{QP}}$		$\varepsilon^{\mathrm{KS}}$	$\varepsilon^{\mathrm{QP,pert}}$	$\varepsilon^{\mathrm{QP}}$
		PBE				PBE	
HOMO-2	-5.412	-7.538	-7.597	HOMO-2	-5.459	-7.616	-7.690
HOMO-1	-5.396	-7.524	-7.595	HOMO-1	-5.456	-7.614	-7.682
HOMO	**-4.786**	**-6.610**	**-6.689**	**HOMO**	**-4.762**	**-6.574**	**-6.650**
LUMO	-2.468	-0.245	-0.348	LUMO	-2.457	-0.231	-0.335
LUMO+1	-2.011	0.536	0.424	LUMO+1	-2.030	0.514	0.384
LUMO+2	-2.000	0.550	0.435	LUMO+2	-2.027	0.520	0.414
		PBEh				PBEh	
HOMO-2	-6.270	-7.570	-7.611	HOMO-2	-6.324	-7.652	-7.701
HOMO-1	-6.256	-7.559	-7.606	HOMO-1	-6.321	-7.652	-7.693
HOMO	**-5.548**	**-6.645**	**-6.702**	**HOMO**	**-5.521**	**-6.615**	**-6.670**
LUMO	-1.755	-0.218	-0.313	LUMO	-1.744	-0.204	-0.297
LUMO+1	-1.200	0.544	0.444	LUMO+1	-1.230	0.514	0.411
LUMO+2	-1.189	0.561	0.457	LUMO+2	-1.219	0.533	0.438

tegration in Eq. (3.56). The convergence limit for the self-consistent GW-cycles in the evGW scheme was set to 10^{-5} Hartree (0.27 meV). The number of occupied and unoccupied levels taken into account for the QP calculations is 327, while for the calculation of the RPA dielectric function the full spectrum of the KS states (1385 levels) is used. The frequency integration in Eq. (3.56) can be performed in VOTCA-XTP using the Fully Analytical Approach [207] (FAA) or a generalized plasmon-pole model (PPM) [199]. The FAA expresses the frequency dependence of the self-energy in the eigenbasis of the full RPA Hamiltonian, which is in turn evaluated in the basis of KS product states. This approach is in principle exact. However, disadvantageously, the N_{b}^6 scaling of the FAA [207] makes its application to molecules of the size of MADN computationally extremely demanding. As
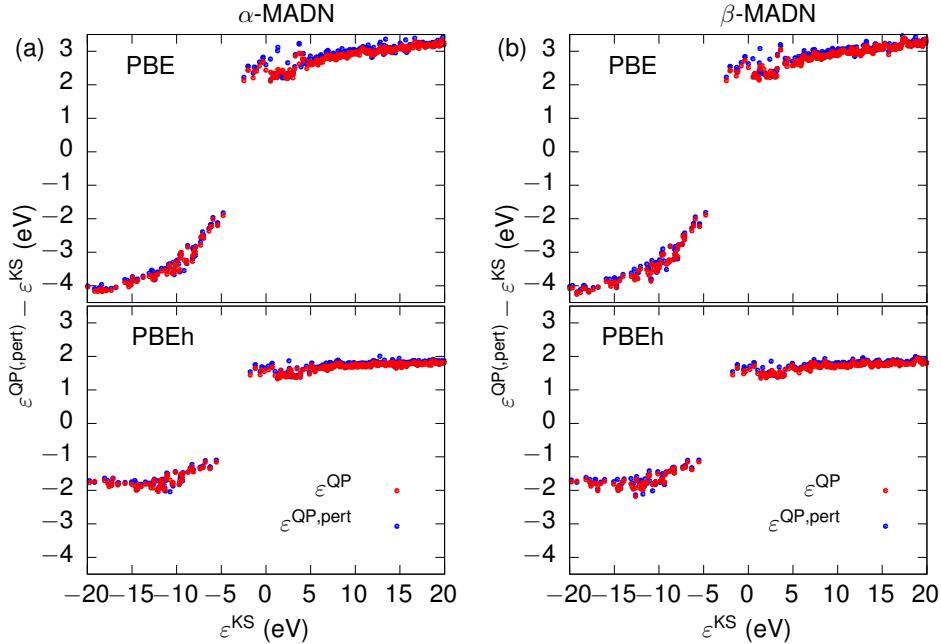
Figure 5.2: Calculated quasiparticle corrections as a function of the Kohn-Sham energy for (a) α-MADN and (b) β-MADN, obtained using the PBE and PBEh DFT functionals. The blue and red symbols give the perturbatively calculated quasiparticle corrections ($\varepsilon^{\mathrm{QP,pert}}$), and the corrections obtained after diagonalization of the quasiparticle Hamiltonian ($\varepsilon^{\mathrm{QP}}$), respectively.

an alternative, the PPM allows for a fast evaluation of the self-energy. For inorganic semiconductors, the quasiparticle energy obtained using the PPM can show deviations of several tenths of eV from the exact result [207, 208]. However, for geometry-optimized α-MADN and β-MADN, we find a difference of only 0.02 eV between the HOMO energies obtained using the FAA and PPM approaches. All things considered, the results reported in this work have been obtained using the PPM.

5.4 QM/MM quasiparticle embedding schemes

Intermolecular interactions in the thin-film environment give rise to additional non-uniform modifications of the quasiparticle energies. We determine the respective corrections to the intramolecular GW energies in a coupled quantum-classical (QM/MM) procedure ("quasiparticle embedding") [209, 210, 211, 212, 213, 200]. Within the MM model, we employ a classical representation of the molecular electrostatic potential based on static and induced multipole moments, located on each of the atoms in the system. A region treated on QM (here GW) level is coupled to suitably defined MM regions with a special scheme, which properly includes the long-range character of electrostatic interactions among the excited and neutral MADN molecules. The math employed is the same describe in Section 3.6. Static atomic partial charges from a CHELPG fit to the neutral molecule's electrostatic potential [214] are used for the classical representation of molecules, and atomic polarizabilities, optimized to reproduce the polarizable volume of the molecule obtained from DFT, account for polarization effects via the induction of atomic dipoles (Thole model [215]). Various schemes for coupling a QM-treated inner region to a MM-treated outer region have been described in the literature. Within an *additive scheme* [216] (here termed GW/aMM and depicted in Figure 3.6), the potential of the MM environment is explicitly included in the GW calculation as an additional external potential to the Hamiltonian. The QM region is directly polarized by the multipole distribution (and vice versa) and coupled solutions are found self-consistently [200]. Within a *subtractive scheme* (GW/sMM), the QM region is replaced by a MM representation of the different states and a purely classical energy correction $E_{\mathrm{MM}}^{(\mathrm{n})} - E_{\mathrm{MM}}^{(\mathrm{qp})}$ is added to the GW vacuum energies. When applying this scheme, we approximate the state of the MADN molecules after the creation of an hole by that of the cation. In both cases, the MM environment includes all molecules inside a region within a cutoff distance r_{c} around the QM molecule. However, both cutoff-based techniques rely on the assumption that only short-ranged local interactions affect the energies of the QM region. In the thin-films of MADN, this is not the case as the deposition simulations reveal a weak net ordering of the small molecular dipole moment (0.59 D and 0.56 D for the α and β isomers). For the simulated morphologies considered, the cumulative calculated electric dipole moment parallel to the surface normal (z-direction) of in total 65.6 D (α-MADN) and 35.7 D (β-MADN). Figure 5.3(a) and (e) show the distributions of the absolute dipole moment for α- and β-MADN thin films, respectively, calculated based on the classical atomic point charge distributions of the constituent molecules. Both distributions are narrow and centered around

the single-molecule values of 0.59 D and 0.56 D. From the distribution of the di-pole moment's z-component (i.e., its component parallel to the surface normal) in Fig. 5.3(b) and (f) one can clearly see that there are more molecular dipoles aligned in positive z-direction. This gives rise to the observed net overall dipole moment of the thin film. Due to interactions among the molecular dipole mo-ments as obtained from single-molecule data, it can be assumed that a more real-istic description of the thin films' electrostatic properties should include mutual polarization effects. In our framework, we therefore first treat the total polar-ization of the film within the pMM approach described in Section 3.6.1. After application of this background pMM, the induced moments primarily lead to a broadening of the distribution of the absolute molecular dipole moments, as can be seen in Fig. 5.3(c) and (g). Similar observations can be made for the respect-ive z-component distributions in Fig. 5.3(d) and (h). The partial screening due to the polarizability of the neighbouring molecules reduces the total accumulated dipole moment in the film by 3.5 D (α-MADN) and 2.8 D (β-MADN). In spite of the small effective reduction of the accumulated thin film dipole moment, the distributions in Fig. 5.3 suggest that the electrostatic potential inside the film and its surfaces shows strong local variations. These manifest themselves directly in a substantial amount of disorder in the calculated excitation energies within the GW/pMM approach. Layer-averaged profiles of the obtained HOMO energies are shown in Fig. 4 of the main text. Figure 5.4 shows the individual HOMO ener-gies as a function of the z-coordinate of the molecule's center-of-mass, as well as their total distributions. The two aforementioned cutoff-based approaches can-not account for long-range electrostatic effects [217] that result as a combination of the thin-film geometry and cumulative electrostatics. Our final calculations are therefore based on a third scheme, here termed GW/pMM. This is an extension of the GW/sMM, in which the long-range electrostatic interaction effects are in-cluded via an infinite periodic embedding based on the traditional classical Ewald summation method [218]. We show in Section 5.6 that this scheme allows us to include electrostatic interactions up to an arbitrarily large cutoff distance. When only the static point charges are considered in both regions, we call this the "static GW/pMM scheme". The final results are obtained by also including polarizable (polar) interactions up to a cut-off distance r_c^p of 3 nm ("polarizable GW/pMM scheme"). Outside that radius, $\alpha_{tt}^{aa'} = 0$. Including these polarizable interactions reveals that the molecular dipole moments are slightly screened, so that the total accumulated dipole moment in the film is reduced by 3.5 D (α-MADN) and 2.8 D (β-MADN).
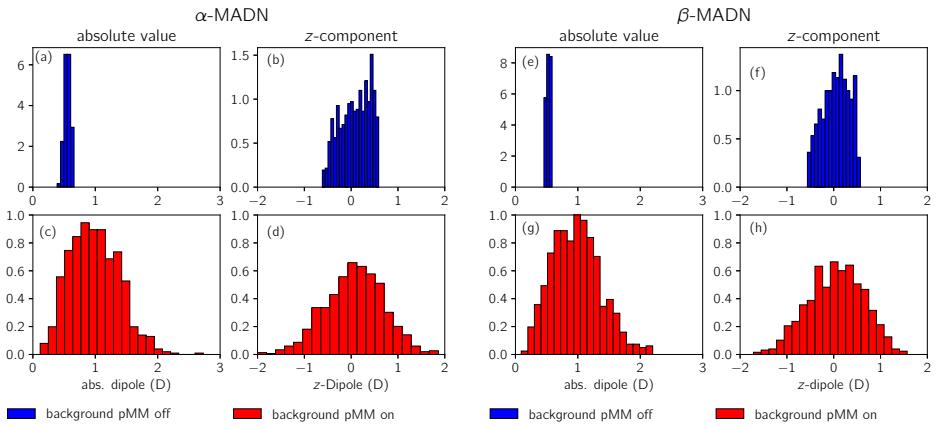
Figure 5.3: Distributions of the absolute value and z-component of molecular dipoles for both α-MADN and β-MADN inside the amorphous films. Without the pre-polarization of the periodic neutral background (background pMM off, (a) and (b) for α-MADN and (e) and (f) for β-MADN) both distributions are quite narrow. When background pMM is on ((c) and (d) for α-MADN, (g) and (h) for β-MADN) induction effects tend to smear out the dipoles' orientation and strength. See text for further discussion.
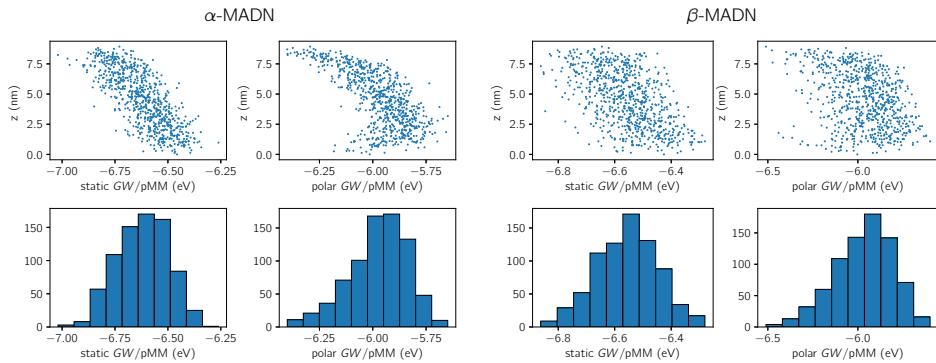
Figure 5.4: Energies of the HOMO as obtained by static and polar GW/pMM simulations for the thin films of α-MADN and β-MADN, respectively. The upper panels show the energies resolved according to the z-component of the individual molecule's center-of-mass, while the lower panels show the total energy distribution (or the total density-of-states) in the respective films.
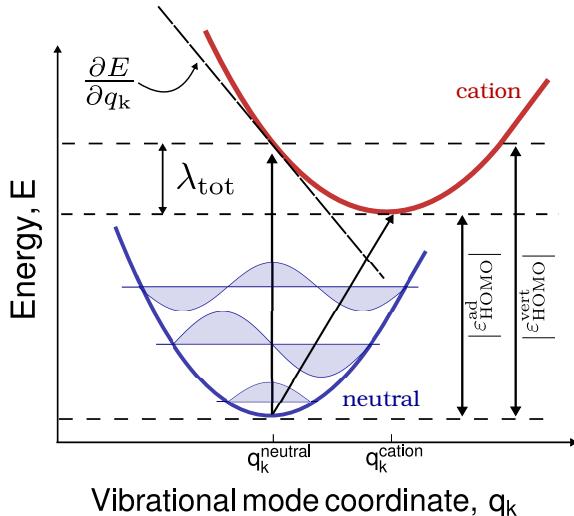
Figure 5.5: Schematic representation of the potential energy surfaces for the neutral (blue) and the cation (red) states, respectively, for a specific vibrational mode k, as a function of the (dimensionless) vibrational coordinate q_k. Adiabatic transitions are the results of coupling of particle-like excitations (vertical transition) with molecular vibrations, observed as the total reorganization energy $\lambda_{\text{tot}} = \sum_k \lambda_k$. Within the full-quantum treatment of carrier-vibrational mode coupling, employed in this chapter, the detailed mode-specific coupling strengths λ_k are included in the expression for the spectral shape shift and broadening function $S_{\text{el-vib}}^{\text{FQ}}(\Delta E)$ (Eq. (5.10)).

5.5 Surface Density of States and Carrier-Vibration Coupling

As a final step, we calculate from quasiparticle energies the HOMO contribution to the UPS spectrum, using Eq. (5.1), by taking the surface-sensitivity of the experiment and the carrier-vibration coupling into account. In the absence of the carrier-vibration coupling, the spectrum would be proportional to the surface density-of-states (SDOS). This is obtained by weighting the z-dependent frontier orbital energy with the exponential function from Eq. (5.1), i.e.

$$\text{SDOS}(E) = \frac{1}{N_\text{m}} \sum_j \delta(E - \varepsilon_j(z_j)) \exp\left(-\frac{z_0(x,y) - z_j}{\Lambda}\right). \tag{5.2}$$

We will adopt a value of $\Lambda = 1\,\text{nm}$ as suggested from experiment. It is compatible with estimates of the inelastic mean free path of the electrons within the random-phase approximation using GW energies, which we consider an upper limit to the electron attenuation length [191].

In the following we focus on estimates of the IMFP within the modeling framework established in this work. Throughout this section, atomic (Hartree) units are used ($\hbar = 1$, $m_\text{e} = 1$, and $e^2/(4\pi\epsilon_0) = 1$, with m_e the electron mass, e the elementary charge, and ϵ_0 the vacuum permittivity).

The IMFP is the mean distance between successive inelastic collisions experienced by an electron in a material. Its energy dependence can be estimated with the help of the Energy Loss Function (ELF),

$$Y_\text{ELF}(q,\omega) \equiv \text{Im}\left[\frac{-1}{\epsilon(q,\omega)}\right] = \frac{\epsilon_2(q,\omega)}{\epsilon_1(q,\omega)^2 + \epsilon_2(q,\omega)^2}, \tag{5.3}$$

where $\epsilon_1(q,\omega)$ and $\epsilon_2(q,\omega)$ are the real and the imaginary parts of the dielectric function, respectively. The ELF represents the probability of a material to absorb energy $\hbar\omega$ and momentum $\hbar q$ from an energetic incoming particle, such as a photon or an electron with kinetic energy E_k. The IMFP is related to the ELF via

$$\lambda_\text{in}^{-1}(E_\text{k}) = \frac{1}{\pi E_\text{k}} \int_{\omega_\text{min}}^{\omega_\text{max}} \int_{q_-}^{q_+} \frac{1}{q} Y_\text{ELF}(q,\omega)\, dq\, d\omega, \tag{5.4}$$

where $\omega_\text{min} = E_\text{gap}$, $\omega_\text{max} = (E_\text{k} + E_\text{gap})/2$, and $q_\pm = \sqrt{2E_\text{k}} \pm \sqrt{2(E_\text{k} - \omega)}$.

The first step is to compute the ELF. To this end we firstly evaluate $\epsilon_2(0,\omega)$ according to the non-interacting electron-hole picture in the Random-Phase Approximation (RPA) as

$$\epsilon_2(0,\omega) = 16\,\pi^2 \sum_{v,c} |\langle \phi_v^{\mathrm{QP}}|\hat{D}|\phi_c^{\mathrm{QP}}\rangle|^2 \delta(\omega - \varepsilon_c + \varepsilon_v), \tag{5.5}$$

where the sum runs over the occupied (v) and unoccupied states (c) and $\hat{D}$ is the dipole moment operator. The real part of the full dielectric function is then obtained using the Kramers-Kronig relation. From this one can straightforwardly obtain the ELF in the optical limit $(q \to 0)$ using Eq. (5.3).

Extending the ELF into the finite-q region is achieved using a model in which the dielectric response of the system is given by a summation of non-interacting component oscillators. In the RPA, valence electrons in the material are approximated by a non-interacting homogeneous gas where the plasmon energy is expanded to the second order in q

$$Y_{\mathrm{ELF,DL}}(q,\omega,\omega_{\mathrm{p}}) = \frac{\gamma\,\omega_{\mathrm{p}}\,\omega}{(\omega^2 - (\omega_{\mathrm{p}} + \omega(q))^2)^2 + (\gamma\,\omega)^2}, \tag{5.6}$$

where $\omega(q) = E_{\mathrm{gap}} + \alpha q^2$ and γ is the damping coefficient. The above optical Drude-Lorentz (DL) ELF in the form of Eq. (5.6) has a singularity at the plasma frequency ω_{p}.

To extend this approach from a non-interacting to an interacting medium, we consider the optical ELF as composed of DL-ELF terms with closely-spaced plasma frequencies ω_i such that

$$Y_{\mathrm{ELF}}(0,\omega) = \sum_i A_i\, Y_{\mathrm{ELF,DL}}(0,\omega,\omega_{\mathrm{p}} = \omega_i). \tag{5.7}$$

Once we have found the amplitude parameters A_i via a fitting procedure to our calculated ELF, we can build a momentum-dependent ELF according to

$$Y_{\mathrm{ELF}}(q,\omega) = \sum_i A_i\, Y_{\mathrm{ELF,DL}}(q,\omega,\omega_{\mathrm{p}} = \omega_i), \tag{5.8}$$

with the extension to finite q as in Eq. (5.6). Entering Eq. (5.8) into Eq. (5.4), we perform the integration over q and ω numerically to obtain $\lambda_{\mathrm{in}}(E_{\mathrm{k}})$. For He-I UPS (photon energy 21.2 eV) and with ε_i in the range of -7.0 to -5.8 eV (see Fig. 4 of the main text), the kinetic energy of interest is approximately $14.2 - 15.4$ eV.

Figure 5.6 shows the kinetic energy dependence of the IMFP as obtained with
vacuum quasiparticle energies. For $E_k = 15.0\,\text{eV}$ we obtain IMFPs of $1.69\,\text{nm}$ for
α-MADN and $2.14\,\text{nm}$ for β-MADN.

These values should be considered as upper limits to the real IMFP, and hence
also the EAL, due to the neglect of, e.g., changes in the full quasiparticle spectrum
due to morphology effects, intermolecular excitations in the RPA, or excitonic
effects. Furthermore, elastic processes can additionally reduce the electrons' mean
free path and hence the attenuation length. Explicit inclusion of these additional
scattering mechanisms in our estimates is beyond the scope of this work.

From coverage-dependent studies of the He-I ($21.2\,\text{eV}$) UPS spectrum of MADN
on Au, we find (1) that the Au-contribution to the spectrum has not yet decreased
significantly for a coverage of $0.6\,\text{nm}$ (α-MADN), (2) that this contribution has
decreased to about 10% for a coverage of $1.2\,\text{nm}$ (β-MADN), and (3) that this con-
tribution has almost vanished for a coverage above $1.6\,\text{nm}$ (α-MADN). Given the
uncertainties in obtaining the attenuation length from theory, detailed above, and
based on these experimental observations, we regard the value of the attenuation
of $1\,\text{nm}$, adopted in the main text for both isomers, as a fair estimate. The SDOS
does not include the effect of the intramolecular reorganization process upon charge
removal and the associated shift and lineshape broadening via carrier-vibration
coupling. Figure 5.7 shows schematically the effect of intramolecular reorganiza-
tion process on the density of states of a molecule. Conventionally, the effect of
the intramolecular reorganization process upon charge removal and the associated
shift and lineshape broadening via carrier-vibration coupling is described using
semi-classical Marcus theory [219, 220]. The spectral shape due to the coupling of
the photoelectrons with vibrational modes is then given by

$$S_{\text{el-vib}}^{\text{Marcus}}(\Delta E) = \frac{1}{\sqrt{4\pi\lambda_{\text{tot}}k_B T}} \exp\left(-\frac{(\Delta E - \lambda_{\text{tot}})^2}{4\lambda_{\text{tot}}k_B T}\right), \tag{5.9}$$

with λ_{tot} total reorganization energy, k_B the Boltzmann constant and T the tem-
perature. The energy difference is defined relative to the adiabatic excitation
energy, $\varepsilon_{\text{HOMO}}^{\text{ad}} = \varepsilon_{\text{HOMO}}^{\text{vert}} + \lambda_{\text{tot}}$ (see the schematic representation in Fig. 5.5).
However, significant coupling with vibrational modes with energies well above
$k_B T$, such as the C-C stretch vibrations of the phenyl rings in the $0.1 - 0.2\,\text{eV}$
range, makes the semiclassical approach for most organic semiconductor materials
invalid. This has been demonstrated for the related problems of the rates of elec-
tron or hole hopping and exciton transfer [221, 222]. Analogous to the full-quantum
(FQ) approach for inter-molecular charge transfer [221], which approximates the
potential energy surface of the excited molecule in the independent mode displaced
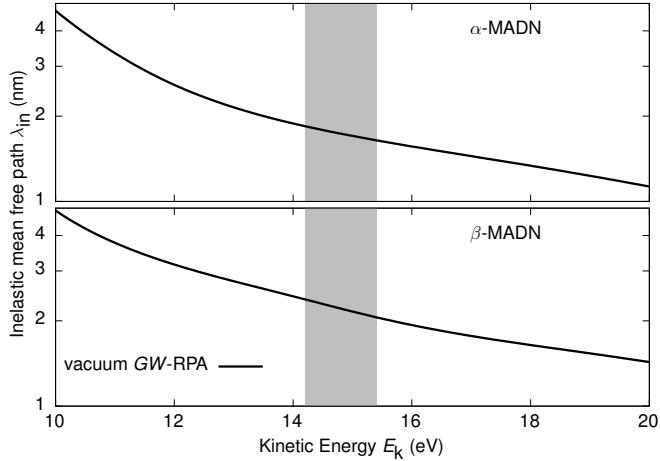
Figure 5.6: Kinetic energy dependence of the inelastic mean free path in α-MADN and β-MADN, obtained using the RPA with vacuum GW quasiparticle energies. The gray shaded area indicates the range of interest (14.2 eV - 15.4 eV).

harmonic oscillator model [223], we find that the spectral shape due to coupling of the photoelectrons with vibrational modes k with an energy $\hbar\omega_k$ and a coupling energy λ_k is given by

$$S_{\text{el-vib}}^{\text{FQ}}\big(\Delta E\big) = \frac{1}{2\pi\hbar} \int_{-\infty}^{+\infty} e^{i\frac{\Delta E}{\hbar}t} e^{-F(0)} e^{F(t)}\, dt, \qquad (5.10)$$

where

$$F(t) = \sum_k \frac{\lambda_k}{\hbar\omega_k} \left(\coth\left(\frac{\hbar\omega_k}{2k_{\text{B}}T} \right) \cos(\omega_k t) + i\sin(\omega_k t) \right). \qquad (5.11)$$

Evaluating the needed parameters (vibrational modes ω_k and coupling energy λ_k) can be simplified under the assumptions that (i) the ground- and excited-state potential energy surfaces are harmonic and (ii) no vibrational frequency alteration or normal mode rotation occurs in the excited state. With these two assumptions, equivalent to the premise of a linear electron-phonon coupling, only the ground-state vibrational modes frequencies ω_k and the gradient of the total energy for the charged (excited) system in the ground state geometry with respect to the
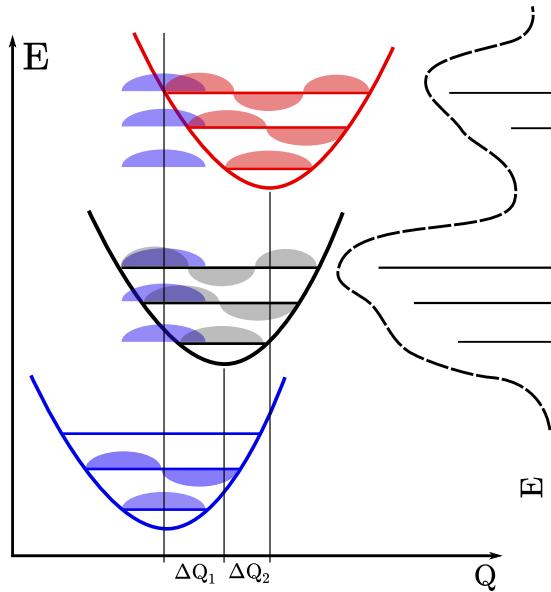
Figure 5.7: Effect of intramolecular reorganization process on the density of states of a molecule. Each excitation is always followed by structural reorganization (relaxation). This reorganization is associated with a shift and lineshape broadening via carrier-vibration coupling.

phonon mode coordinates q_k, $\frac{\partial E}{\partial q_k}$, need to be evaluated as indicated in Fig. 5.5. The mode-specific coupling energies are then determined as $\lambda_k = \frac{1}{2} \frac{\partial E}{\partial q_k}$.

5.6 Results and discussion

5.6.1 Quasiparticle embedding and long-range interactions

To assess the influence of long-range electrostatic interactions on the quasiparticle energies of the two MADN thin films, we analyze the results obtained with the different embedding schemes introduced in Sec. 5.4. First, we consider the effects of the dependence of the cutoff radius in the additive GW/aMM scheme. All results

Figure 5.8: Comparison of the quasiparticle HOMO energies $\varepsilon_{\mathrm{HOMO}}$ obtained using different molecular mechanics embedding schemes, as a function of the cutoff radius r_c up to which electrostatic effects are included, for (a) a surface and (b) a bulk molecule in the β-MADN thin film. For the cutoff-based GW/aMM (blue line) and GW/sMM (red line) methods, the cutoff length r_{c} is varied showing only a slow convergence. The value at $r_{\mathrm{c}} = \infty$ indicates the result after periodic embedding (GW/pMM scheme). In all cases, only the quasiparticle state is considered polarizable while the molecules in the MM region are described by static point charges.

given in this subsection are obtained using only a static embedding approach, within which the polarizability of the molecules is switched off. We show in Fig. 5.8 (blue curve) the calculated ϵ_{HOMO} as a function of r_{c} for a molecule at the surface and in the bulk-like region of the β-MADN film, respectively. The slow decrease of the energy with size of the embedding region indicates, in particular for the surface molecule, that even at a cutoff of $20\,\mathrm{nm}$ no converged result is obtained. Repeating the same analysis for the computationally less demanding subtractive GW/sMM scheme, in which we now allow the classical substitute of the QM molecule to be polarizable as it automatically is in GW/aMM, yields a cutoff dependence given by the red lines in Fig. 5.8. Comparison to the GW/aMM data reveals deviations smaller than $0.02\,\mathrm{eV}$. Based on this good agreement, we then use this parametrization and embed the classically represented QM molecule
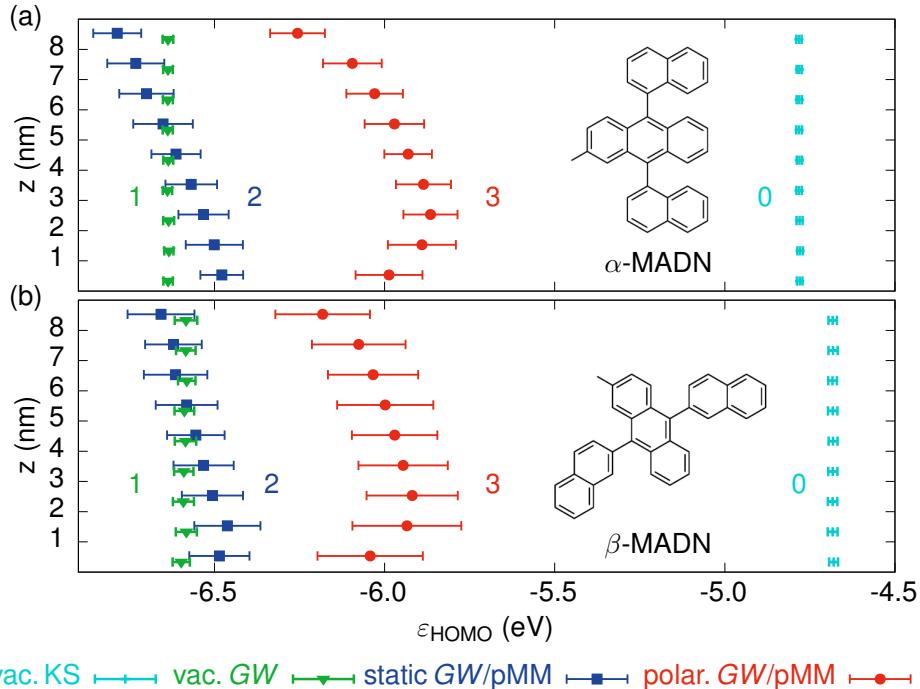
Figure 5.9: Layer-resolved energy levels of (a) α-MADN and (b) β-MADN obtained from vacuum KS (0), vacuum GW (1), static (2) and polarizable (3) GW/pMM calculations, respectively. The error bars correspond to the range of $\pm$ one standard deviation.

in a periodically repeated background in the GW/pMM setup. The results for both the surface and the bulk molecule are shown as data points for $r_{\mathrm{c}} = \infty$ in Fig. 5.8. For the surface molecule, the periodically embedded HOMO energy is $0.07\,\mathrm{eV}$ lower than as obtained from the GW/sMM calculation with the largest cutoff considered. In the bulk, the difference is slightly smaller, viz. $0.03\,\mathrm{eV}$. We adopt the GW/pMM scheme for the following analysis for thin-film energy levels, the SDOS and the UPS spectrum.

5.6.2 Layer-resolved energy levels and DOS

Figure 5.9 shows the laterally-averaged depth dependence of the HOMO energies as resulting from various levels of refinement, labeled "0" to "3". It shows that GW corrections ("level 1") to the vacuum KS levels ("level 0") lower the energies by up to 1.9 eV, nearly uniformly for both isomers. The gas-phase simulations include the molecular deformations in the thin-film morphology, but these cause only a small broadening of the DOS. It is mainly due to disorder in the anthracene-naphthalene torsion angle, which is largest for β-MADN. When long-range electrostatic interactions are included (static GW/pMM, level "2", blue squares in Fig. 5.9), we find for both isomers a nearly linear z-dependence of the mean HOMO energy, which is symmetric with respect to the mean vacuum GW energy ε^{GW}. This is due to accumulating net dipole moment contributions parallel to the surface normal during film growth. Even though the dipole moments of the individual molecules are small (0.59 D and 0.56 D for the α and β isomers) and their average net components parallel to the growth axis are only 0.065 D and 0.040 D, respectively, the resulting energy gradients are a few hundredths of an eV/nm. Adding polarization effects (polar GW/pMM, level "3", red circles in Fig. 5.9) leads to a shift of the mean of the distributions to lower binding energies. The effect is stronger in the bulk-like center of the film (0.7 eV (0.6 eV) for α-MADN (β-MADN)) than at the vacuum surface (0.5 eV).

Differences between the surface and bulk energy level structure of organic materials are well-known from UPS studies. For crystalline anthracene, e.g., the experimental binding energy difference for the first and second monolayer was found to be 0.3 ± 0.15 eV [224]. A similar effect is seen in Fig. 5.9 for the first molecular layer near the vacuum surface, which after subtracting the energy gradient due to dipole orientation shows an increase of the binding energy of about 0.15 eV. Since we simulate freestanding thin films, we also note modifications from the bulk-like behavior at the bottom surface with $z = 0$. In view of our interest in analyzing the UPS spectrum after irradiation from the positive z direction, which is only sensitive to the energy level structure in a thin zone near the top vacuum surface, we focus on that region.

5.6.3 Vertical and Adiabatic Surface Density of States

Fig. 5.10(a,b) show the SDOS for the two isomers (light-red shaded), obtained using Eq. (5.2). The SDOS is based on the vertical excitation energies. These include the effect of the electronic polarization of the environment but do not include the effect of the intramolecular structural reorganization process upon charge removal.
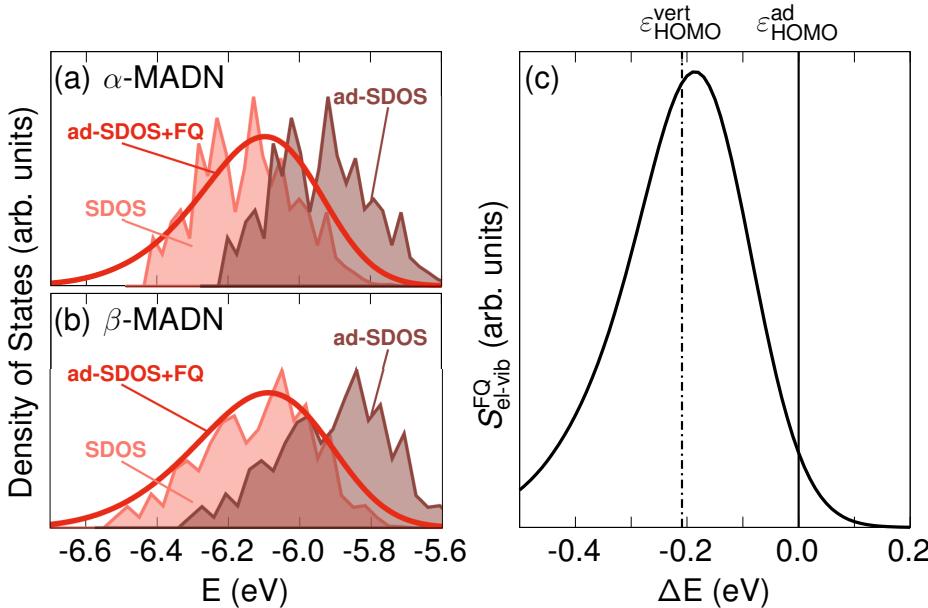
Figure 5.10: Frontier orbital surface density-of-states before (SDOS) and after adiabatic correction (ad-SDOS), as well as the simulated UPS spectra within the full-quantum model (ad-SDOS+FQ) for both α-MADN (a) and β-MADN (b) as obtained from the polarizable GW/pMM calculations. Panel (c) shows for β-MADN the shift of single-molecule vertical HOMO level to the adiabatic one at lower binding energies, and the subsequent application of the lineshape function $S_{\text{el-vib}}^{\text{FQ}}(\Delta E)$ (Eq. (5.10)) which leads to a pronounced broadening (FWHM: $0.25\,\text{eV}$) and shift to higher binding energies with respect to $\varepsilon_{\text{HOMO}}^{\text{ad}}$.

The ad-SDOS curves in Figure 5.10 (a,b) (dark-red shaded) show the adiabatic SDOS, obtained from the SDOS by adding an energy shift equal to the total reorganization energy, which is $0.21\,\text{eV}$ for both isomers. The actual excitation process is not adiabatic, but is accompanied by the excitation of vibrational modes. Figure 5.10(c) shows, for a single β-MADN molecule, the resulting shift of the DOS to a more negative HOMO energy and the resulting broadening to a full-width at half

maximum of approximately $0.25\,\mathrm{eV}$. For α-MADN, the effect is very similar. The absence of multiple satellite peaks, as usually seen for gas-phase spectra of structurally more simple molecules such as pentacene, is due to coupling of multiple modes, which smears out the structure. The peak of the function $S_{\mathrm{el\text{-}vib}}^{\mathrm{FQ}}$ is almost equal to the vertical HOMO energy. Including vibrational effects thus induces for these systems almost no peak shift with respect to the vertical (polarizable GW/pMM) energies, but only a spectral broadening. The resulting calculated UPS spectral intensity function, given by Eq. (5.1), is shown in Figure 5.10(a) and Figure 5.10(b) by the curves labeled "ad-SDOS+FQ".

It is interesting to compare the full-quantum vibrational response function $S_{\mathrm{el\text{-}vib}}^{\mathrm{FQ}}$ to the classical Marcus function. According to Eq. (5.9), the peak energy is shifted to lower energies relative to the adiabatic excitation energy by the total reorganization energy of $0.21\,\mathrm{eV}$ and the function has a Gaussian shape with a full-width at half maximum of $4\sqrt{\ln(2)\lambda_{\mathrm{tot}}k_{\mathrm{B}}T} \cong 0.24\,\mathrm{eV}$. A comparison with Fig. 5.10(c) shows that in this case the full-quantum result differs only weakly from the classical Marcus response function. Apparently, the coupling of the photo-electrons to high-energy vibrational modes is for these systems relatively weak.

5.6.4 Simulated UPS including Carrier-Vibration Coupling

Figure 5.11 shows the final UPS spectra of the frontier orbital of α- and β-MADN thin films, simulated for the four different levels of theory, together with the experimental data. Characteristics of the signals (maximum position, onset, and FWHM) are listed in Tab. 5.2. Following the conventional approach, the onset energy is defined by extrapolating the tangent through the low-binding-energy inflection point of the HOMO peak to zero intensity. The energetic position of the simulated peaks for the different methods reflects the variations discussed for the layer-averages in Fig. 5.9. Comparison to the reference experimental spectrum now allows assessment of the quality of the various methods and the importance of the individual processes for the analysis of the experiment.

Simulations based on vacuum energies which exclude the effects of inhomogeneous local electric fields and environment polarization either over- (KS) or underestimate (GW) the energy of the peak maximum by up to $1.3\,\mathrm{eV}$. The FWHM is nearly exclusively determined by the single-molecule spectral function and results about a third smaller than measured. Inclusion of static local field effects in GW/pMM does not noticeably affect the peak maximum but the additional disorder contributes to further broaden the signal. Accounting for the polarization response of the material upon quasiparticle excitation in GW/pMM we obtain a simulated UPS

signal in excellent agreement with the measurement: the largest deviation is found for the peak maximum of β-MADN and amounts to only 50 meV, which is also the experimental resolution. Most importantly, the comparison emphasizes that it is possible to achieve a predictive modeling of frontier orbital energies at the accuracy needed for an accurate understanding and prediction of device perform- ance. The fact that we achieve the same accuracy by studying two isomers, with different molecular structures and thin film morphologies, supports the robustness of our approach.

In device simulations, the bulk adiabatic ionization energy, $\varepsilon_{\mathrm{HOMO,bulk}}^{\mathrm{ad}}$, is needed. This energy may be obtained from a linear extrapolation of the bulk polariz- able GW/pMM energies shown in Fig. 5.9 to the surface plane at $z = z_0$, plus the reorganization energy λ_{tot} of 0.21 eV. The resulting values, $\varepsilon_{\mathrm{HOMO,bulk}}^{\mathrm{ad}} = -5.91(-5.89) \pm 0.05$ eV for $\alpha(\beta)$-MADN, are located in between the UPS peak and onset energies (see Tab. 5.2). Using either the peak or the onset value would, in this case, thus introduce an error of about 0.1 eV or more. Our refined protocol for the analysis of UPS measurements provides a methodology for avoiding such an error. One may see from Fig. 5.10(c) that when carrying out a measurement for a single molecule, the onset energy would provide an excellent approximation to $\varepsilon_{\mathrm{HOMO,bulk}}^{\mathrm{ad}}$. However, that coincidence is fortuitous, as the peak shape and onset energies depend on the mode-resolved reorganization energies and the temperat- ure. That may already be seen when considering the peak shape obtained within the semiclassical Marcus-theory (Eq. (5.9)). The difference between the onset en- ergy and the adiabatic ionization energy is then equal to $(-\lambda_{\mathrm{tot}} + \sqrt{8\lambda_{\mathrm{tot}}k_{\mathrm{B}}T})$. For a system with $\lambda_{\mathrm{tot}} = 0.2$ eV (close to the value for MADN) and for $k_{\mathrm{B}}T = 0.025$ eV (close to room temperature), the onset and adiabatic ionization energies then in- deed coincide. However, the electron-vibrational mode coupling shows a significant dependence on the molecules considered. The total reorganization energies vary from less than 0.1 eV to more than 0.3 eV, with a tendency to decrease with in- creasing molecular size [225, 226, 175]. Furthermore, in thin films the spectral broadening due to energetic disorder leads to a shift of the onset value to a smaller binding energy, whereas the reduced screening at the thin film surface leads to shift to a larger binding energy. For the two isomers of MADN, the former effect is largest, so that the absolute value of the onset energy is slightly smaller than $|\varepsilon_{\mathrm{HOMO,bulk}}^{\mathrm{ad}}|$.

Table 5.2: Characteristics of the predicted UPS spectrum (see the caption of Fig. 5.11) for α-MADN and β-MADN at the four different levels (0 − 3) of the multiscale quasiparticle embedding procedure. The HOMO peak position, onset, and the full width at half maximum (FWHM) (all in eV) are compared to the respective experimental results. The table also gives the calculated bulk adiabatic ionization energy $\varepsilon_{\text{HOMO,bulk}}^{\text{ad}}$.

	vacuum		GW/pMM		
	KS	GW	Static	Polar.	Exp.
α-MADN					
$\varepsilon_{\text{HOMO,bulk}}^{\text{ad}}$				-5.91	
UPS peak	-4.92	-6.78	-6.76	-6.10	-6.12
UPS onset	-4.71	-6.57	-6.44	-5.79	-5.79
UPS FWHM	0.25	0.25	0.39	0.39	0.37
β-MADN					
$\varepsilon_{\text{HOMO,bulk}}^{\text{ad}}$				-5.89	
UPS peak	-4.80	-6.70	-6.67	-6.09	-6.14
UPS onset	-4.58	-6.48	-6.37	-5.75	-5.73
UPS FWHM	0.25	0.26	0.36	0.41	0.42
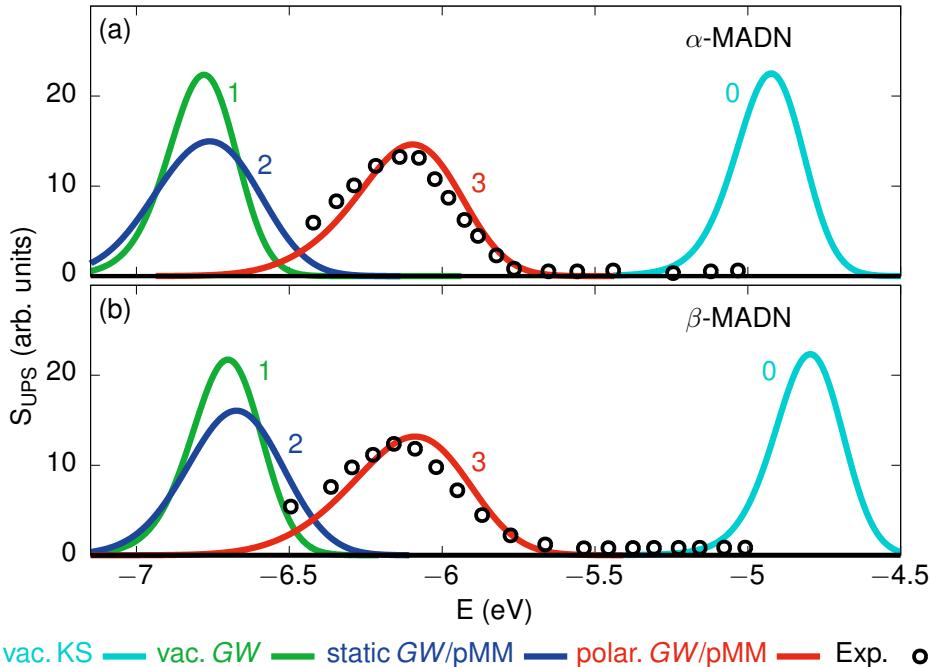
Figure 5.11: UPS spectra for α-MADN (a) and β-MADN (b). Curves $0-3$ give the UPS as depth weighted DOS with vrtical-to-adiabatic shift and vibrational broadening via Eq. (5.10) predicted from vacuum KS (0), GW (1), static (2) and polarizable GW/pMM (3) calculations, respectively. The closed circles give the experimental spectra, obtained using He-I radiation (21.2 eV). The experimental resolution is $\sigma = 0.05$ eV, and has no significant effect on the final spectral width.

5.7 Conclusions

In summary, we have developed a multiscale approach that provides a prediction of the frontier orbital UPS spectrum of amorphous molecular thin films. The approach includes (i) first-principles calculations of a realistic thin-film morphology, (ii) the electronic properties at a state-of-the-art (many-body Green's functions) level of quantum chemistry, (iii) embedding in a polarizable molecular mechanics environment, and (iv) the effects of the vibrational modes that are excited in the experiment. We have focused on two isomers of MADN, for which the non-degeneracy of the HOMO state leads to an exceptionally narrow width of the HOMO orbital UPS spectrum. Our work shows how the spectrum is related to the disorder-induced energy level distribution in the bulk of the organic semiconductor and near the surface. The good agreement between the calculated and experimental peak positions and widths of the UPS spectra indicates that our approach provides a route towards accurately predicting the bulk adiabatic ionization energy $\varepsilon_{\mathrm{HOMO,bulk}}^{\mathrm{ad}}$, which is the HOMO energy needed in device simulations.

We find that neither the HOMO energy that would follow from the UPS peak energy nor the onset energy coincide with $\varepsilon_{\mathrm{HOMO,bulk}}^{\mathrm{ad}}$. For the MADN films studied, both assumptions would introduce an error of about $0.1\,\mathrm{eV}$ or more. Instead, the actual value of $\varepsilon_{\mathrm{HOMO,bulk}}^{\mathrm{ad}}$ is in this case intermediate between the onset and peak values. The error made by taking $\varepsilon_{\mathrm{HOMO,bulk}}^{\mathrm{ad}}$ equal to the UPS onset energy is determined by the balance between the effects of energetic disorder and reduced screening at the thin film surface. For device applications, the *relative* error between different materials is most important. From our study, we expect that the relative error when taking the onset energy is largest for the case of two materials with strongly dissimilar energetic disorder energies or strongly dissimilar molecular polarizabilities.

Chapter 6

Electron affinity and binding energy of excitons in disordered organic semiconductors: First principles predictions using the GW-BSE method and multiscale quasiparticle embedding

This chapter deals with the computation of the Electron Affinity, Optical gap and Exciton Binding Energy in amorphous molecular systems. After a brief introduction about the importance of determining the Exciton binding energy and an overview of the difficulties behind its estimate, a multiscale embedding approach has been used to this end. A comparison between computations and experiments closes the chapter. We present a first-principles-based multiscale simulation study

of the low-energy unoccupied electronic structure, optical absorption and exciton binding energies in thin films of two isomers of 2-methyl-9,10-bis(naphthalen-2-yl)anthracene (MADN), a prototypical material used as an ambipolar host material in organic light emitting diodes. The approach combines many-body Green's Function Theory, polarizable film-embedding, and multimode electron-vibrational coupling calculations. It both allows to access excited states in the film at molecular resolution and provides a molecular-level view on the interactions and processes giving rise to features in inverse photoemisson and absorption spectroscopy on an equal footing. We gain insight into how energetic disorder, surface sensitivity and vibrational coupling in the excitations contribute to the relevant energy levels and spectral features. This is particularly relevant for the unambiguous determination the electron affinity, optical gap, and exciton binding energy of organic semiconductors, all key quantities for tailoring and engineering new opto-electronic devices. The simulated spectra are in excellent agreement with experiment. From extracted excited state energies, we determine exciton binding energies of about $1.0\,\text{eV}$ for both isomers of MADN.

6.1 Introduction

Organic semiconductors offer a wide range of potential applications in novel electronic or optoelectronic devices, such as organic light-emitting diodes (OLEDs) or organic solar cells (OPVs). A detailed understanding and optimization of the observed phenomena and the device operation require knowledge of the fundamental electronic properties of the systems. For instance, the nature of the excited electronic states is of great interest as it is directly related to processes such as light absorption and emission, photo-conductivity, and electroluminescence.
Nevertheless, measuring properties like the exciton binding energy is hard to achieve. Physical properties like size, shape, composition and arrangement of the molecules in materials under investigation strongly influence the nature and dynamics of the electronic excitation. This makes hard to draw general conclusions or unique interpretation about the behavior of excitons in different materials.
In this work, we present a first-principles-based multiscale simulation approach from which the electron affinity, the optical gap, and the exciton binding energy are derived. The method consists of an accurate evaluation of (i) quasiparticle and exciton energy levels within the GW approximation with the Bethe–Salpeter equation(BSE) and (ii) thin-film embedding effects, using a hybrid quantum-mechanics/molecular-mechanics (QM/MM) approach that takes the molecular po-

larizabilities and the long-range interactions due to partially ordered static multipole moments into account, and (iv) a full-quantum treatment of electron-vibration coupling. As prototypical material system, we investigate thin-films of the α and β isomers of 2-methyl-9,10-bis(naphthalen-2-yl)anthracene (MADN) (see insets of Fig. 6.1), materials used extensively as an ambipolar host material in OLEDs containing deep blue fluorescent emitter molecules [227, 228, 229, 230, 231]. In our previous work [232], we have studied the occupied electronic structure of these films, and demonstrated that our multiscale simulation approach allows for a prediction of ultraviolet photoemission spectra (UPS) showing an excellent agreement with experiment. Unoccupied levels can be measured experimentally by low-energy inverse-photoemission spectroscopy (LEIPS) [233]. The technique has recently been used to study the electron affinity in organic solids, alongside UPS measures for the ionization potential [234, 235]. Experimental LEIPS spectra for both α-MADN and β-MADN are shown in Figure 6.1 (see Appendix A for details on the experimental setup). While the UPS signal showed a clear HOMO peak well-separated from the lower-energy parts, the LEIPS signal near the spectral onset and up to the vacuum is featureless. It is not immediately obvious if the reason for the lack of features can be attributed to the small separations between LUMO and higher levels in MADN, strong vibrational broadening, surface effects, experimental conditions, or a combination (of some) of these. It is also unclear how one can relate this measured spectrum to the electron affinity of the material in the bulk. In contrast to this, optical absorption spectra (see Appendix A for details on the experimental setup) exhibit clear vibrational structures (see Figure 6.2 and Figure 6.3), which also hampers an unambiguous determination of the optical gap, here understood as the adiabatic transition energy of the first electron-hole excitation. Combined with the ambiguities of determining the electron affinity, this also severely hampers the determination of the exciton binding energy. To remedy this situation and to remove these ambiguities in the determination of the electron affinity and exciton binding energy in particular, we refine our previous model [232] to account for several GW quasiparticle states (LUMO and higher) and extend it to include also electron-hole excitations from the BSE.
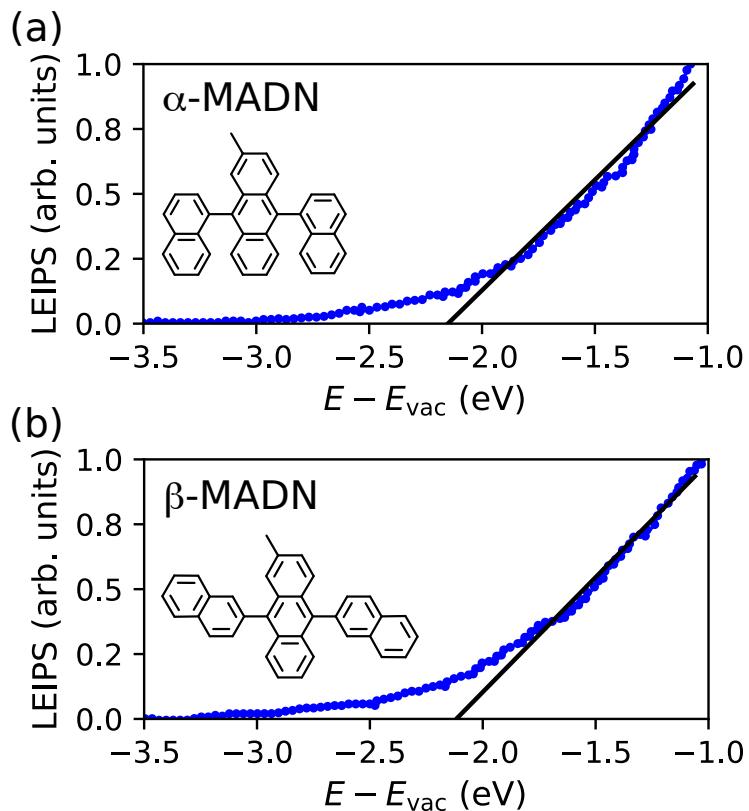
Figure 6.1: Experimental LEIPS for α-MADN and β-MADN at 285 nm. Experiments performed by Prof. Yoshida and his research team [236].
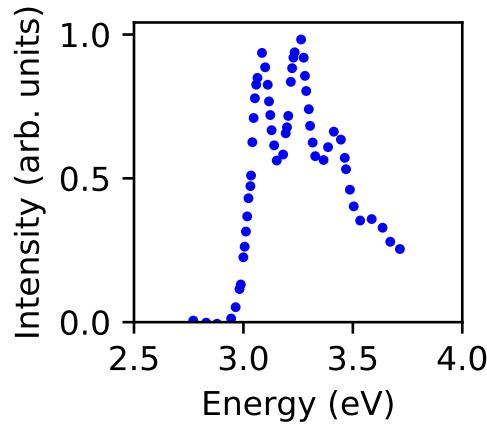
Figure 6.2: α-MADN experimental absorption spectrum. Experiments performed by Prof. R. Coehoorn and his research team [237].
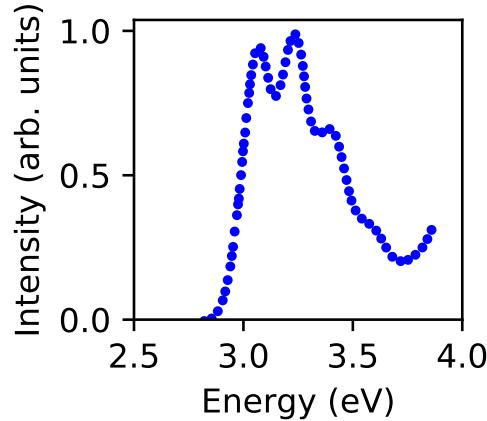
Figure 6.3: β-MADN experimental absorption spectrum. Experiments performed by Prof. R. Coehoorn and his research team [237].

6.2 Methodology

The methodology used in this work contains concepts and formulas already described in Section 2.5, Section 3.4.1 and Section 3.6. In the following only the theory of the QM/MM polarizable embedding with long-range interactions is presented again given some slightly different notational choices. This help the read to get acquainted with notation and theoretical concepts before showing results in Section 6.3.

6.2.1 QM/MM polarizable embedding with long-range interactions

In a material such as the thin-films of the two MADN derivatives, the single-molecule (gas-phase) quasiparticle and electron-hole excitation energies as determined in the previous section are modified due to intermolecular interactions. In an embedding scheme, the associated corrections to the intramolecular GW-BSE energies are evaluated in a coupled quantum-classical (QM/MM) procedure [210, 238, 239, 232]. The MM model consists of atomic static and induced multipole moments to form a classical representation of the molecular electrostatic potential. Within a *subtractive scheme* for coupling a QM- to an MM-region, the same type of classical representation is also used for the molecules in the QM-region with specific parametrizations for the ground ($s = n$) and excited ($s = x$) states of interest, and a purely classical energy correction $E_{\mathrm{MM}}^{(\mathrm{x})} - E_{\mathrm{MM}}^{(\mathrm{n})}$ is added to the GW-BSE gas-phase energies. Specifically, this classical energy for the total system $\mathcal{S}$ in state s is evaluated as

$$E_{\mathrm{MM}}^{(s)} = \frac{1}{2} \sum_{\substack{A,B \in \mathcal{S} \\ A \neq B}} \sum_{a \in A} \sum_{b \in B} \sum_{tu} (Q_t^{a(s)} + \Delta Q_t^{a(s)}) T_{tu}^{ab} Q_u^{b(s)}, \qquad (6.1)$$

where A and B indicate individual molecules in the system, a and b atoms in the respective molecules, Q_t^a are the static atomic multipole moments of rank t associated to atom a, and T_{tu}^{ab} is the tensor describing the interactions between the multipoles moments Q_t^a and Q_u^b [240]. The induced moments ΔQ_t^a are generated by the electric field created by moments t' of atom $a' \neq a$ in molecule A and the one generated by the moment u of atom b in molecule B:

$$\Delta Q_t^a = - \sum_{\substack{A,B \in \mathcal{S} \\ A \neq B}} \sum_{b \in B} \sum_{\substack{a' \in A \\ a' \neq a}} \sum_{tt'u} \alpha_{tt'}^{aa'} T_{t'u}^{a'b} (Q_u^b + \Delta Q_u^b), \qquad (6.2)$$

with $\alpha_{tt'}^{aa'}$ the atomic polarizability on each site. To avoid effects of spurious overpolarization, a damped version of the interaction tensor (Thole damping [240]) is used.

When selecting the specific QM and MM-regions, the QM-region includes only an individual molecule of interest, for which the classical energy corrected to the gas phase excitation energy needs to be computed. For the MM-regions, different choices can be made, and often plain cutoff-based schemes are considered, which assume that only short-ranged local interactions are relevant. For thin-film system like α-MADN and β-MADN structures in this work, such schemes cannot properly account for the spatially inhomogeneous interaction (ranges) due to the structural anisotropy perpendicular and parallel to the film growth direction [241]. Therefore, we use a scheme labeled as GW/pMM or GW-BSE/pMM depending on the type of excitation, in which long-range electrostatic interaction effects are included via an infinite periodic embedding based on the traditional classical Ewald summation method [242]. In this scheme (1) the 2D periodic neutral system is polarized, (2) against this periodic, polarized background a localized, non-periodic excitation is treated within a polarizable cutoff region around the QM region of interest [232]. To parametrize the models, we limit the static moments to partial charges which are obtained from a CHELPG fit to the neutral an excited molecule's electrostatic potential [243], respectively. Atomic polarizabilities, optimized to reproduce the polarizable volume of the molecule obtained from DFT+GW-BSE, account for polarization effects via the induction of atomic dipoles (Thole model) [244]. When only the static point charges are considered in both regions, we call this the "static GW/pMM (GW-BSE/pMM) scheme". The final results are obtained by also including polarizable interactions up to a cut-off distance r_c^p of 6 nm ("polarizable GW/pMM (GW-BSE/pMM) scheme"). Outside that radius, $\alpha_{tt}^{aa'} = 0$.

6.3 Results

6.3.1 Single Molecule GW Calculations

Ground state calculations including geometry optimizations on KS-DFT level are performed with the ORCA [245] package using the PBE0 functional [246] and the cc-pVTZ basis [202]. The VOTCA-XTP [239, 247] software is used for GW steps employing Gaussian-type orbitals as basis functions. An optimized auxiliary basis set [248] is used for resolution-of-identity techniques to efficiently express terms involving four-center Coulomb integrals. The convergence limit for the self-consistent GW-cycles in the evGW scheme was set to 10^{-5} Hartree (0.27 meV).

The number of occupied and unoccupied levels taken into account for the QP calculations is 327. Calculation of the RPA dielectric function requires the full spectrum of the KS states (1385 levels).

Table 6.1: Comparison of the calculated gas-phase energy levels (in eV) for LUMO (L), LUMO+1 (L+1), and LUMO+2 (L+2) of α-MADN and β-MADN, obtained using the PBE0 exchange-correlation functional with the cc-pVTZ basis set, within KS-DFT (KS) and including perturbative quasiparticle corrections from FAA and PPM quasiparticle calculations, respectively. The difference between the latter two is given by $\Delta_{\text{FAA}}^{\text{PPM}}$.

	α-**MADN**			β-**MADN**		
	L	L+1	L+2	L	L+1	L+2
KS	-1.75	-1.20	-1.19	-1.74	-1.23	-1.23
FAA	-0.38	+0.39	+0.41	-0.36	+0.37	+0.36
PPM	-0.23	+0.53	+0.55	-0.21	+0.51	+0.51
$\Delta_{\text{FAA}}^{\text{PPM}}$	-0.15	-0.14	-0.14	-0.15	-0.14	-0.15

We first compare the results for the three lowest unoccupied energy levels as obtained with a Fully Analytical Approach [249] (FAA) or a generalized plasmon-pole model (PPM) [199] for the frequency integration in Eq. (3.56). The FAA is an in principle exact form, in which the frequency dependence of the self-energy is expressed in the eigenbasis of the full RPA Hamiltonian in a KS product state basis. Its application to molecules of the size of MADN is computationally extremely demanding, due to the N_{b}^6 scaling, where N_{b}^6 is the number of basis functions [249]. Use of a PPM, on the other hand, allows for a comparatively fast evaluation of self-energy even for larger systems but can yield deviations of several eV from the exact result [249, 250]. From the results given in Tab. 6.1, we note a nearly constant shift of $\Delta_{\text{FAA}}^{\text{PPM}} = -0.15\,\text{eV}$ for the three lowest unoccupied energy levels of geometry-optimized α-MADN and β-MADN, respectively. To perform the *GW* calculations on the 770 molecules with conformational disorder, we therefore resort to calculations with the PPM and apply $\Delta_{\text{FAA}}^{\text{PPM}}$ for the respective levels from the geometry-optimized structures. Previous studies on anthracene have shown that the inclusion of zero point vibrational energy (ZPVE) effects influences its electron affinity on the order of one tenth of an eV [251]. As both MADN derivatives contain an anthracene core, similar effects on the LUMO energies can be expected

here. We therefore determine ZVPEs for neutral and anionic molecules based on DFT, and find a reduction of the LUMO energy of $\Delta_{\text{ZPVE}} = -0.11\,\text{eV}$ [252].

6.3.2 Layer-resolved unoccupied electronic structure in molecular thin-films

We now turn to determining the unoccupied electronic structure of amorphous thin films of α-MADN and β-MADN. The thin film geometries were generated using a simulated deposition protocol based on classical force fields, see [232] for details. The final freestanding morphologies contain 770 molecules, are periodic in x and y directions with box lengths of approximately $10\,\text{nm}$, and after removal of an artificially dense fixed bottom layer representing a substrate for the deposition extend about $8\,\text{nm}$ in z-direction. Evaluating now the unoccupied quasiparticle energies of level ℓ in these thin film morphologies consists of two steps: first, the *intramolecular* contributions for each molecule M, $\varepsilon_{\ell,M}^{\text{intra}}$ needs to be determined. For this, based on the results discussed in the previous section, we perform GW calculations with the PPM and correct for the effects of the FAA and the ZPVE, according to

$$\varepsilon_{\ell,M}^{\text{intra}} = \varepsilon_{\ell,M}^{\text{intra,PPM}} + \Delta_{\text{FAA}}^{\text{PPM}} + \Delta_{\text{ZPVE}}. \tag{6.3}$$

In a second step, the *intermolecular* modifications are evaluated via the GW/pMM technique outlined in Sec. 6.2.1. To this end, we first need to parametrize the classical embedding model for all states of interest. This includes calculating CHELPG partial charges for neutral ($s = n$) and the unoccupied states of interest ($s = \ell$), and determining the atomic polarizabilities from the molecular polarizability tensors in these states. For the GW states, the latter need to be calculated numerically from the second derivative of the total energy with respect to externally applied electric fields, $\alpha_{ij}^{(\ell)} = \frac{\partial^2 E^{(\ell)}}{\partial F_i \partial F_j}$, where $E^{(\ell)} = E_{\text{DFT}} + \varepsilon_{\ell}^{\text{QP}}$. With the parametrized classical forms, we proceed in evaluating Eq. (6.1) for neutral and quasiparticle states, including polarization effects within a cutoff region of $6\,\text{nm}$. To accommodate such a large cutoff (larger than half of the box size in x and y directions), we first construct a 2×2 supercell. Finally, the embedded QM/MM quasiparticle energies are determined as

$$\varepsilon_{\ell,M}^{\text{QM/MM}} = \varepsilon_{\ell,M}^{\text{intra}} + \varepsilon_{\ell,M}^{\text{inter}} = \varepsilon_{\ell,M}^{\text{intra,PPM}} + \Delta_{\text{FAA}}^{\text{PPM}} + \Delta_{\text{ZPVE}} + E_{\text{MM}}^{(\ell,M)} - E_{\text{MM}}^{(n,M)}. \tag{6.4}$$

Figure 6.4 shows the resulting z-layer averaged dependence of the LUMO energies from gas phase GW (green), static (blue) and polarizable (red) GW/pMM calculations, respectively. Each layer contains 77 molecules and the distributions
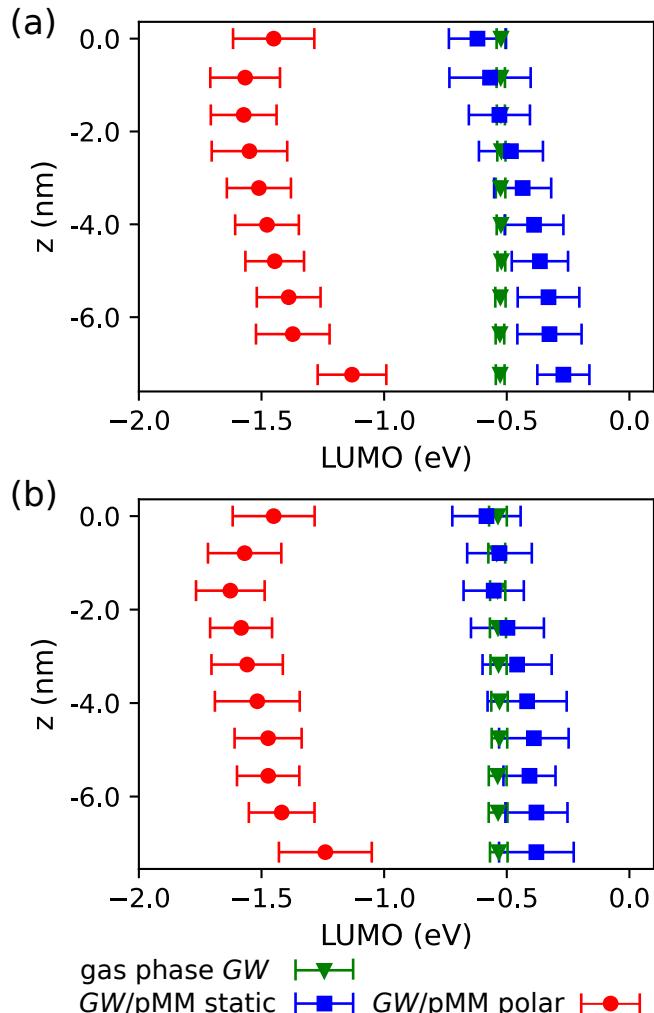
Figure 6.4: Layer-resolved distributions of *vertical* quasiparticle LUMO energies (in eV) as obtained from gas phase *GW* (green), static (blue) and polarizable (red) *GW*/pMM calculations for thin films of (a) α-MADN and (b) β-MADN, respectively.

of the energies in a single layer are represented by violin plots, with the white dot indicating their median. Not shown are the results obtained without embedding, i.e., distributions of $\varepsilon_{\ell,M}^{\text{intra}}$, as conformational disorder in the molecules only adds a negligibly small broadening of about 0.01 eV (0.03 eV) to the vacuum quasiparticle energies of α-MADN (β-MADN). The observed disorder in the static and polar GW/pMM LUMO energies as in Fig. 6.4 is therefore dominated by effects from intermolecular interactions. With 0.16-0.20 eV (0.11-0.17) in the polar (static) case, disorder is slightly larger for β-MADN compared to α-MADN (0.12-0.17 eV and 0.11-0.17 eV, respectively). More importantly, there are also clear differences in the mean/median energies and their dispersion/band shape along the z direction perpendicular to the film. Within static GW/pMM, there is an almost linear band shape due to the interactions with a net dipole moment in the films formed during the deposition process [232]. The band slope is stronger in α-MADN due to a higher dipole moment compared to β-MADN (62.1 D vs. 32.9 D). Including polarizable interactions in polar GW/pMM lowers the LUMO energies by nearly an eV in the center of the films, e.g., to -1.52 eV for α-MADN and -1.45 eV for β-MADN in the $z = 6.2$ nm layer. Near the interfaces with the vacuum at the top and the bottom of the freestanding films, the effects of polarization are smaller as there is fewer polarizable material. As a consequence, the z-dispersion resembles a U shape, with bending of the bands towards less negative energies at the interfaces. Note that this shape is not completely symmetric due to the morphological details and structural disorder. Also a slight "tilt" is visible from the interactions with the net dipole moment as in the static case.

6.3.3 Surface Density of States

We now turn to how the spatially resolved unoccupied electronic structure as discussed above is related to a spectroscopic measurement with (low-energy) inverse photoemission. An important quantity is the density of states at the surface that is accessible to the measurement. Such a *surface density of states* (SDOS), $\zeta(E)$, can in general terms be defined as

$$\zeta(E) = \sum_M \sum_\ell \int f_M(\mathbf{r}) \delta(E - \varepsilon_{\ell,M}^{\text{QM/MM}}(\mathbf{r}))\, d^3r = \sum_M \sum_\ell \zeta_{\ell,M}(E) \qquad (6.5)$$

with $\varepsilon^{\ell,M}$ the ℓ-th energy level for the M-th molecule in the system, as calculated from GW/pMM. The weighting function $f_M(\mathbf{r})$ takes into account how likely it is that electrons are involved in the experiment given their position in the sample. This likelihood is, in turn, related to the electron attenuation length (EAL), Λ,

which is known to possess a sensitive energy-dependence. For instance, at energies of *direct* photoemission, Λ is approximately $1\,\mathrm{nm}$ based on experimental evidence for the MADN derivatives [247]. The relevant SDOS is then modeled with an exponential extinction function $f_M(\mathbf{r}) = \delta(\mathbf{r}_M)\exp\{(-|z_M - z_0(x,y)|/\Lambda)\}$, where $z_0(x,y)$ is the surface profile. At low electron energies as used in the *inverse* photoemission experiments ($< 5\,\mathrm{eV}$), there are indications for the relevant EAL to be significantly larger. *Universal* curves [253] suggest that Λ can be in the range of 10-100 nm, which is also supported by upper limit estimates specific for MADN based on the random-phase approximation using GW energies (see Supplemental Material of Ref. [232]). The latter does not include, among others, contributions of inelastic scattering with longitudinal optical phonons to the macroscopic dielectric function, which has been argued to reduce the EAL at small electron energies [254]. We therefore follow Ref. [255] and estimate the vibrational contributions $\Delta\epsilon_{\mathrm{r,vib}}$ from a combination of DFT calculations of the vibrational-mode (wave number ν_j) resolved infrared band areas Ψ_j with a film-embedding based on the Clausius-Mosotti relation as

$$\Delta\epsilon_{\mathrm{r,vib}} = \left[\frac{(n^2 + 2)^2}{9 - (n^2 + 2)\frac{N\alpha_{\mathrm{vib}}}{\epsilon_0}} \right] \frac{N\alpha_{\mathrm{vib}}}{\epsilon_0}, \tag{6.6}$$

where

$$\alpha_{\mathrm{vib}} = \frac{\epsilon_0}{\pi^2 N_A} \sum_j \frac{n\Psi_j}{\nu_j^2}. \tag{6.7}$$

Here, ϵ_0 is the vacuum dielectric permittivity, N_A the Avogadro number, n the real part of the refractive index, and N the molecular volume density of a homogeneous film. Specifically, we employ $n = 1.7$ and a volume density of $2.55\,\mathrm{mol/l}$ and $2.82\,\mathrm{mol/l}$ for α-MADN and β-MADN, respectively. Figure 6.5 shows that inelastic scattering as a result of the creation of IR-active (optical) vibrations is weak in both MADN isomers compared to other often-used organic semiconductors [255]. Consequently, the total $\Delta\epsilon_{\mathrm{r,vib}}$ of 0.19 for α-MADN and 0.22 for β-MADN, respectively, are small. Combined with the expectations from the universal curve, this corroborates the notion that indeed $\Lambda > 1\,\mathrm{nm}$. For the analysis of the SDOS in our simulated systems we also need to account for the thickness of $5\,\mathrm{nm}$ of the MADN films in the experiment. Instead of using an exponential decay for $f_M(\mathbf{r})$, we consider all molecules with $z_0 > 4\,\mathrm{nm}$ in the SDOS, approximating an effective film thickness as in the experiment, i.e., using $f_M(\mathbf{r}) = \delta(\mathbf{r}_M)\mathcal{H}(z-z_0)$ in Eq. (6.5). This choice also removes the effects of the band bending at the bottom vacuum interface in our simulation.
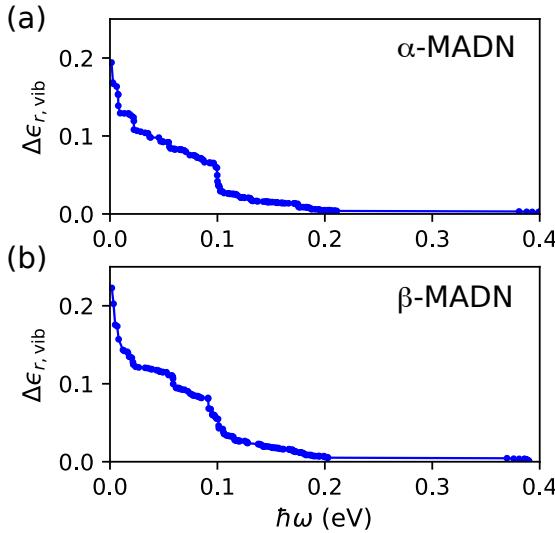
Figure 6.5: Cumulative value of the vibrational contribution to the relative dielectric constant, $\Delta\epsilon_{\mathrm{r,vib}}$, calculated for α-MADN (a) and β-MADN (b).

6.3.4 Inverse photoelectron spectra

With the SDOS, the simulated energy-dependent intensity $I(E)$ of an inverse photoemission experiment can be written as

$$I(E) \propto \sum_{\ell} \sum_{M} \int \zeta_{\ell,M}(E + \omega) S_{\ell,M}^{\mathrm{el\text{-}vib}}(\omega)\,d\omega = \sum_{\ell} I_{\ell}(E). \tag{6.8}$$

Here, $S_{\ell,M}^{\mathrm{el\text{-}vib}}(\omega)$ is a state- and molecule-dependent function, which includes the effect of the intramolecular reorganization process upon charge removal and the associated shift and lineshape broadening due to electron-vibration coupling. It is obtained using the full-quantum (FQ) approach for inter-molecular charge transfer [256], which approximates the potential energy surface of the excited molecule in the independent mode displaced harmonic oscillator model [257]. Specifically, the spectral shape due to coupling of the photoelectrons with vibrational modes k

with an energy $\hbar\omega_k$ and a coupling energy λ_k is given by

$$S_{\ell,M}^{\text{el-vib,FQ}}(\omega) = \frac{1}{2\pi\hbar} \int_{-\infty}^{+\infty} e^{i\frac{\omega}{\hbar}t} e^{-F_{\ell,M}(0)} e^{F_{\ell,M}(t)} \, dt, \qquad (6.9)$$

where

$$F_{\ell,M}(t) = \sum_k \frac{\lambda_k^{\ell,M}}{\hbar\omega_k} \left[\coth\left(\frac{\hbar\omega_k}{2k_{\text{B}}T}\right) \cos(\omega_k t) + i\sin(\omega_k t) \right], \qquad (6.10)$$

with the Boltzmann constant k_{B} and temperature T. The underlying assumptions are that (i) the ground- and excited-state potential energy surfaces are harmonic and (ii) no vibrational frequency alteration or normal mode rotation occurs in the excited state. Only the ground-state vibrational mode frequencies ω_k and the gradient of the total energy for the excited system in the ground state geometry with respect to the phonon mode coordinates q_k, $\partial E^{(\ell,M)}/\partial q_k$, need to be evaluated. The mode-specific couplings are then determined as $\lambda_k^{\ell,M} = \frac{1}{2}\partial E^{(\ell,M)}/\partial q_k$. The sum $\lambda_{\text{tot}}^{\ell,M} = \sum_k \lambda_k^{\ell,M}$ is the total reorganization energy of state ℓ, which can be used to approximate the *adiabatic* excitation energies as $\varepsilon_{\ell,M}^{\text{QM/MM, ad}} = \varepsilon_{\ell,M}^{\text{QM/MM}} - \lambda_{\text{tot}}^{\ell,M}$. Note that the use of the function $S_{\ell,M}^{\text{el-vib,FQ}}(\omega)$ from Eq. (6.9) in Eq. (6.8) implies that the respective adiabatic DOS is used, or equivalently that its argument is shifted accordingly, i.e., $S_{\ell,M}^{\text{el-vib,FQ}}(\omega) \to S_{\ell,M}^{\text{el-vib,FQ}}(\omega + \lambda_{\text{tot}}^{\ell,M})$. In practical calculations, we determine the gradients with numerical differences for $\ell = $ LUMO, LUMO+1, LUMO+2 in the optimized ground state geometry, and employ the same $S_{\ell}^{\text{el-vib,FQ}}(\omega)$ for all molecules M. Finally, instrumental broadening can additionally be accounted for by convolving the simulated spectra with a Gaussian function of width σ_{inst}. The resulting simulated $I_\ell(E)$ signals for

Table 6.2: Simulated LUMO peak position and LEIPS spectral onsets (all in eV) with and without instrumental broadening, as well as the bulk electron transport level $\varepsilon_{\text{LUMO,bulk}}^{\text{ad}}$ for α-MADN and β-MADN, respectively, compared to the experimental spectral onset.

	Peak	Onset(σ_{inst})			
	LUMO	0.0 eV	0.3 eV	Exp.	$\varepsilon_{\text{LUMO,bulk}}^{\text{ad}}$
α-MADN	-1.53	-1.95	-2.19	-2.18	-1.87±0.13
β-MADN	-1.56	-1.97	-2.25	-2.20	-1.88±0.14
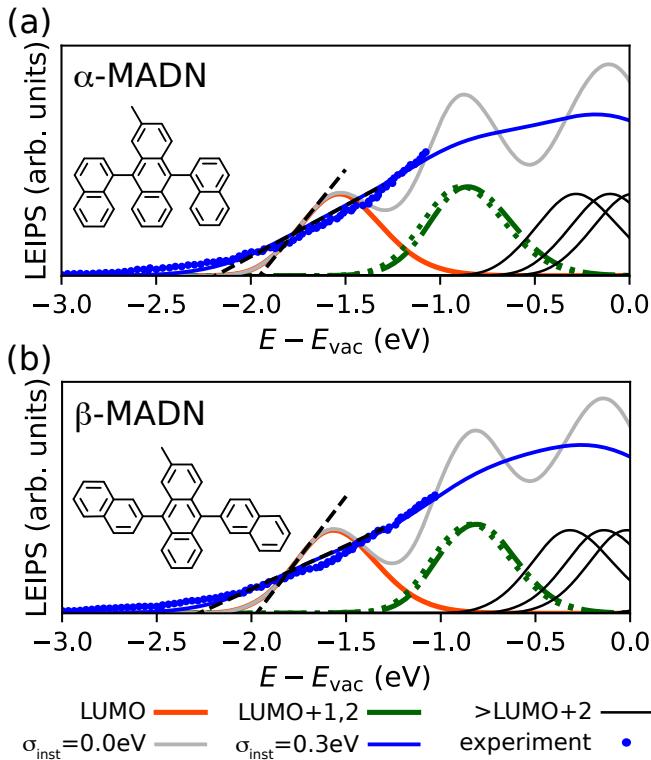
Figure 6.6: Simulated LEIPS spectra for (a) α-MADN (b) and β-MADN. Red and green lines indicate the state-dependent contributions $I_\ell(E)$ for LUMO and the nearly degenerate LUMO+1 and LUMO+2, respectively. Solid black lines indicate approximated signal contributions for levels above LUMO+2 (see text). The total simulated LEIPS signal ($\sigma_{\text{inst}} = 0.0\,\text{eV}$) is depicted by the grey line, while the blue line represents the respective signal with additional instrumental Gaussian broadening of $\sigma_{\text{inst}} = 0.3\,\text{eV}$. Dashed black lines indicate extrapolations of the spectral onsets from the two simulated spectra, and blue dots are the low-energy part of the experimental spectra as in Fig. 6.1.

α-MADN and β-MADN are shown in Figure 6.6. We first focus on the individual contributions of the LUMO (red), LUMO+1, and LUMO+2 (both green) states without instrumental broadening ($\sigma_{\mathrm{inst}} = 0.0\,\mathrm{eV}$). Following Eq. (6.8) the effective line shapes are a combination of the disorder in the energies (the width of the SDOS) and the line shape function. For both MADN derivatives, we find that the respective contributions do not have a Gaussian shape but exhibit a wider tail towards higher energies. The full-width-at-half-maximum is about $0.5\,\mathrm{eV}$ for all cases, with the β-MADN ones minimally wider by $0.03\,\mathrm{eV}$. The peak positions and onsets of the LUMO contributions to the spectrum are -1.53 eV and -1.95 eV for α-MADN, and -1.58 eV and -2.01 eV for β-MADN, see also Tab. 6.2. In Fig. 6.6, we also show with solid black lines contributions from states above LUMO+2. These signals are approximated by shifting the GW/pMM SDOS by the energy difference $\varepsilon_\ell^{\mathrm{QP}} - \varepsilon_{\mathrm{LUMO}}^{\mathrm{QP}}$ for $\ell > 2$ from the vacuum calculation, and by using the same lineshape function as for the LUMO. Those states are interesting for the IPS near the vacuum energy but result sufficiently far from the low-energy part of the spectrum to not influence it. The total simulated IPS is then shown as the grey line. Without instrumental broadening the contributions from the individual excitations to the spectra are clearly discernible. It is also apparent that due to the energy separation of the two peaks ($0.7\,\mathrm{eV}$ in both MADN materials) the low-energy onset area is exclusively determined by the LUMO and is found to be -1.95 eV for α-MADN and -1.97 eV for β-MADN. In the experiment, added as blue dots to Fig. 6.6, one finds more negative energies of the spectral onsets. There is also no clear peak structure in the recorded energy range. According to Ref. [258], typical instrumental broadening in IPS is $\sigma_{\mathrm{inst}} = 0.3\,\mathrm{eV}$, determined by the resolution of photon-detector (bandwidth of the optical filter, 0.1-0.3 eV) and the broadening of the electron kinetic energy ($0.2\,\mathrm{eV}$). We see that with the additional broadening (blue lines in Fig. 6.6), the onset energy is -2.19 eV for α-MADN and -2.25 eV for β-MADN. Furthermore, the broadened spectra exhibit a near featureless increase up to close to the vacuum energy, as found in the LEIPS studies. Note that in Fig. 6.6 the intensities of simulated and experimental spectra have been aligned at energy -1.0 eV. In this representation, both spectra show an excellent agreement with each other. In device simulations, the value of the electron transport level in the bulk, the adiabatic LUMO energies $\varepsilon_{\mathrm{LUMO,bulk}}^{\mathrm{ad}}$, is needed. As in the case for the bulk ionization energy in Ref. [232], we extract this from the z-dependence of $\varepsilon_{\mathrm{LUMO}}^{\mathrm{QM/MM,ad}}$ to the surface plane at $z = 0$. The resulting values are $(-1.87 \pm 0.13)\,\mathrm{eV}$ for α-MADN and $(-1.88 \pm 0.14)\,\mathrm{eV}$ for β-MADN, respectively (see also Tab. 6.2). In contrast to the UPS measurements [232] with a clearly discernible peak structure, the rather featureless broad IPS spectrum does

not allow to make any statements about a relation between peak position and bulk electron transport energy. Focusing on the experimental onsets alone, we notice that they are $0.31\,\text{eV}$ and $0.32\,\text{eV}$ lower than $\varepsilon_{\text{LUMO,bulk}}^{\text{ad}}$ from GW/pMM. The differences of the simulated onsets with $\sigma_{\text{inst}} = 0.0\,\text{eV}$ and $\sigma_{\text{inst}} = 0.3\,\text{eV}$, respectively, suggest that a substantial part of this difference between spectral onset and transport level can be attributed to instrumental broadening. The remainder likely stems from a combination of the intrinsic line width of the excitation and the disorder in the material. As the measurement is not as surface-sensitive as in the UPS case [232], the band bending towards the surface is not sufficient to compensate the offset between bulk transport level and LEIPS onset, even after correcting for instrumental broadening. In conclusion, the use of the onset of a broad and featureless inverse photoemission spectrum as estimate for bulk electron transport levels should at best be considered a lower-energy bound.

6.3.5 Absorption spectra and exciton binding energies

We now turn towards the calculation of electron-hole excitation energies within the GW-BSE/pMM framework. All BSE calculations reported in the following have been performed using transitions between all 117 occupied and the lowest 117 unoccupied molecular orbitals in Eq. (3.68). For single molecules in the optimized geometry, the vertical excitation energies of the first excited state based on the FAA are $\Omega_{\text{S}_1}^{\text{FAA}} = 3.21\,\text{eV}$ for both isomers. With the PPM as a model frequency dependence, we obtain $\Omega_{\text{S}_1}^{\text{PPM}} = 3.21\,\text{eV}$, so that $\Delta_{\text{FAA}}^{\text{PPM}} = 0.03\,\text{eV}$ for the S_1 state. In both cases, the excitation is formed nearly exclusively as a HOMO-LUMO transition. In the absence of additional screening due to the environment (see the strong modification of the LUMO energies from gas phase GW to polarizable GW/pMM), the vertical electron-hole binding energy $\langle \text{S}_1 | 2K^{\text{x}} + K^{\text{d}} | \text{S}_1 \rangle$ is about $3.3\,\text{eV}$ for both isomers. Analogously to the GW/pMM embedding approach for the LUMO energies, the embedded *vertical* GW-BSE/pMM S_1 energies are determined as

$$
\begin{aligned}
\Omega_{\text{S}_1,M}^{\text{QM/MM}} &= \Omega_{\text{S}_1,M}^{\text{intra}} + \Omega_{\text{S}_1,M}^{\text{inter}} \\
&= \Omega_{\text{S}_1,M}^{\text{intra,PPM}} + \Delta_{\text{FAA}}^{\text{PPM}} + \Delta_{\text{ZPVE}} \\
&\quad + E_{\text{MM}}^{(\text{S}_1,M)} - E_{\text{MM}}^{(n,M)},
\end{aligned}
\tag{6.11}
$$

with $\Delta_{\text{ZPVE}} = -0.06\,\text{eV}$ [259]. For the evaluation of $E_{\text{MM}}^{(\text{S}_1,M)}$ CHELPG partial charges are fitted to the electrostatic potential of the S_1 state and atomic polarizabilities to the excited state polarizability $\alpha_{ij}^{(\text{S}_1)} = \frac{\partial^2 E^{(\text{S}_1)}}{\partial F_i \partial F_j}$, with $E^{(\text{S}_1)} = E_{\text{DFT}} + \Omega_{\text{S}_1}$,

all based on the gas phase optimal geometries. They are also used to determine the excited state gradient $\frac{\partial E^{(S_1)}}{\partial q_k}$ for the calculation of the mode-specific exciton-vibration couplings $\lambda_k^{S_1}$. With that, we obtain the total exciton reorganization energy $\lambda_{tot}^{S_1}$ of $0.20\,\text{eV}$ ($0.21\,\text{eV}$) for α-MADN (β-MADN). In Fig. 6.7 we show the resulting *adiabatic* S_1 excitation energies, $\Omega_{S_1,M}^{\text{QM/MM,ad}} = \Omega_{S_1,M}^{\text{QM/MM}} - \lambda_{tot}^{S_1}$, depending on the z-position in the respective thin films as blue squares. In contrast to the behavior of the LUMO in Fig. 6.4, the energy of the optically active lowest exciton state does not exhibit a noticeable bending near the interfaces to the vacuum. This is due to the fact that in the classical part of the embedding, the dominant electrostatic potential change compared to the ground state stems from the dipole moment instead of the total charge and is therefore less sensitive to the environment including the long-range effects. Similarly small effects on the energy of localized electron-hole excitations have been noted before, e.g., for embedded push-pull polymers [210] or small-molecule donor molecules [247]. From the data, we find a bulk adiabatic exciton energy $\Omega_{S_1,\text{bulk}}^{\text{ad}}$ of $(3.00 \pm 0.04)\,\text{eV}$ for α-MADN and $(2.98 \pm 0.04)\,\text{eV}$ for β-MADN, respectively. From the lack of a z-dependence of the exciton energies, it is possible to simulate the intensity of the optical absorption spectrum as

$$I_{\text{Abs}}(E) \propto \sum_M \int \delta(E - \Omega_{S_1,M}^{\text{QM/MM}}(\mathbf{r})) S_{S_1,M}^{\text{el-vib}}(\omega)\, d\omega, \qquad (6.12)$$

with the respective variants of Eq. (6.9) and Eq. (6.10) with $\ell \to S_1$. The resulting spectra are shown as solid blue lines in Fig. 6.8 for the two isomers. Overall, the calculated spectra agree very well with the experimental reference (blue dots) and resolve particularly well the structure of the two lowest energy peaks. The relative intensity of the vibrational contribution near $3.4\,\text{eV}$ is a little too high, in comparison. In addition, the GW-BSE/pMM-based spectra result at slightly lower energies than the experimental reference. Therefore, we additionally show in Fig. 6.8 shifted versions of the simulation results as gray dashed lines. With shifts of $0.07\,\text{eV}$ and $0.05\,\text{eV}$ for α-MADN and β-MADN, respectively, the calculated and measured spectra are practically indistinguishable up to $3.3\,\text{eV}$. With the layer-resolved HOMO energies from [232], LUMO energies from Sec. 6.3.2 and the S_1 energies, we can now turn towards the analysis of the adiabatic exciton binding energy $E_{\text{bind, bulk}}^{\text{ad}}$ in the bulk within the GW/pMM and GW-BSE/pMM framework. In Fig. 6.7, we first consider the z-resolved adiabatic HOMO-LUMO gap, $E_{\text{gap},M}^{GW/\text{pMM,ad}} = \varepsilon_{\text{LUMO,M}}^{GW/\text{pMM,ad}} - \varepsilon_{\text{HOMO,M}}^{GW/\text{pMM,ad}}$, shown as green triangles. It is noteworthy that while the z-dependence of HOMO and LUMO individually is

Table 6.3: Summary of the adiabatic HOMO (from Ref.[232]) and LUMO energies, the HOMO-LUMO gap, S_1 exciton energy, as well as the exciton binding energy (all in eV) in the bulk, as obtained from GW/pMM and GW-BSE/pMM calculations either directly or by extrapolation (see text). Value in parentheses are the respective standard errors.

	α-MADN		β-MADN	
	direct	extrapolated	direct	extrapolated
$\varepsilon_{\text{HOMO,bulk}}^{\text{ad}}$		$-5.91(0.05)$		$-5.89(0.05)$
$\varepsilon_{\text{LUMO,bulk}}^{\text{ad}}$		$-1.87(0.13)$		$-1.88(0.14)$
$E_{\text{gap,bulk}}^{\text{ad}}$	$3.98(0.11)$	$4.04(0.14)$	$4.00(0.13)$	$4.01(0.15)$
$\Omega_{\text{S}_1,\text{bulk}}^{\text{ad}}$	$3.00(0.04)$	$3.00(0.04)$	$2.98(0.04)$	$2.98(0.04)$
$E_{\text{bind,bulk}}^{\text{ad}}$	$0.98(0.11)$	$1.04(0.14)$	$1.02(0.12)$	$1.03(0.15)$

strong, c.f. Figure 4 of [232] and Fig. 6.4, this effect cancels to a large extent when the difference is calculated. For both α-MADN and β-MADN, $E_{\text{gap}}^{\text{ad}}$ in the bulk region is (3.98 ± 0.11) eV and (4.00 ± 0.13) eV, respectively. Near the interfaces to vacuum, the HOMO-LUMO gap increases by about 0.3 eV due to the reduced screening of the charged excitations. With the nearly featureless z-dependence of the adiabatic S_1 energy, the exciton binding energy, first calculated per molecule as

$$E_{\text{bind},M}^{GW\text{-BSE/pMM,ad}} = E_{\text{gap},M}^{GW/\text{pMM,ad}} - \Omega_{\text{S}_1,M}^{GW\text{-BSE/pMM,ad}}, \qquad (6.13)$$

reflects the z-dependence of the gap energy in Fig. 6.7. In the bulk-like region of the two thin films, we find that $E_{\text{bind,bulk}}^{GW\text{-BSE/pMM,ad}} = (0.98 \pm 0.11)$ eV for α-MADN and $E_{\text{bind,bulk}}^{GW\text{-BSE/pMM,ad}} = (1.02\pm0.12)$ eV, respectively. Towards the vacuum interfaces, the binding energies are again larger by about 0.3 eV. Alternatively, the bulk exciton binding energy can be calculated from the individual extrapolated bulk values of HOMO, LUMO and S_1. In this case one obtains a bulk binding energy of (1.04 ± 0.14) eV for α-MADN and (1.03 ± 0.15) eV for β-MADN. All bulk energies are also summarized in Tab. 6.3.
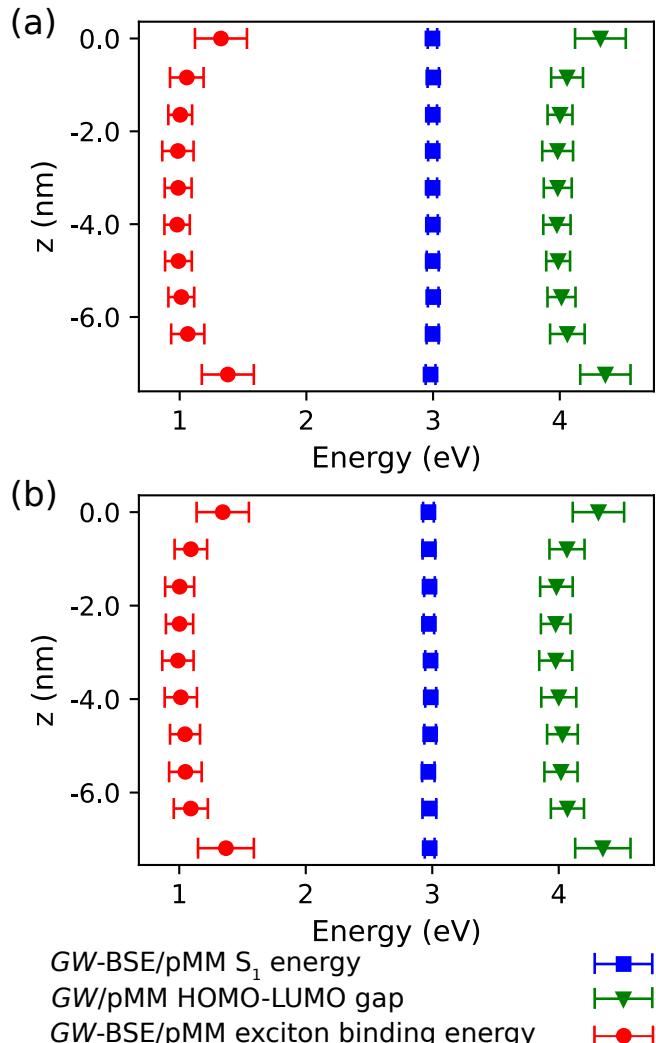
Figure 6.7: Layer-resolved distributions of *adiabatic* quasiparticle HOMO-LUMO gaps (green triangles), S_1 exciton energy (blue squares), and exciton binding energy (red circles) from polarizable (BSE@)GW/pMM calculations for thin films of (a) α-MADN and (b) β-MADN (all in eV), respectively.
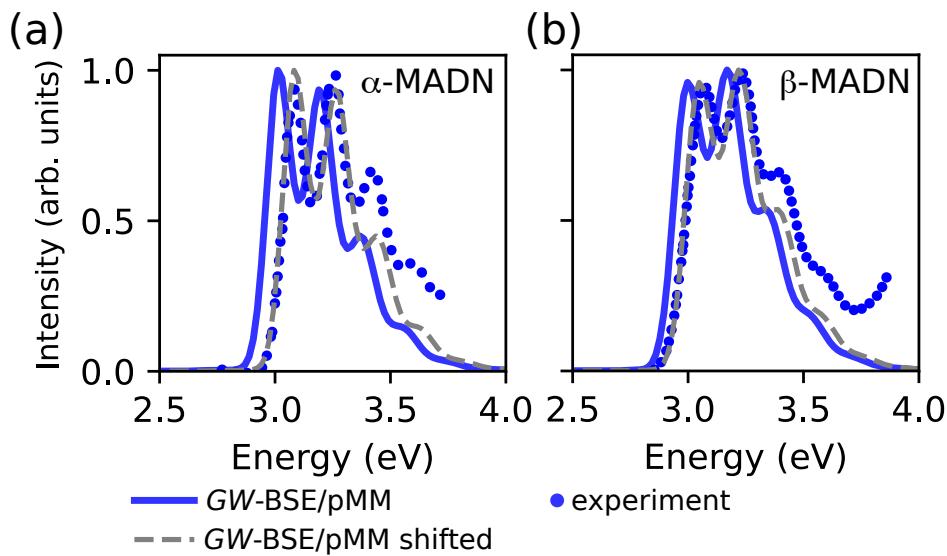
Figure 6.8: Absorption spectra for thin films of (a) α-MADN and (b) β-MADN. Blue solid lines indicate the spectra calculated based on GW-BSE/pMM energies and $I_{\mathrm{Abs}}(E)$ as in Eq. (6.12), while the blue dots represent the experimental measurement. The dashed gray line shows the simulated spectrum shifted by $0.07\,\mathrm{eV}$ and $0.05\,\mathrm{eV}$ for α-MADN and β-MADN, respectively.

6.4 Conclusions

In conclusion, this study presents a comprehensive multiscale approach that offers predictions for the low-energy unoccupied electronic structure, optical absorption, and exciton binding energies. The focus of the investigation has been on two isomers of MADN, which serve as fundamental materials in ambipolar host applications within organic light emitting diodes. The methodology encompasses several key elements: (i) an in-depth analysis of electronic properties utilizing techniques such as Many-body Green's functions and Bethe-Salpeter theory, (ii) incorporation within a polarizable molecular mechanics framework to capture environmental effects, and (iii) accounting for the influence of vibrational modes that become activated during experimental conditions. Through this comprehensive approach, valuable insights have been gained into the role of energetic disorder, surface interactions, and vibrational coupling on excitations, contributing significantly to the understanding of relevant energy levels and spectral characteristics. This holds particular significance in precisely determining vital parameters such as electron affinity, optical gap, and exciton binding energy in organic semiconductors. The simulated spectra remarkably align with experimental observations, underscoring the robustness of our methodology. By extracting energies of excited states, we have successfully determined exciton binding energies of approximately 1.0 eV for both MADN isomers. These findings not only enhance our comprehension of the intricate physics governing organic semiconductor behavior but also provide a solid foundation for designing and optimizing future electronic devices based on these materials.

Chapter 7

Non-adiabatic couplings and conversion dynamics between localized and charge transfer excitations from Many-Body Green's Functions Theory in rubrene-fullerene mixtures.

In this chapter, we determine the different excited states of molecular complexes within the GW-BSE/MM embedding schemes. In particular, we focus on a special type of electron-hole excitation called charge transfer (CT) state. We already

discussed the importance of CT states in photovolatic devices in Ch. 1.1. In short, photovoltaic devices harvest light and transform it into electric current. Their efficiency is mainly dependent on how much electricity can be photogenerated. Excitons form when light shines on these devices. Depending on the material properties, the exciton can transform into another type of excitation called charge transfer (CT) (see Figure 7.1). A CT state requires a Donor (D) and an Acceptor (A) molecule. The electron will go on A as the hole will stay on D, keeping the bound state typical of excitons. This CT state may eventually transform into a charge-separation (CS) state, in which electrons and holes split. Understanding and predicting CT states is thus pivotal for the classification and design of new photovoltaic (in general opto-electronic devices). In complex materials, in which many D-A pairs are available with different mutual distance and orientations, we expect to have a substantial variation in the distribution of the CT energies. In other words, disorder in the composition of the system can lead to different potential excited state energies. To gauge the effect of the material disorder on the CT energy distribution, to understand the role played by it and to measure its influence in experimentally measured quantities, ab-initio calculation can be exploited. In particular, embedding methods, as the additive GW-BSE/MM, can give insights that gas-phase calculations cannot show. We also investigate the determination of non-adiabatic couplings between localized excitations (LEs) and charge-transfer (CT) excitations based on many-body Green's functions theory in the GW approximation with the Bethe–Salpeter equation (GW-BSE). Using a small molecule dimer system, we first study the influence of different diabatization methods, as well as different model choices within GW-BSE, such as the self-energy models or different levels of self-consistency, and find that these choices affect the LE-CT couplings only minimally. We then consider a large-scale low-donor morphology formed from rubrene and fullerene and evaluate the LE-CT couplings based on coupled GW-BSE-molecular mechanics calculations. For these disordered systems of bulky molecules, we observe differences in the couplings based on the Edminston–Ruedenberg compared to the more approximate Generalize Mulliken–Hush and Fragment Charge Difference diabatization formalisms. In a kinetic model for the conversion between LE and CT states, these differences affect the details of state populations in an intermediate timescale but not the final populations.
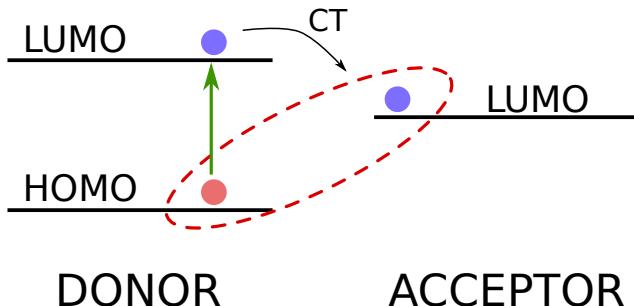
Figure 7.1: A simplistic schematic representation of the formation of a charge-transfer (CT) state. An electronic charge is transferred between molecules, often labelled as electron donor and electron acceptor. The resulting electrostatic attraction provides a stabilizing force for the molecular complex. The resulting excited state is called CT.

7.1 Introduction

7.1.1 Rubrene-fullerene low-donor content system

Here we study an amorphous morphology with low-donor content ($< 10\,\text{mol}\%$), composed of fullerene (C_{60}) and 5,6,11,12-tetraphenyltetracene (rubrene) [261]. Because of the low-donor content, a C_{60} cluster will surround the donor molecule, making the interaction between the single donor molecule with a close shell of neighboring C_{60} acceptors representative of the properties of the system as a whole. These complexes are therefore meaningful candidates for a computational analysis of the influence of donor-acceptor conformations and environment polarization effects in the GW-BSE/MM framework introduced in Sec. 3.6. To obtain representative structures, depicted in Figure 7.2, mixed morphologies have been simulated with ab-initio MD based on Density Functional Tight Binding theory using linear scaling self-consistent field calculations within the CP2K code [262]. Initial configurations have been prepared using packmol [263], targeting experimental values [261] for densities and mole percentages. This structure is first equilibrated at $700\,\text{K}$ in NpT (with velocity rescaling thermostat [264] at atmospheric pressure [265]) for $7\,\text{ps}$ (timestep $1\,\text{fs}$), then annealed to $300\,\text{K}$ within $10\,\text{ps}$. A final NpT equilibration followed for $5\,\text{ps}$. It is worth mentioning that
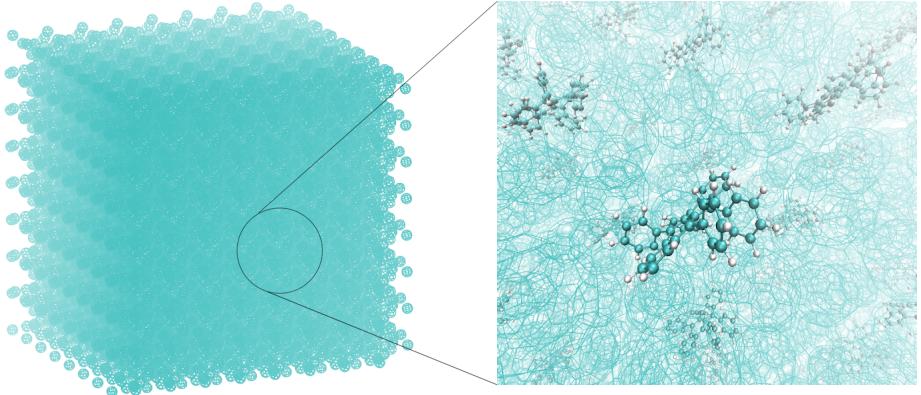
Figure 7.2: Bird's eye view on the simulation supercell for the C60-Rubrene system. The focus on the circled volume show the concentration of Rubrene (ball and stick molecules) is low compared to the C60 (line molecules) one. This effectively allows to consider only a relative small region around each Rubrene. This should account for the average behavior of the system as a whole.

this morphology has been used in a preliminary work [37] to study the effect of a polarizable disordered environment on localized and charge-transfer on two different donor-acceptor complexes excitations using the VOTCA-XTP software. This work served as a test on how variations of the mutual orientations of rubrene and C_{60} in the two complexes are expected to give rise to distinctly different characteristics of electronic excitations, intermolecular charge-transfer excitations above all. The study focus on two different donor-acceptor complexes, with a localized and a delocalized excitation respectively. The main result of this study shows that polarization from the environment plays a crucial role in the computation of excitations energies and how GW-BSE/MM methods can be useful in this regard. Results from [37] are shown in Figure 7.3.
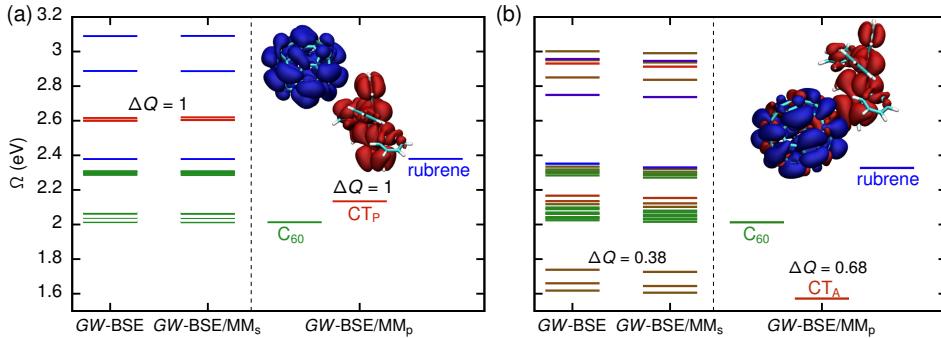
Figure 7.3: Excitation energies Ω (in eV) as obtained for the CT_P (a) and CT_A (b) complexes from GW-BSE calculations in vacuum and embedded in a static (GW-BSE/MM$_s$) and polarizable (GW-BSE/MM$_p$) environment, respectively. Local excitations on C_{60} (rubrene) are marked in green (blue), and excitations with CT character are given by varying shades of red depending on the amount of charge transfer ΔQ. Isosurfaces of the electron-hole densities with isovalue $\pm 10^{-4}\, e/a_B^3$ are shown as insets. CT_P refers to configuration in which the fullerene is close to the phenyl ring of rubrene whereas CT_A refers to the configuration in which the fullerene is close to the anthracene core of rubrene. Results are from [37].

7.1.2 Non-adiabatic couplings and conversion dynamics between localized and CT excitations

Many photochemical processes, such as catalytic processes or the generation of charges in active layer heterostructures of organic solar cells, involve the transfer of an electron triggered by the absorption of a photon. Such photoinduced electron transfer reactions are typically influenced by a variety of properties, ranging from the intrinsic molecular electronic structure of the molecular building blocks of the material, the details of the local mutual arrangement of molecules, to larger scale morphological ordering. In many situations, the inherent disorder of the material systems in which the electron transfer takes place suggests the use of localized diabatic states to describe the reactions and to map the effects of the local and global environment onto them. This idea as given rise to multiscale simulation approaches, in which the transport of excitations across a material is modeled as

a series of bi-molecular transfer events, each of them described by an effective transfer rate. According to Marcus theory [266, 267], in the non-adiabatic high temperature or activated crossing limit, the rate of electronic excitation transfer between two states X (initial) and Y (final) is

$$\omega_{XY} = \frac{2\pi}{\hbar} \frac{|J_{XY}|^2}{\sqrt{4\pi\lambda_{XY}k_BT}} \exp\left\{\left[-\frac{(\Delta E_{XY} - \lambda_{XY})^2}{4\lambda_{XY}k_BT}\right]\right\}, \tag{7.1}$$

where ΔE_{XY} is the free energy difference between initial and final states, and λ_{XY} the reorganization energy. The expression also contains the *non-adiabatic coupling* element, J_{XY}. In principle, it should be possible to evaluate all three quantities that enter the Marcus rate from electronic structure methods. To account for the local and global environment, however, it is typically required to embed electronic structure methods into a classical environment model, as the size of realistic disordered systems at least on the order of several tens of nm exceeds the capabilities of explicit quantum chemistry methods. Besides such quantum-classical embedding, of the key challenges involved in the multiscale modeling approaches of this kind is to use quantum-chemistry methods that allow for an accurate prediction of various excited states involved in the dynamical processes. Especially for the conversion of charge-neutral excitations, e.g., after photo absorption from localized exciton to charge-transfer state as an example of a photoinduced electron transfer reaction, the energetics of both LEs and CTs need to be described on an equal footing. In this context, the use of many-body Green's functions Theory employing the *GW* approximation and the Bethe–Salpeter equation (BSE) has become attractive to model electronically excited states on top of a ground-state reference calculation typically performed on the level of density-functional theory (DFT). It was shown that *GW*-BSE provides an effective single- and two-particle picture with accurate energies of LE and CT states without the need for any adaptations. Previous work has also shown that the additional screening caused by the molecular environment strongly affects the energies (and also densities) of CT states, more so than those of LEs, and that this energetic stabilization is important for finding CT-LE energy differences ΔE_{LE-CT} that are favorable for LE to CT conversion in organic solar cell materials. To fully treat the dynamical process of this conversion in the spirit of Eq. (7.1) requires also the reliable determination of the respective non-adiabatic coupling elements λ_{LE-CT}. In this work, we present a comparative study of determining non-adiabatic coupling elements between localized and charge-transfer excitations in the framework *GW*-BSE, based on three different diabatization methods: Edminston–Ruedenberg (ER) diabatization employing explicit electronic densities and the more approximate Generalize Mulliken–Hush

(GMH) and Fragment Charge Difference (FCD) formalisms. We first validate the predicted $J_{\text{LE-CT}}$ in a small molecule dimer system consisting of naphthalene and tetracyanoethylene (TCNE), for which reference calculations from coupled-cluster and time-dependent density-functional theory are available and allow scrutinizing the individual and combined effects of energy and (effective) wave-function predictions in the Green's functions method. Herein, we also put particular emphasis on how much or little the different model choices within GW-BSE, such as the choice of self-energy models or different levels of self-consistency affect the LE-CT couplings.

We proceed by considering a large-scale low-donor-content morphology formed from rubrene and fullerene and evaluate the LE-CT couplings based on coupled GW-BSE-molecular mechanics calculations.

7.1.3 Adiabatic v. Diabatic representation. Why is this distinction needed?

In the discussion in Ch. 2.3 about the Born-Oppenheimer approximation, it was mentioned that there are cases when the approximation does not hold. In the following a more rigorous discussion is presented, as a preliminary step to discuss diabatic states needed to described CT states. Going back to the Schrödinger equation, once solutions $\{\Psi_i^{\text{el}}(\mathbf{r}, \mathbf{R})\}_{i=1}^{\infty}$ and $\{\text{E}_{\text{el},i}\}_{i=1}^{\infty}$ are found for a number of different fixed nuclear configurations $\mathbf{R}$, one solves an equation of motion for nuclei which is obtained as follows. Since the electronic Hamiltonian is self-adjoint, its eigenfunctions $\{\Psi_i^{\text{el}}(\mathbf{r}, \mathbf{R})\}_{i=1}^{\infty}$ form a complete orthonormal set. Moreover, a function of two independent variables $\Phi(\mathbf{r}, \mathbf{R})$ can be expanded over a complete set of functions of one variable $\{\Psi_i^{\text{el}}(\mathbf{r}, \mathbf{R})\}_{i=1}^{\infty}$ in the following way

$$\Phi(\mathbf{r}, \mathbf{R}) = \sum_{i=1}^{\infty} \Psi_i^{\text{el}}(\mathbf{r}, \mathbf{R}) \chi_i^{\text{nucl}}(\mathbf{R}). \tag{7.2}$$

Inserting the last equation into the Schrödinger equation, multiplication of both sides by Ψ_i^{el}, and integration over electronic coordinates $\mathbf{R}$ only, leads to

$$\sum_{ij} \left(\hat{\text{K}}_{\text{nucl}} \delta_{ij} + \text{E}_{\text{el},j}(\mathbf{R}) \delta_{ij} - \hat{\Lambda}_{ji}(\mathbf{R}) \right) \chi_j^{\text{nucl}}(\mathbf{R}) = E \chi_i^{\text{nucl}}(\mathbf{R}), \tag{7.3}$$

for $j = 1, 2, \ldots, N$, where the *non-adiabatic coupling* operator $\hat{\Lambda}_{ji}$ is

$$\hat{\Lambda}_{ji} = \sum_{\alpha=1}^{N} \left(2 \left\langle \Psi_j^{\mathrm{el}} \right| \nabla_\alpha \left| \Psi_i^{\mathrm{el}} \right\rangle \nabla_\alpha + \left\langle \Psi_j^{\mathrm{el}} \right| \nabla_\alpha^2 \left| \Psi_i^{\mathrm{el}} \right\rangle \right), \qquad (7.4)$$

in which we dropped the coordinate $\mathbf{R}$ for the sake of clarity. Last equation describes a system of differential equations (one equation for each value of j), and once the system is solved and a set of functions χ_i^{nucl} is obtained, one could write down the exact solution of the Schrödinger equation.

The task to solve the Eq. (7.3) equation system is almost impossible. Equations in the system are coupled in a sense that the solution of any i-th equation, enters all other equations via the coupling operator. One way to decouple the equations in the system is assuming that $\hat{\Lambda}_{ji} = 0$ either for all $i \neq j$, or for all i without any exception. This is equivalent to the Born-Oppenheimer approximation presented in Section 2.3. If we equate with zero only all the off-diagonal ($i \neq j$) elements of $\hat{\Lambda}_{ji}$, one falls in the so-called *adiabatic approximation*. Often Λ_{ji} is very small but not zero. In these cases the adiabatic approximation and the Born-Oppehnheimer approximation are used interchangeably.

This approximation is labelled as "adiabatic" because when solving the electronic Schrödinger equation for different fixed nuclear configurations by continuously varying the nuclear coordinates, one assumes that the electronic state of the system continues to be the same. Namely, one presumes that nuclei "stay" on the same potential energy surface (PES). This scenario is reasonable only when PESs for different electronic states are well separated. It is easy to understand that the adiabatic approximation is inadequate in the regions of nuclear coordinates where PESs come close to or even cross each other. If there is some coupling, the nuclei might "jump" from one PES to the other. For all the cases when the off-diagonal terms cannot be neglected introduce the so-called non-adiabatic effects. The problem is that these non-diagonal terms are hard to calculate. A possible solution could be introducing the diabatic states. A diabatic transformation of the adiabatic states replaces these off-diagonal kinetic energy terms with potential energy terms. The main idea is to choose a basis for the wavefunctions in which the derivatives of the electronic wavefunctions with respect to the nuclear coordinates vanish. The concept of diabatization should not be limited to the Born-Oppeheimer approximation failure with respect to the nuclear coordinates only. Within the context of a system that can undergo electron, hole or energy transfer in an environment, another definition is that the diabatic states are the initial and final states of the system before or after the transfer process. In fact, as

we have already seen in the previous discussions, states of the system depend on the environment, in particular, when the environment is polarizable. A realistic scenario is that the adiabatic states of the isolated system will not be the relevant stationary states of the solvated system, and they do not describe the system before or after the transfer event.

In general, going beyond the Born-Oppenheimer approximation, one can use a truncated expansion of the total wave function Eq. (7.2). One then has the freedom to unitarily transform the electronic wave function without affecting the expansion

$$\psi_i^{\text{el}} \rightarrow \phi_i^{\text{el}} = \sum_j \psi_i^{\text{el}} U_{ji}. \tag{7.5}$$

In particular, one can attempt to find a transformation matrix, $U(\mathbf{R})$, that eliminates the non-adiabatic couplings at the cost of introducing couplings by the off-diagonal diabatic potentials. This concept is called diabatization, and $\{\phi_i^{\text{el}}\}$ are diabatic states.

In ab initio calculations, one directly obtains the adiabatic wave functions as eigenstates of the electronic Hamiltonian. These adiabatic electronic wave functions may have appreciable or even singular—nonadiabatic couplings for different nuclear configuration, rendering them unsuitable for subsequent dynamical calculations. Finding the trasformation U helps as a remedy for this problem. The process of finding the transformation is often called diabatization.

7.2 Methodology

In this work, we applied the Many-Body Green's Functions Theory in the *GW* approximation with the BSE for the calculations of electronic excitations in a polarizable embedding. These concepts have been already discussed in this thesis work, respectively in Section 3.4, Section 3.5, Section 3.6 and for the sake of brevity they are not illustrated again in this section. Regarding the technical implementation of the aforementioned methods, the reader can read through Section 4.2.

Diabatization methods, on the other hand, have never been discussed before, and they are the main topic of this section.

7.2.1 Diabatization Methods

Electronic states obtained from as eigenstates of some (approximate) Hamiltonian are adiabatic states $|\Phi_i\rangle$, such as the excitations χ_S obtained from the BSE as introduced in Section 3.5 and Section 4.2. Corresponding diabatic states $\left|\Phi_a^{\text{diabatic}}\right\rangle$,

needed for the evaluation and understanding of electron transfer processes, can be found via a unitary transformation

$$\left|\Phi_a^{\text{diabatic}}\right\rangle = \sum_{j=1}^{N_{\text{states}}} U_{aj} \left|\Phi_j\right\rangle. \tag{7.6}$$

The unitary transformation matrix $\underline{\mathbf{U}}$ is determined by extermalizing some function $f(\underline{\mathbf{U}})$, and various methods differ by the definition of this function, with some choices being discussed below. With this, the adiabatic form of the electronic Hamiltonian H_{el} with adiabatic energies ε_i, i.e., $\langle\Phi_i|\,H_{\text{el}}\,|\Phi_j\rangle = \varepsilon_j\delta_{ij}$ is transformed into the diabatic form

$$H_{ab}^{\text{diabatic}} = \left\langle\Phi_a^{\text{diabatic}}\right|H_{\text{el}}\left|\Phi_b^{\text{diabatic}}\right\rangle = \sum_{ij} U_{ia}\left\langle\Phi_i\right|H_{\text{el}}\left|\Phi_j\right\rangle U_{bj}. \tag{7.7}$$

For the two-state problem ($N_{\text{states}} = 2$), the transformation can be written explicitly as a rotation

$$\underline{\mathbf{U}} = \begin{pmatrix} U_{11} & U_{12} \\ U_{21} & U_{22} \end{pmatrix} = \begin{pmatrix} \cos\theta & -\sin\theta \\ \sin\theta & \cos\theta \end{pmatrix}. \tag{7.8}$$

and the diabatic Hamiltonian as

$$\underline{\mathbf{H}}^{\text{diabatic}} = \begin{pmatrix} \cos\theta & \sin\theta \\ -\sin\theta & \cos\theta \end{pmatrix} \begin{pmatrix} \varepsilon_1 & 0 \\ 0 & \varepsilon_2 \end{pmatrix} \begin{pmatrix} \cos\theta & -\sin\theta \\ \sin\theta & \cos\theta \end{pmatrix}. \tag{7.9}$$

Its off-diagonal elements

$$J_{ab}^{\text{ER}} = \frac{1}{2}\sin(2\theta)(\varepsilon_2 - \varepsilon_1) \tag{7.10}$$

are then the non-adiabatic couplings between the two diabtic states.

Edmiston-Ruedenberg Diabatization

In the Edmiston-Ruedenberg (ER) localized diabatization formalism [268], the objective is the maximization of the self-repulsion of the diabats via

$$f_{\text{ER}}(U) = \sum_{i,j,k,l,m} U_{ji}U_{ki}U_{li}U_{mi}R_{jklm}. \tag{7.11}$$

Here, the tensor R_{jklm} is defined in basis of molecular orbitals as

$$R_{jklm} = \sum_{vcv'c'} D_{vc}^{jk}(vc|v'c')D_{v'c'}^{lm}.$$

(7.12)

with

$$(vc|v'c') = \iint \frac{\phi_v(\mathbf{r})\phi_c(\mathbf{r})\phi_{v'}(\mathbf{r}')\phi_{c'}(\mathbf{r}')}{|\mathbf{r} - \mathbf{r}'|} d\mathbf{r}\, d\mathbf{r}',$$

(7.13)

where the indices v, v' and c, c' spanning the occupied and unoccupied levels, respectively. In Eq. 7.12, $\underline{\mathbf{D}}^{jk}$ is the excited state transition density matrix between the excited states j and k. If the $\phi_n(\mathbf{r})$ are expressed in an atomic orbital basis $\{\chi_\alpha(\mathbf{r})\}$ according to $\phi_n(\mathbf{r}) = \sum_\alpha d_\alpha^n \chi_\alpha(\mathbf{r})$, Eq. (7.12) can be rewritten as

$$R_{jklm} = \sum_{\alpha\beta\gamma\delta} D_{\alpha\beta}^{jk}(\alpha\,\beta|\gamma\,\delta)D_{\gamma\delta}^{lm}.$$

(7.14)

The tensor $(\alpha\,\beta|\gamma\,\delta)$ is part of the standard implementation of DFT-GW-BSE, in which the transition density matrix between states j and k in the atomic orbital basis reads

$$D_{\alpha\beta}^{jk} = D_{\alpha\beta}^0 \delta_{jk} + \sum_{cc'} d_\alpha^c M_{cc'}^{jk} d_\beta^{c'} - \sum_{vv'} d_\alpha^v M_{vv'}^{jk}, d_\beta^{v'}$$

(7.15)

where

$$M_{cc'}^{jk} = \sum_v \left(A_{vc}^j A_{vc'}^k - B_{vc}^j B_{vc'}^k \right)$$

(7.16)

and

$$M_{vv'}^{jk} = \sum_c \left(A_{vc}^j A_{v'c}^k - B_{vc}^j B_{v'c}^k \right).$$

(7.17)

With these definitions, Eq. (7.14) can be computed and the ER functional can be maximized. For the two-state case, there is a closed form for this maximizing angle [269]. It is computed with the help of

$$A_{12} = R_{1212} - \frac{1}{4}\left(R_{1111} + R_{2222} - 2\,R_{1122}\right)$$

(7.18)

$$B_{12} = R_{1112} - R_{2212}$$

(7.19)

as

$$\cos(4\theta) = -\frac{A_{12}}{\sqrt{A_{12}^2 + B_{12}^2}}.$$

(7.20)

Generalized Mulliken–Hush Diabatization

In the Generalized Mulliken–Hush (GMH) approach to diabatization [270, 271], the adabatic-to-diabatic transformation is based on the defition of the diabatic states as eigenstates of the dipole moment. Specifically in a two-state model, the method requires the calculation of the dipole moment of each adiabatic state $\boldsymbol{\mu}_1$ and $\boldsymbol{\mu}_1$, and the transition dipole moment between the two, $\boldsymbol{\mu}_{12}$. The non-adabatic coupling element is then calculated as

$$J_{ab}^{\mathrm{GMH}} = \frac{|\hat{\mu}_{12}|(\varepsilon_2 - \varepsilon_1)}{((\boldsymbol{\mu}_1 - \boldsymbol{\mu}_2)^2 + 4\hat{\mu}_{12}^2)^{1/2}}, \tag{7.21}$$

where $\hat{\mu}_{12}$ is the projection of $\boldsymbol{\mu}_{12}$ on the charge transfer direction $(\boldsymbol{\mu}_1 - \boldsymbol{\mu}_2)/|\boldsymbol{\mu}_1 - \boldsymbol{\mu}_2|$.

Fragment Charge Difference Diabatization

Another alternative is to determine the diabatic states as eigenstates of the so-called fragment charge difference (FCD) matrix [272], based on the definition of donor (D) and acceptor (A) fragments, as $\Delta Q_{ij} = Q_{ij}(D) - Q_{ij}(A)$. The fragment charges are typically obtained from a population analysis of the individual adiabatic densities and the transition density between them. Again, for a two-state model, the coupling is given by

$$J_{ab}^{\mathrm{FCD}} = \frac{|\Delta Q_{12}|(\varepsilon_2 - \varepsilon_1)}{((\Delta Q_{11} - \Delta Q_{22})^2 + 4\Delta Q_{12}^2)^{1/2}}. \tag{7.22}$$

7.3 Results

7.3.1 Naphthalene-TCNE complex

Stacked geometries of naphthalene and TCNE with different intermolecular distances are taken from Ref. [273]. Ground state calculations on KS-DFT level are performed with the ORCA [245] package using both the PBE0 functional [274] and the def2-tzvp basis [275] together with optimized auxiliary basis sets [276] in resolution-of-identity techniques to efficiently express terms involving four-center Coulomb integrals. We compare in the following the results based on G_0W_0 calculations and eigenvalue selfconsistent evGW calculations. The convergence limit for the self-consistent GW-cycles in the evGW scheme was set to 10^{-5} Hartree
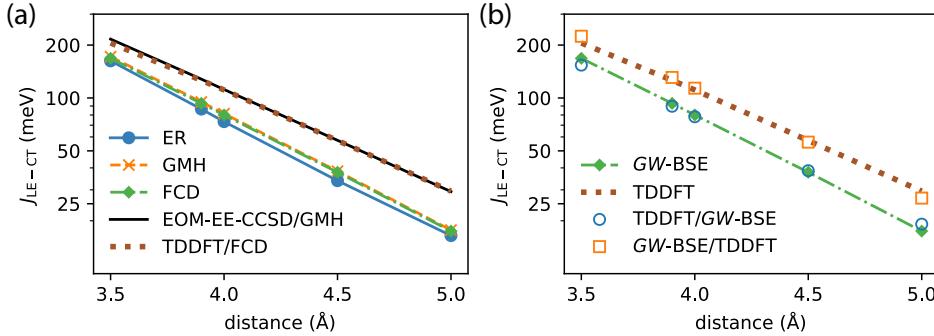
Figure 7.4: Distance dependence of LE-CT coupling elements in the naphthalene-TCNE complex. (a) GW-BSE results with the ER, GMH, and FCD diabatization methods based on full BSE solutions following evGW calculations with FAA frequency integration, employing the def-tzvp basis and PBE0 functional in the ground state DFT run. Reference results on EOM-EE-CCSD and TDDFT levels are taken from Ref. [273]. (b) Pure GW-BSE and TDDFT results based on FCD as in (a) compared to mixed methods, in which the fragment charge factor is taken from TDDFT and the energy difference from GW-BSE (TDDFT/GW-BSE) and vice-versa, showing that the difference between between the pure GW-BSE and TDDFT results originate from the different predicted energies.

(0.27 meV). Quasiparticle corrections are determined for the 197 lowest energy orbitals, and the product basis for the electron-hole wavefunctions are formed from the 66 occupied and 131 lowest unoccupied orbitals. All orbitals are included in the RPA step for calculating the dielectric function, i.e., 320 orbitals for def2-svp, 668 for def2-tzvp, and 1380 for def2-qzvp, respectively. Both, the fully analytic approach (FAA) and a generalized plasmon-pole model as introduced in Section 4.2.3 as used for the frequency integration of the self-energy. The obtained excitation energies for all variants are summarized in Tab. 7.1.

In Fig. 7.4(a), we show the distance-dependent LE-CT couplings as resulting from evGW-BSE calculations with the FAA, the def2-tzvp basis set, and PBE0 in the ground state calculation. We first compare the influence of the choice of diabatization method, with the couplings obtained from ER shown as circles, from GMH as

Table 7.1: Distance-dependence of the low-energy LE and CT excitation energies (in eV) in a naphthalene-TCNE complex, based on different variants of GW-BSE using the def2-tzvp basis set and the PBE0 functional in the DFT ground state calculation.

| | FAA | | | | PPM | | | |
| | evGW | | G_0W_0 | | evGW | | G_0W_0 | |
	full	TDA	full	TDA	full	TDA	full	TDA
LE energy								
3.5 Å	4.309	4.341	3.998	4.022	4.255	4.262	4.006	4.035
3.9 Å	4.306	4.340	4.000	4.024	4.266	4.306	4.007	4.037
4.0 Å	4.306	4.339	4.000	4.024	4.264	4.305	4.006	4.036
4.5 Å	4.305	4.339	3.997	4.022	4.262	4.303	4.003	4.033
5.0 Å	4.300	4.333	3.995	4.020	4.257	4.299	4.000	4.030
CT energy								
3.5 Å	2.214	2.220	1.875	1.880	2.255	2.261	1.976	1.982
3.9 Å	2.387	2.389	2.052	2.054	2.430	2.432	2.157	2.159
4.0 Å	2.424	2.426	2.090	2.092	2.467	2.469	2.195	2.197
4.5 Å	2.589	2.590	2.255	2.255	2.632	2.632	2.360	2.361
5.0 Å	2.727	2.727	2.396	2.396	2.770	2.770	2.501	2.501
LE-CT difference								
3.5 Å	2.095	2.121	2.123	2.141	2.000	2.001	2.030	2.053
3.9 Å	1.920	1.951	1.948	1.970	1.836	1.874	1.850	1.878
4.0 Å	1.881	1.913	1.909	1.932	1.797	1.836	1.811	1.839
4.5 Å	1.716	1.749	1.743	1.767	1.630	1.670	1.642	1.673
5.0 Å	1.572	1.606	1.599	1.623	1.488	1.529	1.499	1.529

crosses, and FCD as diamonds, respectively. While both GMH and FCD methods appear to yield very similar couplings with a maximum deviation of $4\,\mathrm{meV}$ at a separation of $3.5\,\text{Å}$ (see also Tab. 7.2), the $J_{\text{LE-CT}}^{\text{ER}}$ result slightly lower, e.g., by $9\,\mathrm{meV}$ at the closest distance. Note that the respective slopes of the three GW-BSE based data are identical, reflecting the same exponential decay of the LE-CT coupling with distance. Comparing our results to those obtained by EOM-EE-CCSD/GMH and TDDFT/FCD with the ωB97X-D [277] functional [273] shown in Fig. 7.4(a) as solid and dashed lines, respectively, we observe a combination of an offset to lower energies and a slightly stronger slope in GW-BSE. For instance, at the optimal intermolecular distance of $3.9\,\text{Å}$, EOM-EE-CSSD/GMH predicts a LE-CT coupling of $128\,\mathrm{meV}$, TDDFT/FCD $126\,\mathrm{meV}$, compared to $86\,\mathrm{meV}$ from ER, $95\,\mathrm{meV}$ from GMH, and $93\,\mathrm{meV}$ from FCD with GW-BSE. To understand this difference, we take a closer look at the results obtained with FCD diabatization in Fig. 7.4(b). The GW-BSE and TDDFT results are from Fig. 7.4(a) are shown again, now combined with "mixed" versions. In these versions, we first distinguish in the expression for $J_{\text{LE-CT}}^{\text{FCD}}$ between the fragment charge contribution $f_{\text{FCD}} = J_{\text{LE-CT}}^{\text{FCD}}/(\varepsilon_2 - \varepsilon_1)$ and the energy contribution $f_\varepsilon = (\varepsilon_2 - \varepsilon_1)$. Then we combine $f_{\text{FCD}}(\text{TDDFT})$ with $f_\varepsilon(GW\text{-BSE})$ (TDDFT/GW-BSE) and vice versa (GW-BSE/TDDFT). For the former, we find that the resulting couplings are essentially identical to the ones from pure GW-BSE, while the latter results are in close agreement with the full pure TDDFT data. This corroborates the notion that the difference between the pure TDDFT and GW-BSE derived couplings can to a large extend be attributed to differences in the energies. From Tab. 7.1, the LE-CT energy difference at the optimal naphthalene TCNE distance is $1.92\,\mathrm{eV}$ in GW-BSE and $2.70\,\mathrm{eV}$ in TDDFT [273], and their ratio almost exactly translates into the ratio of the respective coupling elements.

Table 7.2 also contains LE-CT couplings as obtained from different variants of GW-BSE, in which we have changed the exact frequency integration in Eq. (4.18) with a PPM, the level of GW from evGW to G_0W_0, and/or the BSE from its full form to the TDA. Overall, the $J_{\text{LE-CT}}$ are not very sensitive to the specific choices in the GW and BSE steps. For the sake of clarity, we will focus on the results from ER diabatization at the optimal separation of $3.9\,\text{Å}$ in the following. First, the use of the TDA of the BSE impacts the couplings by only $1\,\mathrm{meV}$, also the use of the one-shot G_0W_0 method instead on evGW does not show differences exceeding $3\,\mathrm{meV}$. Even the use of the PPM in place of the exact frequency integration (FAA) is of the same order, so that all values are within $3\,\%$ of the FAA/evGW/full BSE result. Similar observations also hold for the other intermolecular distances and diabatization techniques.

Table 7.2: LE-CT coupling elements (in meV) in the naphthalene-TCNE complex at several intermolecular distances, as obatined using ER, GMH, and FCD diabatization with different variants of GW-BSE using the def2-tzvp basis set and the PBE0 functional in the DFT ground state calculation.

	FAA				PPM			
	evGW		G_0W_0		evGW		G_0W_0	
	full	TDA	full	TDA	full	TDA	full	TDA
ER diabatization								
3.5 Å	163	165	158	161	161	163	155	155
3.9 Å	86	87	84	85	88	89	86	86
4.0 Å	73	74	71	72	75	76	73	73
4.5 Å	34	34	33	33	35	35	34	34
5.0 Å	16	17	16	17	17	18	17	17
GMH diabatization								
3.5 Å	172	172	169	169	169	169	165	165
3.9 Å	95	95	93	94	93	93	92	92
4.0 Å	81	81	80	80	80	80	79	79
4.5 Å	38	38	38	38	38	38	37	37
5.0 Å	18	18	18	18	17	17	17	17
FCD diabatization								
3.5 Å	168	168	165	166	165	165	161	162
3.9 Å	93	93	92	92	92	92	90	90
4.0 Å	80	80	79	80	79	79	77	77
4.5 Å	38	38	37	37	37	37	37	37
5.0 Å	17	17	17	17	17	17	17	17

7.3.2 Rubrene-fullerene low-donor content system

We now move from the well-ordered, small molecule naphthalene-TCNE dimer to a disordered cluster of larger molecules and investigate the sensitivity of LE-CT coupling elements based on GW-BSE on the different diabatization methods and if eventual differences propagate to different answers in dynamic models of conversion between LE and CT states. Specifically, we study an amorphous morphology with low-donor content ($< 10\,\text{mol}\%$), composed of fullerene (C_{60}) and 5,6,11,12-tetraphenyltetracene (rubrene) [278]. Because of the low-donor content, a C_{60} cluster will surround the donor molecule, making the interaction between the single donor molecule with a close shell of neighboring C_{60} acceptors representative of the properties of the system as a whole. These complexes are therefore meaningful candidates for a computational analysis of the influence of donor-acceptor conformations and environment polarization effects in the GW-BSE/MM framework introduced in Sec. 3.6 and its consequence on the conversion dynamics between initially excited LE on rubrene (LE_R) to CT excitations.

CT density of states

To obtain representative structures, mixed morphologies have been simulated with ab-initio MD based on Density Functional Tight Binding theory using linear scaling self-consistent field calculations within the CP2K code [279]. Initial configurations have been prepared using Packmol [280], targeting experimental values [278] for densities and mole percentages. This structure is first equilibrated at $700\,\text{K}$ in NpT (with velocity rescaling thermostat [281] at atmospheric pressure [282]) for $7\,\text{ps}$ (time step $1\,\text{fs}$), then annealed to $300\,\text{K}$ within $10\,\text{ps}$. A final NpT equilibration followed for $5\,\text{ps}$.

For calculating the LE and CT densities of states, C_{60} molecules are selected which are approximately in the first neighbor shell around one rubrene molecule. Given the conformation of this low-donor content materials, the behavior of this shell of molecules should be representative of the overall behavior of the material. After selection, polarizable GW-BSE/MM embedding calculations as described in Section 3.6 are performed for all dimers formed by rubrene and fullerene. Specifically, we employ for the GW-BSE calculations the def2-tzvp basis set [275] with an optimized auxiliary basis [276] for the steps including resolution-of-identity. The ground-state DFT calculation uses the PBE0 functional [274]. Eigenvalue self-consistent GW (evGW) calculations are performed to obtain the explicit quasiparticle-corrected energies for the highest 100 occupied and lowest 100 unoccupied orbitals, respectively. All orbitals are included in the RPA step and

not explicitly *GW* corrected levels are scissors shifted according to the highest absolute quasiparticle correction among the explicitly corrected occupied or unoccupied orbitals, respectively. The frequency integration in Eq. (4.18) is performed using the PPM. Coupled electron-hole wavefunctions according to Eq. (3.68) are constructed using transitions between the highest 220 occupied and 220 lowest unoccupied states. In the MM part of the *GW*-BSE/MM, polarizable electrostatic interactions are taken into account within a cutoff of 4 nm. The resulting energies
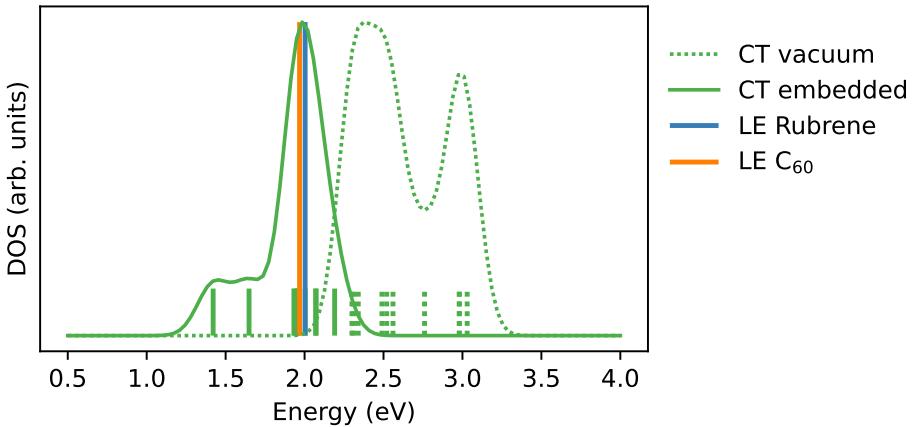
Figure 7.5: Energies of CT excitations (green vertical bars) from vacuum *GW*-BSE (dashed) and *GW*-BSE/MM calculations with polarizable embedding (solid). Solid and dashed curves indicate respective density-of-states obtained by Gaussian broadening with 0.1 eV as a guide-to-the-eye. Blue and orange lines highlight the *GW*-BSE/MM energies of LEs on rubrene and C_{60}, respectively.

of CT and LE excitations are depicted in Fig. 7.5. In general, the effects of polarizable embedding on the LE energies are small, as has been observed before, e.g., for embedded push-pull polymers [210] or small-molecule donor molecules [283]. Therefore, we only show the *GW*-BSE/MM results for the respective LEs, indicated by the blue (rubrene at 2.01 eV) and orange (C_{60} at 1.97 eV) vertical lines as there is no noticeable disorder. For the CT excitations, the *GW*-BSE calculations in vacuum already reveal significant energetic disorder, originating from
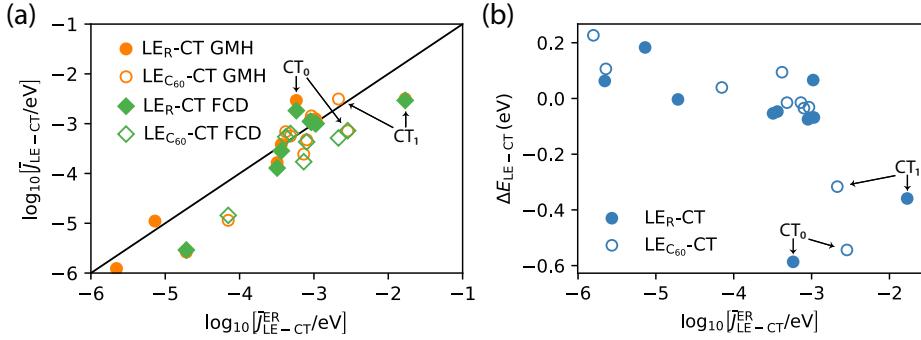
Figure 7.6: (a) Effective LE-CT couplings (see Eq. (7.23)) in the rubrene-C_{60} dimers resulting from polarizable GW-BSE/MM calculations with the GMH and FCD diabatization schemes against those from ER. (b) Relation between LE-CT energy difference $\Delta E_{\text{LE-CT}} = \Omega_{\text{CT}} - \Omega_{\text{LE}}$ and the LE-CT coupling from GW-BSE ER diabatization.

the different rubrene-C_{60} conformations and the long-range electrostatic interaction between electron and hole. Individual CT excitation energies are marked by the short green vertical lines in Fig. 7.5, where we also show a density-of-states obtained by broadening with a Gaussian function of width $0.1\,\text{eV}$. After polarizable embedding in GW-BSE/MM the CT energies (solid green lines) are shifted to lower energies, with energetic stabilization of up to $1\,\text{eV}$. Note that in vacuum, the CT excitation energies result generally higher than both LEs, which would make a conversion process of a LE on rubrene to a CT state energetically unlikely. After embedding, we find that the energetic stabilization brings several high-energy CTs close to the LEs, and some notably very much lower at $1.65\,\text{eV}$ (CT_1)and $1.42\,\text{eV}$ (CT_0), respectively. The latter compares favorably with the experimentally measured CT energy of $1.46\,\text{eV}$ reported in Ref.[278]. However, given the disorder in the CT excitation energies, it is unclear if the measurement truly probes simply the lowest-energy CT state, or one that is preferably dynamically populated during the timescale of the conversion process and the experiment.

Non-adiabatic LE-CT couplings

To proceed beyond considering only the energy difference for the conversion of LE
to CT excitons, we consider the LE-CT couplings and analyze if the disorder in
them could be indicative of some dimers not participating in the process. We also
investigate if for such large bi-molecular structures, the use of GMH, FCD, and
ER diabatization has any influence on the results.

A specific aspect of the rubrene-C_{60} systems that requires extra is the (near)
degeneracy of the 15 lowest LE on C_{60}, stemming from the 5-fold degeneracy of
its HOMO and 3-fold degeneracy of its LUMO. For the same reason, also the
CT states are 3-fold near degenerate. We take this into account by calculating
an *effective* diabatic coupling [284, 285] between N_{LE}-fold degenerate LEs and
N_{CT}-fold degenerate CT excitons as

$$\bar{J}_{LE_x-CT} = \sqrt{\frac{\sum_{m=1}^{N_{LE}} \sum_{n=1}^{N_{CT}} J^2_{LE_{x,m}-CT_m}}{N_{LE} \cdot N_{CT}}}, \tag{7.23}$$

with $J_{LE_{x,m}-CT_n}$ the coupling element between the m-th degenerate LE and the n-
th degenerate CT. The results from the different diabatization methods are shown
in Fig. 7.6(a). There, we plot the couplings obtained with GMH and FCD diabat-
ization against those from ER, and distinguish between LE_R-CT (filled symbols)
and $LE_{C_{60}}$-CT (open symbols) couplings. Roughly speaking, the effective coup-
lings from ER cover a range from 0.02 meV to 17 meV, with many occurring close
to 1 meV. Compared to the small-molecule naphthalene-TCNE dimer with ideal
stacking, we find a stronger dependence on the diabatization method, although
the differences between GMH and FCD seem minor in most cases. Of particu-
lar interest are the couplings of the two low-energy CT states, CT_0 and CT_1, as
marked in Fig. 7.6(a). Specifically, the LE_R-CT couplings are different using ER
(0.6 meV vs. 17 meV), while similar when using GMH at about 3 meV. As the ER
method takes the full details of the electronic (transition) densities into account,
it stands to reason that the extra details have a bigger contribution to the LE-CT
couplings for more disordered structures and larger molecular building blocks.

In Fig. 7.6(b) we show the relation between the energy offset of LE and CT states,
calculated as $\Delta E_{LE-CT} = \Omega_{CT} - \Omega_{LE}$, and the LE-CT couplings obtained with ER.
From Eq. (7.10) one generally expects some dependence of the couplings on the
energy difference. Some dependence is visible in Fig. 7.6(b), although it is hard
to ascribe a definite trend to the data. Noteworthy is that the two dimers with
the most negative energy offsets corresponding to the two low energy CT states
discussed in Section 7.3.2. In particular, CT_1 at energy 1.65 eV is found to have

the highest coupling between the rubrene LE and the CT state. In comparison, the coupling to the lowest CT state, CT_0, is smaller by a factor of 30. This raises the question what impact the differences in couplings have for the LE-CT conversion dynamics, particularly which of the CT states is most likely to be probed over which timescale.

Kinetic Model

To scrutinize the effects of the disorder in energies and LE-CT couplings obtained from the GW-BSE/MM calculations in Sections 7.3.2 and 7.3.2 and the influence of different diabatization methods, we now study the conversion dynamics between LE and CT excitations with a kinetic model based on Marcus rates as in Eq. (7.1). This model requires in addition to the calculation of the LE-CT couplings and the excitation energies Ω also the determination of the respective reorganization energies λ_{ab}. Within the Marcus picture, $\lambda_{\mathrm{LE_x-CT}} = E_{\mathrm{CT}}(\mathrm{LE_x}) - E_{\mathrm{CT}}(\mathrm{CT})$ and $\lambda_{\mathrm{CT-LE_x}} = E_{\mathrm{LE_x}}(\mathrm{CT}) - E_{\mathrm{LE_x}}(\mathrm{LE_x})$, where $x = \mathrm{R,C_{60}}$ and $E_a(G)$ represents the total energy of state a at geometry of state G. As such, this would require the cumbersome optimization of the dimer structures in the respective CT and LR states. Instead, we approximate the energies from monomer calculations, such that

$$E_{\mathrm{CT}}(\mathrm{LE_R}) = E_R^+(R^*) + E_{\mathrm{C_{60}}}^-(\mathrm{C_{60}^0}) \tag{7.24}$$

$$E_{\mathrm{CT}}(\mathrm{LE_{C_{60}}}) = E_R^+(R^0) + E_{\mathrm{C_{60}}}^-(\mathrm{C_{60}^*}) \tag{7.25}$$

$$E_{\mathrm{LE_R}}(\mathrm{CT}) = E_R^*(R^+) + E_{\mathrm{C_{60}}}^0(\mathrm{C_{60}^-}) \tag{7.26}$$

$$E_{\mathrm{LE_{C_{60}}}}(\mathrm{CT}) = E_R^0(R^+) + E_{\mathrm{C_{60}}}^*(\mathrm{C_{60}^-}) \tag{7.27}$$

$$E_{\mathrm{CT}}(\mathrm{CT}) = E_R^+(R^+) + E_{\mathrm{C_{60}}}^-(\mathrm{C_{60}^-}) \tag{7.28}$$

$$E_{\mathrm{LE_R}}(\mathrm{LE_R}) = E_R^*(R^*) + E_{\mathrm{C_{60}}}^0(\mathrm{C_{60}^0}) \tag{7.29}$$

$$E_{\mathrm{LE_{C_{60}}}}(\mathrm{LE_{C_{60}}}) = E_R^0(R^0) + E_{\mathrm{C_{60}}}^*(\mathrm{C_{60}^*}), \tag{7.30}$$

where the superscripts refer to the state of the monomers (0: ground state, +: cation, −: anion, ∗: excited). The total energy calculations and geometry optimizations in this step are performed using (time-dependent) DFT with the same basis set and functional as the GW-BSE calculations in Section 7.3.2, and we obtain $\lambda_{\mathrm{LE_R-CT}} = 0.12\,\mathrm{eV}$, $\lambda_{\mathrm{CT-LE_R}} = 0.12\,\mathrm{eV}$, $\lambda_{\mathrm{LE_{C_{60}}-CT}} = 0.18\,\mathrm{eV}$, and $\lambda_{\mathrm{CT-LE_{C_{60}}}} = 0.21\,\mathrm{eV}$, respectively. In similar spirit, we determine the vertical to adiabatic energy relaxations of the excited states, $\Lambda_a = E_a(0) - E_a(A)$, as $\Lambda_{\mathrm{CT}} = 0.15\,\mathrm{eV}$, $\Lambda_{\mathrm{LE_R}} = 0.16\,\mathrm{eV}$, and $\Lambda_{\mathrm{LE_{C_{60}}}} = 0.23\,\mathrm{eV}$.
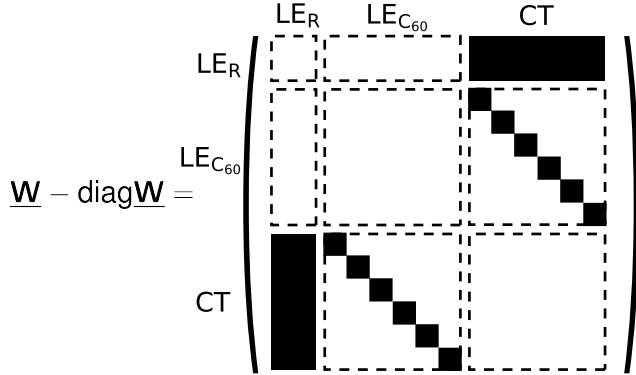
Figure 7.7: Schematic representation of the rate matrix of a kinetic model, with full squares indicating where the respective rates with LE-CT couplings occur.

With all energies and coupling elements at hand, we determine all rates between LE and CT states according to Eq. (7.1) at $T = 300\,\mathrm{K}$ for the kinetic model, which describes the time-evolution of the state population probabilities $\mathbf{P}(t)$ via a system of ordinary differential equations of the kind

$$\frac{d}{dt}\mathbf{P}(t) = \underline{\mathbf{W}}\mathbf{P}(t).$$

(7.31)

In this specific case, $\mathbf{P}^T(t) = [P_{\mathrm{LE_R}}(t), \mathbf{P}^T_{\mathrm{LE_{C_{60}}}}(t), \mathbf{P}^T_{\mathrm{CT}}(t)]$ is of dimension 21, and $\sum_i P_i(t) = 1$ for all t. The structure of the off-diagonal entries of the matrix $\underline{\mathbf{W}}$ is shown in Fig. 7.7, emphasizing again that in this minimal model, we only consider transitions between LE and CT states, not between different LE, and different CTs. The diagonals of $\underline{\mathbf{W}}$ contain the negative of the sum of all other column entries, i.e., $W_{ii} = -\sum_j W_{ji}$.

We initially prepare the system in the $\mathrm{LE_R}$ state, i.e., $\mathbf{P}^T(t = 0) = [1, 0, \ldots, 0]$ and numerically study the evolution of Eq. (7.31) for $t_{\mathrm{max}} = 1\,\mu\mathrm{s}$ using the backward Euler scheme [286] with 10^5 steps. In Fig. 7.8(a), we show the resulting population probabilities with the LE-CT couplings calculated using ER diabatization. Initially, the population of the $\mathrm{LE_R}$ state decays rapidly and it is completely depopulated within 50 ps. This initial decay occurs primarily into three CT states, with a clear preference for the $\mathrm{CT_1}$ state. After 50 ps the two additionally popu-
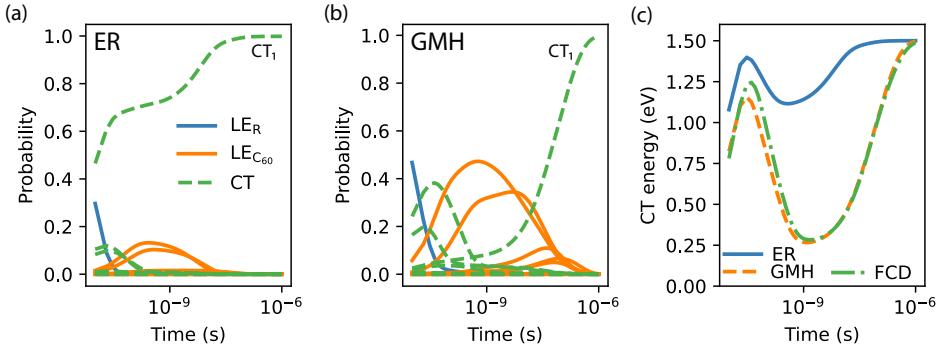
Figure 7.8: (a) Population dynamics of the excited states for $t_{\max} = 1\,\mu s$ as a solution to Eq. (7.31) for LE-CT couplings from ER diabatization. The blue line indicates the population of the $\mathrm{LE_R}$ excited state, orange lines the ones of the respective $\mathrm{LE_{C_{60}}}$, and green dashed lines populations of CT states, respectively. (b) Same for GMH diabatization. (c) Time evolution of the expected CT energy $\langle \Omega_{\mathrm{CT}} \rangle$ from population probabilities based on models with different diabatization methods.

lated CT states convert first into $\mathrm{LE_{C_{60}}}$ as intermediates in the timescale of $100\,[\mathrm{ps}]$ to $10\,\mathrm{ns}$, until they also decay nearly exclusively into $\mathrm{CT_1}$. Note that we do not observe over the timescale of $1\,\mu s$ a noticeable population of the lowest energy CT state, $\mathrm{CT_0}$. As can be seen from Fig. 7.8(b), there are some qualitative similarities when the dynamics are modeled based on GMH diabatization. In particular, the same rapid initial decay of $\mathrm{LE_R}$ and the final near complete population of $\mathrm{CT_1}$ can be seen. Some quantitative difference can be noted in the details of the interme- diate dynamics. Initially, $\mathrm{CT_1}$ does not get populated. Instead, the populations of the two other CT states is much higher and, consequently, also the populations of the two intermediate $\mathrm{LE_{C_{60}}}$ they convert into.

We also report in Fig. 7.8(c) the expectation value of the measured CT energy, calculated according to

$$\langle \Omega_{\mathrm{CT}}(t) \rangle = \sum_{n=1}^{10} P_{\mathrm{CT}_n}(t)\Omega_{\mathrm{CT}_n}, \tag{7.32}$$

for the three different diabatization methods considered in this work. As could

be expected from the individual populations over time, the expected CT energy follows similar trends. At about 50 ps, all methods exhibit a peak, whose height depends slightly on the method. Its energy of more than 1 eV is, however, a consequence of the low population of high energy (~ 2 eV) CT states, and not indicative of the population of either CT_0 or CT_1. The dip following the peak is a combined effect of the depopulation of the high-energy CT states to both CT_1 (in case of ER) and some $LE_{C_{60}}$. In the model based on GMH/FCD, the cumulative population of all CT states is minimal at $t = 1$ ns, leading to the pronounced reduction of the expected CT state energy. On the other hand, in the ER model, the CT_1 state is already populated at this time, but the combination of it being a low energy excitation and only partially populated (around 0.6) still leads to a smaller but noticeable minimum. Only on the timescale of 1 μs, when the CT_1 population is nearly 1, $\langle \Omega_{CT}(t) \rangle$ is indicative of a pure CT state. Interestingly, the value of $\langle \Omega_{CT}(t = 1\,\mu s) \rangle = 1.50$ eV is close to the CT energy reported in experiments (1.46 eV) [278], although we do not want to overstress this apparent agreement due to the limited nature of the model. Noteworthy in this context is also that in both cases (ER and GMH/FCD), no population of CT_0 is observed in the considered timescale. In thermal equilibrium ($t \to \infty$), one would expect the state occupation probabilities to be Boltzmann distributed according to

$$P_i^{\text{th}} = \frac{\exp(-\beta \Omega_i)}{\sum_{i=1}^{21} \exp(-\beta \Omega_i)}, \tag{7.33}$$

and as such, an almost complete population of CT_0. While out limited model appears to run into a different equilibrium with complete CT_1 occupation as in Fig. 7.8, this is misleading, as even in the model a conversion to CT_0 will happen on a much longer timescale. Note, however, that adding additional conversion pathways to the model is expected to reduce the time in which the system reaches thermal equilibrium, but doing so is beyond the scope of this work which focuses on the analysis of different diabatization methods with respect to the calculation of LE-CT couplings.

7.4 Conclusions

In summary, we have developed the determination of LE-CT coupling elements within the framework of GW-BSE. We have shown that in an ideal small-molecule dimer of naphthalene and TCNE, the quantitative estimates of these couplings are largely insensitive to methodological choices in the GW and BSE steps of the calculation, and only small differences are noted between the Edmiston–Ruedenberg,

Generalized Mulliken–Hush, and Fragment Charge Difference diabatization formalisms, respectively. Compared to literature results for this model system on TD-DFT level, we could show that the difference found in the GW-BSE-based calculations can be attributed to different predictions of the adiabatic dimer energies entering the diabatization procedure, and not differences in the densities of the excitations. In larger-scale, disordered molecular complexes, such as the low-donor content rubrene-fullerene mixtures, the LE-CT couplings are found to be more sensitive to the choice of the diabatization formalism. While the two more approximate Generalized Mulliken–Hush and Fragment Charge Difference approaches yield couplings that are largely in agreement with each other, they differ from respective results based on the Edmiston–Ruedenberg approach, which takes full details of the excited state densities into account. To scrutinize the effect of the different predictions both qualitatively and quantitatively, we have employed the respective LE-CT couplings in a minimal kinetic model of the conversion from LE to CT states based on Marcus rates. From the obtained time evolution of state population probabilities, it is apparent that the dynamics are affected on an intermediate timescale, but not the final steady state prediction.

Chapter 8

Conclusion

This thesis addressed various challenges in modeling electronic excitations in complex materials through three distinct and interconnected objectives. The first objective focused on methodological advancements, aiming to explore the feasibility of combining classical and quantum mechanics to gain comprehensive insights into the behavior of realistic materials. By developing a hybrid approach that integrated these two realms, the research enabled accurate modeling of both macroscopic properties (e.g., prediction of spectroscopy profiles) and molecular-detailed properties (e.g., energy spatial profile and diabatic coupling elements) under realistic conditions. This hybrid method allow for the definition of different regions that can be treated at different level of accuracy. This makes it, within a reasonable compuational cost, a valuable "input machines" for bigger scale modeling the macroscopic properties of materials and their response to external perturbations (mainly in Kinetic Monte Carlo simulations). To achieve this objective, the research utilized a hybrid approach, often referred as QM/MM, where the classical part (MM) was modeled using multipole expansions, and the quantum part was developed using GW-BSE (Green's function perturbation theory within the GW approximation and Bethe-Salpeter equation) to capture charged and neutral electronic excitations. The GW approximation is a perturbative method used to obtain a more accurate description of the electronic self-energy compared to traditional density functional theory (DFT) calculations. By considering the electron-electron interactions beyond DFT, GW captures the quasiparticle properties of the system, such as electron addition and removal energies, which are crucial for obtaining quantitative estimates of charged electronic excitations in materials. The

Bethe-Salpeter equation (BSE) on the other hand is a many-body perturbation theory used to calculate the electron-hole correlation responsible for optical excitations like excitons and charge-transfer states. BSE provides accurate excitation energies and wavefunctions, making it a suitable choice for studying neutral excited states. Multipole expansions are a powerful tool in classical mechanics for efficiently describing the electrostatic interactions in large-scale systems. In this approach, the charge distribution of atoms or molecules is represented by a series of multipole moments (e.g., monopole, dipole, quadrupole, etc.). The multipole expansion provides an accurate description of long-range electrostatic interactions while significantly reducing the computational cost compared to explicit treatment of each molecule's electronic structure. On the other hand, the quantum part of the hybrid approach employed the GW-BSE method, which offers a rigorous and accurate description of the electronic interactions at the atomic and molecular level.

The combination of classical embedding and GW-BSE in the hybrid approach offers several advantages:

- Accuracy and Efficiency:
  The GW-BSE method ensures accurate descriptions of electronic excitations at the quantum level, capturing both localized and delocalized excitations. In contrast, the multipole expansion efficiently handles the long-range electrostatic interactions, providing a balance between accuracy and computational cost.

- Large-Scale Systems:
  The classical part based on multipole expansions allows the simulation of large-scale systems, making it possible to study materials with a significant number of atoms or molecules, such as extended solids and molecular aggregates.

- Incorporation of Environment:
  The hybrid approach can naturally account for the influence of the surrounding environment on the electronic excitations, which is particularly important in the study of materials in realistic conditions (e.g., in solution or at interfaces).

- Study of Realistic Materials:
  By combining classical and quantum mechanics, the hybrid approach enables the investigation of realistic materials under experimentally relevant conditions, providing valuable insights into their properties and behavior.

By harnessing the strengths of classical embedding and GW-BSE, the hybrid approach developed in this thesis offers a powerful framework to accurately capture both macroscopic and microscopic properties of materials, advancing the understanding of electronic excitations and their role in determining material behavior. The second objective of this thesis focused on addressing localized and delocalized bi-molecular electronic excitations in specific materials to test and validate computational techniques. In recent years, computational experiments have become increasingly important in bridging the gap between theoretical predictions and experimental observations. These computational experiments allow researchers to gain deeper insights into the behavior of materials and provide valuable guidance for experimental investigations.

For the specific material, MADN the research successfully reproduced the HOMO (Highest Occupied Molecular Orbital) peak in the Ultraviolet Photoelectron Spectroscopy (UPS) spectrum by breaking down the photoelectron spectroscopy into its fundamental parts. This accomplishment demonstrated the effectiveness of the developed hybrid approach, which combined classical multipole expansions and quantum GW-BSE calculations, in accurately predicting electronic excitations in realistic materials. Building upon this success, the research further predicted the properties of other relevant electronic states, such as the LUMO (Lowest Unoccupied Molecular Orbital) and the optical gap (absorption spectra). The research provided a comprehensive understanding of the entire electronic structure of MADN. One significant outcome of accurately predicting the electronic states in MADN is the estimation of the exciton binding energy. Estimating the exciton binding energy is essential because it provides insights into the stability and mobility of excitons in the material. A higher binding energy indicates a more stable exciton, which leads to longer exciton lifetimes and more efficient charge carrier generation and recombination processes. On the other hand, a lower binding energy facilitates exciton dissociation, enabling efficient charge transport, and is desirable for device applications like OLEDs and organic solar cells (OPVs). By accurately predicting the electronic states and optical properties of MADN, including the exciton binding energy, the research opens up new possibilities for designing and engineering materials with improved optoelectronic performance. This knowledge can guide the development of new organic semiconductors with tailored properties, allowing researchers to optimize the performance of devices like OLEDs and achieve more efficient light emission and energy conversion. Additionally, a deeper understanding of exciton behavior in materials like MADN can pave the way for the discovery of novel excitonic materials with unique and desirable characteristics. Another testbed for the methodologies developed in this thesis is disordered

molecular complexes with a low-donor content, in the specific those made out of rubrene-fullerene mixtures. Besides the computation of localized excitations (LE) and charge-transfer states (CT), we have developed the determination of LE-CT coupling elements within the framework of GW-BSE (with classical embedding). Coupling elements require the computation of diabatic states. A diabatic state refers to an electronic state that is localized in nature. It is distinct from an adiabatic state, which represents an eigenstate of the full Hamiltonian, including both electronic and nuclear degrees of freedom. Especially in complex materials and molecular systems, the diabatic states can significantly differ from the adiabatic states, leading to non-adiabatic effects. These non-adiabatic effects play a crucial role in electronic excitations, energy transfer, and chemical reactions. We have shown that in an ideal small-molecule dimer of naphthalene and TCNE, the quantitative estimates of these couplings are largely insensitive to methodological choices in the GW and BSE steps of the calculation, and only small differences are noted between the Edmiston–Ruedenberg, Generalized Mulliken–Hush, and Fragment Charge Difference diabatization formalisms, respectively. Compared to literature results for this model system on TD-DFT level, we could show that the difference found in the GW-BSE-based calculations can be attributed to different predictions of the adiabatic dimer energies entering the diabatization procedure and not differences in the densities of the excitations. In larger-scale, disordered molecular complexes, such as the low-donor content rubrene-fullerene mixtures, the LE-CT couplings are found to be more sensitive to the choice of the diabatization formalism. While the two more approximate Generalized Mulliken–Hush and Fragment Charge Difference approaches yield couplings that are largely in agreement with each other, they differ from respective results based on the Edmiston–Ruedenberg approach, which takes full details of the excited state densities into account. To scrutinize the effect of the different qualitatively and quantitative predictions, we have employed the respective LE-CT couplings in a minimal kinetic model of the conversion from LE to CT states based on Marcus rates. From the obtained time evolution of state population probabilities, it is apparent that the dynamics are affected on an intermediate timescale, but not the final steady-state prediction.

The third objective rounds around implementing multi-scale methods and innovative techniques into an open-source code (VOTCA-XTP). By creating a versatile computational platform that integrates quantum-mechanical simulations, molecular dynamics, and other approaches, the research contributed to accelerating the discovery of new materials with tailored properties. The objective can be broke down in:

- In the context of computational materials science, open-source codes are invaluable for several reasons:

  - Transparency and Reproducibility:
    Open-source codes provide transparency in computational methods, allowing researchers to understand how the calculations are performed and validate the results independently. This transparency promotes reproducibility and fosters trust in the scientific community.

  - Collaboration and Community Contribution:
    By making the code open-source, researchers encourage collaboration within the scientific community. Others can contribute to the code, suggest improvements, and extend its capabilities, which leads to the rapid development and dissemination of new techniques and advancements.

  - Accessibility:
    Open-source codes make cutting-edge computational tools accessible to a broader audience, including researchers with limited resources. This accessibility democratizes computational research and accelerates progress across different scientific disciplines.

- Model Development and Innovation:
  A strong grasp of the technicalities enables researchers to develop new models, algorithms, and methodologies tailored to address specific challenges and bridge existing gaps in the field.

- Code Efficiency and Speed:
  In today's computational landscape, the efficiency of code is paramount for multiple reasons:

  - Scalability: Materials science simulations often involve large-scale systems and require substantial computational resources. Efficient code allows researchers to scale their simulations to larger systems and perform high-throughput computations.

  - Competitive Edge: In the fast-paced world of research, speed and efficiency in computations can provide a competitive edge, allowing researchers to publish results more quickly and stay at the forefront of their field.

Developing an in-house code allows researchers to have full control over the implementation and fine-tune it to their specific needs. This flexibility turns the code

into a testing ground for exploring new scientific and mathematical ideas. Researchers can experiment with novel algorithms and numerical techniques to address complex challenges, which might not be feasible with off-the-shelf software. This flexibility and adaptability foster creativity and innovation in computational materials science.

Overall, the thesis successfully addressed the outlined questions:

1. The findings presented in this thesis demonstrate the effectiveness of merging GW-BSE with classical embedding techniques for the accurate prediction of material properties that involve electronic excitations. By combining these approaches, it becomes possible to enhance the precision and quantitative nature of gas-phase GW-BSE calculations by accounting for the influence of neighboring molecules, specifically through polarization effects. Moreover, the newly developed methodologies offer the capability to generate energy profiles within targeted regions of morphological significance. This feature holds the potential to greatly enhance our comprehension of electronic excitations by creating a 'map' of the energy profile. This is particularly useful when input for ab-initio methods are needed and specific requirements must be met (e.g., need excitation energies in the bulk or at the surface). Consequently, these advancements hold promise for expediting the design of improved devices through a more profound insight into electronic excitations.

2. The research demonstrated the possibility of providing quantitative predictions of experimental spectra, including UPS, IPS, and Absorption, by employing the hybrid approach that combined classical and quantum mechanics. The first-principle analyses enabled the informed development of device models, fostering a deeper understanding of electronic excitations and their impact on material properties, thereby facilitating the design of improved devices. Beside providing a tool to gain more insight on experimental spectra, or even produce insightful spectra when experiments are hard to perform, the quantitative preditioncs together with the methods developed in this thesis can be helpful in application, in particular for parameters-free models used to simulate macroscopic characteristic of opto-electronic devices. The accuracy of the input quantities needed before starting with the macroscopic stage (i.e., KMC simulations) cna be accurately determined with the methods developed in this thesis.

3. It is possible to compute non-adiabatic coupling elements using the GW-BSE/MM approach for use in a rate-based model to describe the dynamic

conversion between localized and charge transfer excitations. This combination of methods holds the potential to provide valuable insights into the intricate interplay between electronic excitations and facilitate a more accurate representation of the conversion dynamics in various systems. By incorporating non-adiabatic coupling elements derived from the GW-BSE framework into a rate-based model, one can enhance the predictive power of the model and gain a deeper understanding of charge transfer processes and their impact on material behavior. Beside the scientific interest, there is an application interest (parameters-free models) in which this new framework can be integrated and use.

Nevertheless, different shortcomings and open problems have not been answered in this work, leaving room for improvement:

- As described in Section 4.2, the GW implementation has, at best, a scaling of $\mathcal{O}(N^4)$, which prohibits its application to many systems of interest. An active field of research is dedicated to this subject and many solutions have been proposed that can be possibly implemented in VOTCA-XTP. For example, it is possible to compute the GW without unoccupied state by using the so-called Sternheimer method [287]. Several $\mathcal{O}(N^3)$ algorithms with gaussian basis functions were developed [288, 289, 290, 291] inspired by the space-time method [292]. Another promising work on low-scaling GW claims a $\mathcal{O}(N^2)$ scaling [293]. Furthermore, a stochastic approach was proposed [294] as a solution towards low-scaling GW.

- The presented QM/MM strategy suffers from the problem of cutting through bonds in macromolecules (e.g., moving side-chains into the MM region, or looking at active parts of a larger polymer, protein). A possible amendment relies on QM/QM'/MM models, based on subsystem-DFT. In other words, a layer between the active region (treated with high accuracy QM method) and the MM region (treated classically), is inserted, and this layer is treated with a low-scaling QM method (usually DFT). For example, see GW-BSE [85].

- Within the QM/MM framework, the MM model does not cover charge-transfer inside the MM region. Possible solutions that do not involve the use of the Thole model, are the explicit calculation of charge-transfer within the Drude model [295] or within the charge-equilibration technique [296].

- The GW-BSE could be explicitly coupled with the Ewald-MM. In fact, the current implementation a fully classical Ewald-MM is used. It is, in principle, possible to compute GW-BSE energies and densities with the

explicit long-range electrostatic embedding. No work has been found on this subject, but there are implementations of this explicit coupling with DFT [297]. The same idea can be explored in the realm of *GW*-BSE and possibly implemented in the VOTCA-XTP software.

- The *GW*-BSE/MM framework relies on the assumption that the environment response is single-reference in character, as described in Section 3.6 and Section 4.2. This assumption allows for an unambiguous identification of the excited states in the self-consistent procedure. Following the state of interest is done via computing oscillator strengths for optical transitions or the amount of transferred charge between two molecules, or directly the density matrix of the excitation. Any of these state-tracking methods are not straightforwardly applicable, e.g., at or close to intersections where at least two states mix strongly. The possible ambiguity in the state detection requires a careful look to each step of the self-consistent cycle. A possible amendment can be adding a classical polarization directly in the *GW* as described in [212].

In summary, this thesis significantly contributed to the understanding of electronic excitations in complex materials, paving the way for further advancements in material science, device engineering, and computational methods. The combination of classical and quantum mechanics, the investigation of specific materials, and the creation of an open-source computational platform collectively represent a valuable and impactful contribution to the scientific community. The research outcomes are expected to inspire future studies in this field and drive innovations in various technological applications.

Bibliography

[1] Richard Phillips Feynman. *The Feynman Lectures on Physics*. Addison-Wesley, 06 2021.

[2] Guglielmo Lanzani. *The Photophysics behind Photovoltaics and Photonics*. Wiley-VCH Verlag GmbH & Co. KGaA, Weinheim, Germany, 3 2012.

[3] Th. Förster. Zwischenmolekulare Energiewanderung und Fluoreszenz. *Annalen der Physik*, 437(1-2):55–75, 1 1948.

[4] D. L. Dexter. A theory of sensitized luminescence in solids. *The Journal of Chemical Physics*, 21(5):836–850, 5 1953.

[5] Bernard Valeur and Mário Nuno Berberan-Santos. *Molecular Fluorescence*. Wiley-VCH Verlag GmbH & Co. KGaA, Weinheim, Germany, 4 2012.

[6] Rajesh Kancherla, Krishnamoorthy Muralirajan, Arunachalam Sagadevan, and Magnus Rueping. Visible Light-Induced Excited-State Transition-Metal Catalysis. *Trends in Chemistry*, 1(5):510, 2019.

[7] J. J.M. Halls, C. A. Walsh, N. C. Greenham, E. A. Marseglia, R. H. Friend, S. C. Moratti, and A. B. Holmes. Efficient photodiodes from interpenetrating polymer networks. *Nature*, 376(6540):498–500, 1995.

[8] V. Helms. *Principles of Computational Cell Biology: From Protein Complexes to Cellular Networks*. Wiley, 2018.

[9] C. W. Tang and S. A. Vanslyke. Organic electroluminescent diodes. *Applied Physics Letters*, 51(12):913–915, 1987.

[10] Björn Baumeier, Falk May, Christian Lennartz, and Denis Andrienko. Challenges for in silico design of organic semiconductors. *Journal of Materials Chemistry*, 22(22):10971–10976, 6 2012.

[11] Chihaya Adachi. Third-generation organic electroluminescence materials. *Japanese Journal of Applied Physics*, 53(6):060101, 5 2014.

[12] C. Hauenstein, X. de Vries, C. H. L. Weijtens, P. Imbrasas, P.-A. Will, S. Lenk, K. Ortstein, S. Reineke, P. A. Bobbert, R. Coehoorn, and H. van Eersel. Suppressing exciton deconfinement and dissociation for efficient thermally activated delayed fluorescence OLEDs. *Journal of Applied Physics*, 130(15):155501, 10 2021.

[13] Christoph Hauenstein, Stefano Gottardi, Engin Torun, Reinder Coehoorn, and Harm van Eersel. Identification of oled degradation scenarios by kinetic monte carlo simulations of lifetime experiments. *Frontiers in Chemistry*, 9, 2022.

[14] Pascal Kordt, Jeroen J. M. van der Holst, Mustapha Al Helwi, Wolfgang Kowalsky, Falk May, Alexander Badinski, Christian Lennartz, and Denis Andrienko. Modeling of organic light emitting diodes: From molecular to device properties. *Advanced Functional Materials*, 25(13):1955–1971, 2015.

[15] Anirban Mondal, Leanne Paterson, Jaeyoung Cho, Kun-Han Lin, Bas van der Zee, Gert-Jan A. H. Wetzelaer, Andrei Stankevych, Alexander Vakhnin, Jang-Joo Kim, Andrey Kadashchuk, Paul W. M. Blom, Falk May, and Denis Andrienko. Molecular library of OLED host materials—Evaluating the multiscale simulation workflow. *Chemical Physics Reviews*, 2(3):031304, 07 2021.

[16] Shosei Kubo and Hironori Kaji. Parameter-free multiscale simulation realising quantitative prediction of hole and electron mobilities in organic amorphous system with multiple frontier orbitals. *Scientific Reports*, 8(1):13462, Sep 2018.

[17] Reinder Coehoorn, Harm van Eersel, Peter Bobbert, and René Janssen. Kinetic monte carlo study of the sensitivity of oled efficiency and lifetime to materials parameters. *Advanced Functional Materials*, 25(13):2024–2037, 2015.

[18] Ben Streetman. *Solid state electronic devices*. Prentice Hall, Upper Saddle River N.J., 5th ed. edition, 2000.

[19] Gregory H. Wannier. The structure of electronic excitation levels in insulating crystals. *Physical Review*, 52(3):191–197, 8 1937.

[20] J. Frenkel. On the transformation of light into heat in solids. i. *Physical Review*, 37(1):17–44, 1 1931.

[21] J.D. Wright. *Molecular Crystals*. Cambridge University Press, 1995.

[22] Zaiyu Wang, Ke Gao, Yuanyuan Kan, Ming Zhang, Chaoqun Qiu, Lei Zhu, Zhe Zhao, Xiaobin Peng, Wei Feng, Zhiyuan Qian, Xiaodan Gu, Alex K.-Y. Jen, Ben Zhong Tang, Yong Cao, Yongming Zhang, and Feng Liu. The coupling and competition of crystallization and phase separation, correlating thermodynamics and kinetics in opv morphology and performances. *Nature Communications*, 12(1):332, Jan 2021.

[23] Marcella Günther, Negar Kazerouni, Dominic Blätte, Jose Dario Perea, Barry C. Thompson, and Tayebeh Ameri. Models and mechanisms of ternary organic solar cells. *Nature Reviews Materials*, 8(7):456–471, Jul 2023.

[24] Gary Hodes. Perovskite-based solar cells. *Science*, 342(6156):317–318, 10 2013.

[25] Ian A. Howard, Michael Meister, Björn Baumeier, Henrike Wonneberger, Neil Pschirer, Rüdiger Sens, Ingmar Bruder, Chen Li, Klaus Müllen, Denis Andrienko, and Frédéric Laquai. Two Channels of Charge Generation in Perylene Monoimide Solid-State Dye-Sensitized Solar Cells. *Advanced Energy Materials*, 4(2):1300640, 1 2014.

[26] Björn Baumeier, Michael Rohlfing, and Denis Andrienko. Electronic excitations in push-pull oligomers and their complexes with fullerene from many-body Green's functions theory with polarizable embedding. *Journal of Chemical Theory and Computation*, 10(8):3104–3110, 8 2014.

[27] Behnaz Bagheri, Björn Baumeier, and Mikko Karttunen. Getting excited: Challenges in quantum-classical studies of excitons in polymeric systems. *Physical Chemistry Chemical Physics*, 18(44):30297–30304, 11 2016.

[28] B. Bagheri, M. Karttunen, and B. Baumeier. Solvent effects on optical excitations of poly para phenylene ethynylene studied by QM/MM simulations based on many-body Green's functions theory. *European Physical Journal: Special Topics*, 225(8-9):1743–1756, 10 2016.

[29] Stephen R. Forrest. Excitons and the lifetime of organic semiconductor devices. *Philosophical Transactions of the Royal Society A: Mathematical, Physical and Engineering Sciences*, 373(2044), 6 2015.

[30] Marc Dvorak, Dorothea Golze, and Patrick Rinke. Quantum embedding theory in the screened Coulomb interaction: Combining configuration interaction with GW/BSE. *Physical Review Materials*, 3(7):070801, 7 2019.

[31] Frederick R. Manby, Martina Stella, Jason D. Goodpaster, and Thomas F. Miller. A simple, exact density-functional-theory embedding scheme. *Journal of Chemical Theory and Computation*, 8(8):2564–2568, 8 2012.

[32] Hayley R. Petras, Daniel S. Graham, Sai Kumar Ramadugu, Jason D. Goodpaster, and James J. Shepherd. Fully Quantum Embedding with Density Functional Theory for Full Configuration Interaction Quantum Monte Carlo. *Journal of Chemical Theory and Computation*, 15(10):5332–5342, 10 2019.

[33] Xuelan Wen, Daniel S. Graham, Dhabih V. Chulhai, and Jason D. Goodpaster. Absolutely Localized Projection-Based Embedding for Excited States. *Journal of Chemical Theory and Computation*, 16(1):385–398, 1 2020.

[34] B. Baumeier, D. Andrienko, Y. Ma, and M. Rohlfing. Excited states of dicyanovinyl-substituted oligothiophenes from many-body Green's functions theory. *J. Chem. Theory. Comput.*, 8(3):997–1002, 3 2012.

[35] Jing Li, Gabriele D'Avino, Anton Pershin, Denis Jacquemin, Ivan Duchemin, David Beljonne, and Xavier Blase. Correlated electron-hole mechanism for molecular doping in organic semiconductors. *Phys. Rev. Mat.*, 1(2):25602, 2017.

[36] Jing Li, Gabriele D'Avino, Ivan Duchemin, David Beljonne, and Xavier Blase. Accurate description of charged excitations in molecular solids from embedded many-body perturbation theory. *Physical Review B*, 97(3):35108, 1 2018.

[37] G. Tirimbó, V. Sundaram, O. Ca¸ylak, W. Scharpach, J. Sijen, C. Junghans, J. Brown, F. Zapata Ruiz, N. Renaud, J. Wehner, and B. Baumeier. Excited-state electronic structure of molecules using many-body Green's functions: Quasiparticles and electron-hole excitations with VOTCA-XTP. *Journal of Chemical Physics*, 152(11):114103, 3 2020.

[38] Ivan Duchemin, Ciro A. Guido, Denis Jacquemin, and Xavier Blase. The Bethe-Salpeter formalism with polarisable continuum embedding: Reconciling linear-response and state-specific features. *Chemical Science*, 9(19):4430–4443, 5 2018.

[39] Landau L.D. and Lifshitz E.M. *Mechanics*. Elsevier, 1976.

[40] W. Heisenberg. Über den anschaulichen Inhalt der quantentheoretischen Kinematik und Mechanik. *Zeitschrift für Physik*, 43(3-4):172–198, 3 1927.

[41] S.M. Blinder. The hydrogen atom and atomic orbitals. In *Introduction to Quantum Mechanics*, pages 129–149. Elsevier, 1 2021.

[42] M. Born and R. Oppenheimer. Zur quantentheorie der molekeln. *Annalen der Physik*, 389(20):457–484, 1927.

[43] B.H. Bransden and C.J. Joachain. Variational Principle. In *Physics of Atoms and Molecules*, pages 116–123. Longman Scientific and Technical, 1 1990.

[44] B.H. Bransden and C.J. Joachain. One-electron atoms. In *Physics of Atoms and Molecules*, pages 128–154. Longman Scientific and Technical, 1 1990.

[45] W. Kohn and L. J. Sham. Self-Consistent Equations Including Exchange and Correlation Effects. *Physical Review*, 140(4A):A1133–A1138, November 1965.

[46] W. Kohn and L. J. Sham. Self-consistent equations including exchange and correlation effects. *Physical Review*, 140(4A):A1133, 11 1965.

[47] Stefano Baroni, Stefano de Gironcoli, Andrea Dal Corso, and Paolo Giannozzi. Phonons and related crystal properties from density-functional perturbation theory. *Rev. Mod. Phys.*, 73:515–562, Jul 2001.

[48] Takao Tsuneda. *Exchange-Correlation Functionals*, pages 101–124. Springer Japan, Tokyo, 2014.

[49] John P. Perdew, Kieron Burke, and Matthias Ernzerhof. Generalized gradient approximation made simple [phys. rev. lett. 77, 3865 (1996)]. *Phys. Rev. Lett.*, 78:1396–1396, Feb 1997.

[50] A. D. Becke. Density-functional exchange-energy approximation with correct asymptotic behavior. *Phys. Rev. A*, 38:3098–3100, Sep 1988.

[51] Chengteh Lee, Weitao Yang, and Robert G. Parr. Development of the colle-salvetti correlation-energy formula into a functional of the electron density. *Phys. Rev. B*, 37:785–789, Jan 1988.

[52] Axel D. Becke. Density-functional thermochemistry. III. The role of exact exchange. *The Journal of Chemical Physics*, 98(7):5648–5652, 04 1993.

[53] Carlo Adamo and Vincenzo Barone. Toward reliable density functional methods without adjustable parameters: The PBE0 model. *J. Chem. Phys.*, 110(13):6158–6170, 1999.

[54] Jochen Heyd, Gustavo E. Scuseria, and Matthias Ernzerhof. Hybrid functionals based on a screened coulomb potential. *Journal of Chemical Physics*, 118:8207–8215, 2003.

[55] D. P. Chong, O. V. Gritsenko, and E. J. Baerends. Interpretation of the Kohn-Sham orbital energies as approximate vertical ionization potentials. *Journal of Chemical Physics*, 116(5):1760–1772, 2 2002.

[56] Eli Kraisler and Leeor Kronik. Fundamental gaps with approximate density functionals: The derivative discontinuity revealed from ensemble considerations. *Journal of Chemical Physics*, 140(18):18–540, 5 2014.

[57] Thomas C. Pitts, Nektarios N. Lathiotakis, and Nikitas Gidopoulos. Generalized Kohn-Sham equations with accurate total energy and single-particle eigenvalue spectrum. *The Journal of Chemical Physics*, 155(22):224105, 12 2021.

[58] A. Seidl, A. Görling, P. Vogl, J. A. Majewski, and M. Levy. Generalized kohn-sham schemes and the band-gap problem. *Phys. Rev. B*, 53:3764–3774, Feb 1996.

[59] M. Dauth, T. Körzdörfer, S. Kümmel, J. Ziroff, M. Wiessner, A. Schöll, F. Reinert, M. Arita, and K. Shimada. Orbital density reconstruction for molecules. *Phys. Rev. Lett.*, 107:193002, Nov 2011.

[60] D. P. Chong, O. V. Gritsenko, and E. J. Baerends. Interpretation of the Kohn-Sham orbital energies as approximate vertical ionization potentials. *The Journal of Chemical Physics*, 116(5):1760–1772, 02 2002.

[61] Giovanni Borghi, Andrea Ferretti, Ngoc Linh Nguyen, Ismaila Dabo, and Nicola Marzari. Koopmans-compliant functionals and their performance against reference molecular data. *Physical Review B - Condensed Matter and Materials Physics*, 90(7):075135, 8 2014.

[62] F. J. Himpsel. Angle-resolved measurements of the photoemission of electrons in the study of solids. *Advances in Physics*, 32(1):1–51, 1 1983.

[63] E. W. Plummer and W. Eberhardt. *Angle-Resolved Photoemission as a Tool for the Study of Surfaces.* John Wiley & Sons, Ltd, 3 2007.

[64] Stefan Hüfner. *Photoelectron spectroscopy.* Springer Berlin, Heidelberg, 2013.

[65] V. Dose. Momentum-resolved inverse photoemission. *Surface Science Reports*, 5(8):337–378, 1 1985.

[66] Neville V. Smith. Inverse photoemission, 9 1988.

[67] G. Strinati. Application of the Green's Functions Method to the Study of the Optical Properties of Semiconductors. *Riv. Nuovo Cimento 1978-1999*, 11(12):1–86, 1988.

[68] Qi Ou and Joseph E. Subotnik. Comparison between the Bethe-Salpeter Equation and Configuration Interaction Approaches for Solving a Quantum Chemistry Problem: Calculating the Excitation Energy for Finite 1D Hubbard Chains. *Journal of Chemical Theory and Computation*, 14(2):527–542, 2 2018.

[69] Friedhelm Bechstedt. *Set of Fundamental Equations*, pages 231–253. Springer Berlin Heidelberg, Berlin, Heidelberg, 2015.

[70] Mark S Hybertsen and Steven G Louie. First-principles theory of quasiparticles: Calculation of band gaps in semiconductors and insulators. *Phys. Rev. Lett.*, 55(13):1418–1421, 1985.

[71] Wilfried G Aulbur, Lars Jönsson, and John W Wilkins. Quasiparticle Calculations in Solids. In Henry Ehrenreich and Frans Spaepen, editors, *Solid State Physics - Advances in Research and Applications*, pages 1–218. Academic Press, 2000.

[72] Michael Rohlfing. Excited states of molecules from Green's function perturbation techniques. *Int. J. Quantum Chem.*, 80(4-5):807–815, 2000.

[73] Lars Hedin and Stig Lundqvist. Effects of Electron-Electron and Electron-Phonon Interactions on the One-Electron States of Solids. *Solid State Physics - Advances in Research and Applications*, 23(C):1–181, 1970.

[74] G Strinati. Application of the Green's functions method to the study of the optical properties of semiconductors. *La Rivista Del Nuovo Cimento Series 3*, 11(12):1–86, 1988.

[75] Michael Rohlfing and Steven G. Louie. Electron-hole excitations and optical spectra from first principles. *Phys. Rev. B*, 62:4927–4944, 2000.

[76] Pierre François Loos and Xavier Blase. Dynamical correction to the Bethe-Salpeter equation beyond the plasmon-pole approximation. *Journal of Chemical Physics*, 153(11):114120, 9 2020.

[77] Alexander L Fetter and John Dirk Walecka. *Quantum Theory of Many-Particle Systems*. Courier Corporation, 2003.

[78] Tonatiuh Rangel, Samia M. Hamed, Fabien Bruneval, and Jeffrey B. Neaton. An assessment of low-lying excitation energies and triplet instabilities of organic molecules with an ab initio Bethe-Salpeter equation approach and the Tamm-Dancoff approximation. *J. Chem. Phys.*, 146(19), 2017.

[79] Denis Jacquemin, Ivan Duchemin, Aymeric Blondel, and Xavier Blase. Benchmark of Bethe-Salpeter for Triplet Excited-States. *J. Chem. Theory. Comput.*, 13(2):767–783, 2017.

[80] Yuchen Ma, Michael Rohlfing, and Carla Molteni. Excited states of biological chromophores studied using many-body perturbation theory: Effects of resonant-antiresonant coupling and dynamical screening. *Phys. Rev. B*, 80(24):241405, 2009.

[81] Jacopo Tomasi, Benedetta Mennucci, and Roberto Cammi. Quantum mechanical continuum solvation models, 2005.

[82] B. Mennucci, S. Caprasecca, and C. A. Guido. Computational Studies of Environmental Effects and Their Interplay With Experiment. *Advances in Physical Organic Chemistry*, 50:203–241, 1 2016.

[83] Continuum Solvation Models in Chemical Physics: From Theory to Applications — Wiley.

[84] Ivan Duchemin, Denis Jacquemin, and Xavier Blase. Combining the GW formalism with the polarizable continuum model: A state-specific non-equilibrium approach. *Journal of Chemical Physics*, 144(16):164106, 4 2016.

[85] Jógvan Magnus Haugaard Olsen, Casper Steinmann, Kenneth Ruud, and Jacob Kongsted. Polarizable density embedding: A new QM/QM/MM-based computational strategy. *Journal of Physical Chemistry A*, 119(21):5344–5355, 5 2015.

[86] Csaba Daday, Carolin König, Omar Valsson, Johannes Neugebauer, and Claudia Filippi. State-specific embedding potentials for excitation-energy calculations. *Journal of Chemical Theory and Computation*, 9(5):2355–2367, 5 2013.

[87] Jing Li, Gabriele D'Avino, Ivan Duchemin, David Beljonne, and Xavier Blase. Combining the Many-Body GW Formalism with Classical Polarizable Models: Insights on the Electronic Structure of Molecular Solids. *Journal of Physical Chemistry Letters*, 7(14):2814–2820, 7 2016.

[88] Erik D. Hedegård and Markus Reiher. Polarizable Embedding Density Matrix Renormalization Group. *Journal of Chemical Theory and Computation*, 12(9):4242–4253, 9 2016.

[89] Johannes Tölle, Thorsten Deilmann, Michael Rohlfing, and Johannes Neugebauer. Subsystem-Based GW/Bethe-Salpeter Equation. *Journal of Chemical Theory and Computation*, 17(4):2186–2199, 4 2021.

[90] Zachary C. Holden, Ryan M. Richard, and John M. Herbert. Periodic boundary conditions for QM/MM calculations: Ewald summation for extended Gaussian basis sets. *The Journal of Chemical Physics*, 139(24):244108, 12 2013.

[91] Anthony Stone. *The Theory of Intermolecular Forces*. Oxford University Press, Oxford, 2nd editio edition, 2013.

[92] B. T. Thole. Molecular polarizabilities calculated with a modified dipole interaction. *Chem. Phys.*, 59(3):341–350, 1981.

[93] Piet Th Van Duijnen and Marcel Swart. Molecular and atomic polarizabilities: Thole's model revisited. *J. Phys. Chem. A*, 102(14):2399–2407, 1998.

[94] Jens Wehner, Lothar Brombacher, Joshua Brown, Christoph Junghans, Onur Çaylak, Yuriy Khalak, Pranav Madhikar, Gianluca Tirimbó, and Björn Baumeier. Electronic Excitations in Complex Molecular Environments: Many-Body Green's Functions Theory in VOTCA-XTP. *Journal of Chemical Theory and Computation*, 14(12):6253–6268, 12 2018.

[95] Changsheng Zhang, Chao Lu, Zhifeng Jing, Chuanjie Wu, Jean-Philip Piquemal, Jay W. Ponder, and Pengyu Ren. Amoeba polarizable atomic multipole force field for nucleic acids. *J. Chem. Theory Comput.*, 14(4):2084–2108, 2018.

[96] Curt M. Breneman and Kenneth B. Wiberg. Determining atom-centered monopoles from molecular electrostatic potentials. the need for high sampling density in formamide conformational analysis. *Journal of Computational Chemistry*, 11(3):361–373, 1990.

[97] Anthony J. Stone. Distributed multipole analysis: Stability for large basis sets. *J. Chem. Theory Comput.*, 1(6):1128–1132, 2005.

[98] Trygve Helgaker, Wim Klopper, Henrik Koch, and Jozef Noga. Basis-set convergence of correlated calculations on water. *The Journal of Chemical Physics*, 106(23):9639–9646, 1997.

[99] Asger Halkier, Trygve Helgaker, Poul Jørgensen, Wim Klopper, and Jeppe Olsen. Basis-set convergence of the energy in molecular hartree–fock calculations. *Chemical Physics Letters*, 302(5):437–446, 1999.

[100] Kirk A. Peterson, David E. Woon, and Thom H. Dunning. Benchmark calculations with correlated molecular wave functions. iv. the classical barrier height of the h+h2→h2+h reaction. *The Journal of Chemical Physics*, 100(10):7410–7415, 1994.

[101] David E. Woon and Thom H. Dunning. Benchmark calculations with correlated molecular wave functions. vi. second row a2 and first row/second row ab diatomic molecules. *The Journal of Chemical Physics*, 101(10):8877–8893, 1994.

[102] David Feller, Kirk A. Peterson, and J. Grant Hill. On the effectiveness of ccsd(t) complete basis set extrapolations for atomization energies. *The Journal of Chemical Physics*, 135(4):044102, 2011.

[103] Jan M.L. Martin. Ab initio total atomization energies of small molecules — towards the basis set limit. *Chemical Physics Letters*, 259(5):669–678, 1996.

[104] Asger Halkier, Trygve Helgaker, Poul Jørgensen, Wim Klopper, Henrik Koch, Jeppe Olsen, and Angela K. Wilson. Basis-set convergence in correlated calculations on ne, n2, and h2o. *Chemical Physics Letters*, 286(3):243–252, 1998.

[105] David B. Cook. *Handbook of Computational Quantum Chemistry*. Dover publications, 08 2005.

[106] Dmitrij Rappoport and Filipp Furche. Property-optimized gaussian basis sets for molecular response calculations. *The Journal of Chemical Physics*, 133(13):134105, 2010.

[107] Angela K. Wilson, Tanja van Mourik, and Thom H. Dunning. Gaussian basis sets for use in correlated molecular calculations. vi. sextuple zeta correlation consistent basis sets for boron through neon. *Journal of Molecular Structure: THEOCHEM*, 388:339–349, 1996.

[108] Rick A. Kendall, Thom H. Dunning, and Robert J. Harrison. Electron affinities of the first-row atoms revisited. systematic basis sets and wave functions. *The Journal of Chemical Physics*, 96(9):6796–6806, 1992.

[109] Thom H. Dunning. Gaussian basis sets for use in correlated molecular calculations. i. the atoms boron through neon and hydrogen. *The Journal of Chemical Physics*, 90(2):1007–1023, 1989.

[110] Jorge Kohanoff. *Electronic structure calculations for solids and molecules: Theory and computational methods*. Cambridge University Press, 2006.

[111] Sergey V. Levchenko, Xinguo Ren, Jürgen Wieferink, Rainer Johanni, Patrick Rinke, Volker Blum, and Matthias Scheffler. Hybrid functionals for large periodic systems in an all-electron, numeric atom-centered basis framework. *Computer Physics Communications*, 192:60–69, 7 2015.

[112] Xinguo Ren, Patrick Rinke, Volker Blum, Jürgen Wieferink, Alexandre Tkatchenko, Andrea Sanfilippo, Karsten Reuter, and Matthias Scheffler. Resolution-of-identity approach to Hartree-Fock, hybrid density functionals, RPA, MP2 and GW with numeric atom-centered orbital basis functions. *New Journal of Physics*, 14(5):053020, 5 2012.

[113] Igor Ying Zhang, Xinguo Ren, Patrick Rinke, Volker Blum, and Matthias Scheffler. Numeric atom-centered-orbital basis sets with valence-correlation consistency from H to Ar. *New Journal of Physics*, 15(12):123033, 12 2013.

[114] Gang Bao, Guanghui Hu, and Di Liu. Numerical solution of the kohn-sham equation by finite element methods with an adaptive mesh redistribution technique. *Journal of Scientific Computing*, 55(2):372–391, 5 2013.

[115] Huajie Chen, Xiaoying Dai, Xingao Gong, Lianhua He, and Aihui Zhou. Adaptive finite element approximations for Kohn-Sham models. *Multiscale Modeling and Simulation*, 12(4):1828–1869, 12 2014.

[116] Eric J. Bylaska, Michael Holst, and John H. Weare. Adaptive finite element method for solving the exact kohn-sham equation of density functional theory. *Journal of Chemical Theory and Computation*, 5(4):937–948, 4 2009.

[117] Or Cohen, Leeor Kronik, and Achi Brandt. Locally refined multigrid solution of the all-electron Kohn-Sham equation. *Journal of Chemical Theory and Computation*, 9(11):4744–4760, 11 2013.

[118] Jian Wang and Thomas L. Beck. Efficient real-space solution of the Kohn-Sham equations with multiscale techniques. *Journal of Chemical Physics*, 112(21):9223–9228, 6 2000.

[119] Laura E. Ratcliff, William Dawson, Giuseppe Fisicaro, Damien Caliste, Stephan Mohr, Augustin Degomme, Brice Videau, Viviana Cristiglio, Martina Stella, Marco D'Alessandro, Stefan Goedecker, Takahito Nakajima, Thierry Deutsch, and Luigi Genovese. Flexibilities of wavelets as a computational basis set for large-scale electronic structure calculations. *The Journal of chemical physics*, 152(19):194110, 5 2020.

[120] Erin L. Ratcliff, Jens Meyer, K. Xerxes Steirer, Neal R. Armstrong, Dana Olson, and Antoine Kahn. Energy level alignment in PCDTBT: PC 70BM solar cells: Solution processed NiO x for improved hole collection and efficiency. *Org. Electron. Phys. Mater. Appl.*, 13(5):744–749, 2012.

[121] Victor Rühle, Christoph Junghans, Alexander Lukyanov, Kurt Kremer, and Denis Andrienko. Versatile object-oriented toolkit for coarse-graining applications. *J. Chem. Theory. Comput.*, 5(12):3211–3223, 2009.

[122] Victor Rühle, Alexander Lukyanov, Falk May, Manuel Schrader, Thorsten Vehoff, James Kirkpatrick, Björn Baumeier, and Denis Andrienko. Microscopic simulations of charge transport in disordered organic semiconductors. *J. Chem. Theory. Comput.*, 7(10):3335–3345, 2011.

[123] Jens Wehner, Lothar Brombacher, Joshua Brown, Christoph Junghans, Onur Çaylak, Yuriy Khalak, Pranav Madhikar, Gianluca Tirimbó, and Björn Baumeier. Electronic Excitations in Complex Molecular Environments: Many-Body Green's Functions Theory in VOTCA-XTP. *J. Chem. Theory. Comput.*, 14(12):6253–6268, 2018.

[124] Frank Neese. The ORCA program system. *Wiley Interdiscip. Rev. Comput. Mol. Sci.*, 2(1):73–78, 2012.

[125] Daniele Varsano, Stefano Caprasecca, and Emanuele Coccia. Theoretical description of protein field effects on electronic excitations of biological chromophores. *J. Phys. Cond. Mat.*, 29(1):13002, 2017.

[126] Gianluca Tirimbó, Xander de Vries, Christ H. L. Weijtens, Peter A. Bobbert, Tobias Neumann, Reinder Coehoorn, and Björn Baumeier. Quantitative predictions of photoelectron spectra in amorphous molecular solids from multiscale quasiparticle embedding. *Phys. Rev. B*, 101:035402, 2020.

[127] Björn Baumeier, James Kirkpatrick, and Denis Andrienko. Density-functional based determination of intermolecular charge transfer properties for large-scale morphologies. *Phys. Chem. Chem. Phys.*, 12(36):11103–11113, 2010.

[128] Jens Wehner and Björn Baumeier. Intermolecular Singlet and Triplet Exciton Transfer Integrals from Many-Body Green's Functions Theory. *Journal of Chemical Theory and Computation*, 13(4):1584–1594, 4 2017.

[129] Swapnil Baral, Matthew Phillips, Han Yan, Joseph Avenoso, Lars Gundlach, Björn Baumeier, and Edward Lyman. Ultrafast formation of the charge transfer state of prodan reveals unique aspects of the chromophore environment. *J. Phys. Chem. B*, 3 2020.

[130] Jens Wehner and Björn Baumeier. Multiscale Simulations of Singlet and Triplet Exciton Dynamics in Disordered Molecular Systems based on Many-Body Green's Functions Theory. *New Journal of Physics*, 2020.

[131] S. Obara and A. Saika. Efficient recursive computation of molecular integrals over Cartesian Gaussian functions. *J. Chem. Phys.*, 84(7):3963–3974, 1986.

[132] Simen Reine, Trygve Helgaker, and Roland Lindh. Multi-electron integrals. *Wiley Interdiscip. Rev. Comput. Mol. Sci.*, 2(2):290–303, 2012.

[133] K. Eichkorn, O. Treutler, H. Öhm, M. Häser, and R. Ahlrichs. Auxiliary basis sets to approximate Coulomb potentials (Chem. Phys. Letters 240 (1995) 283) (PII:0009-2614(95)00621-4). *Chem. Phys. Lett.*, 242(6):652–660, 1995.

[134] X. Blase, C. Attaccalite, and V. Olevano. First-principles GW calculations for fullerenes, porphyrins, phtalocyanine, and other molecules of interest for organic photovoltaic applications. *Phys. Rev. B*, 83(11):115103, 2011.

[135] Dorothea Golze, Jan Wilhelm, Michiel J. van Setten, and Patrick Rinke. Core-Level Binding Energies from ¡i¿GW¡/i¿ : An Efficient Full-Frequency Approach within a Localized Basis. *J. Chem. Theory. Comput.*, 14(9):4856–4869, 2018.

[136] D. Golze, M. Dvorak, and P. Rinke. The GW compendium: A practical guide to theoretical photoemission spectroscopy. *Frontiers in Chemistry*, 7:377, 2019.

[137] Jonathan Laflamme Janssen, Bruno Rousseau, and Michel Côté. Efficient dielectric matrix calculations using the Lanczos algorithm for fast many-body G0W0 implementations. *Phys. Rev. B*, 91(12):125120, 2015.

[138] V.I. Anisimov, editor. *Strong Coulomb Correlations in Electronic Structure Calculations: Beyond the Local Density Approximation*. CRC Press, Boca Raton, FL, 2000.

[139] Mark S. Hybertsen and Steven G. Louie. Electron correlation in semiconductors and insulators: Band gaps and quasiparticle energies. *Phys. Rev. B*, 34:5390–5413, 1986.

[140] R. W. Godby and R. J. Needs. Metal-insulator transition in kohn-sham theory and quasiparticle theory. *Phys. Rev. Lett.*, 62:1169–1172, 1989.

[141] Michael Rohlfing, Peter Krüger, and Johannes Pollmann. Efficient scheme for GW quasiparticle band-structure calculations with applications to bulk Si and to the Si(001)-(2×1) surface. *Phys. Rev. B*, 52(3):1905–1917, 1995.

[142] Florian Weigend and Reinhart Ahlrichs. Balanced basis sets of split valence, triple zeta valence and quadruple zeta valence quality for H to Rn: Design and assessment of accuracy. *Physical Chemistry Chemical Physics*, 7(18):3297–3305, 9 2005.

[143] Florian Weigend, Andreas Köhn, and Christof Hättig. Efficient use of the correlation consistent basis sets in resolution of the identity MP2 calculations. *J. Chem. Phys.*, 116(8):3175–3183, 2002.

[144] ISO. *ISO\IEC 14882:2014 Information technology — Programming languages — C++*. International Organization for Standardization, Geneva, Switzerland, 2014.

[145] Gaël Guennebaud, Benoît Jacob, and others. Eigen v3. http://eigen.tuxfamily.org, 2010.

[146] Intel. *Intel Math Kernel Library. Reference Manual*. Intel Corporation, 2009.

[147] The HDF Group. Hierarchical Data Format, version 5, 1997-2019. https://www.hdfgroup.org/HDF5/.

[148] Susi Lehtola, Conrad Steigemann, Micael J.T. Oliveira, and Miguel A.L. Marques. Recent developments in LIBXC — A comprehensive library of functionals for density functional theory. *SoftwareX*, 7:1–5, 2018.

[149] Boris Schling. *The Boost C++ Libraries*. XML Press, 2011.

[150] D. Luebke. Cuda: Scalable parallel programming for high-performance scientific computing. In *2008 5th IEEE International Symposium on Biomedical Imaging: From Nano to Macro*, pages 836–838, May 2008.

[151] Ernest R Davidson. The iterative calculation of a few of the lowest eigenvalues and corresponding eigenvectors of large real-symmetric matrices. *J. Comput. Phys.*, 17(1):87–94, 1975.

[152] James Demmel, Jack Dongarra, Axel Ruhe, and Henk van der Vorst. *Templates for the Solution of Algebraic Eigenvalue Problems: A Practical Guide.* Society for Industrial and Applied Mathematics, Philadelphia, PA, USA, 2000.

[153] Eugene Vecharynski, Jiri Brabec, Meiyue Shao, Niranjan Govind, and Chao Yang. Efficient block preconditioned eigensolvers for linear response time-dependent density functional theory. *Comp. Phys. Comm.*, 221:42–52, 2017.

[154] Matthew L. Leininger, C. David Sherrill, Wesley D. Allen, and Henry F. Schaefer. Systematic Study of Selected Diagonalization Methods for Configuration Interaction Matrices. *J. Comput. Chem.*, 22(13):1574–1589, 2001.

[155] Ronald B Morgan. Computing interior eigenvalues of large matrices. *Linear Algebra Its Appl.*, 154-156:289–309, 1991.

[156] Feliciano Giustino, Marvin L. Cohen, and Steven G. Louie. GW method with the self-consistent Sternheimer equation. *Phys. Rev. B*, 81(11):115105, 2010.

[157] Joshua D. Elliott, Nicola Colonna, Margherita Marsili, Nicola Marzari, and Paolo Umari. Koopmans Meets Bethe–Salpeter: Excitonic Optical Spectra without GW. *J. Chem. Theory. Comput.*, 15(6):3710–3720, 2019.

[158] C. Faber, P. Boulanger, C. Attaccalite, E. Cannuccia, I. Duchemin, T. Deutsch, and X. Blase. Exploring approximations to the GW self-energy ionic gradients. *Phys. Rev. B*, 91(15):155109, 2015.

[159] Susi Lehtola. Curing basis set overcompleteness with pivoted Cholesky decompositions. *J. Chem. Phys.*, 151(24):241102, 2019.

[160] Lan Nguyen Tran, Jacqueline A. R. Shea, and Eric Neuscamman. Tracking Excited States in Wave Function Optimization Using Density Matrices and Variational Principles. *J. Chem. Theory. Comput.*, 15(9):4790–4803, 2019.

[161] Andrew T. B. Gilbert, Nicholas A. Besley, and Peter M. W. Gill. Self-Consistent Field Calculations of Excited States Using the Maximum Overlap Method (MOM). *J. Phys. Chem. A*, 112(50):13164–13171, 2008.

[162] C. W. Tang and S. A. VanSlyke. Organic electroluminescent diodes. *Appl. Phys. Lett.*, 51(12):913, 1987.

[163] Junji Kido, Masato Kimura, and Katsutoshi Nagai. Multilayer White Light-Emitting Organic Electroluminescent Device. *Science*, 267(5202):1332, 1995.

[164] M. A. Baldo, D. F. O'Brien, Y. You, A. Shoustikov, S. Sibley, M. E. Thompson, and S. R. Forrest. Highly efficient phosphorescent emission from organic electroluminescent devices. *Nature*, 395(6698):151, 1998.

[165] Chihaya Adachi. Third-generation organic electroluminescence materials. *Jpn. J Appl. Phys.*, 53(6):060101, 2014.

[166] J. J. M. Halls, C. A. Walsh, N. C. Greenham, E. A. Marseglia, R. H. Friend, S. C. Moratti, and A. B. Holmes. Efficient photodiodes from interpenetrating polymer networks. *Nature*, 376:498, 1995.

[167] G. Yu, J. Gao, J. C. Hummelen, F. Wudl, and A. J. Heeger. Polymer Photovoltaic Cells: Enhanced Efficiencies via a Network of Internal Donor-Acceptor Heterojunctions. *Science*, 270(5243):1789, 1995.

[168] Wenchao Zhao, Sunsun Li, Huifeng Yao, Shaoqing Zhang, Yun Zhang, Bei Yang, and Jianhui Hou. Molecular Optimization Enables over 13% Efficiency in Organic Solar Cells. *J. Amer. Chem. Soc.*, 139(21):7148–7151, 2017.

[169] Peter Peumans, Aharon Yakimov, and Stephen R. Forrest. Small molecular weight organic thin-film photodetectors and solar cells. *J. Appl. Phys.*, 93(7):3693, 2003.

[170] Ross D. Jansen-van Vuuren, Ardalan Armin, Ajay K. Pandey, Paul L. Burn, and Paul Meredith. Organic Photodiodes: The Future of Full Color Detection and Image Sensing. *Adv. Mater.*, 28(24):4766, 2016.

[171] Marcin Kielar, Olivier Dhez, Gilles Pecastaings, Arnaud Curutchet, and Lionel Hirsch. Organic Photodiodes: The Future of Full Color Detection and Image Sensing. *Sci. Rep.*, 6:39201, 2016.

[172] W. R. Salaneck, C. B. Duke, W. Eberhardt, E. W. Plummer, and H. J. Freund. Temperature-Dependent Ultraviolet Photoemission Linewidths of Molecular Solids: Isopropyl Benzene. *Phys. Rev. Lett.*, 45(4):280–283, 1980.

[173] M. Malagoli, V. Coropceanu, D. A. da Silva Filho, and J. L. Brédas. A multimode analysis of the gas-phase photoelectron spectra in oligoacenes. *J. Chem. Phys.*, 120(16):7490, 2004.

[174] Satoshi Kera, Hiroyuki Yamane, and Nobuo Ueno. First-principles measurements of charge mobility in organic semiconductors: Valence hole–vibration coupling in organic ultrathin films. *Prog. Surf. Sci.*, 84(5):135–154, 2009.

[175] Satoshi Kera and Nobuo Ueno. Photoelectron spectroscopy on the charge reorganization energy and small polaron binding energy of molecular film. *J. Electron Spectrosc.*, 204:2–11, 2015.

[176] I. G. Hill, A. Kahn, Z. G. Soos, and R. A. Pascal. Charge-separation energy in films of π-conjugated organic molecules. *Chem. Phys. Lett.*, 327(3):181–188, 2000.

[177] Brian W. D'Andrade, Shubhashish Datta, Stephen R. Forrest, Peter Djurovich, Eugene Polikarpov, and Mark E. Thompson. Relationship between the ionization and oxidation potentials of molecular organic semiconductors. *Org. Electron.*, 6(1):11–20, 2005.

[178] S. Krause, M. B. Casu, A. Schöll, and E. Umbach. Determination of transport levels of organic semiconductors by UPS and IPS. *New J. Phys.*, 10(8):085001, 2008.

[179] Hiroyuki Yoshida, Kazuto Yamada, Jun'ya Tsutsumi, and Naoki Sato. Complete description of ionization energy and electron affinity in organic solids: Determining contributions from electronic polarization, energy band dispersion, and molecular orientation. *Phys. Rev. B*, 92(7):075145, 2015.

[180] John P. Perdew. Density functional theory and the band gap problem. *Int. J. Quantum Chem.*, 28(S19):497–523, 1985.

[181] Paula Mori-Sánchez, Aron J. Cohen, and Weitao Yang. Localization and Delocalization Errors in Density Functional Theory and Implications for Band-Gap Prediction. *Phys. Rev. Lett.*, 100(14):146401, 2008.

[182] S. M. Tadayyon, H. M. Grandin, K. Griffiths, L. L. Coatsworth, P. R. Norton, H. Aziz, and Z. D. Popovic. Reliable and reproducible determination of work function and ionization potentials of layers and surfaces relevant to organic light emitting diodes. *Org. Electron.*, 5(4):199–205, 2004.

[183] The surface profile $z_0(x,y)$ is determined from a fit to the highest COM coordinates. For surface corrugations $\delta z \ll \lambda_{in}$, $\exp\{[-(z_0(x,y)-z_j)/\lambda_{in}]\} \simeq \exp\{[-(z_0-z_j)/\lambda_{in}]\}$ in Eq. (5.1).

[184] Meng-Ting Lee, Hsian-Hung Chen, Chi-Hung Liao, Chih-Hung Tsai, and Chin H. Chen. Stable styrylamine-doped blue organic electroluminescent device based on 2-methyl-9,10-di(2-naphthyl)anthracene. *Appl. Phys. Lett.*, 85(15):3301–3303, 2004.

[185] M.-T. Lee, C.-H. Liao, C.-H. Tsai, and C.-H. Chen. Highly Efficient, Deep-Blue Doped Organic Light-Emitting Devices. *Adv. Mater.*, 17(20):2493–2497, 2005.

[186] Chi-Hung Liao, Meng-Ting Lee, Chih-Hung Tsai, and Chin H. Chen. Highly efficient blue organic light-emitting devices incorporating a composite hole transport layer. *Appl. Phys. Lett.*, 86(20):203507, 2005.

[187] Meng-Huan Ho, Yao-Shan Wu, Shih-Wen Wen, Meng-Ting Lee, Teng-Ming Chen, Chin H. Chen, Kwong-Chau Kwok, Shu-Kong So, Kai-Tai Yeung, Yuen-Kit Cheng, and Zhi-Qiang Gao. Highly efficient deep blue organic electroluminescent device based on 1-methyl-9,10-di(1-naphthyl)anthracene. *Appl. Phys. Lett.*, 89(25):252903, 2006.

[188] Jinhai Huang, Jian-Hua Su, and He Tian. The development of anthracene derivatives for organic light-emitting diodes. *J. Mater. Chem.*, 22(22):10977, 2012.

[189] Meng-Huan Ho, Meng-Yu Liu, Kuan-Heng Lin, Chin H. Chen, and Ching W. Tang. 39.2: Efficient Single-Layer Small Molecule Blue OLEDs Based on a Multifunctional Bipolar Transport Material. *SID Symp. Dig. Tech. Pap.*, 41(1):552, 2010.

[190] Dae Hyun Ahn, Jae Ho Jeong, Jie Song, Ju Young Lee, and Jang Hyuk Kwon. Highly Efficient Deep Blue Fluorescent Organic Light-Emitting Diodes Boosted by Thermally Activated Delayed Fluorescence Sensitization. *ACS Appl. Mater. Interf.*, 10(12):10246, 2018.

[191] C.H.L. Weijtens at al., unpublished.

[192] Tobias Neumann, Denis Danilov, Christian Lennartz, and Wolfgang Wenzel. Modeling disordered morphologies in organic semiconductors. *J. Comput. Chem.*, 34(31):2716–2725, 2013.

[193] Pascal Friederich, Reinder Coehoorn, and Wolfgang Wenzel. Molecular Origin of the Anisotropic Dye Orientation in Emissive Layers of Organic Light Emitting Diodes. *Chem. Mater.*, 29(21):9528–9535, 2017.

[194] Pascal Friederich, Vadim Rodin, Florian von Wrochem, and Wolfgang Wenzel. Built-In Potentials Induced by Molecular Order in Amorphous Organic Thin Films. *ACS Appl. Mater. Interfaces*, 10(2):1881–1887, 2018.

[195] Brent H. Besler, Kenneth M. Merz, and Peter A. Kollman. Atomic charges derived from semiempirical methods. *J. Comput. Chem.*, 11(4):431–439, 1990.

[196] L. J. Sham and T. M. Rice. Many-Particle Derivation of the Effective-Mass Equation for the Wannier Exciton. *Phys. Rev.*, 144(2):708–714, 1966.

[197] Lars Hedin and Stig Lundqvist. Effects of Electron-Electron and Electron-Phonon Interactions on the One-Electron States of Solids. In Frederick Seitz, David Turnbull, and Henry Ehrenreich, editors, *Solid State Physics*, volume 23, pages 1–181. Academic Press, January 1970.

[198] Mark S. Hybertsen and Steven G. Louie. First-Principles Theory of Quasiparticles: Calculation of Band Gaps in Semiconductors and Insulators. *Phys. Rev. Lett.*, 55(13):1418–1421, September 1985.

[199] Michael Rohlfing, Peter Krüger, and Johannes Pollmann. Efficient scheme for GW quasiparticle band-structure calculations with applications to bulk Si and to the Si(001)-(2×1) surface. *Phys. Rev. B*, 52(3):1905–1917, July 1995.

[200] Jens Wehner, Lothar Brombacher, Joshua Brown, Christoph Junghans, Onur Çaylak, Yuriy Khalak, Pranav Madhikar, Gianluca Tirimbó, and Björn Baumeier. Electronic Excitations in Complex Molecular Environments: Many-Body Green's Functions Theory in VOTCA-XTP. *J. Chem. Theory Comput.*, 14(12):6253–6268, 2018.

[201] Frank Neese. The ORCA program system. *WIREs Comput. Mol. Sci.*, 2(1):73–78, 2012.

[202] Rick A. Kendall, Thom H. Dunning, and Robert J. Harrison. Electron Affinities of the First-row Atoms Revisited. Systematic Basis Sets and Wave Functions. *J. Chem. Phys.*, 96(9):6796–6806, 1992.

[203] Florian Weigend, Andreas Köhn, and Christof Hättig. Efficient use of the correlation consistent basis sets in resolution of the identity MP2 calculations. *J. Chem. Phys.*, 116(8):3175–3183, 2002.

[204] John P. Perdew, Kieron Burke, and Matthias Ernzerhof. Generalized Gradient Approximation Made Simple. *Phys. Rev. Lett.*, 77(18):3865–3868, 1996.

[205] Carlo Adamo and Vincenzo Barone. Toward reliable density functional methods without adjustable parameters: The PBE0 model. *J. Chem. Phys.*, 110(13):6158–6170, 1999.

[206] Matthias Ernzerhof and Gustavo E. Scuseria. Assessment of the Perdew–Burke–Ernzerhof exchange-correlation functional. *J. Chem. Phys.*, 110(11):5029–5036, 1999.

[207] Dorothea Golze, Marc Dvorak, and Patrick Rinke. The GW Compendium: A Practical Guide to Theoretical Photoemission Spectroscopy. *Front. Chem.*, 7:377, 2019.

[208] Paul Larson, Marc Dvorak, and Zhigang Wu. Role of the plasmon-pole model in the *GW* approximation. *Phys. Rev. B*, 88(12):125205, 2013.

[209] Falk May, Björn Baumeier, Christian Lennartz, and Denis Andrienko. Can Lattice Models Predict the Density of States of Amorphous Organic Semiconductors? *Phys. Rev. Lett.*, 109(13):136401, 2012.

[210] Björn Baumeier, Michael Rohlfing, and Denis Andrienko. Electronic Excitations in Push–Pull Oligomers and Their Complexes with Fullerene from Many-Body Green's Functions Theory with Polarizable Embedding. *J. Chem. Theory Comput.*, 10(8):3104–3110, 2014.

[211] Tobias Schwabe, Kristian Sneskov, Jógvan Magnus Haugaard Olsen, Jacob Kongsted, Ove Christiansen, and Christof Hättig. PERI–CC2 A Polarizable Embedded RI-CC2 Method. *J. Chem. Theory Comput.*, 8(9):3274–3283, 2012.

[212] Jing Li, Gabriele D'Avino, Ivan Duchemin, David Beljonne, and Xavier Blase. Combining the Many-Body GW Formalism with Classical Polarizable Models: Insights on the Electronic Structure of Molecular Solids. *J. Phys. Chem. Lett.*, 7(14):2814–2820, 2016.

[213] Jing Li, Gabriele D'Avino, Ivan Duchemin, David Beljonne, and Xavier Blase. Accurate description of charged excitations in molecular solids from embedded many-body perturbation theory. *Phys. Rev. B*, 97(3):035108, 2018.

[214] Curt M. Breneman and Kenneth B. Wiberg. Determining atom-centered monopoles from molecular electrostatic potentials. The need for high sampling density in formamide conformational analysis. *J. Comput. Chem.*, 11(3):361–373, 1990.

[215] Anthony Stone. *The Theory of Intermolecular Forces, 2nd Edition*. Oxford University Press, Oxford, 2nd edition edition, 2013.

[216] Lili Cao and Ulf Ryde. On the Difference Between Additive and Subtractive QM/MM Calculations. *Front. Chem.*, 6:89, 2018.

[217] Eric G. Kratz, Robert E. Duke, and G. Andrés Cisneros. Long-range electrostatic corrections in multipolar/polarizable QM/MM simulations. *Theor. Chem. Acc.*, 135(7), 2016.

[218] Axel Arnold and Christian Holm. Efficient Methods to Compute Long-Range Interactions for Soft Matter Systems. In Christian Holm and Kurt Kremer, editors, *Advanced Computer Simulation Approaches for Soft Matter Sciences II*, Advances in Polymer Science, pages 59–109. Springer Berlin Heidelberg, Berlin, Heidelberg, 2005.

[219] Heinz Gerischer and Frank Willig. Reaction of Excited Dye Molecules at Electrodes. *Top. Curr. Chem.*, 61:31–84, 1976.

[220] Martin Pope and Charles E. Swenberg. *Electronic Processes in Organic Crystals and Polymers*. Monographs on the Physics and Chemistry of Materials. Oxford University Press, 2 edition, 1999.

[221] Xander de Vries, Pascal Friederich, Wolfgang Wenzel, Reinder Coehoorn, and Peter A. Bobbert. Full quantum treatment of charge dynamics in amorphous molecular semiconductors. *Phys. Rev. B*, 97(7):075203, 2018.

[222] Xander de Vries, Pascal Friederich, Wolfgang Wenzel, Reinder Coehoorn, and Peter A. Bobbert. Triplet exciton diffusion in metalorganic phosphorescent host-guest systems from first principles. *Phys. Rev. B*, 99(20):205201, may 2019.

[223] Taras Petrenko and Frank Neese. Analysis and prediction of absorption band shapes, fluorescence band shapes, resonance raman intensities, and excitation profiles using the time-dependent theory of electronic spectroscopy. *J. Chem. Phys.*, 127(16):164319, 2007.

[224] W. R. Salaneck. Intermolecular Relaxation Energies in Anthracene. *Phys. Rev. Lett.*, 40(1):60–63, 1978.

[225] A. Devos and M. Lannoo. Electron-phonon coupling for aromatic molecular crystals: Possible consequences for their superconductivity. *Phys. Rev. B*, 58(13):8236–8239, 1998.

[226] Wei-Qiao Deng and William A. Goddard. Predictions of Hole Mobilities in Oligoacene Organic Semiconductors from Quantum Mechanical Calculations. *J. Phys. Chem. B*, 108(25):8614–8621, jun 2004.

[227] M.-T. Lee, C.-H. Liao, C.-H. Tsai, and C. H. Chen. Highly Efficient, Deep-Blue Doped Organic Light-Emitting Devices. *Advanced Materials*, 17(20):2493–2497, 2005.

[228] Chi-Hung Liao, Meng-Ting Lee, Chih-Hung Tsai, and Chin H. Chen. Highly efficient blue organic light-emitting devices incorporating a composite hole transport layer. *Appl. Phys. Lett.*, 86(20):203507, May 2005.

[229] Meng-Huan Ho, Yao-Shan Wu, Shih-Wen Wen, Meng-Ting Lee, Teng-Ming Chen, Chin H. Chen, Kwong-Chau Kwok, Shu-Kong So, Kai-Tai Yeung, Yuen-Kit Cheng, and Zhi-Qiang Gao. Highly efficient deep blue organic electroluminescent device based on 1-methyl-9,10-di(1-naphthyl)anthracene. *Appl. Phys. Lett.*, 89(25):252903, December 2006.

[230] Jinhai Huang, Jian-Hua Su, and He Tian. The development of anthracene derivatives for organic light-emitting diodes. *J. Mater. Chem.*, 22(22):10977–10989, May 2012.

[231] Dae Hyun Ahn, Jae Ho Jeong, Jie Song, Ju Young Lee, and Jang Hyuk Kwon. Highly Efficient Deep Blue Fluorescent Organic Light-Emitting Diodes Boosted by Thermally Activated Delayed Fluorescence Sensitization. *ACS Appl. Mater. Interfaces*, 10(12):10246–10253, March 2018.

[232] Gianluca Tirimbó, Xander de Vries, Christ H. L. Weijtens, Peter A. Bobbert, Tobias Neumann, Reinder Coehoorn, and Björn Baumeier. Quantitative predictions of photoelectron spectra in amorphous molecular solids from multiscale quasiparticle embedding. *Phys. Rev. B*, 101(3):035402, January 2020.

[233] Hiroyuki Yoshida. Measuring the electron affinity of organic solids: An indispensable new tool for organic electronics. *Anal Bioanal Chem*, 406(9):2231–2237, April 2014.

[234] Hiroyuki Yoshida, Kazuto Yamada, Jun'ya Tsutsumi, and Naoki Sato. Complete description of ionization energy and electron affinity in organic solids: Determining contributions from electronic polarization, energy band dispersion, and molecular orientation. *Phys. Rev. B*, 92(7):075145, August 2015.

[235] Yuki Uemura, Syed A. Abd-Rahman, Susumu Yanagisawa, and Hiroyuki Yoshida. Quantitative analysis of the electrostatic and electronic polarization energies in molecularly mixed films of organic semiconductors. *Phys. Rev. B*, 102(12):125302, September 2020.

[236] H.Yoshida et al., unpublished.

[237] R.Coehoorn at al., unpublished.

[238] Jing Li, Gabriele D'Avino, Ivan Duchemin, David Beljonne, and Xavier Blase. Accurate description of charged excitations in molecular solids from embedded many-body perturbation theory. *Phys. Rev. B*, 97(3):035108, January 2018.

[239] Jens Wehner, Lothar Brombacher, Joshua Brown, Christoph Junghans, Onur Çaylak, Yuriy Khalak, Pranav Madhikar, Gianluca Tirimbó, and Björn Baumeier. Electronic Excitations in Complex Molecular Environments: Many-Body Green's Functions Theory in VOTCA-XTP. *J. Chem. Theory Comput.*, 14(12):6253–6268, December 2018.

[240] Anthony J. Stone. Distributed Multipole Analysis: Stability for Large Basis Sets. *Journal of Chemical Theory and Computation*, 1(6):1128–1132, November 2005.

[241] Eric G. Kratz, Robert E. Duke, and G. Andrés Cisneros. Long-range electrostatic corrections in multipolar/polarizable QM/MM simulations. *Theor Chem Acc*, 135(7), July 2016.

[242] Axel Arnold and Christian Holm. Efficient Methods to Compute Long-Range Interactions for Soft Matter Systems. In Christian Holm and Kurt Kremer, editors, *Advanced Computer Simulation Approaches for Soft Matter Sciences II*, Advances in Polymer Science, pages 59–109. Springer Berlin Heidelberg, Berlin, Heidelberg, 2005.

[243] Curt M. Breneman and Kenneth B. Wiberg. Determining atom-centered monopoles from molecular electrostatic potentials. The need for high sampling density in formamide conformational analysis. *Journal of Computational Chemistry*, 11(3):361–373, 1990.

[244] B.T. Thole. Molecular polarizabilities calculated with a modified dipole interaction. *Chemical Physics*, 59(3):341–350, August 1981.

[245] Frank Neese. The ORCA program system. *WIREs Computational Molecular Science*, 2(1):73–78, 2012.

[246] Carlo Adamo and Vincenzo Barone. Toward reliable density functional methods without adjustable parameters: The PBE0 model. *The Journal of Chemical Physics*, 110(13):6158–6170, March 1999.

[247] G. Tirimbó, V. Sundaram, O. Çaylak, W. Scharpach, J. Sijen, C. Junghans, J. Brown, F. Zapata Ruiz, N. Renaud, J. Wehner, and B. Baumeier. Excited-state electronic structure of molecules using many-body Green's functions: Quasiparticles and electron–hole excitations with VOTCA-XTP. *J. Chem. Phys.*, 152(11):114103, March 2020.

[248] Florian Weigend, Andreas Köhn, and Christof Hättig. Efficient use of the correlation consistent basis sets in resolution of the identity MP2 calculations. *J. Chem. Phys.*, 116(8):3175–3183, February 2002.

[249] Dorothea Golze, Marc Dvorak, and Patrick Rinke. The GW Compendium: A Practical Guide to Theoretical Photoemission Spectroscopy. *Front. Chem.*, 7, 2019.

[250] Paul Larson, Marc Dvorak, and Zhigang Wu. Role of the plasmon-pole model in the GW approximation. *Phys. Rev. B*, 88(12):125205, September 2013.

[251] Nicolas Dupuy, Samira Bouaouli, Francesco Mauri, Sandro Sorella, and Michele Casula. Vertical and adiabatic excitations in anthracene from quantum Monte Carlo: Constrained energy minimization for structural and

electronic excited-state properties in the JAGP ansatz. *J. Chem. Phys.*, 142(21):214109, June 2015.

[252] As in bare anthracene, the respective correction is negligible for the ionization potential (HOMO) and was not included in the results in [232].

[253] M. P. Seah and W. A. Dench. Quantitative electron spectroscopy of surfaces: A standard data base for electron inelastic mean free paths in solids. *Surface and Interface Analysis*, 1(1):2–11, February 1979.

[254] Yusuke Ozawa, Yasuo Nakayama, Shin'ichi Machida, Hiroumi Kinjo, and Hisao Ishii. Maximum probing depth of low-energy photoelectrons in an amorphous organic semiconductor film. *Journal of Electron Spectroscopy and Related Phenomena*, 197:17–21, December 2014.

[255] X. de Vries and R. Coehoorn. Vibrational mode contribution to the dielectric permittivity of disordered small-molecule organic semiconductors. *Phys. Rev. Materials*, 4(8):085602, August 2020.

[256] Xander de Vries, Pascal Friederich, Wolfgang Wenzel, Reinder Coehoorn, and Peter A. Bobbert. Full quantum treatment of charge dynamics in amorphous molecular semiconductors. *Phys. Rev. B*, 97(7):075203, February 2018.

[257] Taras Petrenko and Frank Neese. Analysis and prediction of absorption band shapes, fluorescence band shapes, resonance Raman intensities, and excitation profiles using the time-dependent theory of electronic spectroscopy. *J. Chem. Phys.*, 127(16):164319, October 2007.

[258] Weining Han, Hiroyuki Yoshida, Nobuo Ueno, and Satoshi Kera. Electron affinity of pentacene thin film studied by radiation-damage free inverse photoemission spectroscopy. *Appl. Phys. Lett.*, 103(12):123303, September 2013.

[259] The ZPVE correction for the S_1 state has been estimated using time-dependent DFT.

[260] Gianluca Tirimbò and Björn Baumeier. Non-adiabatic couplings and conversion dynamics between localized and charge transfer excitations from many-body green's functions theory. *ChemRxiv*, 2023.

[261] Elisa Collado-Fregoso, Silvina N. Pugliese, Mariusz Wojcik, Johannes Benduhn, Eyal Bar-Or, Lorena Perdigón Toro, Ulrich Hörmann, Donato Spoltore, Koen Vandewal, Justin M. Hodgkiss, and Dieter Neher. Energy-gap law for photocurrent generation in fullerene-based organic solar cells: The case of low-donor-content blends. *Journal of the American Chemical Society*, 141(6):2329–2341, 2019.

[262] Jürg Hutter, Marcella Iannuzzi, Florian Schiffmann, and Joost VandeVondele. cp2k: atomistic simulations of condensed matter systems. *Wiley Interdiscip. Rev. Comput. Mol. Sci.*, 4(1):15–25, 2014.

[263] L. Martínez, R. Andrade, E. G. Birgin, and J. M. Martínez. PACKMOL: A package for building initial configurations for molecular dynamics simulations. *J. Comput. Chem.*, 30(13):2157–2164, 2009.

[264] Giovanni Bussi, Davide Donadio, and Michele Parrinello. Canonical sampling through velocity rescaling. *J. Chem. Phys.*, 126(1):014101, 2007.

[265] Giovanni Bussi, Tatyana Zykova-Timan, and Michele Parrinello. Isothermal-isobaric molecular dynamics using stochastic velocity rescaling. *J. Chem. Phys.*, 130(7):074101, 2009.

[266] Rudolph A. Marcus. Electron transfer reactions in chemistry. Theory and experiment. *Rev. Mod. Phys.*, 65(3):599–610, July 1993.

[267] Geoffrey R. Hutchison, Mark A. Ratner, and Tobin J. Marks. Hopping Transport in Conductive Heterocyclic Oligomers: Reorganization Energies and Substituent Effects. *J. Am. Chem. Soc.*, 127(7):2339–2350, February 2005.

[268] Joseph E. Subotnik, Robert J. Cave, Ryan P. Steele, and Neil Shenvi. The initial and final states of electron and energy transfer processes: Diabatization as motivated by system-solvent interactions. *J. Chem. Phys.*, 130(23):234102, June 2009.

[269] Clyde Edmiston and Klaus Ruedenberg. Localized Atomic and Molecular Orbitals. *Rev. Mod. Phys.*, 35(3):457–464, July 1963.

[270] Robert J. Cave and Marshall D. Newton. Generalization of the Mulliken-Hush treatment for the calculation of electron transfer matrix elements. *Chemical Physics Letters*, 249(1):15–19, January 1996.

[271] Robert J. Cave and Marshall D. Newton. Calculation of electronic coupling matrix elements for ground and excited state electron transfer reactions: Comparison of the generalized Mulliken–Hush and block diagonalization methods. *J. Chem. Phys.*, 106(22):9213–9226, June 1997.

[272] N. S. Hush. Adiabatic theory of outer sphere electron-transfer reactions in solution. *Trans. Faraday Soc.*, 57(0):557–580, January 1961.

[273] Yuezhi Mao, Andrés Montoya-Castillo, and Thomas E. Markland. Excited state diabatization on the cheap using DFT: Photoinduced electron and hole transfer. *J. Chem. Phys.*, 153(24):244111, December 2020.

[274] Carlo Adamo and Vincenzo Barone. Toward reliable density functional methods without adjustable parameters: The PBE0 model. *J. Chem. Phys.*, 110(13):6158–6170, April 1999.

[275] Florian Weigend and Reinhart Ahlrichs. Balanced basis sets of split valence, triple zeta valence and quadruple zeta valence quality for H to Rn: Design and assessment of accuracy. *Phys. Chem. Chem. Phys.*, 7(18):3297–3305, August 2005.

[276] Florian Weigend, Marco Häser, Holger Patzelt, and Reinhart Ahlrichs. RI-MP2: Optimized auxiliary basis sets and demonstration of efficiency. *Chemical Physics Letters*, 294(1):143–152, September 1998.

[277] Jeng-Da Chai and Martin Head-Gordon. Long-range corrected hybrid density functionals with damped atom–atom dispersion corrections. *Phys. Chem. Chem. Phys.*, 10(44):6615–6620, November 2008.

[278] Elisa Collado-Fregoso, Silvina N. Pugliese, Mariusz Wojcik, Johannes Benduhn, Eyal Bar-Or, Lorena Perdigón Toro, Ulrich Hörmann, Donato Spoltore, Koen Vandewal, Justin M. Hodgkiss, and Dieter Neher. Energy-Gap Law for Photocurrent Generation in Fullerene-Based Organic Solar Cells: The Case of Low-Donor-Content Blends. *J. Am. Chem. Soc.*, 141(6):2329–2341, February 2019.

[279] Jürg Hutter, Marcella Iannuzzi, Florian Schiffmann, and Joost VandeVondele. Cp2k: Atomistic simulations of condensed matter systems. *WIREs Computational Molecular Science*, 4(1):15–25, 2014.

[280] L. Martínez, R. Andrade, E. G. Birgin, and J. M. Martínez. PACKMOL: A package for building initial configurations for molecular dynamics simulations. *Journal of Computational Chemistry*, 30(13):2157–2164, 2009.

[281] Giovanni Bussi, Davide Donadio, and Michele Parrinello. Canonical sampling through velocity rescaling. *J. Chem. Phys.*, 126(1):014101, January 2007.

[282] Giovanni Bussi, Tatyana Zykova-Timan, and Michele Parrinello. Isothermal-isobaric molecular dynamics using stochastic velocity rescaling. *J. Chem. Phys.*, 130(7):074101, February 2009.

[283] G. Tirimbó, V. Sundaram, O. Çaylak, W. Scharpach, J. Sijen, C. Junghans, J. Brown, F. Zapata Ruiz, N. Renaud, J. Wehner, and B. Baumeier. Excited-state electronic structure of molecules using many-body Green's functions: Quasiparticles and electron–hole excitations with VOTCA-XTP. *The Journal of Chemical Physics*, 152(11):114103, March 2020.

[284] Marshall D. Newton. Quantum chemical probes of electron-transfer kinetics: The nature of donor-acceptor interactions. *Chem. Rev.*, 91(5):767–792, July 1991.

[285] James Kirkpatrick. An approximate method for calculating transfer integrals based on the ZINDO Hamiltonian. *International Journal of Quantum Chemistry*, 108(1):51–56, 2008.

[286] J.C. Butcher. *Numerical Methods for Ordinary Differential Equations*. John Wiley & Sons Inc, New York, second edition edition, 2008.

[287] Martin Schlipf, Henry Lambert, Nourdine Zibouche, and Feliciano Giustino. Sternheimergw: A program for calculating gw quasiparticle band structures and spectral functions without unoccupied states. *Computer Physics Communications*, 247:106856, 2020.

[288] Jan Wilhelm, Dorothea Golze, Leopold Talirz, Jürg Hutter, and Carlo A. Pignedoli. Toward ¡i¿GW¡/i¿ Calculations on Thousands of Atoms. *J. Phys. Chem. Lett.*, 9(2):306–312, 1 2018.

[289] Arno Förster and Lucas Visscher. Low-order scaling g0w0 by pair atomic density fitting. *Journal of Chemical Theory and Computation*, 16(12):7381–7399, 2020. PMID: 33174743.

[290] D. Foerster, P. Koval, and D. Sanchez-Portal. An O(N3) implementation of Hedin's GW approximation for molecules. *The Journal of Chemical Physics*, 135(7):074105, 08 2011.

[291] Ivan Duchemin and Xavier Blase. Separable resolution-of-the-identity with all-electron Gaussian bases: Application to cubic-scaling RPA. *The Journal of Chemical Physics*, 150(17):174120, 05 2019.

[292] H N Rojas, R W Godby, and R J Needs. Space-time method for ab initio calculations of self-energies and dielectric response functions of solids. *Phys. Rev. Lett.*, 74(10):1827–1830, 1995.

[293] Jan Wilhelm, Patrick Seewald, and Dorothea Golze. Low-scaling gw with benchmark accuracy and application to phosphorene nanosheets. *Journal of Chemical Theory and Computation*, 17(3):1662–1677, 2021.

[294] Vojtech Vlcek, Eran Rabani, Daniel Neuhauser, and Roi Baer. Stochastic gw calculations for molecules. *Journal of Chemical Theory and Computation*, 13(10):4997–5003, 2017.

[295] Steven W. Rick. A polarizable, charge transfer model of water using the drude oscillator. *Journal of Computational Chemistry*, 37(22):2060–2066, 2016.

[296] Sudipta Kumar Sinha, Mohit Mehta, and Sandeep Patel. A charge equilibration formalism for treating charge transfer effects in md simulations: Application to water clusters. *Journal of Computational Chemistry*, 38(16):1389–1409, 2017.

[297] John P. Pederson and Jesse G. McDaniel. DFT-based QM/MM with particle-mesh Ewald for direct, long-range electrostatic embedding. *The Journal of Chemical Physics*, 156(17):174105, 05 2022.

[298] S. Palm, Prasad D., and Mukherjee D. On certain correspondences among various coupled-cluster theories for closed-shell systems. *Pramana – Journal of Physics — Indian Academy of Sciences*, pages 261–270, 1982.

[299] Troy Van Voorhis and Martin Head-Gordon. Benchmark variational coupled cluster doubles results. *Journal of Chemical Physics*, 113(20):8873–8879, 11 2000.

[300] Bridgette Cooper and Peter J. Knowles. Benchmark studies of variational, unitary and extended coupled cluster methods. *Journal of Chemical Physics*, 133(23):234102, 12 2010.

[301] Francesco A. Evangelista. Alternative single-reference coupled cluster approaches for multireference problems: The simpler, the better. *Journal of Chemical Physics*, 134(22):224102, 6 2011.

[302] Bogumil Jeziorski and Hendrik J. Monkhorst. Coupled-cluster method for multideterminantal reference states. *Physical Review A*, 24(4):1668–1681, 10 1981.

[303] Ingvar Lindgren and Debashis Mukherjee. On the connectivity criteria in the open-shell coupled-cluster theory for general model spaces. *Physics Reports*, 151(2):93–127, 7 1987.

[304] Kristian Sneskov and Ove Christiansen. Excited state coupled cluster methods. *WIREs Computational Molecular Science*, 2(4):566–584, 2012.

[305] Xiao Wang and Timothy C. Berkelbach. Excitons in Solids from Periodic Equation-of-Motion Coupled-Cluster Theory. *Journal of Chemical Theory and Computation*, 16(5):3095–3103, 5 2020.

[306] Thomas Gruber, Ke Liao, Theodoros Tsatsoulis, Felix Hummel, and Andreas Grüneis. Applying the coupled-cluster ansatz to solids and surfaces in the thermodynamic limit. *Phys. Rev. X*, 8:021043, May 2018.

[307] Felix Hummel. Finite temperature coupled cluster theories for extended systems. *Journal of Chemical Theory and Computation*, 14(12):6505–6514, 2018.

[308] Malte F. Lange and Timothy C. Berkelbach. Active space approaches combining coupled-cluster and perturbation theory for ground states and excited states. *Molecular Physics*, 118(19-20):e1808726, 10 2020.

[309] Yang Gao, Qiming Sun, Jason M. Yu, Mario Motta, James McClain, Alec F. White, Austin J. Minnich, and Garnet Kin-Lic Chan. Electronic structure of bulk manganese oxide and nickel oxide from coupled cluster theory. *Phys. Rev. B*, 101:165138, Apr 2020.

[310] Luning Zhao and Eric Neuscamman. Variational Excitations in Real Solids: Optical Gaps and Insights into Many-Body Perturbation Theory. *Physical Review Letters*, 123(3):036402, 7 2019.

[311] A. Williamson, Randolph Q. Hood, R. Needs, and G. Rajagopal. Diffusion quantum Monte Carlo calculations of the excited states of silicon. *Physical Review B - Condensed Matter and Materials Physics*, 57(19):12140–12144, 5 1998.

[312] R. J. Hunt, M. Szyniszewski, G. I. Prayogo, R. Maezono, and N. D. Drummond. Quantum Monte Carlo calculations of energy gaps from first principles. *Physical Review B*, 98(7):075122, 8 2018.

[313] Fengjie Ma, Shiwei Zhang, and Henry Krakauer. Excited state calculations in solids by auxiliary-field quantum Monte Carlo. *New Journal of Physics*, 15(9):093017, 9 2013.

Appendix A

Experimental details for LEIPS and Absorption expertiments for MADN isomers

In the following the details on the experimental setups used to produce

Low-energy inverse photoemission

The experimental setup was the following: ITO-coated glass plates were used as substrates. The ITO substrates were washed with acetone and isopropanol and then treated by UV-ozone. The MADN thin films were chosen to be of 5 nm or 10 nm thicknesses. They were prepared by the vacuum deposition technique. The LEIPS measurements were performed without exposing the sample to air. Regarding the experiments, they were performed with different detection photon wavelengths of 193 nm, 260 nm, 285 nm and 335 nm. The electron affinities (EA), measured not directly but by taking the onset of the tangent, at the three detection wavelengths of 260 nm, 285 nm and 335 nm nm distributed between 2.09 and 2.24 eV. The smaller the detection wavelength is 1 eV, the higher the electron affinity becomes. Although the reason of the photon energy dependence is not clear,

a slight sample charging seems to be reason for this wavelength dependency, in particular for α-MADN.

Absorption spectra

The author of the manuscript is currently awaiting the provision of detailed information pertaining to the experimental setup from the individuals responsible for executing the experiments.

Appendix B

Dirac's bra-ket notation

Bra–ket notation is a notation for linear algebra and linear operators on complex vector spaces together with their dual space both in the finite-dimensional and infinite-dimensional case. It is specifically designed to ease the types of calculations that frequently come up in quantum mechanics.

In quantum mechanics , the state of physical system is indentified with a vector in a complex separable Hilbert space $\mathcal{H}$, or equivalently by a point in the projective Hilbert space of the system. Each vector in this space is called *ket*, indicated with the symbol $|\cdot\rangle$. In a finite dimensional space, a ket can be seen as a column vector given a basis for the Hilbert space, written out in components,

$$|\psi\rangle = \begin{bmatrix} c_1 \\ c_2 \\ \vdots \\ c_m \end{bmatrix} \tag{B.1}$$

In infinite dimensional space there are inifinitely many components (possibly even uncountably many). The nice thing about this notation is the possibility of express these ininitely many components vectors with the same notation of finite-dimensional ones, allowing to have a simple tool for manipulate quantum-mechanical states.

Every ket $|\psi\rangle$ has a dual *bra*, indicated as $|\psi\rangle$. In a finite dimensional space the bra corresping to Eq. (B.1) would be

---

$$\langle\psi| = \begin{bmatrix} c_1 & c_2 & \cdots & c_m \end{bmatrix}. \tag{B.2}$$

This is a continuous linear functional from $\mathcal{H}$ to the complex numbers $\mathbb{C}$, defined by:

$$\langle\psi| : \mathcal{H} \longrightarrow \mathbb{C} : \langle\psi|\,(|\phi\rangle) = IP(|\psi\rangle, |\phi\rangle) \quad \text{for all kets } |\phi\rangle \tag{B.3}$$

where $IP(\cdot, \cdot)$ indicates the inner product defined on the Hilbert space. The inner product is thus usually indicated using $\langle\psi|\phi\rangle$, from which the name bra-ket notation.

Since bras and kets are vectors in a Hermitian vector space they can be manipulated using the usual rules of linear algebra.

- Given any bra $\langle\psi|$, and kets $|\phi_1\rangle$ and $|\phi_2\rangle$, and complex numbers c_1 and c_2, since bras are linear functionals

$$\langle\psi|\,(c_1\,|\phi_1\rangle + c_2\,|\phi_2\rangle) = c_1\,\langle\psi|\phi_1\rangle + c_2\,\langle\psi|\phi_2\rangle \tag{B.4}$$

- Given any kets $|\phi_1\rangle$ and $|\phi_2\rangle$, and complex numbers c_1 and c_2, from the property of the inner product

$$c_1\,|\phi_1\rangle + c_2\,|\phi_2\rangle \quad \text{is dual to} \quad c_1^*\,\langle\phi_1| + c_2^*\,\langle\phi_2| \tag{B.5}$$

- Given ant bra $\langle\psi|$ and ket $ket\phi$, by property of the inner product

$$\langle\psi|\phi\rangle = \langle\phi|\psi\rangle^* \tag{B.6}$$

In quantum-mechanics linear operator are ubiquitous. For instance, observable physical quantities are represented by self-adjointe operators whereas transformation processes are represented with unitary linear operators. These linear operators $A : \mathcal{H} \to \mathcal{H}$ act on kets $|\phi\rangle$ and spits out another ket $A\,|\phi\rangle$. Operators can also be viewed as acting on bras from the right hand side. Composing the bra $\langle\psi|$ with the operator A results in the bra $\langle\psi|\,A$, defined as a linear functional on $\mathcal{H}$ by the rule

$$(\langle\psi|\,A)\,|\phi\rangle = \langle\psi|\,(A\,|\phi\rangle) \tag{B.7}$$

this is usualy expressed as $\langle\psi|\,A\,|\phi\rangle$. Sometimes linear operator on $\mathcal{H}$ are defined by the outer product: if $\langle\psi|$ is a bra and $|\phi\rangle$ is a ket, the outer product $|\psi\rangle\,\langle\phi|$ denotes the rank one operator that maps the ket $|\chi\rangle$ to the ket $|\psi\rangle\,\langle\phi|\chi\rangle$. Just as kets and bras can be transformed into each other, the element from the dual space

correspoding to $A\,|\psi\rangle$ is $\langle\psi|\,A^\dagger$, with $A^\dagger$ the Hermitian conjugate of the operator A.

Two Hilber spaces V and W may form a third Hilbert space $V \otimes W$ by a tensor product. This may comes hany if one has to deal with a system of subsystems described by V and W respectively. If $|\psi\rangle$ is a ket in V, and $|\phi\rangle$ is a ket in W, the tensor product of the two kets is a ket in $V \otimes W$. This is usually written in different ways

$$|\psi\rangle\,|\phi\rangle = |\psi\rangle \otimes |\phi\rangle = |\psi, \phi\rangle \tag{B.8}$$

Sometimes in quantum-mechanics it is useful to work with the projections of state vectors onto particular basis, rather than the vectors themselves. The projections are simply complex numbers, and can be formulated in terms of partial differential equations. For instance, the space of a zero-spin point particle is spanned by a position basis $\{|\mathbf{r}\rangle\}$, where the label $\mathbf{r}$ spans over the set of position vectors. Given any ket ψ, we can define the complex scalar function of $\mathbf{r}$, known as wavefunction is defined as

$$\psi(\mathbf{r}) := \langle\mathbf{r}|\psi\rangle. \tag{B.9}$$

The same holds for linear operators acting on wavefunctions. For a linear operator A acting on a wavefunction we have the equality

$$A\psi(\mathbf{r}) = \langle\mathbf{r}|\,A\,|\psi\rangle. \tag{B.10}$$

Appendix C

Quantum Mechanics Principles

Quantum Mechanics Theory can be constructed based on three ingredients (postulates):

- Quantum mechanics degree of freedom can be discrete or continuous. They can be one or infinitely many. Each one is denoted by ϕ; the collection of all its values forms the space F.

- The state space in quantum mechanics is a Hilbert space. The state space is denoted by V and an element of V is $|\psi\rangle \in V$. The dual space V_D consists of all the mapping, denoted by $\langle\chi|$, of V to complex numbers. The expression $\langle\psi|\chi\rangle = \langle\chi|\psi\rangle^*$ is the inner product.

- Operators $\hat{O}$ that act on V and map it to itself $\hat{O} : V \to V$. The space of operators is denoted by $Q = V \otimes V_D$. The tensor of two states vectors is given by $|\chi\rangle \otimes \langle\psi| = |\chi\rangle \langle\psi| \in V \otimes V_D$.

- All eigenvalues of a Hermitian operator $\hat{O} = \hat{O}^\dagger$ are real and can represent physically observed quantities. The Hermitian conjugation of an operator, denoted by $\langle\chi| \hat{O} |\psi\rangle^* = \langle\psi| \hat{O}^\dagger |\chi\rangle$.

In general given two observables we have that $[\hat{O}_i, \hat{O}_j] \neq 0$. The physical observed value is given by $\langle\psi| \hat{O} |\psi\rangle$ with $|\psi\rangle$ being the quantum state describing the observable state.

Consider the eigenfunctions and eigenvalues of a Hermitian operator given by

$$\hat{O}\left|\psi_n\right\rangle = \lambda_n\left|\psi_n\right\rangle;\left\langle\psi_n|\psi_m\right\rangle = \delta_{n,m} \tag{C.1}$$

All Hermitian operators have the following spectral decomposition in terms of their eigenvalues and eigenfunctions

$$\hat{O} = \sum_n \lambda_n\left|\psi_n\right\rangle\left\langle\psi_n\right| \tag{C.2}$$

Therefore the eigenvectors form a complete set of vectors (just using $\hat{O} = \hat{\mathbb{1}}$, the unity operator)

$$\hat{\mathbb{1}} = \sum_n\left|\psi_n\right\rangle\left\langle\psi_n\right| = \sum_n\hat{P}_n \tag{C.3}$$

where we define the projection operator $\hat{P}_n = \hat{P}_n^2$.
Every state vector has its decomposition

$$\left|\chi\right\rangle = \hat{\mathbb{1}}\left|\chi\right\rangle = \sum_n\left|\psi_n\right\rangle\left\langle\psi_n|\chi\right\rangle = \sum_n c_n\left|\psi_n\right\rangle \tag{C.4}$$

with

$$c_n = \left\langle\psi_n|\chi\right\rangle \tag{C.5}$$

it follows that

$$\left\langle\chi|\chi\right\rangle = 1 \rightarrow \sum_n|c_n|^2 = 1 \rightarrow |c_n|^2 \in [0,1] \tag{C.6}$$

Appendix D

Second quantization and Fock space

In many-body theory one often starts from a product wave function describing a set of non interacting particles that occupy given orbits (called the reference state). This could be a Slater determinant for fermions or a macroscopic condensate orbit for bosons.

Since removing a hole orbit from the reference state leads to a systems with fewer particles, we extend the use latin hole indices to indicate states of $N-1, N-2, \ldots$ particles. Here, N is the number of particles in the referecnce state. Analogously, particle indices will be used to distinguish states of $N-1, N-2, \ldots$ particles. This notation will include labelling exact many-body eigenstates of the Hamiltoninan.

D.1 Second Quantization

Most of the processes described by many-body Green's functions involve the transfer of particles to/from the intital sysytem. Thus it is useful to extend the Hilbert space to allow for states with different particle numbers. In fact we will use the Fock space which includes a complete basis set for each possible number of particles, from zero (the vacuum) to infinity. The basis states of the Fock space can be taken to be product of one-body wave functions and must be automatically symmetrized or antisymmetrized (for bosons and fermions, respectively). Using Dirac's bra and ket notation one can specify the basis states just by saying how many particles n_α

are contained in each single particle orbit α. For istance we can build a state with $\sum_\alpha n_\alpha = 8$ particles distributed over different orbitals such as

$$|n_1 = 2, n_2 = 0, n_3 = 1, n_4 = 5, \ldots\rangle \tag{D.1}$$

Of course this example represents a bosonic state (Pauli's exclusion principle is violated here).

In general the completeness relation here reads as

$$\mathbb{1} = \sum_{n_1}^{n_{max}} \sum_{n_2}^{n_{max}} \cdots \sum_{n_\alpha}^{n_{max}} \cdots |n_1, n_2, n_3, \ldots\rangle \langle n_1, n_2, n_3, \ldots| \tag{D.2}$$

and includes the vacuum state $|0\rangle = |n_\alpha = 0, \forall \alpha\rangle$. n_{max} is 1 for fermions and ∞ for bososns. States with different number of particles are orthogonal by definition. A brief summary of fermions and bosons.

D.1.1 Creation and annihilation particles operators

Changes in the particle numbers are performed by the so-called creation and annihilation operators. These operators act on vectors in Fock space and, as their names suggest. they add or remove one particle in a specific orbital. Their effect on Fock states is the same as that for the creation and annihilation of harmonic oscillator quanta in the linear oscillator problem

$$c_\alpha^\dagger |n_1, n_2, n_3, \ldots, n_\alpha, \ldots\rangle = \phi_\alpha \sqrt{1 + n_\alpha} |n_1, n_2, n_3, \ldots, n_\alpha + 1, \ldots\rangle \tag{D.3}$$

$$c_\alpha |n_1, n_2, n_3, \ldots, n_\alpha, \ldots\rangle = \phi_\alpha \sqrt{n_\alpha} |n_1, n_2, n_3, \ldots, n_\alpha - 1, \ldots\rangle \tag{D.4}$$

where ϕ_α is a phase factor that should embody the symmetry of the wavefunction (symmetric for boson; antisymmetric for fermions). Distinction between fermion and boson can be achieved defining proper commutation rules between these operators retrieving the correct Pauli statistics (i.e, occupation number for fermions is either 1 or 0)

$$[c_\alpha, c_\beta^\dagger] = \delta_{\alpha,\beta}, \quad [c_\alpha, c_\beta] = [c_\alpha^\dagger, c_\beta^\dagger] = 0, \quad \text{for Bosons} \tag{D.5}$$

$$\{c_\alpha, c_\beta^\dagger\} = \delta_{\alpha,\beta}, \quad \{c_\alpha, c_\beta\} = \{c_\alpha^\dagger, c_\beta^\dagger\} = 0, \quad \text{for Fermions} \tag{D.6}$$

The anticommutator implies antysymmetrization of the fermions wavefunctions and fix the fermion occupation number to be 1 or 0. For Bosons $\phi_\alpha = 1$. For

Fermions the phase is usually chosen as

$$c_\alpha^\dagger \left|n_1, n_2, n_3, \ldots, n_\alpha, \ldots\right\rangle = \delta_{0,\alpha}(-1)^{s_\alpha}\sqrt{1+n_\alpha}\left|n_1, n_2, n_3, \ldots, n_\alpha + 1, \ldots\right\rangle \quad \text{(D.7)}$$

$$c_\alpha \left|n_1, n_2, n_3, \ldots, n_\alpha, \ldots\right\rangle = \delta_{1,\alpha}(-1)^{s_\alpha}\sqrt{n_\alpha}\left|n_1, n_2, n_3, \ldots, n_\alpha - 1, \ldots\right\rangle \quad \text{(D.8)}$$

with $s_\alpha = n_1 + n_2 + n_3 + \cdots + n_{\alpha-1}$.

From these relations it follows that $c_\alpha^\dagger c_\alpha \left|n_\alpha\right\rangle = n_\alpha \left|n_\alpha\right\rangle$. We can thus define the number of particles operator as

$$\hat{N} = \sum_\alpha c_\alpha^\dagger c_\alpha \tag{D.9}$$

The eigenvalues of $\hat{N}$ are non negative integers and its eigenstates are wave functions with a definite number of particle. To create a basis vector we can apply several times on $\left|0\right\rangle$ with creation operators. The normalized many-body wavefunctions reads

$$\left|n_1, n_2, n_3, \ldots\right\rangle = \frac{1}{\sqrt{n_1! n_2! n_3! \ldots}} (c_1^\dagger)^{n_1} (c_2^\dagger)^{n_2} (c_3^\dagger)^{n_3} \ldots \left|0\right\rangle \tag{D.10}$$

D.1.2 Creation and annihilation field operators

The creation operator for a particle in position r of coordinate space is indicated by $\psi(\mathbf{r})$. If $\{u_\alpha(\mathbf{r})\}$ are the single particle wave functions of a general orthonormal basis, the creation (and annihilation) operators in the two representation are related via a unitary transformation

$$\psi^\dagger(\mathbf{r}) = \sum_\alpha c_\alpha^\dagger u_\alpha^*(\mathbf{r}) \tag{D.11}$$

$$c_\alpha^\dagger = \int \psi^\dagger(\mathbf{r}) u_\alpha(\mathbf{r}) d\mathbf{r} \tag{D.12}$$

It follows that to create a particle in a state α one simply superimposes eigenstates of position with weights given by the corresponding wave function

$$\left|\alpha\right\rangle = c_\alpha^\dagger \left|0\right\rangle = \int u_\alpha(\mathbf{r}) \left|\mathbf{r}\right\rangle d\mathbf{r} \tag{D.13}$$

with $\left|\mathbf{r}\right\rangle = \psi^\dagger(\mathbf{r}) \left|0\right\rangle$ being a particle localized at position $\mathbf{r}$. Analogously, one can extract the first quantization wave function corresponding to a one-body Fock state by

$$u_\alpha(\mathbf{r}) = \left\langle \mathbf{r} | \alpha \right\rangle \tag{D.14}$$

These relations can be generalized to states of any number of particles as

$$|\mathbf{r}_1, \mathbf{r}_2, \cdots, \mathbf{r}_N\rangle = \frac{1}{\sqrt{N!}} \psi^\dagger(\mathbf{r}_1) \psi^\dagger(\mathbf{r}_2) \dots \psi^\dagger(\mathbf{r}_N) |0\rangle \tag{D.15}$$

$$\langle \mathbf{r}_1, \mathbf{r}_2, \cdots, \mathbf{r}_N | n_1, n_2, \dots\rangle = \Phi(\mathbf{r}_1, \mathbf{r}_2, \mathbf{r}_3, \dots; \{n\}) \tag{D.16}$$

D.2 Operators in Fock space

We build a formalism for describing operators in second quantization. Although it is possible to make it general, we will focus on one- and two-particles operators as they are important in describing the many-electron Hamiltonian. We explicitly derive the operator form for the one-body operator keeping in mind that the same approach should be use for higher order operators.

D.2.1 One body operators

Let $O = O(r)$ be a one-body operator that acts independently on each particle of the systems. The expression for its matrix elements in coordinate systems depends on the number of particles N and is

$$\langle \mathbf{r}_1, \mathbf{r}_1, \dots | O | \mathbf{r}_1, \mathbf{r}_1, \dots\rangle = \Big(\prod_{j=1}^N \delta(\mathbf{r}_j - \mathbf{r}'_j) \Big) \sum_{i=1}^N O(\mathbf{r}_i) \tag{D.17}$$

for a generic Fock state

$$\langle n'_1, n'_2, \dots | O | n_1, n_2, \dots\rangle =$$

$$= \sum_{i=1}^N \int d\mathbf{r}_1 \int d\mathbf{r}_2 \cdots \int d\mathbf{r}_N \langle n'_1, n'_2, \dots | \mathbf{r}_1, \mathbf{r}_2, \cdots, \mathbf{r}_N\rangle O(\mathbf{r}_i) \times$$

$$\langle \mathbf{r}_1, \mathbf{r}_2, \cdots, \mathbf{r}_N | n_1, n_2, \dots\rangle =$$

$$= \frac{1}{N!} \sum_{i=1}^N \int d\mathbf{r}_1 \int d\mathbf{r}_2 \cdots \int d\mathbf{r}_N \langle n'_1, n'_2, \dots | \psi^\dagger(\mathbf{r}_1) \dots \psi^\dagger(\mathbf{r}_N) |0\rangle O(\mathbf{r}_i) \times$$

$$\langle 0 | \psi(\mathbf{r}_N) \dots \psi(\mathbf{r}_1) | n_1, n_2, \dots\rangle =$$

$$= \frac{1}{(N-1)!} \int d\mathbf{r}_1 \int d\mathbf{r}_2 \cdots \int d\mathbf{r}_N \langle n'_1, n'_2, \dots | \psi^\dagger(\mathbf{r}_1) \dots \psi^\dagger(\mathbf{r}_N) |0\rangle O(\mathbf{r}_1) \times$$

$$\langle 0 | \psi(\mathbf{r}_N) \dots \psi(\mathbf{r}_1) | n_1, n_2, \dots\rangle$$

Now recalling that $|0\rangle\langle 0| = \mathbb{1}$, $\int d\mathbf{r}\psi^\dagger(\mathbf{r})\psi(\mathbf{r}) = N$ we are left with

$$\langle n'_1, n'_2, \ldots| O |n_1, n_2, \ldots\rangle = \int d\mathbf{r}\, \langle n'_1, n'_2, \ldots| \psi^\dagger(\mathbf{r})O(\mathbf{r})\psi(\mathbf{r}) |n_1, n_2, \ldots\rangle \quad \text{(D.18)}$$

so we have

$$O = \int d\mathbf{r}\psi^\dagger(\mathbf{r})O(\mathbf{r})\psi(\mathbf{r}) = \sum_{\alpha\beta} O_{\alpha\beta}c_\alpha^\dagger c_\beta \quad \text{(D.19)}$$

with

$$O_{\alpha\beta} = \int d\mathbf{r}u_\alpha^*(\mathbf{r})O(\mathbf{r})u_\beta(\mathbf{r}) \quad \text{(D.20)}$$

D.2.2 Two bodies operators

Given a two-body operator

$$V = \sum_{i<j}^{N} V(\mathbf{r}_i, \mathbf{r}_j) \quad \text{(D.21)}$$

one obtain

$$V = \int d\mathbf{r}_1 \int d\mathbf{r}_2 \psi^\dagger(\mathbf{r}_1)\psi^\dagger(\mathbf{r}_2)V(\mathbf{r}_1, \mathbf{r}_2)\psi(\mathbf{r}_2)\psi(\mathbf{r}_1) =$$
$$= \frac{1}{2}\sum_{\alpha,\beta,\gamma,\delta} V_{\alpha,\beta,\gamma,\delta}c_\alpha^\dagger c_\alpha^\dagger c_\delta c_\gamma \quad \text{(D.22)}$$

with

$$V_{\alpha,\beta,\gamma,\delta} = \int d\mathbf{r}_1 \int d\mathbf{r}_2 u_\alpha^*(\mathbf{r}_1)u_\beta^*(\mathbf{r}_2)V(\mathbf{r}_1, \mathbf{r}_2)u_\gamma(\mathbf{r}_2)u_\delta(\mathbf{r}_1) \quad \text{(D.23)}$$

D.3 Expectation values

Let's asume that that we have a state $|\psi^N\rangle$ of a system of N particles. The expectation value of a one-body operator O can be calculated with a simple sum involving the one-body reduced density matrix, which is defined as

$$\rho_{\alpha\beta} = \langle\psi^N| c_\beta^\dagger c_\alpha |\psi^N\rangle \quad \text{(D.24)}$$

so the expectation value is

$$\left\langle \psi^N \middle| O \middle| \psi^N \right\rangle = \sum_{\alpha\beta} \rho_{\beta\alpha} O_{\alpha\beta} = Tr(\rho\, O) \qquad (D.25)$$

and of course

$$Tr(\rho) = N \qquad (D.26)$$

These results are particularly interesting since the theory of many-body Green's functions does not attempt any calculation of the full many-body wave function. Rather the focus is on determining directly quantities related to the density matrices, which are calculated in terms of basic excitation modes of the system. Thus, even if one does not compute the complete ground state wave function, these eqautions tell us that it is still possible to extract the expectation values of interesting observables.

It is also useful to insert the complete set of eigenstates $\{\left|\psi^{N-1}\right\rangle\}$ of the (N-1)-body system in Eq.D.24 we obtain

$$\rho_{\alpha\alpha} = <c_\alpha^\dagger c_\alpha> = \sum_k |\left\langle \psi_k^{N-1} \middle| c_\alpha \middle| \psi_k^N \right\rangle|^2 \qquad (D.27)$$

This result is interesting because the overlap function $\left\langle \psi_k^{N-1} \middle| c_\alpha \middle| \psi_k^N \right\rangle$ gives the probability amplitude that the system collapses into a state $\left|\psi_k^{N-1}\right\rangle$ after remove of a particle in the state α in $\left|\psi_k^N\right\rangle$.

In an analogous way, we introduce the two-body reduced density matrix

$$\Gamma_{\alpha\beta\gamma\delta} = \left\langle \psi_k^N \middle| c_\alpha^\dagger c_\beta^\dagger c_\gamma c_\delta \middle| \psi_k^N \right\rangle \qquad (D.28)$$

Appendix E

Quantum Mechanics picture

Different quantum mechanics pictures:

Heisenberg picture

- Ket state: Constant
- Observable: $A_H(t) = \exp\{iH_S t\} A_S \exp\{-iH_S t\}$
- Density: Constant

Interaction picture

- Ket state: $|\psi_I(t)\rangle = \exp\{-iH_{0,S}\} |\psi_I(t)\rangle$
- Observable: $A_I(t) = \exp\{iH_{0,S} t\} A_S \exp\{-iH_{0,S} t\}$
- Density: $\rho_I(t) = \exp\{iH_{0,S} t\} \rho_S \exp\{-iH_{0,S} t\}$

Schrödinger picture

- Ket state: $|\psi_S(t)\rangle = \exp\{iH_S t\} |\psi_S(0)\rangle$
- Observable: constant
- Density: $\rho_S(t) = \exp\{-iH_S t\} \rho_S(0)$

Appendix F

Many-electron wave-function approaches

Coupled Cluster Theory

Coupled cluster (CC) theory exploits the basic Hartree–Fock molecular orbital method and constructs multi-electron wave functions using the exponential cluster operator to account for electron correlation:

$$|\psi\rangle = \exp(T) \left|\Psi_0^{\mathrm{HF}}\right\rangle, \tag{F.1}$$

with $T = \sum_{i=1} T_i$ the cluster operator and T_i the i-th excitation operator ($i = 1$ single excitation, $i = 2$ double excitation and so on). This formulation provides in principle the exact solution to the time-independent Schrödinger equation Eq. (2.6) but makes the problem non-Hermitian and the obtained energy non-variational.

Variationally optimized coupled cluster [298] overcomes this problem but can only be applied to small systems [299, 300, 301]. Another drawback is the computational cost of most coupled-cluster implementations that makes these methods suitable only for small molecules, in general. CC methods scale at best as $\mathcal{O}(N^p)$, where p is a relatively high power (e.g., $p = 7$ for coupled cluster including single and double excitations, with triples treated perturbatively) and development of a efficient techniques is an active field of

research. CC has been successfully used for excited state calculations [302, 303, 304]. Wang and Berkelback [305] have recently shown that Equation-of-Motion Coupled-Cluster Theory can yield promising results for optical excitation energies, exciton binding energies, exciton dispersion relations, and exciton–phonon interaction energies of simple crystalline solids like Si, C, SiC, MgO, or LiF. Other attempts are made in this direction for ground-state and excited-state methods that combine CC and perturbation theory based on a partitioning of excitations that are internal or external to an active space [306, 307, 308, 309].

Configuration interaction

Configuration interaction (CI) is another post-Hartree–Fock linear variational method for quantum chemical multi-electron systems. Mathematically, *configuration* describes the linear combination of Slater determinants used for the wave function. In order to account for electron correlation, CI uses a variational wave function that is a linear combination of configuration state functions (CSFs) built from spin orbital Slater determinants of the kind of Eq. (2.31)

$$|\psi\rangle = \sum_{I=0} c_I |\Psi_I\rangle. \tag{F.2}$$

If the expansion includes all possible CSFs of the appropriate symmetry, then this is a full configuration interaction procedure which exactly solves the electronic Schrödinger equation within the space spanned by the one-particle basis set. If only one spin orbital differs, we describe this as a single excitation determinant. If two spin orbitals differ it is a double excitation determinant and so on. Due to the long CPU time and large memory required for CI calculations, the method is limited to relatively small systems.

Quantum Monte Carlo

Quantum Monte Carlo (QMC) has been very successful in performing large-scale calculations for extended systems in quantum chemistry. The method

relies on the stochastic estimation of the energy of a trial wave function according to

$$E_{\text{trial}} = \frac{\int \psi_{\text{trial}}(\mathbf{r}) \widehat{H} \psi_{\text{trial}}(\mathbf{r}) \mathrm{d}^{3N}\mathbf{r}}{\int \psi_{\text{trial}}(\mathbf{r}) \psi_{\text{trial}}(\mathbf{r}) \mathrm{d}^{3N}\mathbf{r}}. \tag{F.3}$$

For the calculation of excited-states, many refined QMC methods have been developed. Variational Monte Carlo (VMC) as presented by Zhao *et al.* [310] allows for the application of a rigorous variational principle to both ground and excited state wave functions. Diffusion Quantum Monte Carlo (DQMC) is very promising for applications to condensed-matter because it explicitly includes electron-electron correlation effects, and it scales reasonably well with system size as shown in the case of a silicon crystal in [311]. These QMC methods offer an accurate means of probing both the ground- and excited-state properties of atoms, molecules, and solids from first principles and with system-size scaling as $\mathcal{O}(N^3)$, albeit with a large prefactor. The methods have been thoroughly reviewed by Hunt *et al.* [312] discussing isolated molecules (anthracene, tetracyanoethylene, benzothiazole and boron trifluoride) and three-dimensional systems (diamond, silicon, cubic boron nitride) and free-standing monolayer phosphorene.

While describing excited states, a major reason of failure is the intrinsic difficulty of maintaining orthogonality with the lower-lying states when the targeted many-body excited state is being represented stochastically in an imaginary-time projection method. Auxiliary-field Quantum Monte Carlo (AFQMC) as discussed in [313] offers a new framework for addressing this difficulty and for performing excited state calculations in solid. Ma *et al.* studied the fundamental gap of prototypical semiconductors, Si and diamond, and of the more challenging wurtzite ZnO crystal being in good agreement with *GW* calculations (see Section 3.4) and experiment, offering a non-perturbative and free of empirical parameters methods for correlated materials.

Curriculum Vitae

Gianluca Tirimbó was born in Frosinone, Italy, in 1992. He obtained his bachelor's degree (*cum laude*) in Physics from Universitá degli studi di Roma Tor Vergata in Rome, Italy, in 2015. In his bachelor's thesis he investigated the statistical mechanics models of turbulent fluids with helicity. He obtained his master's degree (*cum laude*) in Condensed Matter Physics from from Universitá degli studi di Roma Tor Vergata in Rome, Italy, in 2017. In his master's dissertation he investigated Silicon/Germanium nanostructures using ab-initio techniques. Later the same year he started his PhD project at the Technische Universiteit Eindhoven in the Centre of Applied analysis, Scientific computing and Applications (CASA) at the Department of Mathematics and Computer Science, supervised by Björn Baumeier. The results of this research are presented in this dissertation.

List of Publications

[314] Gianluca Tirimbò and Björn Baumeier. Non-adiabatic couplings and conversion dynamics between localized and charge transfer excitations from many-body green's functions theory. *ChemRxiv*, 2023.

[315] Gianluca Tirimbò, Xander de Vries, Christ H. L. Weijtens, Peter A. Bobbert, Tobias Neumann, Reinder Coehoorn, and Björn Baumeier. Quantitative predictions of photoelectron spectra in amorphous molecular solids from multiscale quasiparticle embedding. *Phys. Rev. B*, 101:035402, Jan 2020.

[316] Gianluca Tirimbò and Björn Baumeier. Ab initio modeling of excitons: from perfect crystals to biomaterials. *Advances in Physics: X*, 6(1):1912638, 2021.

[317] Gianluca Tirimbò, V. Sundaram, O. Çaylak, W. Scharpach, J. Sijen, C. Junghans, J. Brown, F. Zapata Ruiz, N. Renaud, J. Wehner, and B. Baumeier. Excited-state electronic structure of molecules using many-body green's functions: Quasiparticles and electron–hole excitations with votca-xtp. *The Journal of Chemical Physics*, 152(11):114103, Sep 2020.

[318] Jens Wehner, Lothar Brombacher, Joshua Brown, Christoph Junghans, Onur Çaylak, Yuriy Khalak, Pranav Madhikar, Gianluca Tirimbò, and Björn Baumeier. Electronic excitations in complex molecular environments: Many-body green's functions theory in votca-

xtp. *Journal of Chemical Theory and Computation*, 14(12):6253–6268, 2018.

Conference contributions

[319] Gianluca Tirimbò. Multiscale polarizable embedding of quasiparticle and electron-hole excitations from many-body Green's functions (GW-BSE) with VOTCA-XTP. In *Faraday joint interest group conference*, volume 2021, march 2021.

[320] Gianluca Tirimbò and Björn Baumeier. Multiscale polarizable embedding of quasiparticle and electron-hole excitations from many-body Green's functions (GW-BSE) with VOTCA-XTP. In *APS March Meeting Abstracts*, volume 2021 of *APS Meeting Abstracts*, march 2021.

[321] Gianluca Tirimbò, Xander de Vries, Peter Bobbert, Reinder Coehoorn, and Björn Baumeier. First-principles photoelectron spectroscopy in molecular solids from multiscale GW-BSE/MM embedding. In *APS March Meeting Abstracts*, volume 2019 of *APS Meeting Abstracts*, page G70.280, January 2019.

[322] Gianluca Tirimbò, Xander de Vries, Peter Bobbert, Reinder Coehoorn, and Björn Baumeier. Quantitative Predictions of Photoelectron Spectra in Amorphous Molecular Solids from Multiscale Quasiparticle Embedding . In *Deutschen Physicalischen Gessellschaft (German Physical Society)*, 2020.

[323] Gianluca Tirimbò, O. Çaylak, and Björn Baumeier. Kernel based Machine Learning Approach to Computing Quasiparticle Energies

within Many-Body Green's Functions Theory. In *Machine Learning for Molecules Workshop @ NeurIPS 2020*, 2020.

Acknowledgements

This Ph.D. journey has been a tapestry of emotions, challenges, and growth. As I stand at the summit, I find it almost impossible to express the depth of my gratitude for the countless individuals and experiences that have shaped this endeavor.

Starting with my supervisor, Björn: Your guidance, mentorship, and unwavering support throughout this research journey have been invaluable. Your insights, feedback, and encouragement have been instrumental in shaping this thesis and more importantly, the man I am today. You have been the compass guiding me through this intellectual wilderness. Your belief in my abilities, your patience in moments of doubt, and your relentless pursuit of excellence have left an indelible mark on me. My deepest thanks for being not just a mentor but also a true inspiration. You give all of yourself for this job, and through all the highs and lows, your students will look back at the time spent together as one of the most important of their lives. I am no exception to that. Thanks again, and I hope all your dreams might come true.

I extend my heartfelt appreciation to the members of my thesis committee, prof. dr. M. Rohlfing, prof.dr.ir. R.A.J. Janssen, dr. P. Rinke and Dr. L. Leppert for their constructive feedback, valuable suggestions, and expertise that enriched the quality of this work. Special mention to R. Coehoorn, who not only played the role of the co-promotor but also showed me that keeping your curiosity and passion about science alive is not impossible. That is the fabric of a great researcher. You will always be an example for me. I would like to acknowledge my research collaborators, both within

and outside the University, whose contributions have significantly enhanced the depth and breadth of my research. Your collaboration has been both inspiring and enlightening.

I would like to thank B. Koren and M. Peletier for leading the CASA group at the University. Your presence, ideas, and support have paved the way for building up an amazing team of gifted and productive people. To all the other members of CASA, both professors and students, I will remember you for the fun moments during parties, coffee breaks, knowledge sharing, and many other activities we have had together. For those in CASA that I never met personally, I wish you the best too. I acknowledge the administrative and technical staff at the University for their assistance and support in various aspects of my research and academic activities. In particular, the secretaries at ICMS and CASA Wendy, Cindy, and Enna for the hard work and dedication you put into your job. Thank you.

Most of my days as a Ph.D. student were spent in the office with the BauRG members: Onur, Vivek, Wouter, Zhong, Jens, Pranav, and Yuri. I think we made the most heterogeneous but incredibly dynamic and intellectually stimulating team I've ever been part of. Each member brought a unique perspective and expertise to our research group, creating an environment that was not only diverse but also exceptionally productive. Working alongside these brilliant individuals was a truly enriching experience that pushed the boundaries of our collective knowledge and created an atmosphere of constant learning and innovation. Thanks for being the best company during this arduous trip. I wish you the best of luck and to find a bit of "our office" in your future.

My deepest appreciation goes to my family for their continuous encouragement. You've stood by me through thick and thin, offering unwavering love and support. This accomplishment is as much yours as it is mine. A Mamma e Papa, grazie per la tenacia, la forza e la capacità di mantenere insieme la nostra famiglia nonostante le distanze. Spero siate orgogliosi di me. Questo, come ogni successo della mia vita, non sarebbe stato possibile senza di voi. Vi sarò grato per sempre, e come sempre, a modo mio. A Lisa, Giuseppe e i piccoli Tommaso e Federico; avete costruito una bellissima famiglia che sono certo vi darà tante soddisfazioni ed emozioni. Sono

contento di farne parte. A Francesco, sono orgoglioso del ragazzo che stai diventando, del tuo impegno costante e della tua dedizione verso i tuoi obiettivi. La tua capacità di affrontare le sfide dell'adolescenza con saggezza e maturità è veramente ammirevole, e so che il tuo futuro sarà luminoso grazie alla tua determinazione. Continuerò a sostenerti in ogni passo del tuo cammino. Un pensiero ai miei nonni che non ci sono più, che so sarebbero orgogliosi di questo mio traguardo. Questo è per voi.

To my friends, who laughed with me in joy and held me through tears of frustration, you made this journey bearable. Your companionship has been my solace. I start with the people I first met when I came to the Netherlands: Daniela, Alberto, Carmine, Luca, Morena, Teresa, Gianmarco, Humberto, Federica, Marta, Christian, Emanuele e Zandra. Thanks for all the good moments, for the help and guidance, and for having made this town a little less colder. To Raj, Alessia, Francesco S., Tommaso, Elisa, Atul, and Victor thanks for I am grateful for the moments we've shared and the bonds we've formed. Your friendship has been an essential part of my life, and I look forward to the adventures we'll continue to embark on together. Last but not least, I would like to thank Vignesh, Angie, Ruud, and Francesco C.; Each of you brings something different to my life, and the diversity of perspectives and experiences you've introduced me to has enriched my world in countless ways. Your friendship and presence have been invaluable, and I cherish the unique qualities and shared moments that you've all contributed to this beautiful mosaic of life we've crafted together.

This acknowledgment would not be complete without mentioning Alice, the pillar of strength in my life, the rock on which I can always rest when tired, and the reference point for my heart's true north. Thanks for joining me in this adventure, for the patience, and, above all, for the love you give me. I love you too.

To all those whose names I may have inadvertently omitted but have nonetheless played a role in my academic journey, your support has not gone unnoticed and is deeply appreciated. To all those who may not find their names here but have, in myriad ways, contributed to my journey - thank you. Your influence is woven into the fabric of my academic and life

tapestry.

This thesis is more than just words on paper; it is a testament to the collective effort of everyone who has touched my life along the way. Your belief in me fueled my perseverance. Your love and support carried me through.

With a heart overflowing with gratitude, I offer my deepest thanks.

<div align="right">

Gianluca Tirimbò
Eindhoven, December 2023

</div>